

The role of the fluid composition in the formation of
hydrothermal Sn-W ores:
Insights from in situ analyses of fluid inclusions
by UV-fs-LA-ICP-MS

Von der Naturwissenschaftlichen Fakultät der
Gottfried Wilhelm Leibniz Universität Hannover

zur Erlangung des Grades

Doktor der Naturwissenschaften (Dr. rer. nat.)

genehmigte Dissertation

von

Moritz Albrecht, M.Sc.

[2017]

Referent: PD Dr.rer.nat Ingo Horn

Korreferent: Prof. Dr.rer.nat Axel Müller

Tag der Promotion: 10.01.2017

Table of Contents

1. Abstract.....	6
2. Zusammenfassung	7
3. Introduction.....	8
3.1 Fluid inclusion analyses in geosciences	8
3.2 Laser ablation of fluid inclusions	13
3.3 Complexation of Sn and its distribution between melt and fluid	16
3.4 Source of metals: Geochemical heritage or fractional crystallization.....	19
4. Development of the UV-fs-LA-ICP-MS method for frozen fluid inclusions	21
4.1 Instrumentation.....	21
4.2 Experimental observations during low temperature ablation	26
4.3 Calibration	28
4.4 Synthetic fluid inclusions for method validation.....	29
4.5 Ablation procedure	31
4.6 Data Processing	32
4.7 Results and discussion.....	33
4.7.1 Accuracy and precision	33
4.7.2 Limits of detection.....	37
4.8 Conclusions	38
4.9 Incorporation of a <i>Linux CNC</i> controlled laser stage	39
5. Case study: Fluid inclusions in Sn-W granites	50
5.1 Introduction	50
5.2 Sample locations.....	52
5.2.1 Erzgebirge.....	52
5.2.1.1 Altenberg-Teplice caldera (ATC).....	52
5.2.1.2 Gottesberg – Grummetstock.....	55

5.2.2	Porth Ledden - Land's End granite (Cornwall, UK).....	58
5.3	Analytical methods	60
5.3.1	Microthermometry	60
5.3.2	fs-LA-ICP-MS	61
5.3.2.1	Trace elements in fluid inclusions	61
5.3.2.2	Trace elements in quartz	62
5.4	Results.....	68
5.4.1	Fluid inclusion petrography and microthermometry	68
5.4.1.1	Zinnwald Sn-W-Li deposit (sample: ZinQ)	68
5.4.1.2	Schellerhau granite.....	72
5.4.1.3	Porth Ledden – tourmaline granite.....	74
5.4.1.4	Gottesberg – Grummetstock hydrothermal smoky quartz	76
5.4.2	fs-LA-ICP-MS results	77
5.4.2.1	Fluid inclusions: Zinnwald, Schellerhau and Porth Ledden	78
5.4.2.2	Fluid inclusions: Gottesberg - Grummetstock	80
5.4.2.3	Analytical uncertainty	81
5.4.2.4	Trace elements in quartz	90
5.5	Discussion	97
5.5.1	Fluid chemistry	97
5.5.1.1	Chemical evolution of mineralizing fluids.....	97
5.5.1.2	Relation Sn and W	101
5.5.1.3	Comparison of Zinnwald fluid inclusion literature data	112
5.5.1.4	Comparison: Erzgebirge vs. Cornwall	116
5.5.2	Quartz chemistry	119
5.5.2.1	Comparing fluid and quartz chemistry.....	125
5.5.3	Geothermobarometry with “TitaniQ”	127
5.6	Conclusions.....	132
6.	Outlook.....	135

7. References	139
8. Acknowledgements	156
9. Curriculum Vitae	158
10. List of Publications	160

1. Abstract

We have developed a new analytical setup for the determination of trace element concentrations in frozen fluid inclusions by UV-fs-LA-ICP-MS. Laser ablation was performed at a low temperature of -40°C by using a modified heating-freezing stage as the ablation cell. With this method it was possible to successfully analyze 53 of 55 frozen synthetic NaCl-H₂O fluid inclusions in quartz, covering a size range between $8\mu\text{m}$ and $25\mu\text{m}$ down to a depth of $50\mu\text{m}$. The high success rate could be achieved as the 194nm UV-fs-laser allows an excellent control for the opening procedure of frozen fluid inclusions and is an improvement compared to analyses by ns-LA at room temperature. A *Linux CNC* controlled laser stage enables the analyses of inclusions $> 25\mu\text{m}$ in diameter by a fast moving spiral pattern ablation. Trace element analyses were performed with a fast scanning magnetic sector field ICP-MS. The lower limits of detection for fluid inclusion analyses vary from $0.1\mu\text{g/g}$ (for ^{209}Bi) to $10\mu\text{g/g}$ (for ^{39}K) in inclusions $< 25\mu\text{m}$ and can go down to $0.0006\mu\text{g/g}$ (^{182}W) with the spiral ablation in larger and high saline inclusions. The typical analytical uncertainty, depending on the element and respective concentration level, ranges between 10% and 30% (1RSD), based on the reproducibility of experimentally synthesized fluid inclusions. All elements from a stock solution, which behaved inert during the HP/HT experiments (B, K, Cd, Te, Tl, Pb and Bi), could be recovered in the synthetic inclusions at concentrations that correspond within their specific analytical uncertainties to their original concentration of $53\mu\text{g/g}$. The method represents a highly efficient tool for the determination of accurate trace element data on low concentration levels in small fluid inclusions with a high success rate of $> 90\%$. The latter is particularly advantageous considering the commonly time consuming characterization of fluid inclusions.

In a case study about granite related Sn-W mineralizations, we have analyzed fluid inclusions by microthermometry and UV-fs-LA-ICP-MS to investigate the role of the fluid composition during the formation of granite-derived hydrothermal Sn-W-Li ores. Different fluid inclusion generations in a single crystal of miarolitic quartz from the mineralized zone of the Zinnwald Sn-W-Li deposit (Erzgebirge) were analyzed. It could be demonstrated that medium saline fluids (5 – 8 mass% NaCl_{eq}) as well as high saline brines (28 – 31 mass% NaCl_{eq}) carried significant amounts of Sn and W into the cupola part of the pluton and were involved into the ore formation in the greisen and vein style deposit. Primary two-phase inclusions yielded $140\mu\text{g/g}$ Sn and $30\mu\text{g/g}$ W. A decreasing trend in the metal content towards younger inclusion generations is correlating with decreasing salinity. Immiscibility from an originally single-phase fluid resulted in the enrichment of metals and other trace elements in the brine phase ($224\mu\text{g/g}$ Sn; $84\mu\text{g/g}$ W). Additional measurements of the trace elements in the host quartz allow a better understanding of the PT conditions prevailing during the quartz (and ore-) formation. Ti-in-quartz thermobarometry in combination with the fluid inclusion isochores indicate a PT range of 0.35 – 1.14 kbar at $405 - 510^{\circ}\text{C}$, based on the very low Ti concentration of $1.31 \pm 0.45\mu\text{g/g}$. Trace elements in quartz that are sensitive to fractional crystallization processes (e.g. Ge, Ti, Al, Li) yield information about the parental fluid of the quartz that originated from an extremely fractionated melt. The combination of the concentration values from the hydrothermal quartz with the values from the underlying zinnwaldite and biotite granite quartz result in a fractionation trend from the less evolved biotite granite quartz towards the stronger evolved hydrothermal quartz.

The processes leading to the extraction of Sn and W from a pre-enriched melt are discussed on the basis of fluid inclusion analyses of primary brine inclusions in the magmatic quartz from two different Sn-W specialized granites (Schellerhau granite, Altenberg-Teplice caldera and Land's End granite, Cornwall). The F-rich Schellerhau fluids were able to leach up to $2370\mu\text{g/g}$ Sn and $1000\mu\text{g/g}$ W from the melt, whereas the Land's End fluids carried up to $370\mu\text{g/g}$ Sn and $300\mu\text{g/g}$ W.

Keywords: Femtosecond laser ablation, fluid inclusions, quartz, trace elements, hydrothermal tin-tungsten deposits, metal mobility, Ti-in-quartz geothermobarometry.

2. Zusammenfassung

Mit der Entwicklung einer neuartigen Methode zur Analyse von Spuren-, Neben- und Hauptelementgehalten in Flüssigkeitseinschlüssen mittels UV-fs-LA-ICP-MS im gefrorenen Zustand wurde eine Verbesserung der bisherigen Analysetechniken erlangt. Eine modifizierte Heiz-Kühlzelle dient als Laserablationzelle und erlaubt es Analysen bei niedrigen Temperaturen durchzuführen. Anhand einer Validierung der Methode mittels Messungen an synthetischen Flüssigkeitseinschlüssen in Quarz mit bekannten Elementgehalten im Fluid konnte gezeigt werden, dass mit dieser Methode eine sehr hohe Zuverlässigkeit beim Öffnen der Einschlüsse erreicht wird. 53 von 55 analysierten Einschlüssen lieferten zeitaufgelöste Laserablationssignale, die zur Datenauswertung verwendet werden konnten. Mit der Analyse im gefrorenen Zustand konnten die aus der Analytik mit ns-Lasern bekannten Probleme, wie z.B. das unkontrollierte Platzen der Einschlüsse und damit verbundener Probenmaterialverlust, überwunden werden und die Zuverlässigkeit der Analysen auf eine Erfolgsquote von über 90 % für Flüssigkeitseinschlüsse in Quarz mit einem Durchmesser von 8 – 25 μm und einer Tiefe bis zu 50 μm gesteigert werden. Eine Steuerung des XYZ-Tisches der Laserablationseinheit mittels *Linux CNC* Software erlaubt es auch Einschlüsse zu analysieren, die wesentlich größer sind als der eigentliche Laserspot. Hierzu wird ein benutzerdefiniertes, sich schnell bewegendes Spiralmuster mit dem Laserspot mit einer hohen Laserfrequenz von bis zu 500 Hz abgefahren. Typische Nachweisgrenzen für die Punktanalysen liegen zwischen 0.1 $\mu\text{g/g}$ (^{209}Bi) bis 10 $\mu\text{g/g}$ (^{39}K). Analysen größerer Einschlüsse mit den CNC Spiralmustern können die Nachweisgrenzen bis auf 0.0006 $\mu\text{g/g}$ für ^{182}W senken. Die Messungenauigkeiten belaufen sich auf 10 – 30 % (1RSD), basierend auf der Reproduzierbarkeit der Ergebnisse der synthetischen Einschlüsse.

Die Anwendung der Methode auf natürliche Proben wurde anhand von Flüssigkeitseinschlüssen aus Sn-W Graniten und damit assoziierten mineralisierten Zonen durchgeführt. Verschiedene Einschlussgenerationen in einem hydrothermalen Quarz-Einkristall aus der Sn-W-Li Lagerstätte Zinnwald (Erzgebirge) wurden mikrothermometrisch und anschließend mittels UV-fs-LA-ICP-MS untersucht. In medium salinaren Fluiden (5 – 8 mass% NaCl_{eq} ; 140 $\mu\text{g/g}$ Sn, 30 $\mu\text{g/g}$ W) und hochsalinaren Laugen (28 – 31 mass% NaCl_{eq} ; 224 $\mu\text{g/g}$ Sn, 84 $\mu\text{g/g}$ W) konnten signifikante Mengen Sn und W nachgewiesen werden, die sie in die oberen Bereiche des Granit-Plutons transportierten und dort die Erzmineralisation generierten. Der Metallgehalt der Fluide nimmt dabei mit ihrer Salinität ab, was für eine Komplexierung von Sn und W mit Cl^- spricht. Ein superkritisches einphasiges Fluid reicherte sich über die Zeit in Salinität und Metallgehalt ab, ehe eine Phasentrennung nach einem Druckverlust die hochsalinaren Laugen-Einschlüsse produzierte, wo sich die Metalle erneut anreicherten. Spurenelementmessungen am Quarz-Einkristall erlaubten es den druck- und temperaturabhängigen Ti-Gehalt im Quarz zu bestimmen und mittels Ti-in-Quarz Thermobarometrie in Kombination mit den berechneten Isochoren der Einschlüsse einen Druck-Temperatur Bereich für die Bildung des Quarzes abzuschätzen (0.35 – 1.14 kbar bei 405 – 510°C). Weitere Spurenelemente im Quarz (Ge, Al, Li) sind Indikatoren des Fraktionierungsgrades der Schmelze. In Kombination mit den Spurenelementdaten aus magmatischen Quarzen des Granitkörpers ergibt sich ein klarer Fraktionierungstrend mit zunehmender Fraktionierung zum hydrothermalen Quarz.

Die Mobilisierung von Sn und W aus der angereicherten Schmelze wurde anhand hochsalinärer, primärer Einschlüsse in magmatischen Quarzen untersucht. Die Fluide zweier Sn-W spezialisierter Granite (Schellerhau Granit, Erzgebirge und Land's End Granit, Cornwall) wurden hierzu verglichen. In den Einschlüssen des F- und Cl-reichen Schellerhau Granits wurden bis zu 2370 $\mu\text{g/g}$ Sn und 1000 $\mu\text{g/g}$ W gefunden, während in den Fluiden des B- und Cl-reichen Land's End Granits 370 $\mu\text{g/g}$ Sn und 300 $\mu\text{g/g}$ W nachgewiesen wurden.

Schlagwörter: Femtosekunden Laser Ablation, Flüssigkeitseinschlüsse, Quarz, Spurenelemente, hydrothermale Zinn-Wolfram Lagerstätten, Mobilität von Metallen, Ti-in-Quarz Geothermobarometrie.

3. Introduction

3.1 Fluid inclusion analyses in geosciences

The only way to get information about crustal paleo-fluids is to investigate fluid inclusions that can be hosted in many different minerals of the earth crust (e.g. quartz, calcite, fluorite). Fluids in the earth interior are important for the transport of materials, volatiles, the heat transfer, chemical water-rock interactions, metasomatism and the development of several types of hydrothermal ore deposits. The insight into geological processes that we can earn from investigations of fluid inclusions is therefore of huge importance and provides an important geochemical tool that increased our understanding of crustal processes in the last decades. Fluid inclusions provide a variety of information about fluid properties like the fluid salinity, density, temperature and chemical composition at the time of trapping (Roedder 1984). The determination of fluid inclusion compositions can be achieved by several micro analytical methods, with the cryometric observation of phase transitions by microthermometry being the most important and primary method in fluid inclusion research. The interpretation of the temperature of phase transitions in an inclusion yields to its chemical composition in terms of dissolved major cations and possible contributions of other volatile phases than H₂O, like CO₂ or CH₄. The characterization of phase equilibria for binary and ternary aqueous systems (e.g. NaCl – H₂O or NaCl – KCl – H₂O) has been achieved by experimental studies with synthetic fluid inclusions or by theoretical calculations. The research group of Bodnar et al. has published 20 synthetic fluid inclusion studies about different aqueous systems including the NaCl-H₂O system (Bodnar and Sterner 1985, Bodnar and Vityk 1994, Figure 1), NaCl-KCl-H₂O (Sterner et al. 1988), NaCl-CaCl₂-H₂O (Vanko et al. 1988) and NaCl-FeCl₂-H₂O (Steele-MacInnis et al. 2015). The melting temperature of the last solid phase during heating is used to calculate the bulk salinity in the system NaCl-H₂O, expressed as NaCl equivalent (NaCl_{eq}) in mass% NaCl_{eq}. (Bodnar and Vityk 1994). This value represents the sum of all dissolved major cations in the fluid without giving information about the ratio of Na⁺/ K⁺ / Ca²⁺ and others. But the identification of other solutes than Na⁺ can be achieved by microthermometry when considering the temperature of first melting (first appearance of liquid in a frozen inclusion during heating), which is generally representing the eutectic point of a specific aqueous system (Table 1). If possible, the melting temperature of other phases like salt-hydrates (e.g. hydrohalite NaCl*2H₂O or antarcticite CaCl₂*6H₂O) can be determined

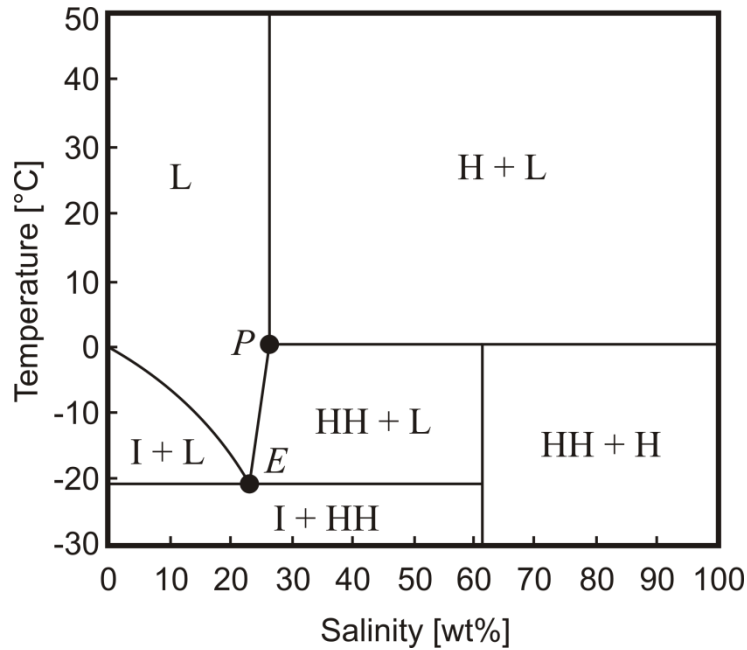


Figure 1: Vapor-saturated phase relations in the NaCl-H₂O system at low temperatures from Bodnar and Vityk (1994). I = ice, L = liquid, H = halite, HH = hydrohalite, P = peritectic (0.1°C, 26.3 wt% NaCl), E = eutectic (-21.2°C, 23.2 wt% NaCl)

during heating, which allows an precise estimation of the ratio Na/K (Hall et al. 1988), Na/Ca²⁺ (Steele-MacInnis et al. 2011) or Na/Fe²⁺ (Lecumberri-Sanchez et al. 2015) if the melting temperatures are applied on the specific phase equilibria of an aqueous system.

What makes a fluid inclusion study even more meaningful is the combination of the microthermometric results with hereon based in-situ micro analytical analyses with LA-ICP-MS or micro-PIXE. The first micro analytical approaches to determine trace and minor element contents in fluid inclusions were conducted by Tsui and Holland 1979 as well as by Bennett and Grant 1980, Shepherd and Chenery 1995. The numbers of conducted studies increased with the development of the first LA-ICP-MS method for fluid inclusions by Shepherd and Chenery 1995 and its enhancement by Günther et al. 1998. Since at least Heinrich et al. 2003 and Allan et al. 2005 validated the results of this complicated analytical procedure to be accurate and precise, the number of conducted studies increased and LA became the method of choice for trace element determinations in fluid inclusions. The in-situ analyses by LA overcomes most of the reported problems of bulk crush-leach analyses (e.g. Yardley et al. 1993) and others (PIXE, Ryan et al. 1991; ICP-OES, Rankin et al. 1992) with the big advantage to sample individual fluid inclusion generations (Goldstein and Reynolds 1994) instead of the whole fluid inclusion contingent of a sample chip. The developments in

mass spectrometry of the last decades leading to faster data acquisition, higher sensitivities and the ability to detect all

Table 1: Eutectic temperatures (T_e) of different aqueous systems; adapted from Steele-MacInnes et al. (2016). I = ice, HH = hydrohalite, Syl = sylvine, Ant = antarctite. Compositions are eutectic liquid compositions in wt% salt.

System		T_e	Solid phases	Composition
<i>Binaries</i>	H ₂ O – NaCl	-21.2	I, HH	23.2
	H ₂ O – KCl	-11	I, Syl	19.7
	H ₂ O – CaCl ₂	-49.5	I, Ant	30.8
	H ₂ O – MgCl ₂	-33	I, MgCl ₂ + 12H ₂ O	21.3
	H ₂ O – FeCl ₂	-37	I, FeCl ₂ + 6H ₂ O	30.4
<i>Ternaries</i>	H ₂ O – NaCl- KCl	-23	I + HH + Syl	20.6, 5.3
	H ₂ O – NaCl – CaCl ₂	-51	I + HH + Ant	2.2, 29.1
	H ₂ O – NaCl – FeCl ₂	-39	I + HH + FeCl ₂ + 6H ₂ O	1.7, 29.4

elements of the periodic table but the noble gases contributed to the successful history of LA analyses in geosciences at all and its special application for fluid inclusions (and melt inclusions; Halter et al. 2002).

Applications of combined microthermometric and LA-ICP-MS studies comprise a broad field of geological questions. But the majority of publications are based on materials from magmatic-hydrothermal ore deposits and other hydrothermal systems (Appold and Wenz 2011, Audétat 2014, Bertelli et al. 2009, Beuchat et al. 2004, Burisch et al. 2016, Catchpole et al. 2011, Fusswinkel et al. 2013, Fusswinkel et al. 2014, Hammerli et al. 2013, Heijlen et al. 2008, Klemm et al. 2004, Kostova et al. 2004, Lerchbaumer and Audétat 2013, Li et al. 2015, Marsala et al. 2013, Miron et al. 2013, Morales et al. 2016, Rauchenstein-Martinek et al. 2014, Richard et al. 2010, Scambelluri et al. 2015, Schlegel et al. 2013, Sirbescu et al. 2013, Stoffell et al. 2008, Su et al. 2009, Sun et al. 2013, Pelch et al. 2015, Williams-Jones et al. 2010, Zhitova et al. 2016). Experimental studies with synthetic fluid inclusions and combined LA-ICP-MS analyses could provide huge progress in the understanding of metal solubility, the partitioning of metals between immiscible fluid phases (liquid-vapor, melt-liquid) and the speciation of metals in magmatic-hydrothermal fluids. Elements of interest in synthetic fluid inclusion studies have been Au (Derrey et al. 2016, Loucks and Mavrogenes 1999, Simon et al. 2005, Simon et al. 2007, Zajacz et al. 2010), Cu (Zajacz et al. 2012, Frank et al. 2011, Berry et al. 2006, Hack and Mavrogenes 2006, Simon et al. 2006, Lerchbaumer and Audétat 2009), Pt (Hanley et al. 2005, Simon and Pettke 2009), Fe (Simon et al. 2004), Mo (Derrey et

al. 2016, Ulrich and Mavrogenes 2008) Sn (Duc-Tin et al. 2007) and W (Derrey et al. 2016) so far.

The evolution of ore forming magmatic systems has become a frequently studied field of research in the last decades, with several studies focusing on the processes during the magmatic - hydrothermal transition in the ore generating plutons (Halter and Webster 2004, Veksler 2004, Thomas and Davidson 2016, Drivenes et al. 2016). The understanding of near-solidus to subsolidus processes and reactions with the specific focus on the transport of ore forming metals gained large progress by the implementation of experimental studies, including solubility experiments with high pressure, high temperature vessels (Linnen et al. 1995, Linnen et al. 1996, Bhalla et al. 2005), and investigations on natural samples like fluid and melt inclusion studies from mineralized systems (Audétat et al. 2000a, Borisova et al. 2012, Günther et al. 1998, Heinrich et al. 2003, Kotzeva et al. 2011, Müller et al. 2001, Ulrich et al. 2001). With the development of the first LA-ICP-MS method for fluid inclusions, Günther et al. 1998 initiated a new era in micro analytical techniques that was followed by the publication of several studies concerning the above described topics. Different deposit types were the subject of research, including porphyry Cu-mineralized intrusions, porphyry Mo-mineralized intrusions, hydrothermal Pb-Zn mineralizations, Th-U-REE-mineralized intrusions and Sn-W mineralized granitic intrusions (Audétat et al. 2008). The partitioning of trace elements and metals between coexisting melt and fluid phases has been recognized as a key process during the formation of ore deposits and is another important approach for fluid and melt inclusion analyses by LA-ICP-MS. Furthermore, fluid inclusion boiling assemblages of coexisting vapor and brine inclusions could reveal important information about the partitioning of the elements of interest during phase separation in the subsolidus regime and related enrichment processes that lead to the precipitation of ore minerals (Heinrich et al. 1999).

It is still a highly active field of research since the understanding of evolutionary processes in the magmatic – hydrothermal stage need further input, even though the general knowledge was extended dramatically in the last decade. A detailed fluid inclusion study of a specific mineralized system can contribute to our understanding of the ore forming processes and the distribution behavior of the associated ore metals in the investigated location. The comparison of ore-bearing intrusions from different locations should reveal the characteristics of a specific deposit type (e.g. Sn-W granites), after searching for possible analogies between the different locations with identical mineralizations in their fluid and melt chemistry and their

evolutionary trends. The number of conducted fluid and melt inclusion studies for Sn-W mineralized systems is despite of the developments of the last decade still quite low and, thus, further investigations of important mining sites need to be carried out. Audétat et al. 2000b managed to conduct the first study on a Sn-W mineralized system by publishing a detailed study of the fluid inclusion contingent of a hydrothermally grown miarolitic quartz from the Mole Granite, Australia. The authors could demonstrate that a medium saline, medium dense single phase fluid was responsible for the transport of Sn from the melt into the upper parts of the intrusion. Subsequent boiling and the formation of a hypersaline brine phase were identified as further important steps during the evolution of the magmatic derived fluid. The metals were further enriched in the brine phase in comparison with the single phase fluid and later mixing of meteoric waters with the magmatic derived fluids initiated the precipitation of ore minerals.

3.2 Laser ablation of fluid inclusions

Fluid inclusion studies are commonly conducted in order to gain information about pressure-temperature conditions, and in particular about the chemical composition of deep crustal fluids (Shepherd et al. 1985). Concerning the latter, laser ablation inductively coupled plasma mass spectrometry (LA-ICP-MS) is regarded as the most reliable technique for the determination of concentrations of solutes in fluid inclusions for a large number of elements (Pettke et al. 2012). This technique provides a high dynamic range which allows detecting elemental concentrations from the $\mu\text{g/g}$ to the wt% level. Laser Ablation-ICP-MS measurements can provide trace element concentrations (*e.g.* Cu, Zn, Au, Sn, Sr, Rb, Cs, Mo, Pb) as well as major element concentrations (*e.g.* Na, K, Ca, Mg) from small sample volumes of fluid inclusions from a short transient signals acquired by ICP-MS (Heinrich et al. 2003). Even isotope ratio determinations have been carried out on fluid inclusion using this highly versatile technique (Pettke et al. 2011). The basic principles for LA- ICP-MS analyses of fluid inclusions have been pioneered by Günther et al. 1998 using a nanosecond UV laser ablation system (193 nm, ArF Excimer) in combination with a quadrupole ICP-MS (QMS). The method was refined during the last decade by Günther et al. 2001, Halter et al. 2002, Heinrich et al. 2003 and Allan et al. 2005, but did not change in general. Besides the common determination of cation contents, it is also possible to quantify elements that exist as anions in the fluid inclusions, such as Cl, Br, and S (Guillong et al. 2008a, Seo et al. 2011).

A high control over the laser ablation process is required to achieve a representative fluid inclusion analysis. Problems can occur when fragments of the host mineral (most commonly quartz) quarry out during ablation and the fluid is lost through cracks before the ablation process reaches the inclusion. Other problems arise from incomplete mobilization of the inclusion, or the lack in mass spectrometric acquisition speed leading to an under-estimation of the elemental concentrations. In order to achieve a representative analysis the complete volume of the inclusion, which may be composed of gas, liquid, and crystals, needs to be mobilized and transported to the ICP-MS. Opening the inclusions is described as one of the most critical steps in fluid inclusion analyses (Günther et al. 1998). Especially the analyses of shallow inclusions ($< 10\mu\text{m}$ depth) is often accompanied by an uncontrolled release of the fluid inclusion content due to overpressure in the inclusions and splashing of material out of the ablation pit (Figure 2). Allan et al. 2005 estimated that the sampling process frequently controls the precision achieved for fluid inclusion analyses. Depending on their extent, most

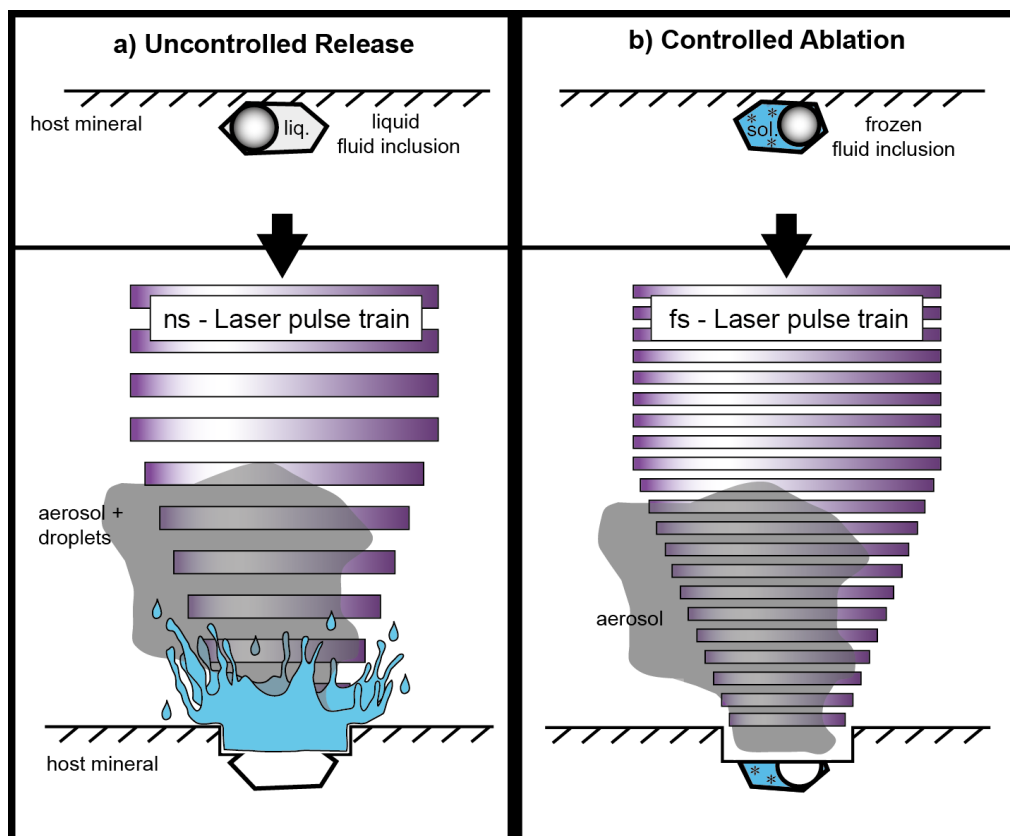


Figure 2: Comparative drawing of a) UV-ns-LA of shallow fluid inclusions at room temperature and b) UV-fs-LA of fluid inclusions with the freezing technique. The ablation of shallow fluid inclusions tends to lead to uncontrolled release of the fluid with UV-ns-LA, which results in unstable ICP-MS signals in this case. UV-fs-LA with frozen fluids inclusions ensures very high control on the opening of inclusions, which results in a higher success rate and very reliable data production from single fluid inclusion analysis. Illustration is not to scale.

elemental concentrations can be determined with a precision on the order of 20 – 30 % RSD. Better precisions have been reported for elements with high concentration levels (e.g. up to the wt%-range) in relatively large fluid inclusions (Pettke et al. 2012).

Quadrupole MS systems have been favoured over magnetic sector field mass spectrometers as they are capable of fast peak scanning which is essential for the sequential analysis of the transient signal that is typically generated during laser ablation analyses of fluid inclusions. Sweep times as short as 260 ms have been used for QMS analyses of a set of 20 isotopes (Pettke et al. 2012). However, more recently fast scanning sector field mass spectrometers with a high transmission and a large dynamic detection range such as the Element XRTM from ThermoScientificTM have been developed. These are particular suitable for short laser ablation analyses of low concentration levels.

Advantages of 196nm UV-fs-LA over UV-ns-LA have been reported for the determination of isotopic ratios of heavy stable isotope systems (Horn and Blanckenburg 2006, Steinhoefel et al. 2009a, 2009b, Steinhoefel et al. 2010) as well as Pb-U mineral dating (Horn and Blanckenburg 2007), but only preliminary experience has yet been documented for trace element analyses with single collector ICP-MS applications (Pettke et al. 2012). To our knowledge, only one study has been published using femtosecond laser ablation (fs-LA) for the analyses of fluid inclusions with respect to solute quantification. Borisova et al. 2012 used a NIR-fs-LA-QMS system in their study. Pettke et al. 2012 speculate that, particularly for fluid inclusion analyses with fs-LA, problems such as cracking at the crater bottom and associated material loss or phase explosions and an uncontrolled opening of the inclusion may arise. Nevertheless, the greatest advantage of fs-LA is the minimal heat transfer from the laser spot into the sample during ablation (Pronko et al. 1995) resulting in minimized elemental fractionation effects (Horn et al. 2007).

The aim of this study is to develop a new analytical setup for the determination of major, minor and trace element concentrations in fluid inclusions. A 194 nm UV-fs laser is coupled with a fast scanning sector field ICP-MS. To use the low heat transfer of the fs-laser to its full capacity, we adapted a heating-freezing stage as the ablation cell and perform the ablations at low temperatures (*e.g.* -40°C). This new approach was tested in this study by the analysis of different types of synthetic fluid inclusions with known concentrations. Thereby we focus on smaller inclusions with an elemental load of $\leq 53 \mu\text{g/g}$, which is of high significance for the chemical characterization of natural fluid inclusion but analytically challenging. In a case study about Sn-W granites we investigate the applicability of the freezing method on natural fluid inclusions in quartz for geological relevant questions, like the transport of metals in magmatic-hydrothermal fluids.

3.3 Complexation of Sn and its distribution between melt and fluid

The development of Sn-specialized granite is mainly dependent on the speciation of Sn in the melt. A mixture of Sn-enrichment in the source rock of the granitic intrusion and following internal fractionation processes with progressive enrichment of incompatible elements define the fundamental prerequisites for the formation of Sn-W deposits in the granitic systems (Lehmann 1982, Romer and Kroner 2014, 2016). The exsolution of an aqueous fluid phase from a water-saturated melt which is able to leach the metals and other elements from the melt is usually the last step leading to economically interesting concentrations of ore minerals. The questions how Sn and other metals are mobilized by the exsolved magmatic fluid phase are recently subject of research. Fluid-melt partition coefficients for Sn are basically low (Hu et al. 2008), suggesting the dissolution process from the melt to be difficult and inefficient. Nevertheless, experimental studies about the hydrothermal transport of Sn have shown that different ligands can be responsible for the complexation of Sn in crustal fluids (Duc-Tin et al. 2007). The transport of Sn^{2+} can be achieved by Cl^- , F^- and OH^- (Paterson et al. 1981). The mechanisms of Sn mobilization from an enriched melt into an exsolving fluid are still under debate. Especially fluoride and chloride complexes like SnF_2 , $\text{Sn}(\text{OH})\text{Cl}$ and SnCl_2 are important for the transport of Sn in hydrothermal solutions (Duc-Tin et al. 2007, Pirajno 2010). Tin has a high solubility in acidic, Cl-rich fluids under reducing conditions where it is present as the divalent Sn^{2+} ion. Sherman et al. 2000 proposed the existence of Sn^{2+} -complexes ($(\text{SnCl}_3)^-$, $(\text{SnCl}_4)^{2-}$) in Cl-bearing hydrothermal solutions $< 350^\circ\text{C}$ and a Sn^{4+} -complex ($(\text{SnCl}_6)^{2-}$) in oxidized Cl-brines. Cassiterite solubility experiments have shown that alkali bearing F-rich fluids can yield to an effective Sn-mobilization, too (Duc-Tin et al. 2007). High abundances of F in Sn-specialized granitic melts are very frequently observed, due to the strong enrichment of incompatible elements in those melts. The amount of F in the melts can thereby easily reach several wt% (Müller et al. 2006b). Linnen et al. 1995 and Linnen et al. 1996 conducted experiments to investigate the influence of $f\text{O}_2$, peralkalinity and excess Al on Sn solubility in granitic melts. The determined Sn solubility was higher at reducing conditions (2.8 wt% SnO_2 at FMQ -0.84) than under oxidizing conditions (0.08 wt% SnO_2 at FMQ +3.12). Bhalla et al. 2005 extended the experiments of Linnen et al. 1995, 1996 to lower temperatures in F-bearing peraluminous granitic melts and found strong effects of temperature, $f\text{O}_2$ and the amount of excess Al in the melt. Fluorine was described to have a minor effect on SnO_2 solubility at $f\text{O}_2$ of NNO, because Sn^{2+} is the dominant valence state of Sn and a positive effect of F on solubility would only be expected if Sn is dissolved as Sn^{4+} .

Dissolved F can increase the solubility of high field strength elements, which is Sn^{4+} , due to the formation of HFSE complexes with non-bridging oxygen atoms that are excluded from coordination with Al by reaction with F (Keppler 1993). The amount of excess Al was found to be another parameter controlling SnO_2 solubility under reducing conditions, demonstrated by positive correlations between normative corundum and Sn in glass inclusions (Bhalla et al. 2005).

Tin-specialized granites are known to form in moderately-reduced environments associated with the lithophile element association of the ilmenite series. At low $\text{Fe}^{3+}/\text{Fe}^{2+}$ ratios, Sn is in the divalent state (Sn^{2+}) in silicate melts, incompatible for the early crystallizing minerals like biotite and, therefore, Sn can be enriched in the residual melts which allows the formation of the Sn-specialized granites. Solubility experiments of cassiterite in Cl- and F- bearing aqueous fluids demonstrated that the fluid/melt partition coefficients of Sn is rather low between 2 – 4 in peraluminous systems with $f\text{O}_2$ near NNO . Experimental data show that $D_{\text{Sn}}^{\text{Fluid/Melt}}$ is controlled by the $f\text{HCl}/f\text{HF}$ ratio of the melt. Cassiterite solubility is by two orders of magnitude higher in HCl-bearing fluids compared to the HF-bearing fluids and even relatively acidic fluids are not able to leach Sn effectively from the melt as demonstrated by high Sn concentrations in peraluminous melt inclusions (Duc-Tin et al. 2007). As reported by Audétat et al. 2000b, F plays an important role during the process of fluid exsolution by controlling the salinity of the fluid phase, since the fluid-melt distribution of Cl is controlled by the F content. Rising F contents in the melt lower the Cl contents in the fluid phase and vice versa. Additionally, the crystal-melt partition coefficients of W, Sn and other incompatible elements are lowered by rising amounts of F in the melt and the lowered solidus temperature of a F-rich melt allows a progressive crystal fractionation and further enrichment of the incompatible elements. Duc-Tin et al. 2007 report a possible way to extract Sn from the magmas by an alkaline, F-bearing residual melt as it could be the case for pegmatites and granites as reported by Thomas et al. 2005. But nevertheless, it is the Cl concentration in the fluid that was found to control the fluid-melt partition of Sn and other Cl-complexed ore forming metals. Audétat et al. 2000b demonstrated that early exsolved Cl-rich fluids in the Mole granite (Australia) carried larger amounts of Sn than younger, medium-saline and F-rich fluids.

Another example for a possible way of Sn transport in fluids was proposed by Johan et al. 2012, who suggest a preferred complexation of Sn as SnF_4 , assuming Sn to be oxidized and fluid mobile as the tetravalent Sn^{4+} ion, which is in contrast with the theory that Sn is

preferentially incorporated as Sn^{2+} in silicate melts in reduced regimes. However, Sn and W are not being leached from a melt by fluid-melt immiscibility processes here, but rather mobilized from the prior crystallized micas during the transition of lithian annite to zinnwaldite, triggered by a F-rich fluid.

3.4 Source of metals: Geochemical heritage or fractional crystallization

The formation of greisens ore systems is generally related to highly fractionated magmas that have emanated from deep-seated granite batholiths and are strongly enriched in volatile components, Cl, B, F and metals like Sn, W, U, Mo, Be, Bi and Li (Pirajno 2010). The crystallized products of these source magmas belong to a group of geochemically specialized rocks that have intruded into the upper crust where they form greisens ore deposits. The apical parts of a granitic intrusion gets affected by the late- to post-magmatic emanation of a volatile rich phase which triggers metasomatic reactions that finally result in the transformation of K-feldspar, plagioclase and micas into quartz and muscovite or other mica compositions like lithian siderophyllite, protolithionite or zinnwaldite (Smirnov 1976, Kinnaird 1985). Especially the replacement of plagioclase and biotite is meant to play an important role in the formation of Sn-W ore deposits, due to their ability to incorporate large amounts of trace metals and their possible release during the metasomatic reaction with F- and Cl-rich volatile phases. Biotite, for example, can host up to 1000 $\mu\text{g/g}$ Sn, 10 $\mu\text{g/g}$ W, 60 $\mu\text{g/g}$ Mo and 100 $\mu\text{g/g}$ Nb (Eugster 1985). A characteristic feature of this model is the existence of trace metal depleted altered zones in the lower parts of a Sn-W system, as it was found by the mica trace element study of Johan et al. 2012 in the Zinnwald granite cupola.

While the geochemical processes that lead to the formation of greisen style deposits seem to be well understood, it is still highly discussed what causes the enrichment of metals in the specialized (Sn-W) granitic systems. By now, two theories exist, putting the focus on crystal fractionation on the one hand and the geochemical heritage of the source rocks on the other hand. Lehmann 1982 proposed that magmatic differentiation and fractional crystallization are mainly responsible for the elevated concentrations of volatiles and trace metals in the residual liquids, which would subsequently accumulate in the cupola parts of the granitic pluton. The theory of a geochemical heritage was established by Pollard et al. 1983, based on the assumption that the specialization of the magma in the sense of volatile and metal enrichment was acquired from the source region where partial melting occurs. The formation of the specialized Sn-W granites and their deposits would therefore require melting of crustal protoliths with extraordinary high concentrations of Sn and W or other elements like F and B. Pirajno 2010 suggests that a mixture of both theories could be imaginable, i.e. the partial melting of enriched source rocks and the subsequent differentiation and fractional crystallization of the melt to reach the extreme volatile and metal contents of the residual

melts. This approach of both processes being active in the formation of specialized Sn-W granites is further supported by Romer and Kroner *2014, 2016* who investigated the worldwide distribution of granite hosted Sn and/or W deposits and lithium-cesium-tantalum (LCT) pegmatites. The authors concluded that large deposits formed in regions where sedimentary debris of the Cadomian magmatic arc and the melting of these source rocks during later tectonic events were responsible for the specialization of granitic magmas. According to the authors, three independent processes are necessary to generate Sn-W granites. Enrichment of Sn and W in the sediment source by chemical weathering is followed by the redeposition and tectonic accumulation of these sediments to create large amounts of Sn-W enriched sedimentary rocks and finally, the melting of these sediments. Where these requirements are fulfilled, magmatic differentiation and the formation of highly evolved melts are the final step to create a Sn-W granite. The balance of the mixture between “magmatic differentiation” and “geochemical heritage” in the theory of Romer and Kroner *2016* lies clearly on the side of the latter one, since a Sn-W granite only forms if appropriate climatic conditions and a stable craton result in the weathering-related Sn-W enrichment in the sediments, meaning that the observed Sn and W deposits would not have formed without these enriched source rocks even if the magmas underwent strong differentiation.

The Zinnwald Sn-W deposit and all late- and post-Variscan granites of the European continent are associated with the former Laurussia-Gondwana plate boundary zone that is one of the global tectonic accumulation zones for Sn-W enriched sediments. Concerning the theory of Romer and Kroner *2014*, the late Variscan fold and thrust belt would not have generated any Sn-W granite without its tectonic relationship to the supercontinental boundary zone. The Zinnwald granite and its related Sn-W granites in the Erzgebirge region underwent internal processes of magma differentiation and crystal fractionation that finally produced those extremely high fractionated granites with the enrichment of several incompatible elements and metals.

4. Development of the UV-fs-LA-ICP-MS method for frozen fluid inclusions

4.1 Instrumentation

Analyses have been processed with an Element XRTM fast scanning sector field inductively coupled plasma mass spectrometer (ThermoScientificTM, Bremen, Germany) in combination with an in-house build laser ablation system which is based on a Spectra-PhysicsTM femtosecond (Ti:Sapphire) laser (SolsticeTM) operating in the deep UV at 194nm. The laser system produces a pulse energy of 70 – 90 μJ in the fourth harmonic. This ultra short pulsed laser generates a soft ablation with high control and avoids elemental fractionation at the sample site. The ablations of the standard reference materials (*NIST610*) were carried out with a repetition rate of 10 Hz. For fluid inclusion analyses, the repetition rate was adjusted depending on the depth of the inclusions. For shallow inclusions, between near surface and 30 μm depth, a repetition rate of 2 – 5 Hz was used, resulting in signal intensities significantly above the respective detection limits (Table 2). Inclusions deeper than 30 μm were analyzed with 10 Hz for faster drilling. The laser repetition rate controls the signal shape, intensity and finally the limits of detections (LOD) for the measured elements. A higher repetition rate results in shorter and higher signals and subsequently in better LODs (Pettke et al. 2012). The selected spot size on the sample surface is chosen to be bigger than the analyzed fluid inclusion in order to guarantee that the whole fluid inclusion is ablated and subsequently transported to the ICP-MS. An adjustable aperture in the beam path controls the spot size. It is possible to use spot sizes of up to 30 μm for the ablation of quartz. Ablations of quartz with bigger spot diameters would result in insufficient ablation rates, because of a reduced laser energy density. The spot size was held constant during the analysis which differs from the ablation procedure described by Günther et al. 1998. With our technique there is no need for a stepwise opening of the inclusions, because an explosion of the inclusion or splashing of material out of the ablation pit can be excluded when the inclusions are frozen. Especially the analysis of CO₂ bearing inclusions are expected to be simplified since the pressure is stringly decreased upon phase transformation of CO₂(gas) to CO₂(solid). We expected that this approach works especially with femtosecond laser pulses due to their low thermal energy transfer, keeping even fluid inclusions with low ice melting temperatures (e.g. -65°C) in their frozen state. The heat-affected zone during fs-LA has been investigated in earlier studies.

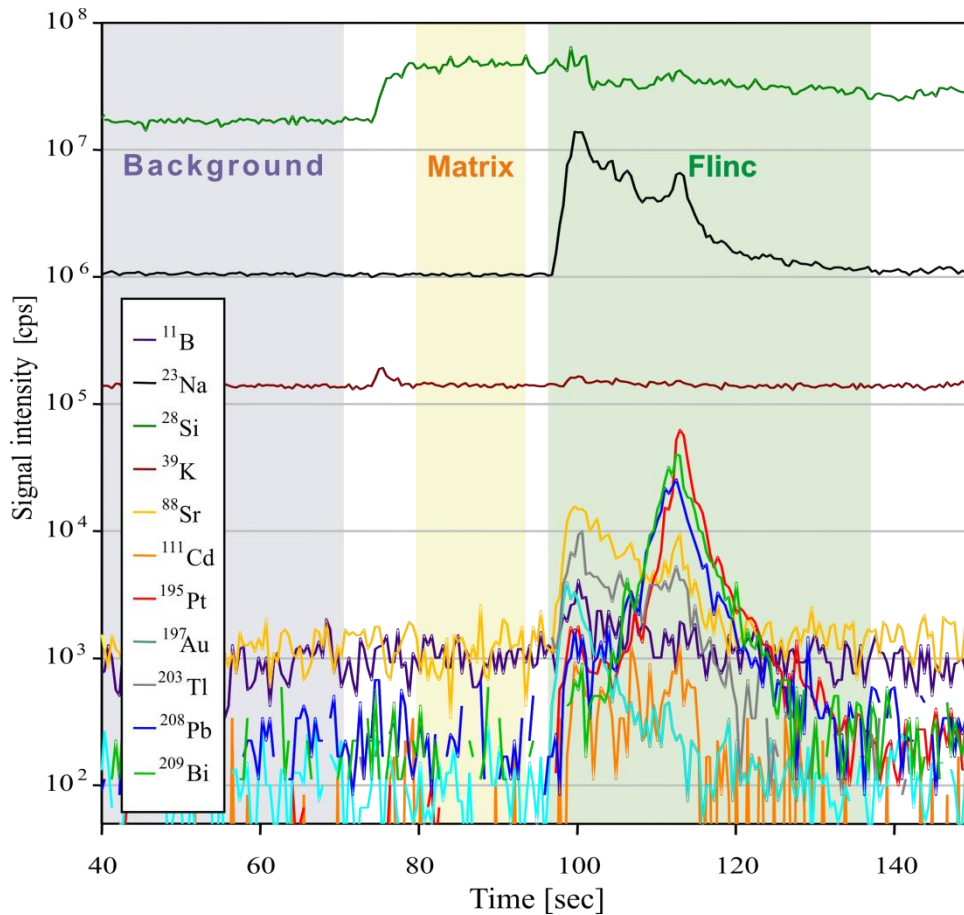


Figure 3: Fluid inclusion signal from analysis *19nov37* on sample ID189-Pt. Filled areas show integration windows for background, matrix and inclusion signal chosen for data evaluation. The size of the inclusion was 21 μm in diameter, located at 20 μm depth. The laser repetition rate was 2 Hz.

Hirayama and Obara *2005* showed that the layer affected by heating with a femtosecond laser is only of a few nm thickness. In contrast, nanosecond laser ablation results in significant conductive heat transfer within a layer of several μm (Hergenroeder *2006*).

Table 2: Intensities of background and fluid inclusion signal from analysis *19nov22*; $3SD_{\text{Background}}$ defines the LODs; $\text{Signal}_{\text{Flinc}}$ shows background corrected count rates of fluid inclusion; all values in counts per second (cps)

Isotope	Background	$3SD_{\text{Background}}$	$\text{Signal}_{\text{Flinc}}$
^{23}Na	1258057	65932	4375165
^{88}Sr	1327	1306	7089
^{197}Au	113	205	728

For analyses, the Element XRTM is operated in “speed mode” which provides an optimized data acquisition for short transient signals as produced during LA of fluid inclusions. Due to a

faster magnetic scanning and a faster scanning of the electrical field in the electrostatic analyzer unit, the sweep time is much shorter than commonly used for analyses with sector field instruments. For 20 isotopes ranging between ^9Be and ^{209}Bi , one sweep takes 477 ms. A short sweep time is essential for fluid inclusion measurements, because the signal peak commonly occurs subsequent to the opening of the fluid inclusion (Figure 3) and a slow data acquisition may result in a preliminary signal cut-off and artificially fractionated element concentrations. Further ICP-MS operational settings are shown in Table 3.

For this study, we used a modified heating-freezing cell for laser ablation in order to overcome some fundamental limitations of LA-ICP-MS analyses of fluid inclusions. One of the aims was to improve the fluid inclusion opening procedure and thereby avoid the explosive ejection of material during opening. With frozen inclusions and the small ablation rate of the UV-fs laser, we aimed to enhance the control during the opening process and as a result to improve the success rate of fluid inclusion analyses.

Table 3: ICP-MS settings for fluid inclusion analyses

Spectrometer	ElementXR TM
RF Power	950 W
Carrier gas flow (He)	0.27 – 0.3 L/min
Auxillary gas flow	0.65 L/min
Cool gas flow	14.5 L/min
Cones	Ni “Jet” sampler, Ni “H” skimmer
Sample time	0.003 s (0.01 s for Au and Pt)
Samples per peak	100
Mass window	4 %

While frozen, cracking at the bottom of the fluid inclusion would only result in the loss of gases, which are not frozen and cannot be detected with the instrumentation used. Furthermore, we expected that the transient signal could be stretched in time using low repetition rates and frozen solid fluid inclusion. Additionally, we aimed to improve the standardization process by using frozen matrix matched calibration standards prepared from standard solution in addition to the *NIST610* and *NIST612* glass standards. The matrix-matched standards enabled precise quantifications even at low counting rates. Independent of

the external standard used, the precision of the analysis still depends on size, shape and position of the inclusions, as well as on the laser repetition rate.

The analytical setup was realized with a modified 'HCS622V' cell from INSTEC™, Colorado, U.S.A. The cell is vacuum tight and provides an appropriate cell window to sample distance suiting the use of an objective with a focal length of 20 mm. It provides precise temperature control over the range from -190°C and +600°C. To optimize the cell volume, the cell was modified to carry a removable 3 cm³ cell made from Teflon, which is sealed to the main cell by means of O-rings (Figure 4). The small cell connects to the gas in and outlet with Teflon tubes. With this modification the washout time is reduced dramatically. Helium, a gas with much higher thermal conductivity compared to Argon, can be used with flow rates of up to 0.8 L/min limiting the lowest reachable temperature to -100°C. Without the small Teflon cell we observed a strong signal loss between room temperature and -40°C which exceeded 70 % for all measured isotopes due to the rising viscosity of helium at lower temperatures. This deficiency was reduced to a signal loss of < 5 % when the modified Teflon cell was inserted. Furthermore, the transient signal shape from a raster analysis, *e.g.* on NIST glasses, does not differ to those obtained at ambient temperature. The cooled sample area is large enough to provide space for a standard reference material (SRM) and several sample chips. Hence it is not necessary to open the cell during the data acquisition for calibration.

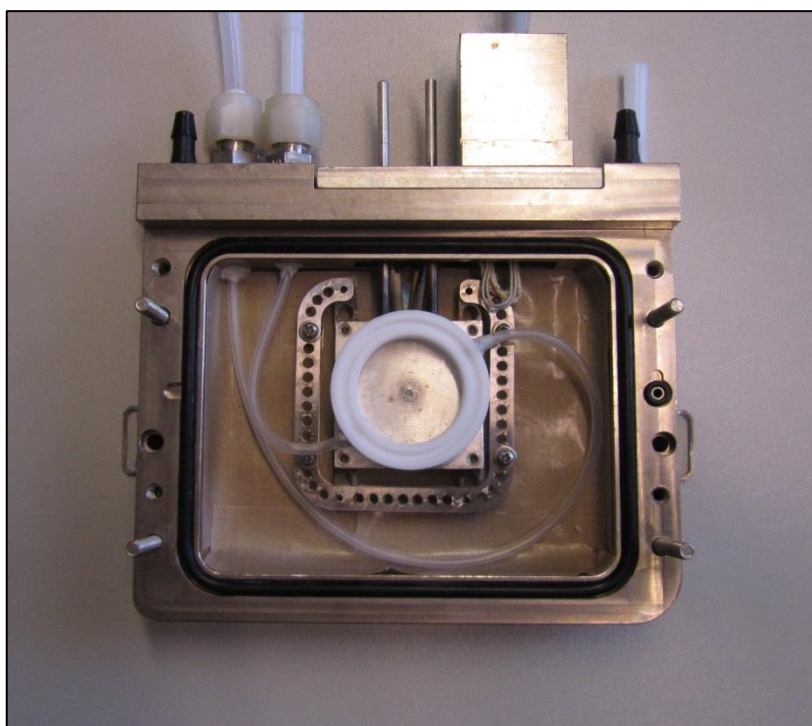


Figure 4: Modified INSTEC™ heating-freezing cell. The cell volume is reduced by the central Teflon ring to 3 cm³.

A Linkam™ “FTIR600” heating-freezing cell was also tested for its use as a laser ablation cell. The attempt to generate undisturbed and continuous time resolved laser ablation signals was complicated by the characteristics of the cell design. For example, the sample window is smaller than in the INSTEC™ cell, resulting in a smaller sample area. Furthermore, the distance between the cover window and the heating-freezing block is too short to provide a fully focused laser spot on the sample surface. A spacer between the cover glass and the casing would have been necessary. The crucial part for the integration of the FTIR600 into a laser ablation system are the gas in- and outlets. The INSTEC™ cell is equipped with two screwed connections, making it very easy to connect the cell with the 0.6 mm Teflon tubing of the laser ablation system, but the connection of the FTIR600 requires larger modifications of the factory-provided connectors. Integrating the Teflon ring into the INSTC™ cell was rather simple, since the underlying Ag-block provides enough space and is larger than the cell cover window. Such a modification is not as easily possible with the Linkam™ cell due to an Ag-block of an identical size with the cover glass. Thus, we finally decided to use the INSTEC™ cell for our purpose of fluid inclusion analyses.

4.2 Experimental observations during low temperature ablation

During the integration of the INSTEC™ heating-freezing stage in to the UV-fs-LA system, a major experimental finding was discovered during the analysis of Si rich matrices like quartz. At low temperatures between -100°C to 0°C we observed that the ^{28}Si or ^{29}Si signal faded out and disappeared completely although the laser was switched on and well focussed on the sample surface. This effect is not ubiquitous in the ablation with freezing conditions and after hundreds of analyses of different quartz crystals, we still could not discover any systematic in the occurrence of this effect. We suspected the sample aerosol to form condensates at some places in the freezing cell and to agglomerate major fractions of the sample matrix. When the cell temperature was increased after the Si signal disappeared, we commonly observed a huge rise in the Si count rate at temperatures between -20°C to -10°C, indicating a sudden input of large amounts of Si. Those observations did not appear during room temperature ablations with the freezing cell.

We decided to perform a systematic experiment with a stepwise and slow increase of the cell temperature to identify the possible Si releasing phase by its characteristic melting temperature. The experiment started with a 2 minutes lasting ablation on quartz at -100°C with a 20 μm focussed spot at 10 Hz repetition rate that should initiate the agglomeration of the Si bearing condensate. The ^{28}Si , ^{29}Si and ^{30}Si count rates were permanently recorded by the ICP-MS in high resolution mode. A disappearing Si signal during sample ablation was not observed this time but the here described results were reproducible. Figure 5 shows the time resolved Si signals during a stepwise increase of the cell temperature. The peak in ^{28}Si count rate between -12°C and -11°C could be observed at any execution of the heating experiment and probably indicates the melting of the Si absorbing phase. The heating-freezing cell was not calibrated by synthetic fluid inclusions since a rough adjustment of the temperature is usually enough for the fluid inclusion analysis where the solidification of the inclusion content can be visually controlled with the microscope camera of the laser ablation system. Thus, the observed temperature of Si mobilization is not as accurate as the phase transitions observed during microthermometry and the uncertainty must be estimated with $\pm 1^\circ\text{C}$.

A dry and water-free ablation procedure would probably avoid the condensation of any hydrogen based phase. But small amounts of residual H_2O in the carrier gas He (quality grade 4.6) cannot be excluded to influence the ablation process. A leaky tubing or cell-cover would the ambient air allow to enter the freezing cell and can be another reason for a strong

condensation of hydrates or H₂O ice. We interpret the temperature of Si release as an indicator for the existence of a silan (Si_nH_{2n+2}) that has formed by the reaction of the ablated matrix material and intruding H₂O molecules. Disilan (Si₂H₆) has a boiling temperature of -14.5°C and its vaporization could be responsible for the strong Si input into the ICP-MS at the observed temperature. To identify the crucial phase irrevocable it is necessary to conduct this experiment with a GC-MS.

But the quintessence of this finding is the ability of the freezing cell to retain the matrix element quantitatively. With a higher control for this process, the freezing cell could be used to separate large amounts of Si (or even other elements) and matrix induced plasma effects or molecular interferences might be reduced or eliminated.

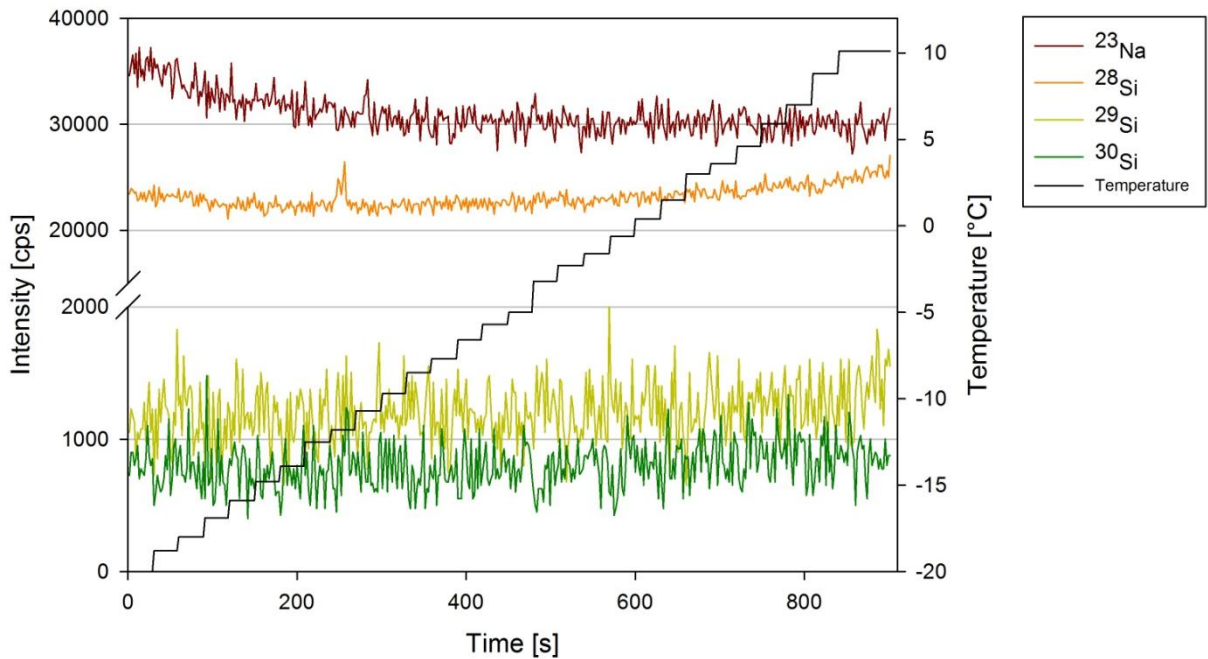


Figure 5: Time resolved Si and Na signals acquired during the heating experiment with slow and stepwise increase in temperature. The countrate of ²⁸Si shows a peak between -12 and -11°C, which was reproducible and might indicate the vaporization of a Si-bearing phase, e.g. Si_nH_{2n+2}.

4.3 Calibration

To prove that LA analyses at low temperatures results in adequate values, we measured the *NIST612* glass against the *NIST610* glass at -40°C . Results indicate that the preferred concentration values of most elements (Jochum et al. 2011) can be measured with an accuracy of $\pm 5\%$.

To test the performance of our method for analyses of frozen liquids, we analyzed a self-prepared standard solution against the *NIST610* glass (Figure 6). As low partition coefficients of most elements between aqueous solution and ice results in the formation of micro-nuggets on grain boundaries, it was necessary to freeze the solution with a high cooling rate to hamper the growth of the ice crystals and generate small grain sizes resulting in a more homogeneous elemental distribution. Raster ablations (2 Hz, 30 μm spot size) on larger areas were carried out to contribute to homogeneous sampling. The calculated results agree within analytical uncertainties (1RSD) with the specific values of 108 $\mu\text{g/g}$ (Figure 6).

Because of easier handling, for fluid inclusion analyses the *NIST610* glass rather than frozen standard solutions was used for external calibration of element ratios in the fluids. The analyses were performed using the standard-bracketing method, with a standard ablation after every fourth sample. Final ice melting temperatures were determined by microthermometry and provided the NaCl_{eq} values which were used as internal standard for the calculation of elemental concentrations (Günther et al. 1998) using the SILLs software.

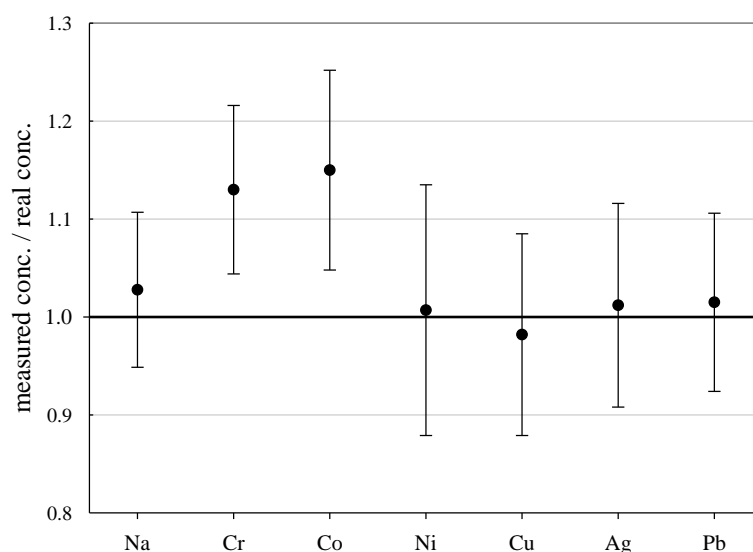


Figure 6: Analysis of a self-prepared frozen standard solution against *NIST610* glass. The real concentration of all elements is 108 $\mu\text{g/g}$. Error bars show 1RSD values of 11 analysis.

4.4 Synthetic fluid inclusions for method validation

To test our analytical setup we used synthetic fluid inclusions in quartz, which were generated from a standard solution of known concentration. The solution was prepared as a 1:1 mixture from the MERCKTM VIII ICPMS-multi-element-standard and a 20 % NaCl solution; its composition is given in Table 4.

Table 4: Composition of the stock solution for HP/HT experiments; all values in $\mu\text{g/g}$; * Na in wt%.

Al	B	Ba	Be	Bi	Ca	Cd	Co	Cr	Cu	Fe	Ga
52.3	52.8	52.8	53.3	53.3	52.8	52.8	52.8	52.3	53.3	52.8	53.9
K	Li	Mg	Mn	Na	Ni	Pb	Se	Sr	Te	Tl	Zn
52.8	52.8	54.4	52.8	9.7*	52.8	52.8	53.9	53.3	53.9	52.8	53.3

Preparation for fluid inclusion synthesis generally followed the workflow described by Bodnar et al. 1985 with minor modifications. Cores of 2.5 mm in diameter and ca. 2 mm length were drilled from inclusion free alpine quartz, heated to 350°C and subsequently immersed in concentrated hydrofluoric acid for 10 minutes to widen the cracks.

Two experiments were performed, one in a gold (*ID188-Au*) and one in a platinum (*ID189-Pt*) capsule, respectively, with dimensions of 20 mm length, 3.2 mm outer diameter and a wall thickness of 0.2 mm. In each capsule one pre-fractured quartz cylinder was placed together with 5 μg silicagel (to accelerate crack healing) and 30 μl of the standard solution. The capsules were pressurized to 200 MPa and heated isobarically in a rapid-heat/rapid-quench hydrothermal autoclave of a design described in Matthews et al. 2003, using argon as pressure medium. Uncertainties of temperature and pressure measurements are considered to be $\pm 5^\circ\text{C}$ and ± 5 MPa, respectively. After a runtime of 5 days the autoclave was slowly cooled to room temperature. The recovered capsules were weighed to check for potential leaks during the run. The quartz cylinders were cleaned, dried and embedded in Araldite to be cut and polished to chips of 300 μm thickness.

From both experiments the quartz chips contained abundant synthetic fluid inclusions and 55 inclusions were selected for microthermometric and LA-ICP-MS analyses. Microthermometric measurements of ice melting temperatures $T_{\text{m}}(\text{ICE})$ of $-6.2 \pm 0.1^\circ\text{C}$

correspond to a salinity of 9.47 ± 0.13 mass% NaCl_{eq} , calculated after Bodnar 1993, which is in full agreement with the standard solution composition.

4.5 Ablation procedure

In this study we followed the workflow for fluid inclusion analysis reported by Heinrich et al. 2003. Since the inclusions are analyzed in a frozen state, problems such as explosive opening and sputtering of the inclusion content during ablation could be excluded, and we were able to use the so called ‘straight ablation’ for the measurements. In contrast to the stepwise opening procedure which is used especially for polyphase inclusions, the “straight ablation” procedure holds some advantages, as reported by Pettke et al. 2012. These are 1) a lower amount of surface contamination, 2) higher signal/background ratios and 3) lower limits of detection (LOD).

Prior to ablation the samples and reference materials were cleaned with deionised water and acetone, and the heating-freezing cell was wiped out carefully with dilute nitric acid. The positions of the inclusions were mapped off-line prior to the analysis using a standard petrographic microscope, which simplifies the search with the video system of the LA stage.

In a first step the fluid inclusions are frozen quickly by lowering the sample temperature to -100°C. Depending on the fluid inclusion chemistry, the temperature is subsequently raised to a temperature sufficiently below the solution’s eutectic point, so that the inclusions remain entirely frozen. Reference materials were analyzed at the same temperatures since the tuning of the mass spectrometer is also performed under these conditions. For the synthetic fluid inclusions the heating-freezing cell was set to -40°C, since they were generated from a simple binary NaCl-H₂O fluid.

A gas blank of at least 40 seconds was recorded prior to each single analysis before the start of ablation. The scan speed for the raster pattern performed on the used SRM was set to 20 µm/s.

4.6 Data Processing

For calculation of trace element concentrations in fluid inclusions it is necessary to separate the inclusion signal from the chemically distinct signal of the host mineral. We used the data reduction software SILLIS (Guillong et al. 2008b), which is able to separate the short transient signal of the inclusion by a matrix correction. The software follows the procedures and equations from Allan et al. 2005, Halter et al. 2002, Heinrich et al. 2003 and Longerich et al. 1996. As silicon in the inclusion is negligible compared to silicon in the quartz, it was used as the matrix-only tracer. Three integration windows for background, matrix and inclusion signal were defined for each single analysis. The length of the integrated inclusion signal was adjusted to that of Na, because Na was used as the internal standard for the quantification of the elemental concentrations. Sample compositions were calculated using the mass balance approach of SILLIS.

As reported from Pettke et al. 2012, the best way to determine concentration values and analytical uncertainties for LA-ICP-MS analyses of fluid inclusions is to calculate the mean value and the external error from a batch of analyses of individual inclusions belonging to the same assemblage. The analytical error is based on the external precision (1SD) and is defined as the relative standard deviation (RSD) in %. Since all inclusions in our samples are considered to be chemically identical, we calculated the average concentration and the RSD from all single analyses of one sample.

4.7 Results and discussion

4.7.1 Accuracy and precision

Synthetic fluid inclusions were used to check the analytical precision and accuracy of our method. By dividing the measured concentration with the theoretical value of the starting solution used for the high pressure/high temperature (HP/HT) experiment, the relative accuracy of these measurements can be estimated. The experimental solution contains 24 elements from the MERCK™ VIII ICPMS-standard-solution with known concentrations (Table 4). However, only 10 of them could be recovered in the synthesized fluid inclusions. The missing elements most likely reacted with the capsule material (*e.g.* the transition metals with Au or Pt) or have been enriched at the surface of the quartz host phase due to diffusive processes, like Li, Mg, Al and K. Subsequently the original concentration of ~53 µg/g in the experimentally synthesized fluid inclusions could be recovered for only a few elements (Figure 7). The two samples *ID188-Au* and *ID189-Pt* were analyzed in separate sessions. In total 53 from 55 measured inclusions could be analyzed successfully. Only two inclusions that were located directly under the sample surface could not be used for quantification, as a matrix correction could not be performed due to the missing separation of the host mineral signal from the inclusion signal. Single values, which lie beyond the 2SD threshold, were considered as outliers and have not been included in the calculation of mean values and standard deviations (Table 5 + Table 6). To note, ¹⁹⁵Au and ¹⁹⁷Pt are not added through the MERCK™ VIII standard solution and were likely leached out from the capsule material. The results for ¹¹B, ¹¹¹Cd, ¹²⁵Te, ²⁰³Tl, ²⁰⁸Pb, and ²⁰⁹Bi (Figure 7, Table 5 + Table 6) indicate that these elements have been nearly completely recovered in the synthetic fluid inclusions. The recovery of the those elements in the fluid inclusions relative to the starting material is taken as a measure of the accuracy assuming a partition coefficient in favour of the fluid, illustrated by values of > 90 %. The calculated mean value for these elements is in accordance with the original fluid compositions and is within analytical uncertainties (1RSD) *i.e.* between 13 % (²⁰³Tl) and 25 % (¹²⁵Te) for sample *ID188-Au* and 17 % (¹¹¹Cd) to 25 % (¹¹B) for sample *ID189-Pt* (Figure 8). ³⁹K was only measured for sample *ID189-Pt* and could also be detected in the host mineral (quartz). After matrix correction, the determined K concentration of 42µg/g (RSD = 37 %) is in accordance with the original fluid composition. ⁶⁴Zn was only analyzed in some inclusions of sample *ID189-Pt*, with an average value of 37 µg/g (25 % RSD). The concentrations determined for ⁹Be, ⁵⁹Co, ⁶⁹Ga, ⁸⁸Sr and ¹³⁷Ba in the synthesized

fluid inclusions of both samples are significantly below the concentration of the original standard solution.

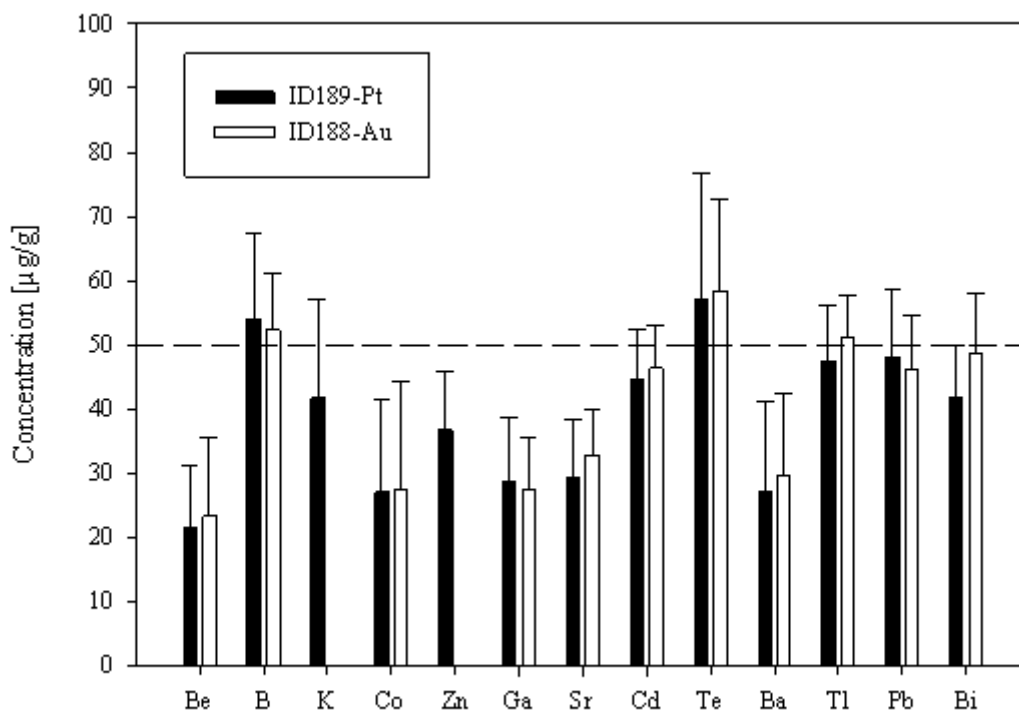


Figure 7: Results of the analysis of synthetic fluid inclusions from experiment *ID188-Au* (white columns) and *ID189-Pt* (black columns). The dashed line represents the starting composition of the experimental fluid, which was identical for both experiments. Only B, K, Cd, Te, Tl, Pb and Bi (for *ID188-Au*) could be fully recovered in the inclusions. Error bars show 1SD of the mean values from all analyzed inclusions from the specific sample.

Furthermore, the reproducibility for these elements was in most cases lower than that determined for the other elements. Beryllium, Co, and Ba show the highest variability with RSDs between 40 % and 60 %. Gold and Pt have also been analyzed, because they were expected to be leached out of the capsule walls during the experiments. The inclusions in sample *ID188-Au* which were synthesized in gold capsules contain 1.6 wt% Au (RSD = 29 %), which seems to be an extraordinary high value compared to Au concentrations in natural fluid inclusions that do not exceed the lower µg/g range (Ulrich et al. 2001, Heinrich et al. 1999). The mixture between the MERCK™ VIII solution, which is 1M HNO₃, and the NaCl-fluid may support the leaching of capsule material during the experiments by the formation of nitro-hydrochloric acid. Similarities have been observed for the inclusions in sample *ID189-Pt* which were synthesized in platinum capsules and contain higher concentrations of Pt (124 µg/g) which is heterogeneously distributed (with 73 % RSD), and 11 µg/g Au (RSD = 26 %). The inclusions can be separated into two groups with ~200 µg/g and ~50 µg/g Pt,

respectively. Both groups have relatively homogeneous Pt concentrations with an RSD of 38 % respective 34 %. This may indicate the formation of two generations of fluid inclusions in experiment *ID189-Pt*, which can only be identified due to their Pt concentration since all other elements show similar values in both groups. None of the other analyzed elements, except Pt and Au, could be identified to originate from the capsule material.

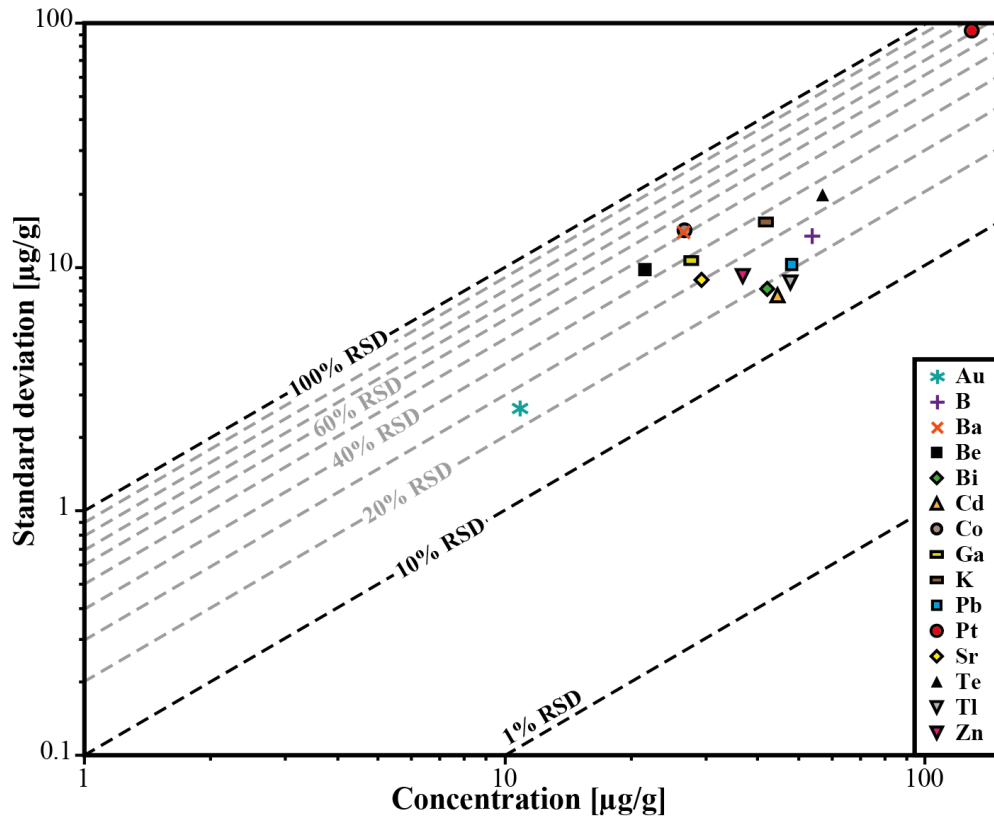


Figure 8: relative standard deviation for the determined concentrations in sample *ID189-Pt*. Pt and Au were not part of the stock solution and were leached out of the capsule material.

4.7.2 Limits of detection

The lower limits of detection vary for the measured isotopes over a range of three orders of magnitude (10^{-1} to 10^2 $\mu\text{g/g}$). They were calculated after the method of Pettke et al. 2012 for integration windows, based on the total signal length of Na. The LODs are controlled by the laser repetition rate, the total integration time and the volume of the inclusions, thus are

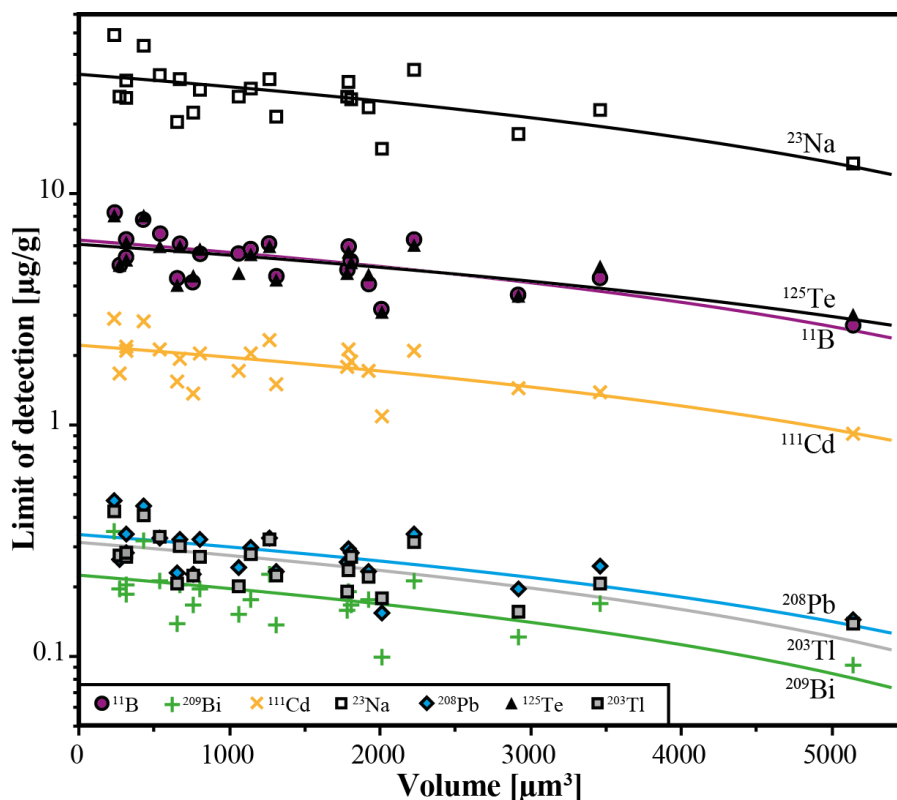


Figure 9: Limits of detection as a function of the inclusion volume for the 6 completely transferred elements (B, Cd, Te, Tl, Pb, Bi) and Na from all individual analyses from sample *IDI88-Au*.

related to counting statistics. Even though the differences in size of the analyzed inclusions are not large (8 – 26 μm), a significant correlation between LODs and inclusion size can still be observed (Figure 9) which is the same for all analyzed elements. For lighter isotopes like ^{11}B or ^{39}K , the LODs vary between 4 $\mu\text{g/g}$ and 16 $\mu\text{g/g}$. Isotopes in the medium mass range like ^{59}Co , ^{69}Ga , or ^{88}Sr have LODs between 0.3 $\mu\text{g/g}$ and 1.8 $\mu\text{g/g}$. Heavy isotopes like ^{195}Pt and ^{209}Bi show the lowest LODs (0.09 $\mu\text{g/g}$ – 0.6 $\mu\text{g/g}$). Furthermore, ^{195}Pt and ^{197}Au have been analyzed with a longer dwell time of 10 ms, resulting in a longer total integration time which improved the lower limit of detection. These results underline, the instrumental response of the mass spectrometer showing a lower sensitivity of light masses compared to heavy masses.

4.8 Conclusions

We have tested a new analytical setup for the determination of trace element concentrations in fluid inclusion with UV-fs-LA-ICP-MS. Ablation with femtosecond laser pulses allows analyzing fluid inclusions in their frozen state. With this technique, 53 of 55 synthetic fluid inclusions hosted in quartz, covering a size range between 8 μm and 25 μm in diameter and down to a depth of 50 μm , could be analyzed successfully. The 194 nm UV-fs-laser system allows an excellent control for the opening procedure of fluid inclusions. Due to the low thermal heat transfer onto the sample surface the inclusions stay frozen while the sample material is mobilized. It is even possible to measure very shallow inclusions that frequently explode during the opening procedure, resulting in material loss during analysis under room temperature conditions with a nanosecond laser.

The use of a fast scanning magnetic sector field ICP-MS with a SEM and a Faraday detector allows the detection of elements across the concentration range from $\mu\text{g/g}$ to wt%. The lower limits of detection for fluid inclusion analyses vary between 0.1 $\mu\text{g/g}$ (for ^{209}Bi) and 10 $\mu\text{g/g}$ (for ^{39}K). The detection of 20 isotopes over the whole mass range takes 477 ms using a measurement time of 12 microseconds per isotope. The typical analytical uncertainty ranges between 15 % and 30 % (1RSD). This is a significant improvement in precision compared to earlier studies for samples with such low concentration levels. Elements from the stock solution which did not react with the capsule material or host mineral during the HP/HT experiments could be fully recovered in the synthetic fluid inclusions at their original concentrations. The results illustrate that our method is able to produce adequate data for natural fluid inclusions.

The preparation and characterization of fluid inclusion especially the microthermometry, is time consuming when compared to the analyses time, therefore our method offers a highly efficient tool for the quantification of fluid inclusions with a success rate of > 90 %. First tests with natural inclusions in quartz have shown that the success rate similar to the results obtained for synthetic fluid inclusions can be expected. Given that most natural samples often host only very few inclusions of sufficient size ($\geq 10 \mu\text{m}$), this method provides new possibilities for fluid inclusion studies. The applicability of our approach to the widespread UV-ns-LA systems needs to be tested. If successful, it may become a tool enhancing the overall success-rate during fluid inclusion analyses by LA-ICP-MS.

4.9 Incorporation of a *Linux CNC* controlled laser stage

The above described method for fluid inclusion analyses provides a reliable way to determine the trace, minor and major element contents in small size inclusions from 8 – 25 μm in diameter. For the best ablation behavior on quartz and therefore the highest drilling rate into depth, the here used UV-fs-LA device had to be hardly focused onto the sample surface with the smallest possible energy dispersion which increases the fluence to 1.4 J/cm^2 . The resulting crater does not exceed 30 μm in diameter on the surface and is getting even smaller with depth due to the Gaussian shape of the laser beam, which is a typical feature of all solid state lasers. This, however defeats the analyses of bigger inclusions, which would offer some crucial technical advantages compared to the ablation of small inclusions. As the lower limit of detection (LOD) depends on the ablated sample volume, the analysis of inclusions $> 30 \mu\text{m}$ could demonstrate the existence of smallest amounts of various elements in the ppb range, a very important capability especially for the investigation of the metal contents in crustal fluids. Larger sample volumes would also extend the duration of the transient sample signals, resulting in lower counting statistical errors and finally in a better analytical precision and accuracy. Fluid inclusions of diameters $> 30 \mu\text{m}$ are very rare in most samples, but if available, they are often easier to handle during microthermometry and phase transitions, e.g. ice melting, are easier to observe on the larger scale than for smaller inclusions. Therefore, the investigation of larger inclusions can result in very precise determination of the salinity and therefore provide a good base for trace element measurements by laser ablation.

Since a static fs laser ablation spot is not able to generate crater diameters $> 30 \mu\text{m}$ on quartz without losing the ability to drill several tens of micrometers deep into the crystal during the relative short time interval of data acquisition, the solution was found in a fast moving sample under the laser spot that follows a circular pattern of adequate size. In our case the laser beam of the UV-fs system is fixed on its pathway through the optical lenses and mirrors, the only possible way to achieve this without the implementation of a flying lens system, as developed by Pécheyran et al. 2007, is by moving the XY-table of the laser stage. Discrepancies between the flying lens system and the here presented CNC approach are the larger wavelength (1030 nm), higher repetition rates (1 – 10000 Hz) and the faster beam-movement (280 mm/s) of the flying lens system. Claverie et al. 2009 described the ability of the pattern controlled LA system to drill craters of 15 μm depth in 6.4 seconds by applying a repetition rate of 100 Hz, which demonstrates the possible ablation of large volumes in short time intervals.

The laser ablation software from New Wave Research (NWR) controlling visualization and the stage movement has a limited support for self-programmed patterns. Therefore, we installed the Linux based open source software *Linux CNC* and connected it with the laser stage to establish the control of the XY-stage, the laser shutter and the Z-focus by *Linux CNC*. The controller hardware for the XYZ-stage has been replaced by a self-build XYZ-controller unit, which allows real-time control of all axes using the LPT interface and a real-time *Linux* kernel, and is designed for plug and play switching between NWR and *Linux* control. Due to the open-source character of *Linux CNC* advantages such as wireless control of all parameters is implemented increasing the ease of use during analysis.

With *Linux CNC* it is possible to ablate “g-code” based patterns (known to control CNC based machines such as laces and mills) of every shape in the XYZ space, including very complex three dimensional patterns and simple two dimensional geometric shapes. Another feature of the *Linux CNC* control is the possibility to extend the maximum velocity of the XY-table compared to the NWR software. With those settings we were able to create an ablation pattern that is suitable for analyses of large fluid inclusion using the limited spot diameter available from our fs-laser.

For our needs, we created a g-code pattern which lets the XY-table follow the shape of an Archimedean spiral with an adaptable diameter for fluid inclusions of different sizes. Several parameters can be modified and control the flatness of the ablated layer when adequately fitted to spot size, speed and repetition rate. The velocity of the table movement is with up to 5 mm/s extremely fast providing an acceleration/deceleration of 15 mm/sec² in real time. The programmed pattern repeats as often as requested by the user, which results in the simulation of a constant spot ablation of any possible spot size between 30 and 300 μm. The fast movement requires the use of high laser repetition rate to ensure that enough material is ablated during one pass over the pattern and the requirement that mounting of the sample can withstand the acceleration without movement. Typical repetition rates for the ablation of several tens of micrometers into depth have been achieved with 100 – 500 Hz, depending on the laser pulse energy. For shallow inclusions of 5 - 30 μm depth, it could be demonstrated that the lower repetition rates of 42 – 250 Hz can generate a suitable crater depth with a sharp entry and withdrawal of the fluid inclusion signal. The ablation of inclusions below 30 μm in depth require very high repetition rates of 250 – 500 Hz, in order to hit the inclusion in the time-window selected. Otherwise the inclusion gets hit to late or at the end of the acquisition time window. If the laser does not reach the necessary depth to mobilize the deepest part of

the inclusion, the recorded signals fade out very slowly and the high concentrated elements like Na, K or Cs do not reach the background counting rate, even if the acquisition time was extended to 4 minutes. At this stage the analysis is regarded to be incomplete and is disregarded. A clear and fast decrease of Na, K, Cs and Pb is a typical sign for a complete ablation of the inclusion that could be observed more frequently in shallow inclusions. Analyses of inclusions deeper than 60 μm can result in incomplete signals within the given and therefore fixed acquisition time.

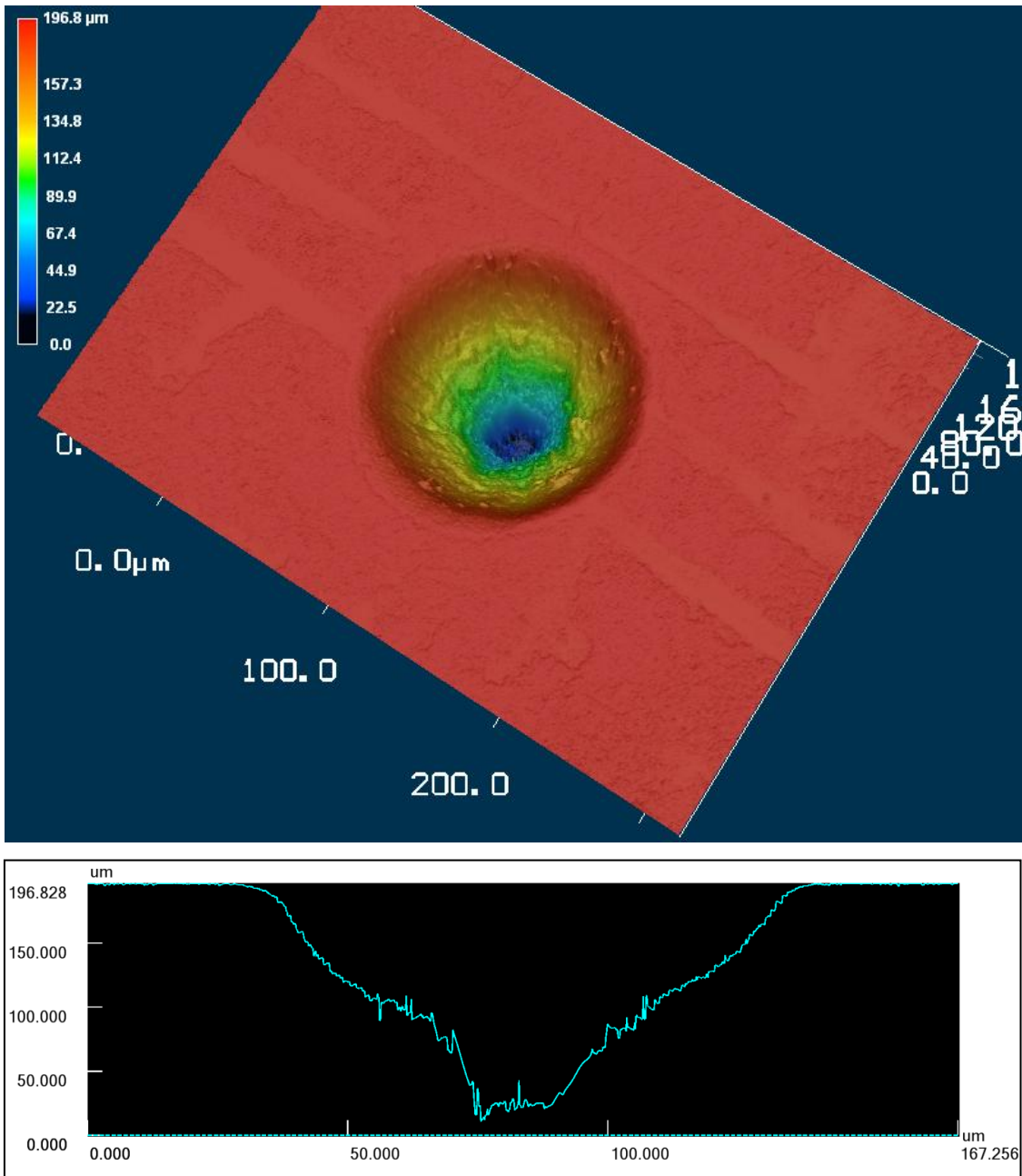


Figure 10: Crater shape of a 100 μm *Linux CNC* spiral, acquired by laser microscopy.

The size and shape of the ablation crater has been measured and visualized by a confocal laser microscope (Keyence VK-X100) at the Institute for Soil Science, Hannover. A crater that was produced on a polished quartz surface by a 100 μm spiral pattern with 500 Hz repetition rate, 120 seconds duration and 20 μm laser spot size was analyzed using magnification of 100x. The visualization of small ablation craters with low aspect ratios (diameter/depth) often resulted in a disturbed illustration in the deepest parts of the crater, which is probably related to the transparency of the quartz. Measurements of ablation craters on opaque high-reflecting materials created high detailed pictures without any spikes in the deepest areas. Therefore, a

carbon coating has been applied on the quartz sample, giving the laser microscope the ability to produce uninterrupted three-dimensional pictures of the ablation crater on quartz (Figure 10).

The shape of the here generated crater is perfectly circular framed and similar to the beam craters generated by beam-homogenized ns-lasers. The surface diameter is slightly above 100 μm , due to the natural spot diameter of $\sim 20 \mu\text{m}$ that overlaps the *Linux CNC* ablation pattern. The three-dimensional picture of the crater shows a 196 μm deep pit that is tapered towards the center. The crater diameter decreases continuously with depth and is reduced to $\sim 50 \mu\text{m}$ at 100 μm depth, followed by the steeply, nearly vertical sloping central part of the crater with $\sim 20 \mu\text{m}$ in diameter. The tapered profile and the proportionally strong ablation in the crater center is related to the fact that the spiral pattern is converging towards the inner parts of the spiral and that the laser beam is not shielded after it reaches the center and starts the outward directed movement. Consequently, the sample is penetrated longer at the inner parts of the spiral and the overlap of the 20 μm beam on the converging spiral line is of higher significance, resulting in the spatially deducted crater core. In turn, this suggests that the depth profile of the spiral patterns gets more homogenous and steeper with decreasing spiral diameters. The smaller the spiral diameter, the deeper the laser beam drills into the sample in identical time intervals. As mentioned above, the spiral parameters can be adapted so that the ablation pattern produces a crater profile with a nearly flat bottom.

With the example of a 100 μm spiral pattern it could be proven by laser microscopy that the spiral technique is able to mobilize the whole content of large fluid inclusions up to a size of several tens of micrometers in diameter in a realistic time interval for the data acquisition by ICP-MS. The large crater diameter of 50 μm in 100 μm depth is suitable for most flincks $< 100 \mu\text{m}$ in diameter, as long as their spatial arrangement (depth below surface, horizontal or vertical orientation) meets those requirements.

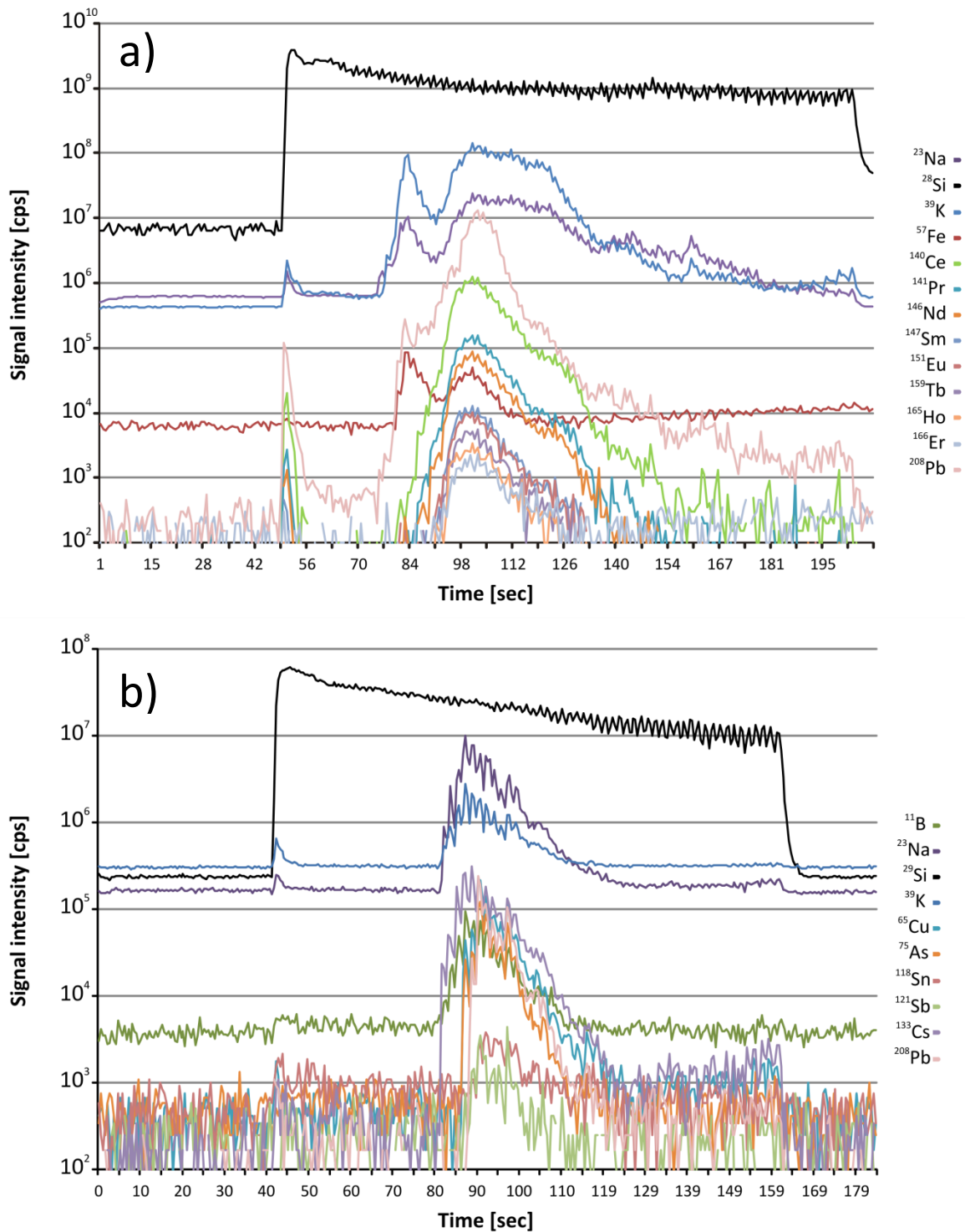


Figure 11: a) Fluid inclusion signal from a multi-phase inclusion of 40 μm in diameter hosted 80 μm in depth (45 mass% NaCl_{eq}), opened with a 50 μm *Linux CNC* spiral with 500 Hz. b) Signal from a 25 μm large two-phase inclusion in 50 μm depth with 7.8 mass% NaCl_{eq} , opened by a 30 μm spiral with 42 Hz repetition rate.

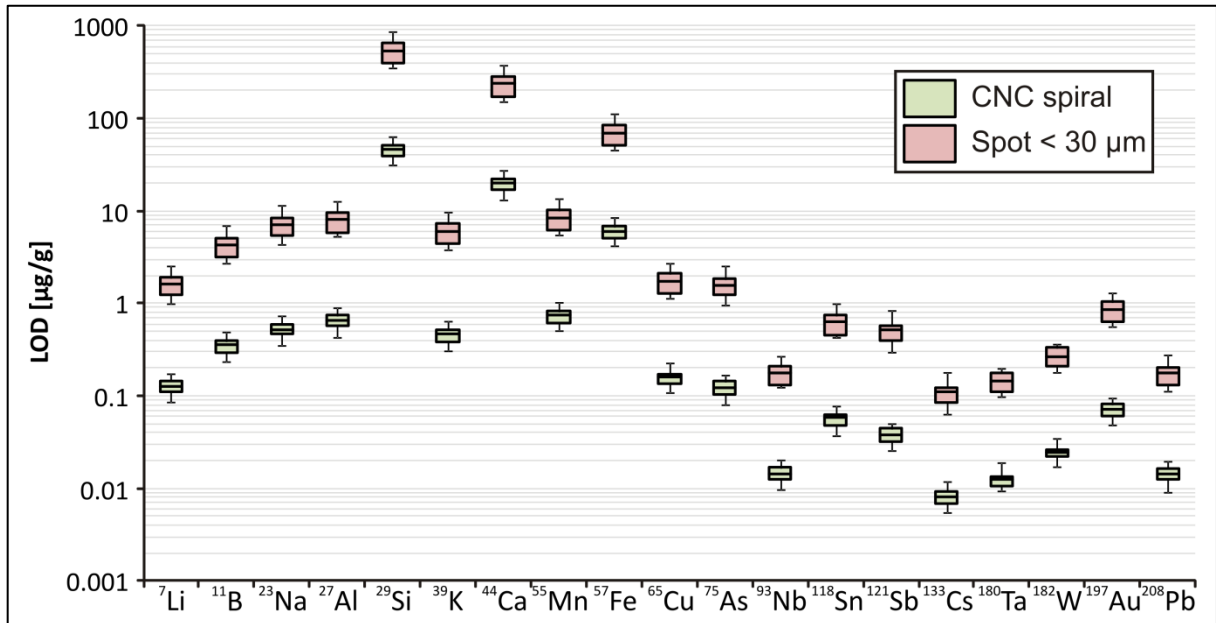


Figure 12: Box and whisker plot of the calculated lower limits of detection from two data sets. Green: Linux CNC spiral ablation technique with 42 Hz laser repetition rate (n=10). Red: ordinary spot ablation of fluid inclusion < 30 µm in diameter (n=15). The average LOD of the spiral technique is for all isotopes about one order of magnitude lower than by spot ablation.

In the example of Figure 11a) and b) two different fluid inclusions were analyzed with the CNC spiral technique. Figure 11a shows the recorded time resolved signal of a multi-phase flinc that was hosted in ~80 µm deep and had a diameter of 40 µm. The inclusion contained different types of daughter crystals and a salinity of 45 mass% NaCl_{eq} has been determined by microthermometry. For the penetrating of the host mineral to a depth of 80 microns a spiral diameter of 50 µm, a repetition rate of 500 Hz and a cell temperature of -60°C were used. After 25 seconds of drilling into the host mineral, the laser beam reached the inclusion and mobilized major amounts of the gas and liquid phase as represented by the first short signal ascent for the elements Na, K, Fe and Pb. About 10 seconds later another signal increase can be observed for the whole range of measured elements, including Na and K. This second increase of signal intensities is nearly stable over a time interval of 30 seconds before the slow decrease begins and the last minute of acquisition time passes by before the count rates reach their gas blank intensities again. This probably represents the ablation of the daughter minerals and their gradually removal by the laser beam. Since the recorded intensities of REE and Pb correlate mainly with the second signal peak, this suggests that the daughter minerals carry those elements. Over all, the ablation of this 40 µm large flinc at 80 µm depth below the surface resulted in a ~ 120 seconds long transient signal with maximum count rates of > 10⁸ cps for K. The relative slow signal decrease towards the end of data acquisition shows that the

spiral is working close to its maximal depth and a re-focusing of the laser beam would be necessary here to prevent the signal from fading out slowly resulting in a more clear separation of the underlying host quartz.

The signal in Figure 11b was recorded from a medium saline inclusion (7,8 mass% NaCl_{eq.}) of 25 µm size in diameter, hosted 50 µm below the sample surface. For this analysis a repetition rate of 42 Hz was used which is relatively low compared to the analysis described above, since this analysis was performed with a higher laser pulse energy. It took an ablation time of 40 seconds in order to penetrate the flint, which generated a 50 second long signal illustrated by the strong increase in Na, K and other elements. Even for trace amounts of Sn a distinct peak can be observed, clearly separated from that of the host mineral signal. This again illustrates that the LODs in laser ablation are strongly depending on the amount of material ablated and transported to the ICP and that this parameter can be controlled even if the initial beam size is limited by the adaption of higher repetition rates together with fast sample movement which simulates conditions obtained with a larger spot size at lower repetition rates.

The above mentioned characteristics are well reflected by the comparison of the calculated LODs from a series of *Linux CNC* analyzed large inclusions (30 – 50 µm) with the LODs from a series of small inclusions (< 30 µm) that have been measured with the ordinary spot size. All inclusions of both series belong to the same fluid inclusion assemblage. The LODs of the investigated elements show large differences between both methods and are generally by one order of magnitude lower when using the *Linux CNC* spiral technique (Figure 12). The here presented LODs refer to spiral analyses that were performed with a relatively low laser repetition rate of 42 Hz. This rate has been accounted to be the lowest possible repetition rate for the spiral technique that is still delivering a suitable ablation rate into the depth. With the exception of the isotopes with strong molecular interferences like ²⁹Si, ⁴⁴Ca and ⁵⁷Fe, all LODs in the light to medium mass range could be improved to a level of approx. 1 µg/g, including ⁷Li (0.15 µg/g), ²⁷Al (0.6 µg/g), ⁵⁵Mn (0.7 µg/g), ⁶⁵Cu (0.16 µg/g) and ⁷⁵As (0.13 µg/g). The LODs of ¹¹⁸Sn (0.05 µg/g), ¹²¹Sb (0.035 µg/g), ¹⁸²W (0.025 µg/g) and ²⁰⁸Pb (0.015 µg/g) were pushed down into the ppb range, with ¹³³Cs (0,008 µg/g) having the lowest LOD of all measured elements. Higher repetition rates of 100 Hz – 500 Hz would result in even lower LODs, but the proper repetition rate must be estimated from sample to sample depending on the energy density applied to the sample. If the ablation rate is too fast, it is possible that no distinct signal interval for the host mineral can be acquired so that the

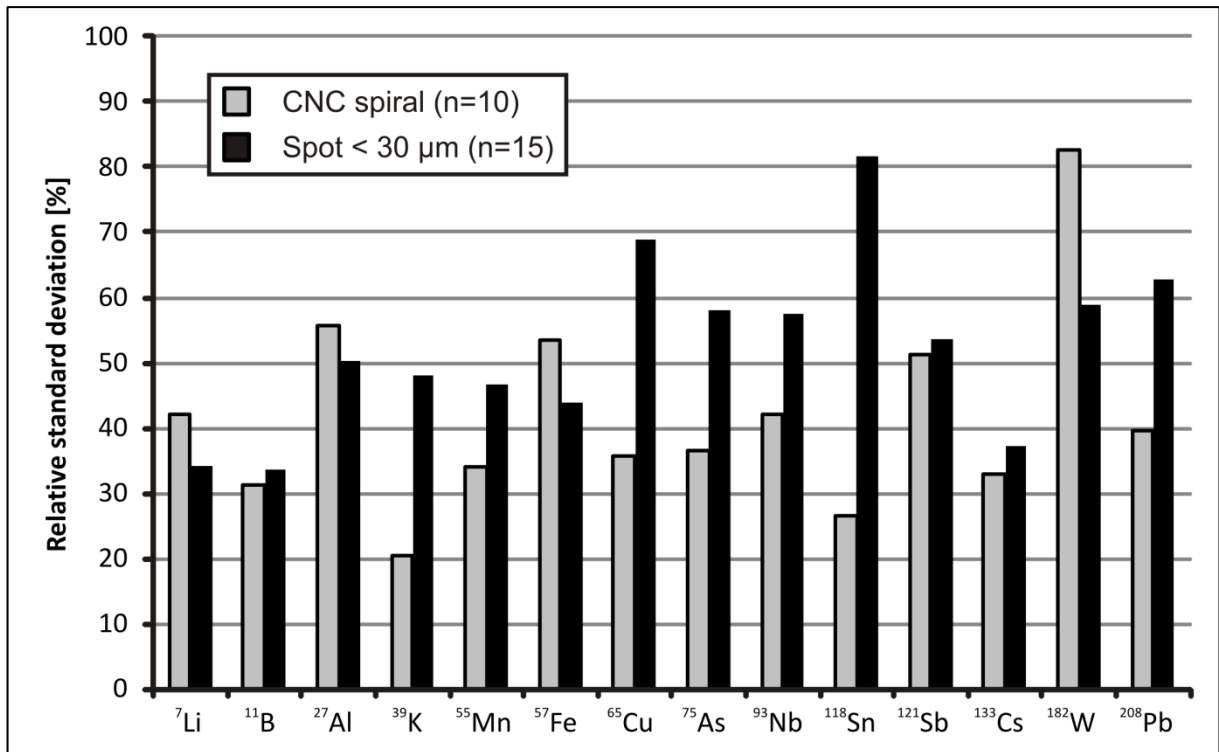


Figure 13: Comparison of the relative standard deviation (RSD) in % between inclusions analyzed with the *Linux CNC* spiral technique and inclusions analyzed by spot ablation. All inclusion belong to the same fluid inclusion assemblage (two-phase inclusions, 7,8 mass% NaCl_{eq}).

inclusion signal appears immediately after the laser shutter is opened. As a result a proper host mineral correction cannot be applied for fast appearing fluid inclusion signals. Since higher laser repetition rates and the bigger sampling area of the spiral pattern also increase the mobilization of potential contaminations on the sample surface and regularly incorporated trace elements of the host, a sufficient temporal distance of the host and inclusion signals is of great importance.

In order to compare the analytic performance of the *Linux CNC* based analyses, we have measured several inclusions from the same fluid inclusion assemblage (7.85 mass% NaCl_{eq}) from sample ZinQ with both ablation techniques. Fifteen inclusions with a diameter < 30 μm have been opened by the ordinary spot analysis with low repetition rates of 2 – 10 Hz and crater diameters of ~ 25 μm and ten bigger inclusions from 30 – 50 μm size were opened with a *Linux CNC* spiral using a slightly larger pattern than the inclusion diameter and repetition rates of 42 Hz or 100 Hz. Figure 13 shows the relative standard deviation of both data sets for the analyzed isotopes. The RSD of 10 of the 14 measured elements is smaller with the spiral technique when compared to the spot analysis. K, Mn, Cu, As, Nb, Sn and Pb show the most significant gain in analytic precision using the spiral technique. The RSD of ³⁹K decreases from 48% to 20%, ⁵⁵Mn from 47% to 34%, ⁶⁵Cu from 69% to 36%, ⁷⁵As from 58% to 37%,

^{208}Pb from 63% to 40% and the RSD of ^{118}Sn even decreases from 82% to 26%. Other isotopes like ^{11}B , ^{121}Sb and ^{133}Cs show only minor or negligible improvements in the RSD values of a few percent. In contrast to the observed improvements for the majority of isotopes, ^7Li , ^{27}Al , ^{57}Fe and ^{182}W cannot follow this trend and were measured with stronger variations by the spiral technique compared to the spot ablation. The uncertainty in the ^7Li values increased from 34% to 42%, for ^{27}Al from 50% to 56%, for ^{57}Fe from 44% to 54% and for the ^{182}W values from 59% to 83%.

Table 7: Average concentration values, standard deviation [$\mu\text{g/g}$] and relative standard deviation [%] of fluid inclusion assemblage “ZinQ 21”, measured with spot and spiral technique.

		^7Li	^{11}B	^{27}Al	^{39}K	^{55}Mn	^{57}Fe	^{65}Cu	^{75}As	^{93}Nb	^{118}Sn	^{121}Sb	^{133}Cs	^{182}W	^{208}Pb
Spot <30 μm	average	307	726	3488	3583	170	406	1327	504	1.1	73	7	237	11	265
	1SD	105	245	1752	1725	79	179	913	292	0.6	60	4	88	6	167
	RSD %	34	34	50	48	47	44	69	58	58	82	53	37	59	63
Spiral <30 μm	average	225	901	7442	4225	218	225	1825	636	0.5	34	10	373	8	313
	1SD	95	281	4138	862	74	121	650	233	0.2	9	5	123	7	124
	RSD %	42	31	56	20	34	54	36	37	42	26	51	33	83	40
change in conc.	in %	-27	24	113	18	28	-45	38	26	-54	-53	47	58	-22	18

The strong improvement in precision goes hand in hand with changes in the average concentration values that differ in relation to the spot analyzed inclusions by several tens of percent (Table 7). ^{27}Al , as an extreme example, was measured with 7442 $\mu\text{g/g}$ by the spiral technique and with 3488 $\mu\text{g/g}$ by the spot ablation. This intense variation of 113% might be a result of the higher host mineral signal generated by the spiral technique and an inadequate host mineral correction, which is especially important for Al, the most abundant trace element in quartz, and is caused by a host mineral signal interval which is for a statistical evaluation too short in time. Other elements show smaller variations which lie in-between -54% (^{93}Nb) and +58% (^{133}Cs). However, the majority of concentration values lie within a range of -30% to +30% when comparing both ablation modes. As illustrated by the laser microscopic observation of the ablation craters, it is likely that the whole content of the inclusions can be mobilized by the spiral technique. The most important requirements for correct measurements of fluid inclusions are therefore fulfilled by the spiral technique. The Gaussian shape of the fs laser beam generally complicates the ablation of deeper inclusions when using the spot ablation technique. Therefore the method of choice seems to be the spiral technique, delivering in general better LOD's and precision. The adaption of the spiral parameter in order

to obtain a more cylindrical shape of the crater may improve the results obtainable by defining the end of the fluid inclusion removal more clearly.

Due to the high laser repetition rates of > 100 Hz and the mobilization of bigger sample volumes in identical time intervals of spot ablations, the possible occurrence of mass load induced matrix effects needs to be discussed. Kroslakova and Günther 2007 demonstrated that especially volatile elements with low melting points (Cu, Zn, Cd, Pb) are prone to mass load dependent ICP-induced matrix effects, resulting in decreasing elemental ratios (X/Ca) of up to 25%, when the mass load of the ICP is increased by crater diameters from 30 to 120 μm . Fietzke and Frische 2016 visualized the change in plasma ion population by testing different spot sizes under different plasma conditions. Matrix contributions of 10% compared to the amount of Ar^+ ions, which can be easily reached by ns-LA with spot sizes > 30 μm , were described to be critical depending on the plasma conditions. The authors suggest a strict matrix-matching or to simply avoid matrix fractions $> 1\%$ in the plasma to overcome those mass-load effects.

The here used spiral technique might imply to generate identical mass-load problems, since the applicable spot sizes of > 100 μm are described to be critical by Kroslakova and Günther 2007 and by Fietzke and Frische 2016. Furthermore, both studies were performed with ns-LA at 10 Hz repetition rate, which is significantly lower than the here used > 100 Hz. A 60 s lasting ablation of a 100 μm spiral with 20 μm spot size at 200 Hz leads to an ablated crater volume of $V = 0.3 \cdot 10^6$ μm^3 (quantified by laser microscopy) and a calculated ablation rate of 0.0035 $\mu\text{m}/\text{pulse}$ on quartz. This is by two orders of magnitude lower than the typical ablation rate of a ns laser (0.25 $\mu\text{m}/\text{pulse}$, Kroslakova and Günther 2007) resulting in a significantly lower sample volume than achieved with a comparable 120 μm ns-LA spot with 60 s duration at 10 Hz ($V = 1.6 \cdot 10^6$ μm^3). According to this, the mass-load effect during fs-LA spiral ablation with extreme repetition rates is less pronounced than during ns-LA spot ablations at ‘normal’ repetition rates of 10 Hz. Nevertheless, practical investigations with different spiral diameters for the UV-fs-LA need to be carried out to clarify if plasma induced matrix effects exist at all and to what extent they influence the LA-ICP-MS results.

5. Case study: Fluid inclusions in Sn-W granites

5.1 Introduction

One of the most famous and best studied Sn-districts of the world is the European late Variscan Sn-W belt that extends from the Bohemian Massif towards Cornwall. Several Sn and/or W deposits exist along the former boundary of the Gondwana and Avalonia continental plate with different characteristics related to individual source rocks of the related granitic melts. Romer and Kroner 2014 described the distribution of Sn-W granites to be strongly connected to the existence of Sn-W enriched Paleozoic sediments and their melting during the formation of Pangea or during post-orogenic crustal extension and mantle upwelling.

In this study, we focus on the granites of the Altenberg-Teplice Caldera (ATC) in the Eastern Erzgebirge region that are known to be F- and Li-rich, and the Land's End granite in Cornwall with its characteristic enrichment of B. Despite of their differences in chemistry, both locations have large analogies concerning the formation of the granitic plutons and the associated deposits. Müller et al. 2005 proposed a two stage deposition model for the granites of the ATC which was recently confirmed for the Land's End granite by Drivenes et al. 2016. Near-solidus and subsolidus processes were responsible for the formation of the ore deposits in the cupola regions of the individual plutons in both locations. A magmatic fluid is suspected to have transported the metals (Sn, W, Cu) from the melt towards their final deposition places, but further detailed studies of the chemistry of the ore generating fluid need to be carried out to learn more about the metal transport in the hydrothermal regime and to reveal possible differences between the F-rich systems and the B and Cl dominated locations.

Our study ties up to the issue of metal-mobilization processes and their transport from the water-saturated melts and the transition from the magmatic to the hydrothermal stage. Therefore we investigated the fluid inclusion contingent of magmatic granite quartz crystals from the Schellerhau granite (ATC) and the Porth Ledden tourmaline granite (Land's End) which should host the earliest extracted fluids from the respective melt, represented by high saline brine inclusions, by means of micro analytical methods (microthermometry, fs-LA-ICP-MS). The Zinnwald/Cínovec Sn-W-Li deposit (ATC) serves as a representative location for the hydrothermal stage of the Sn-specialized granites. A hydrothermal grown miarolitic quartz single crystal from a Sn-W-mineralized vein, so-called "Flöz", representing the

hydrothermal stage was investigated in terms of its fluid inclusion contingent. The trace, minor and major element composition of the fluid inclusions and the host quartz were determined by fs-LA-ICP-MS. Calculations using the Ti-in-quartz thermobarometer were applied on the basis of the detected Ti content in the hydrothermal Zinnwald quartz and are combined with fluid inclusion isochores in order to identify the crystallization and trapping conditions of the primary inclusions.

5.2 Sample locations

5.2.1 Erzgebirge

5.2.1.1 Altenberg-Teplice caldera (ATC)

The Altenberg-Teplice caldera as part of the eastern Erzgebirge volcano-plutonic complex (EVPC) is located in the eastern part of the Erzgebirge mountains and hosts several Sn granites with historically important mining sites (e.g., Štemprok et al. 2003, Müller et al. 2005) (Figure 14 + Figure 15). The EVPC is located in the NW part of the Bohemian Massif and belongs to the Saxothuringian Zone of the Variscan orogenic belt. It is defined by an accumulation of acidic volcanic rocks and subvolcanic intrusions that are preserved in this eastern part of the Erzgebirge with a relative shallow erosion level. The formation of the ATC was triggered by the eruption of the voluminous Teplice rhyolite melts followed by late- to post-orogenic Variscan uplift and exhumation processes in combination with erosion, which shaped the topography of the ATC.

The major episode of Variscan granitic magmatism in the Erzgebirge and the ATC occurred over a relatively short period of about 10 Ma between 324 – 315 Ma (Romer et al. 2007). Tin mineralizations of the Erzgebirge are mainly related to the emplacement of ~320 Ma old granites, although some smaller Sn-specialized granites may have slightly younger ages (301 Ma, Förster and Rhede 2006). The border of the ATC is clearly defined by the intrusion of granite porphyry dyke system cross-cutting older biotite granites, e.g. the Fláje granite. The granite porphyries correspond in chemistry to the biotite granites, but show a different SiO₂ content and a metaluminous composition including accessory hornblende crystals. These characteristics are interpreted to be a result of mixing between a felsic and a more mafic melt (Seltmann et al. 2001, Müller and Seltmann 2002). With the collapse structure of the caldera, large amounts of acid volcanic products (e.g. the Teplice rhyolite) are preserved filling major parts of the caldera area exposed today. The Teplice rhyolite is dominated by crystal-rich ignimbrites which form the predominant part of the up to 2 km thick volcanic sequence (Štemprok et al. 2003). Several younger granite intrusions occur along a NW-SE trending zone in the central area of the EVPC. Outcrops of those granites in Germany are the Schellerhau, Sadisdorf, Altenberg and Sachsenhöhe granite, in the Czech Republic the

Preisselberg and Knötel granite near Krupka and at the state border the Zinnwald/Cínovec granite. Tin mineralized zones can be found in most of these young granites, but some, like the Schellerhau granite, were strongly eroded and lost its apical part and previously existing mineralizations. The Zinnwald granite was only slightly affected by erosion and the greisens-style tin deposits of the cupola are well preserved.

5.2.1.1.1 Zinnwald Sn-W-Li deposit

The Zinnwald/Cínovec Sn-W-Li deposit is closely related to the cupola part of the Zinnwald granite body. The mineralization can be distinguished into two morphological distinct types. Metasomatic irregular greisens bodies within the granite, which can exceed several tens of meters in diameter, and the sub-horizontal, up to 2 m thick quartz-zinnwaldite greisen veins, so-called “Flöze”. Those occur predominantly in the center of the cupola but extend partially into the host rocks and contain the main ore minerals cassiterite, wolframite and scheelite. Sample “ZinQ” is a single smoky quartz crystal which was sampled from a miarolitic cavity within the “Flöz” of the Militär Shaft on the Czech side of the Zinnwald/Cínovec deposit. Therefore it is likely that the quartz has trapped the fluids that were directly involved in the formation of the Sn-W mineralization. To make a maximum of its fluid inclusion contingent accessible, the ~2 cm long crystal was cut along the C-axis into two halves and polished from both sides.

A detailed investigation of the chemical evolution of the cupola part of the Zinnwald granite was given by Johan et al. 2012. Their crystallo-chemical study of micas from the Zinnwald granite and underlying, genetically related biotite granite with the focus on the key elements Sn, W, Nb and Ta yielded to the thesis that a metasomatic transition of the lithian annite in the biotite granite formed the Sn, Nb and Ta depleted zinnwaldite in the overlaying Zinnwald granite and the involved volatile phase, that was enriched in F⁻ and OH⁻, transported the metals to the coolest parts of the intrusion where they finally formed the mineralized zones.

According to Thomas et al. 2005 and Webster et al. 2004 the Zinnwald granite has developed from an extremely F-rich hydrous peraluminous melt with evolving H₂O content of 3 – 30 wt% and F content of 1.9 – 6.4 wt% during ongoing magma differentiation. An originally homogenous melt separated into a H₂O-rich melt and an extremely H₂O-rich melt. Both melt types separated different fluid phases that carried very high amounts of volatiles and halogens. Since fluorine breaks bridging oxygen bonds in a siliceous melt, it causes depolymerization and decreases the viscosity of the melt (Giordano et al. 2004). This results in a decrease of the solidus and supports the magma to reach an extremely high degree of

fractionation. Furthermore, the low viscosity enhanced the formation of an interconnected network of fractures which opened the way for the melt into the uppermost parts of the granite cupola. Thomas et al. 2005 suggest that the high F and B content supported the formation of $\text{HBF}_2(\text{OH})_2$ which is an excellent solvent for metal oxides. Thus, Sn may have been transported as $[\text{Sn}(\text{BF}_4)_2]$ and was extracted from the melt by the onset of volatile saturation (at 3.5 wt% F) until the end of crystallization of the magma.

5.2.1.1.2 Schellerhau granite

The Schellerhau granite suite is one of the youngest intrusions of the eastern Erzgebirge volcano-plutonic complex. It intruded into the Teplice rhyolite after the ATC collapsed and represents one of the high-F, low P_2O_5 Li-mica granites of the Erzgebirge. Müller et al. 2005 figured out that one deep magma reservoir fed all extrusive and intrusive volcanic rocks of the ATC. Therefore, the genetic relation of the Schellerhau granite and the Zinnwald granite is very close. Both granites belong to a group of topaz-bearing rare metal granites that formed several bigger and smaller mineralizations in their cupolas. Since the top of the Schellerhau intrusion has been eroded by an estimated level of 500 – 1000 m it is likely that a former mineralization in the cupola of the Schellerhau body has been eroded, too. However, minor Sn mineralizations have been preserved and were mined at the Paradies-Fundgrube and Pöbelknochen area in the southern part of Schellerhau granite body (Müller et al. 2000). The Schellerhau granite complex can be divided into three facies (SG1, SG2 and SG3), which can be interpreted as the result of progressive fractionation products of one deep-seated magma chamber. All generations represent P-poor and Li-F-rich leucogranites that evolve chemically from the SG1 to SG3. In particular, the already elevated Rb, Li, F and Sn content increases from SG1 to SG3 (Förster et al. 1999).

Müller et al. 2006a estimated the water content of the melt during its intrusive phase to more than 5% H_2O . The high water content featured the formation of highly evolved residual melts that finally resulted in the generation of Sn-W deposits. The fluids which leached out the metals from the melt are subject to this study and are suspected to be found as primary, multi-phase fluid inclusions in the quartz phenocrysts of the Schellerhau granites.

5.2.1.2 Gottesberg – Grummetstock

The Gottesberg volcano-plutonic complex belongs to the western Erzgebirge-Vogtland region, which is part of the Saxothuringian Zone in the Variscan orogen (Figure 14). Large masses of granitic rocks were emplaced during the Late Carboniferous with S-type or mixed I-S type chemistries (Förster et al. 1995). The Gottesberg subvolcanic rocks intruded into the Eibenstock multiphase S-type pluton and represents a group of felsic, non-peralkaline A-type subvolcanic rocks, that formed in a post-collisional extensional collapse setting. It consists of two rhyolites and two microgranites with similar petrographic and chemical characteristics that differ significantly from the older Eibenstock pluton, which can be classified as a high-P topaz granite. The biotite granites of the Gottesberg suite are higher in HREE, Y, Zr, Hf, Th and Nb but have less Sn, Li, Rb, Cs, F and P (Förster and Tischendorf 1994).

The Gottesberg Sn deposit is related to breccia and greisen type mineralizations which have formed in multiple events by the release of overpressured fluids when the highly evolved H₂O- and F-rich melts crystallized and reached volatile saturation. Seltmann et al. 1993 described the formation of the breccia type deposits, which are located at the contact between the Eibenstock granite and the subvolcanic rhyolite, as a result of fluid enrichment and subsequent pressure increase at the contact leading to decrepitation processes and the explosive formation of breccias pipes. The greisen deposits formed in the cupola parts of the intrusion. A large greisen body ranging about 900 m into depth and is the result of the volatile rich fluids that exsolved from the underlying F-rich, P-poor biotite granite. Mineralizations of W, Sn, Cu and U can be found in the Gottesberg complex.

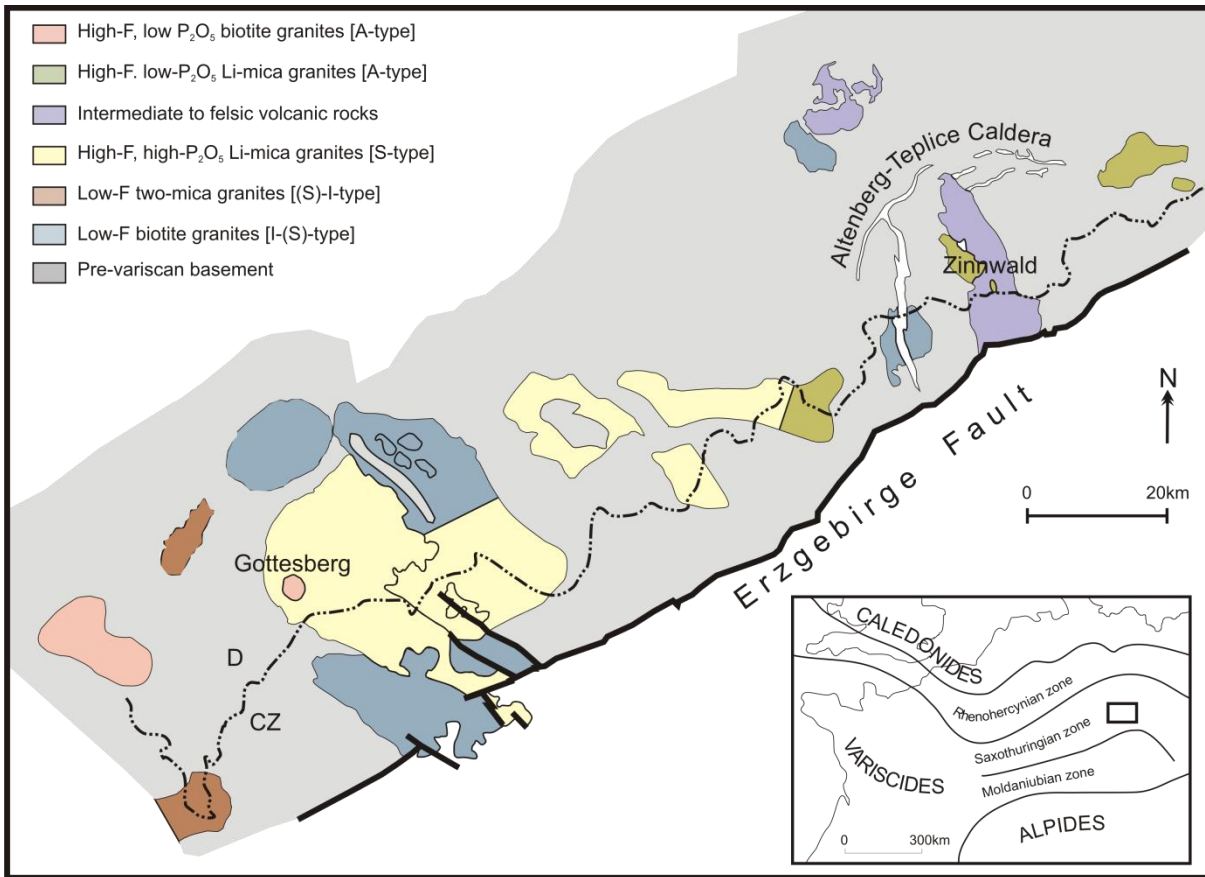


Figure 14: Simplified map of the Erzgebirge (after Förster et al. 1999).

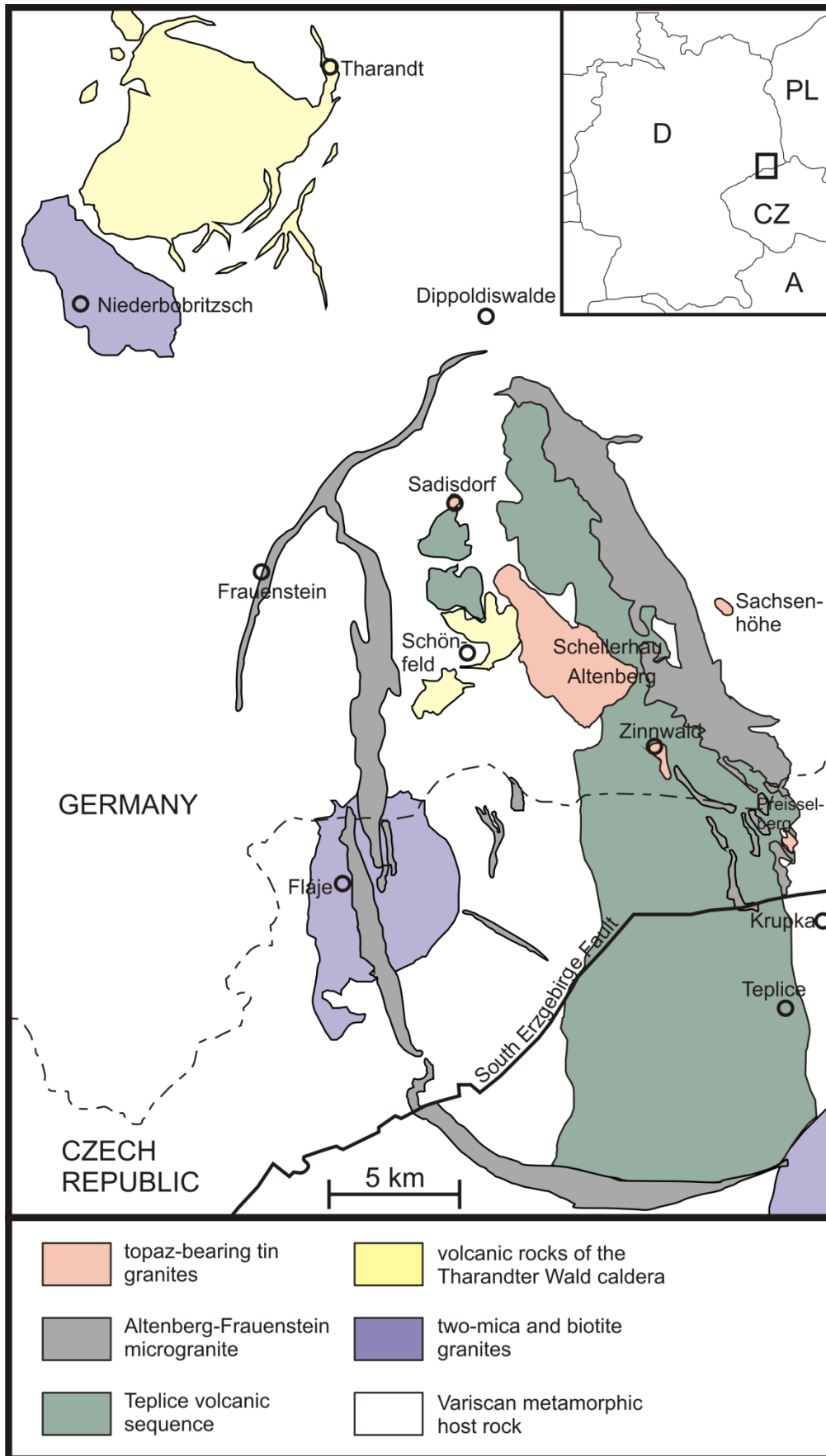


Figure 15: Detailed map of the Erzgebirge volcano-plutonic complex (EVPC) with the Altenberg-Teplice caldera (ATC); after Müller et al. 2005a.

5.2.2 Porth Ledden - Land's End granite (Cornwall, UK)

The Cornubian batholith in SW England is defined by five individual granitic plutons (Dartmoor, Bodmin, St. Austell, Carnmenellis and Land's End) with the Land's End pluton being the youngest one (277 – 274,5 Ma; Chen et al. 1993). Mineralizations can be found in each of the five granite plutons which have been formed at the end of the Variscan orogeny. The Land's End granite (Figure 16) hosts the Sn-Cu-As mineralization of the St. Just mining district and has been intensely studied in terms of its petrographic and textural characteristics as well as their chemical evolution (Müller et al. 2006a, Van Marcke De Lummen, G. 1986). The granitic complex was emplaced in multiple intrusive events (Powell et al. 1999) but differentiated from a single magma reservoir (Müller et al. 2006a). Geochemical and mineralogical studies of the magmatic evolution of the Land's End pluton were studied during the last decade and were integrated with the field evidence to contribute to the theory of magmatic evolution (Müller et al. 2006a). The granites were classified as S-type granites with peraluminous chemistry ($A/CNK = 1.1 - 1.4$). The crystallization history of the Land's End pluton begins with fine-grained biotite (Mg-siderophyllite) granites (FGG) which are followed by the coarse-grained biotite (MG-siderophyllite) granite (CGG), both containing K-feldspar megacrysts of > 3 cm in lengths. The youngest intrusive stage is represented by fine-grained porphyritic Li-siderophyllite granites containing poor K-feldspar megacrysts and coexisting medium-grained equigranular Li-siderophyllite granites. Differentiates and minor intrusions of tourmaline granite and massive quartz-tourmaline rock (MQT) can be found in spatial and temporal relation to the CGG and Li-siderophyllite granites.

Porth Ledden is one of the locations where the whole intrusive sequence is exposed on a small scale. A special feature at Porth Ledden is the MQT that consist to 99% of quartz and tourmaline and is the result of an extreme fractional crystallization process and later unmixing from a tourmaline-rich granite melt (Charoy 1986, Charoy and Evans A.M. 1982). It crystallized from a residual boron-silicate fluid, which intruded after the megacrystic biotite granite was solidified. The B-rich phase could not escape into the country rock and kept on reacting with the underlying tourmaline granite under hydrothermal temperatures. The feldspars were completely dissolved during this greisenization process, resulting in a pronounced porosity of the reaction product, namely the MQT rocks (Müller et al. 2006a).

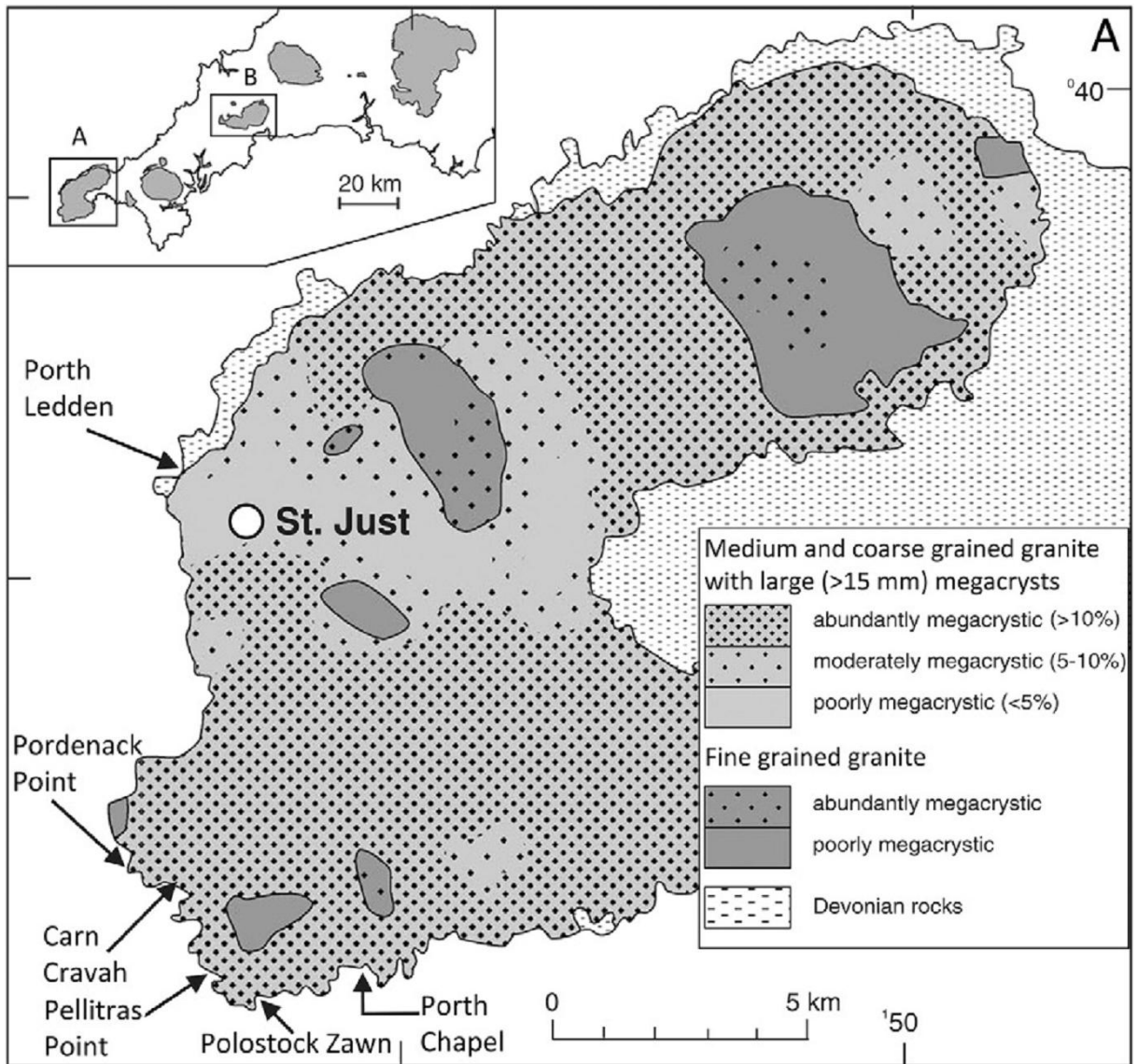


Figure 16: Geological map of the Land's End granite in Cornwall, UK. From Drivenes et al. 2016.

5.3 Analytical methods

5.3.1 Microthermometry

The microthermometric investigations were performed at the Institute for Mineralogy at the Leibniz Universität Hannover with a Linkam FTIR600 heating-freezing stage that was equipped with a heating-freezing silver block from the Linkam THMSG600 stage. The device is mounted on a Leica DM2700P research microscope with a Leica DFC295 three megapixel camera for high-resolution live images with a fast frame rate and a 50x magnification long-working distance objective to allow a precise determination of phase transitions in fluid inclusions. The system was calibrated on a daily basis with in-house produced synthetic CO₂-H₂O and pure H₂O fluid inclusions. The three-point calibration curve was based on the CO₂ melting point for $T < 0^{\circ}\text{C}$, the H₂O melting point for $T \approx 0^{\circ}\text{C}$ and the $T_{\text{h}}(\text{LV} \rightarrow \text{L})$ value of the pure H₂O inclusions for high $T > 0^{\circ}\text{C}$. For the observation of ice melting temperatures we have chosen a heating rate of 0.3°C/min to guarantee a precise determination of the ice melting point, uninfluenced by overheating phenomena. Homogenization temperatures were determined with a heating rate of 1°C/min. The uncertainties for $T_{\text{m}}(\text{Ice})$ and $T_{\text{h}}(\text{LV} \rightarrow \text{L})$ measurements were $\pm 0.1^{\circ}\text{C}$ and $\pm 1^{\circ}\text{C}$, respectively. Calculations of the fluid salinity, density, pressure at homogenization and dP/dT isochore slope were carried out with the MS Excel based spreadsheet “HOKIEFLINCS_H2O-NACL” (Steele-MacInnis et al. 2012).

5.3.2 fs-LA-ICP-MS

5.3.2.1 Trace elements in fluid inclusions

The above described fluid inclusion assemblages were analyzed with UV-femtosecond laser ablation SF-ICPMS, using the freezing technique of Albrecht et al. 2014. The *NIST610* glass was used for external standardization and the NaCl_{eq} values, which have been determined by microthermometry, were used as the internal standard to calculate concentration values from the recorded laser ablation signals. Analyses have been conducted at different days, but the methodological list of elements was only marginally modified from time to time. The following isotopes were always used: ^7Li , ^{11}B , ^{23}Na , ^{27}Al , ^{44}Ca , ^{55}Mn , ^{57}Fe , ^{63}Cu , ^{75}As , ^{118}Sn , ^{121}Sb , ^{133}Cs , ^{182}W , ^{208}Pb and complemented with ^{39}K , ^{66}Zn , ^{85}Rb , ^{88}Sr , ^{95}Mo , or ^{180}Ta from day to day. ^{28}Si or ^{29}Si served as the matrix tracer element for the host correction of mixed fluid and quartz signals. The sweep times were kept as short as possible and usually lie below 600 ms with the Element XR working in the fast scan mode and measuring the isotopes in the peak center mode on 4 or 5 lines with 12 ms dwell time per peak. Mass offset corrections were conducted on a daily basis during machine tuning. Data acquisition was not started before the ThO/Th ratio reached values $< 0.3\%$. For inclusions of diameters smaller than 20 μm , we performed a spot ablation with a maximum focused laser beam and a repetition rate of 2 to 10 Hz, depending on the depth of the inclusion. Flincs with bigger diameters than 20 μm have been opened with a fast moving spiral pattern and very high laser repetition rates of 100 Hz to 500 Hz. In that case, major elements like Si or Na produced signals of very high intensities ($> 5 \cdot 10^8$ cps) that could only be recorded in the Faraday detection mode of the Element XRTM. Hence, the cross calibration of all detection modes was checked and adjusted if necessary during tuning. The spiral patterns were adjusted to the inclusion size so that they were always slightly larger than the inclusion. This technique allows drilling deep into the sample over a short time span on a bigger area compared to static femtosecond laser spot analyses.

The temperature in the heating-freezing cell was selected with respect to the first melting temperatures of the analyzed fluid inclusions. Consequentially, analytical temperatures lay in a range between -40°C and -80°C and were kept constant all day. If any impurities have been spotted on the sample surface, we performed a low frequency cleaning shot before starting

data acquisition. A gas blank of 40 seconds was recorded prior to the ablation of the sample, enabling a precise background correction.

5.3.2.2 Trace elements in quartz

The analyses have been conducted with the above (see chapter 1.3) described UV-fs-LA-ICP-MS device. The following isotopes were measured in low resolution mode: ^7Li , ^9Be , ^{11}B , ^{23}Na , ^{25}Mg , ^{27}Al , ^{28}Si , ^{39}K , ^{45}Sc , ^{49}Ti , ^{51}V , ^{53}Cr , ^{55}Mn , ^{57}Fe , ^{65}Cu , ^{66}Zn , ^{73}Ge , ^{75}As , ^{85}Rb , ^{88}Sr , ^{89}Y , ^{93}Nb , ^{95}Mo , ^{107}Ag , ^{118}Sn , ^{121}Sb , ^{133}Cs , ^{137}Ba , ^{181}Ta , ^{182}W , ^{208}Pb and ^{209}Bi . All isotopes were measured with 15 ms dwell time and the “gas blank” signal was measured over 40 s prior to each analysis (Figure 18). ^{28}Si Silicon was measured in the Faraday detection mode, while the triple mode was used for all other isotopes. A cross calibration between the three detection modes was done during the tuning of the machine. The oxide formation has been checked with the ThO/Th intensity ratio and was tuned to < 0.2 % before the analyses were started. To reach the lowest possible detection limits (LOD) (Table 13), the Linux CNC spiral laser ablation technique was used with the maximum repetition rate of 500 Hz and a spiral diameter of 100 μm . Ablation spots have been selected carefully, to avoid accidental ablation of smallest fluid/solid inclusions. For that reason, the transection of ablation spots over the quartz grain shows some slight curvatures (Figure 28). Nevertheless, it cannot be excluded that some micro inclusions were hit by the laser even if the ablation side appeared to be clean in the video image of the LA device. Therefore, all acquired time resolved signals were checked for extraordinary high signal intervals (Na & K for fluid inclusions, Pb for possible solid inclusions) and if necessary, the contaminated parts were excluded from the data processing. The Sills evaluation software allows selecting several sample signal intervals that get merged for the concentration calculations, which simplifies those quality checks (Figure 18). A line of 45 sample spots was chosen along a cross sectional profile through the crystal in order to determine the possibility of a chemical zonation (Figure 28). The *NIST612* glass was used for external calibration and the calculation of concentration values was based on the assumption that an amount of total oxides of 99.95% was measured. The calculation of the LODs follows the procedure from Pettke et al. 2012. Average LODs of all measured elements can be found in Table 13.

5.3.2.2.1 Importance of trace elements in quartz for petrological investigations

Quartz is known to be one of the most abundant minerals in the earth crust and its formation can be related to both, magmatic and hydrothermal environments. It can form under a wide range of pressure and temperature conditions and especially in hydrothermal ore deposits quartz plays a significant role as the major gangue mineral (Götze and Möckel 2012). The parental fluids where quartz precipitates from can have highly varying chemical compositions, which in the first place depends on the degree of fractionation of the melt and the type of magma protolith. The trace element contingent of quartz crystals can be used to reconstruct the development of magmatic systems, such as granite bodies, pegmatites and porphyry, epithermal or orogenic ore deposits. The high resistivity of quartz against chemical and physical alteration supports the trace element contingents to be unaffected by those secondary processes, which strengthens the reliability of the data sets in general. Although quartz has a very simple chemical composition and incorporates only small amounts of trace elements that are often settled in the lower ppm to ppb range (Figure 17), it contains some important elements like Al, Ti, Ge and Li that can provide information about the conditions of formation. For example Huang and Audétat 2012 reported that the incorporation of Ti into quartz is pressure and temperature dependent, which gives the Ti content the ability to be used as a geothermobarometer (“TitaniQ” – “titanium in quartz”). In addition, Ti and other elements reflect the degree of melt differentiation, thus enabling the reconstruction of melt evolution from the trace element content of quartz. The biggest variations in trace element concentrations have been observed in hydrothermal quartz, so far. Other geological settings provide a smaller variability in quartz chemistry, because the physical and chemical conditions of formation are much wider for the hydrothermal settings (Rusk et al. 2008).

The incorporation of trace elements result generally in point defects in the quartz lattice, which supports foreign ions to enter the lattice at interstitial positions (preferentially small ions) or substitute for Si or O. Only a few ions can substitute for Si^{4+} in the quartz crystal lattice, because of its small ionic radius and high valence. Aluminium is the most abundant trace element in quartz and can reach a 5000 $\mu\text{g/g}$ level (e.g. Götze and Möckel 2012). The similar ionic radii of Si^{4+} (0.39 pm) and Al^{3+} (0.5 pm) and the high availability of Al in the earth crust facilitate its incorporation into quartz. Other multivalent ions like Ga^{3+} , Fe^{3+} , Ge^{4+} , Ti^{4+} and P^{5+} can also substitute for Si^{4+} , but do not reach the same concentrations as Al (Götze 2009). In the case of an $[\text{AlO}_4]^-$ centre in the crystal lattice, a monovalent cation is needed for charge compensation and placed in an interstitial position adjacent to the diamagnetic centre. The most abundant cations for charge balancing are Li^+ , H^+ , Na^+ and K^+ . Therefore, Li is

typically correlating with Al and varies between a few $\mu\text{g/g}$ to $\sim 100 \mu\text{g/g}$. Other cations with relative high concentrations up to $100 \mu\text{g/g}$ can be Ti, K, Sb, Fe, Ca, Na and P. Further elements like H, B, Ge, Ga, Sn, Ba, Cs and As usually do not exceed the $10 \mu\text{g/g}$ level and are often concentrated below $1 \mu\text{g/g}$ (Figure 17).

Rusk *2012* investigated the quartz chemistry in different ore deposit types and concluded that trace elements in quartz can be a useful tool to fingerprint the type of ore deposit, including porphyry-type (Cu-Mo-Au), orogenic Au and epithermal deposits. In these cases Al and Ti concentrations show the greatest variability, thus, the different deposit types plot in separate fields with the Ti content being the stronger separating parameter than Al. Ti decreases from porphyry-type ($1 - 100 \mu\text{g/g}$), orogenic ($0.2 - 3 \mu\text{g/g}$) to epithermal deposits ($<0.1 - 1 \mu\text{g/g}$). The epithermal locations have the highest range in Al (20 to $4000 \mu\text{g/g}$), followed by orogenic Au ($10 - 1000 \mu\text{g/g}$) and porphyry deposits ($50 - 500 \mu\text{g/g}$) (Rusk *2012*).

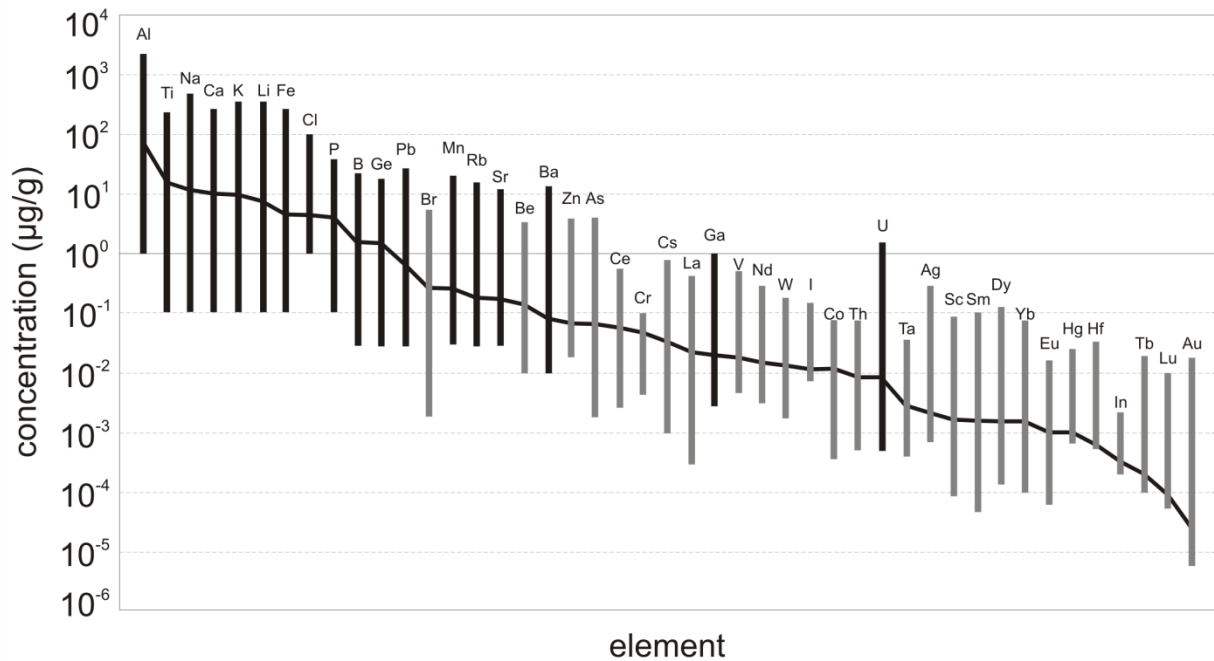


Figure 17 : Average abundance and variations of trace elements in quartz. (from Götze, 2009)

Several studies about quartz chemistry in different volcanic and magmatic regimes have been conducted, with a sharp rise in number of studies especially in the last decade, as a consequence of the latest improvements in micro analytical techniques, in particular LA-ICP-MS. For example pegmatitic quartz has been studied frequently by different authors (Beurlen et al. 2011, Breiter and Müller 2009, Flem et al. 2002, Larsen et al. 2004, Müller et al. 2008,). In addition, a number of studies on volcanic quartz (e.g., Audétat 2013, Watt et al. 1997, Wark et al. 2007,) and plutonic quartz have been conducted in the last two decades (e.g., Breiter et al. 2013, Jacamon and Larsen 2009, Müller et al. 2000, Müller et al. 2010, Wiebe et al. 2007). A detailed project about trace elements in magmatic quartz from the eastern Erzgebirge volcanic complex also includes the quartz chemistry of the Zinnwald granite (Breiter et al. 2012). The latter data provide a solid basement for the here studied hydrothermal quartz, which is associated with the Zinnwald granite.

The Al/Ti ratio has been used as an indicator of the parental melt degree of fractionation and provides a good basis to describe the behavior of different trace elements during the evolution of a specific pluton. While Ti usually decreases with the ongoing differentiation of the parental melt, Al undergoes a strong enrichment in the higher fractionated granites. This trace element behavior was first discovered by Müller et al. 2002 on the example of Podlesí granite system in the Western Erzgebirge, Germany. In the example of the Bohemian Massif granites from Czech Republic (Breiter et al. 2013), the Al/Ti ratio varies from 0.1 – 2.2 in the less

evolved granites, up to 5 - 50 and even >100 in the strongly fractionated granites of the Erzgebirge. The Ge/Ti ratio is another tracer of melt fractionation established by Jacamon and Larsen 2009 on the example of the Kleivan granite in Norway. The changing ratio with degree of fractionation is mainly controlled by a continuous decrease of the Ti content, while Ge stays constant over a wide range of fractionation, only rising in the strongest differentiated granites with Ti <50 µg/g. Germanium concentrations usually do not exceed 3 µg/g (Figure 17).

Furthermore, the crystallization sequence of the minerals affects the contents of Li and Ge. Lithium basically correlates well with Al with Li/Al atomic ratios of 0.5 in most granites. But quartz crystals from some late crystallizing granites that contain Li-micas have a Li deficit, compared to their Al contents. Breiter et al. 2013 explain this with the order of crystallization where quartz that forms after Li-mica is depleted in Li compared to quartz that forms before the mica.

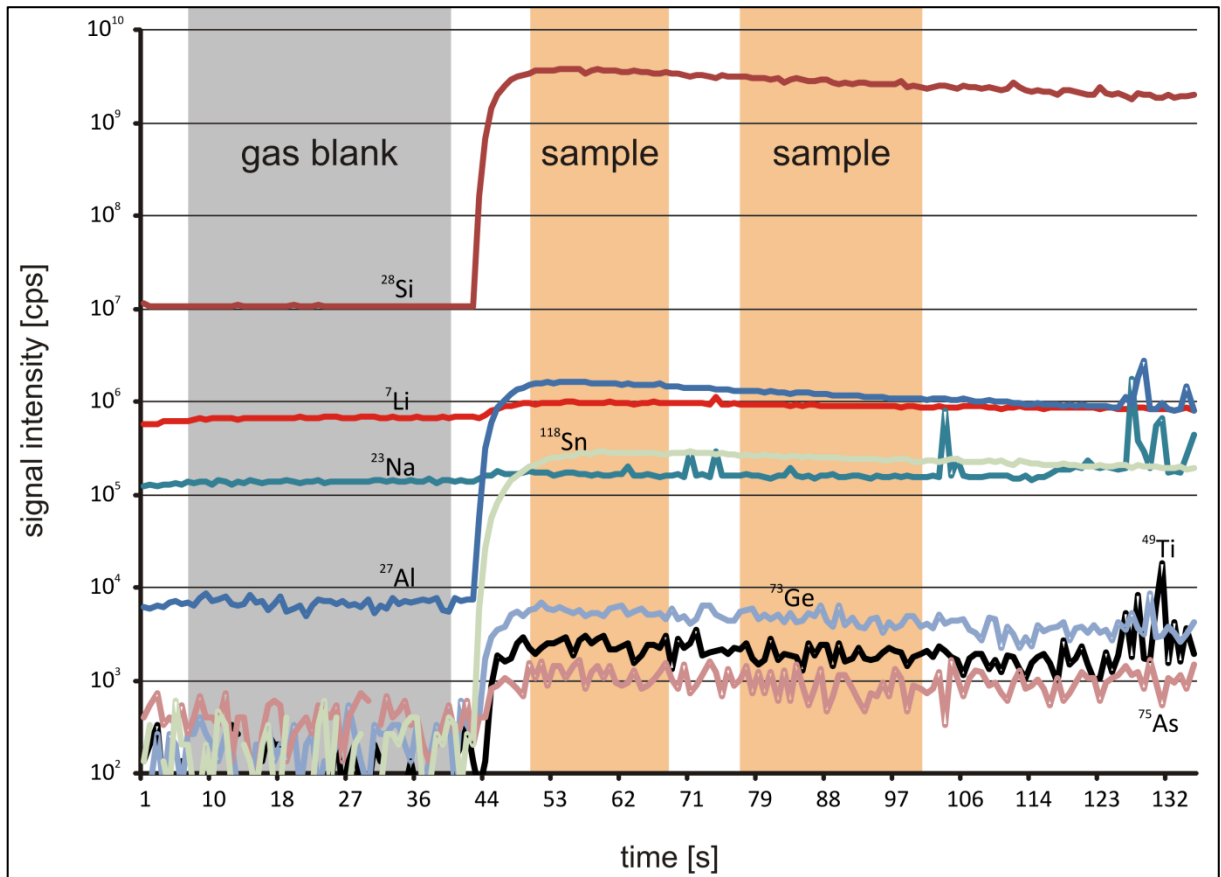


Figure 18: Time resolved laser ablation ICP-MS signal on Zinnwald hydrothermal quartz. The repetition rate was 500 Hz and a spiral pattern of 100 μm in diameter has been ablated. The grey area marks the gas blank interval for background correction and the orange areas show the integration intervals for the sample signal. The ^{23}Na signal shows some spikes, which have been excluded from the integration interval to avoid an influence of micro fluid inclusions on the concentration values.

5.4 Results

5.4.1 Fluid inclusion petrography and microthermometry

5.4.1.1 Zinnwald Sn-W-Li deposit (sample: ZinQ)

The investigated quartz crystal (Figure 19) shows a high spatial density of fluid inclusion trails coming from the left rim (with respect to the orientation in Figure 19) proceeding into its central parts. These two-phase inclusions are of secondary origin and carry low density fluids with a low degree of fill and NaCl_{eq} contents below 1 mass%. The tip and the upper third of the crystal are free of any fluid inclusions, but on the right hand side, several trails and groups of inclusions could be identified. These inclusions are suitable for investigations, because they are not as closely spaced as the secondary trails on the left side and therefore provide many potential laser ablation sites. Five distinct fluid inclusion assemblages could be identified in this part of the crystal. Assemblages S1 and S2 are secondary trails that cross cut from the rim into the inner areas of the quartz. Both types are similar looking two-phase inclusions with medium densities (S1: 0.61 g/cm³, S2: 0.52 g/cm³), but the salinities differ significantly, since S1 flincs have 5.7 mass% and S2 flincs 0.88 mass% NaCl_{eq} . Due to the low salinity, the latter could have been affected by meteoric fluids. Homogenization temperatures $T_{\text{h}}(\text{LV} \rightarrow \text{L})$ of both secondary trails are nearly identical (S1: 386°C, S2: 388°C). Since the meniscus was fading out during homogenization, the process can be called ‘supercritical’. In relation to S1 and S2, the trails PS3 and PS4 host older fluids, since both end up in front of the rim and were overgrown by the youngest zones of the quartz crystal. The characteristics of these fluid inclusion assemblage (FIA) are quite similar, with salinities, densities and T_{h} in a narrow range (PS3: 4.2 mass%, 0.63 g/cm³, $T_{\text{h}}(\text{LV} \rightarrow \text{L})$ 380°C. PS4: 4.8 mass%, 0.59 g/cm³, $T_{\text{h}}(\text{LV} \rightarrow \text{L})$ 377°C). Both, PS3 and PS4 FI homogenize into the liquid phase.

Additionally, FIA P3 was trapped in the area between S1 and S2. These flincs are arranged in a cloudy shape that tends to be parallel to the growth zones of the crystal and perpendicular to S1 and S2. Therefore, P3 can be interpreted as a primary FIA with a slightly higher salinity (8.5 mass% NaCl_{eq}) but identical densities (0.63 g/cm³) and homogenization temperatures with supercritical homogenization (400°C).

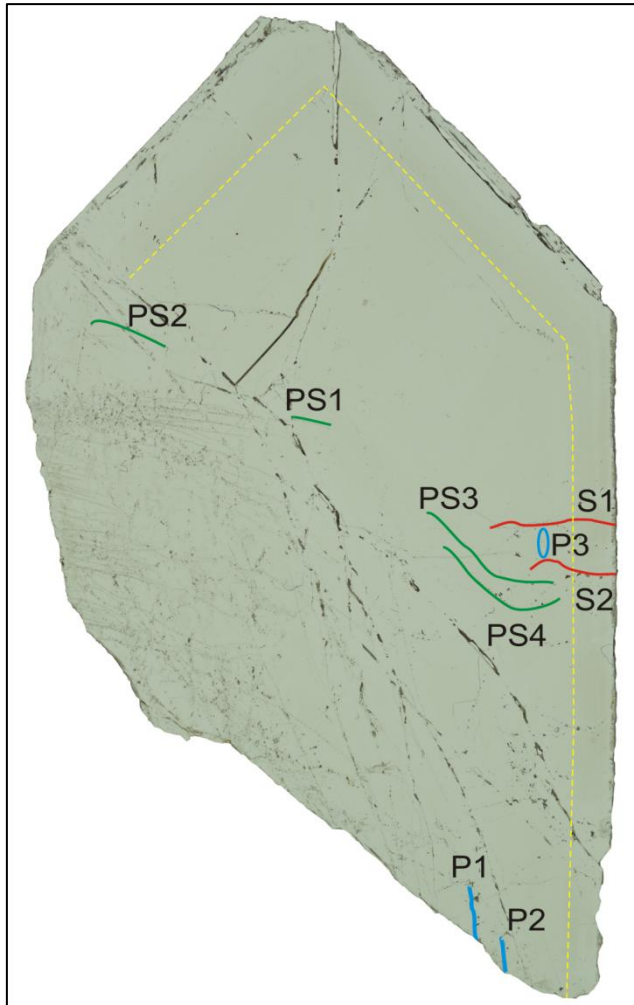


Figure 19: Sample “ZinQ”, single smoky quartz crystal from the Sn-W-Li mineralized zone, sampled in the “military shaft” on the Czech side of the Zinnwald/Cinovec deposit. The crystal has been cut along the c-axis and polished from both sides to a thickness of ~ 300 μm . The colored lines represent fluid inclusion assemblages that have been investigated by microthermometry and fs-LA-ICP-MS. Blue lines (P1 – P3) are primary fluid inclusions that appear to be parallel to the zoning (dashed yellow line) of the crystal. Green lines (PS1 – PS4) represent pseudosecondary trails and red lines (S1 & S2) secondary inclusion trails that could have been entrapped during the healing of cracks.

Despite their different position in the crystal, PS1 and PS2 assemblages show closely related characteristics to the already presented FIAs. The PS1 trail has 5.6 mass% NaCl_{eq} with a $T_{\text{h}}(\text{LV} \rightarrow \text{L})$ of 396°C and 0.59 g/cm^3 and is hosted in the center of the quartz. PS2 inclusions are in close agreement to P3 flincs, with 7.8 mass% NaCl_{eq} , 0.65 g/cm^3 and a T_{h} of 385°C, but have been trapped in a former fracture on the opposite side of the crystal. Both, P1 and P2 homogenize into the liquid phase.

The only brine inclusions that could be found in the sample were trapped in two relative short trails at the bottom of the crystal. P1 and P2 are three-phase inclusions (liquid + solid + vapor) of small sizes (<10 μm) and salinities of 28 mass% (P1) and 31 mass% NaCl_{eq} (P2). The densities of the P1 fluids have been calculated with 0.97 g/cm^3 while the P2 fluids are slightly denser (1.03 g/cm^3). Salinities were determined from halite melting temperatures Liquid-vapor homogenization appeared into the liquid phase at 367°C in P1 and 290°C in P2, respectively.

Based on the petrographic observations, it is difficult to set all FIA into a genetic relation and to establish a trapping history. Nevertheless, it is obvious that S1 and S2 represent the youngest fluids of all groups, followed by the pseudosecondary and primary trails. Due to the central position, PS1 can be interpreted as the oldest of all pseudosecondary trails. PS3 and PS4 represent fluids of the same age and PS2 could be chronologically close to P3, because of their similar salinities. In contrast, P1 and P2 can be considered as A) primary FIAs due to their growth zone parallel appearance or B) as secondary FIAs, because they end up at the lower rim of the crystal and were trapped along a trail that could represent the filling of a healed crack. In the first case A), P1 would represent the earliest trapped fluids of all FIA followed by P2, PS1, P3 and PS2, PS3 and PS4, S1 and S2. In the latter case B), it is purely speculative if P1 and P2 were trapped earlier or later than the other FIA.

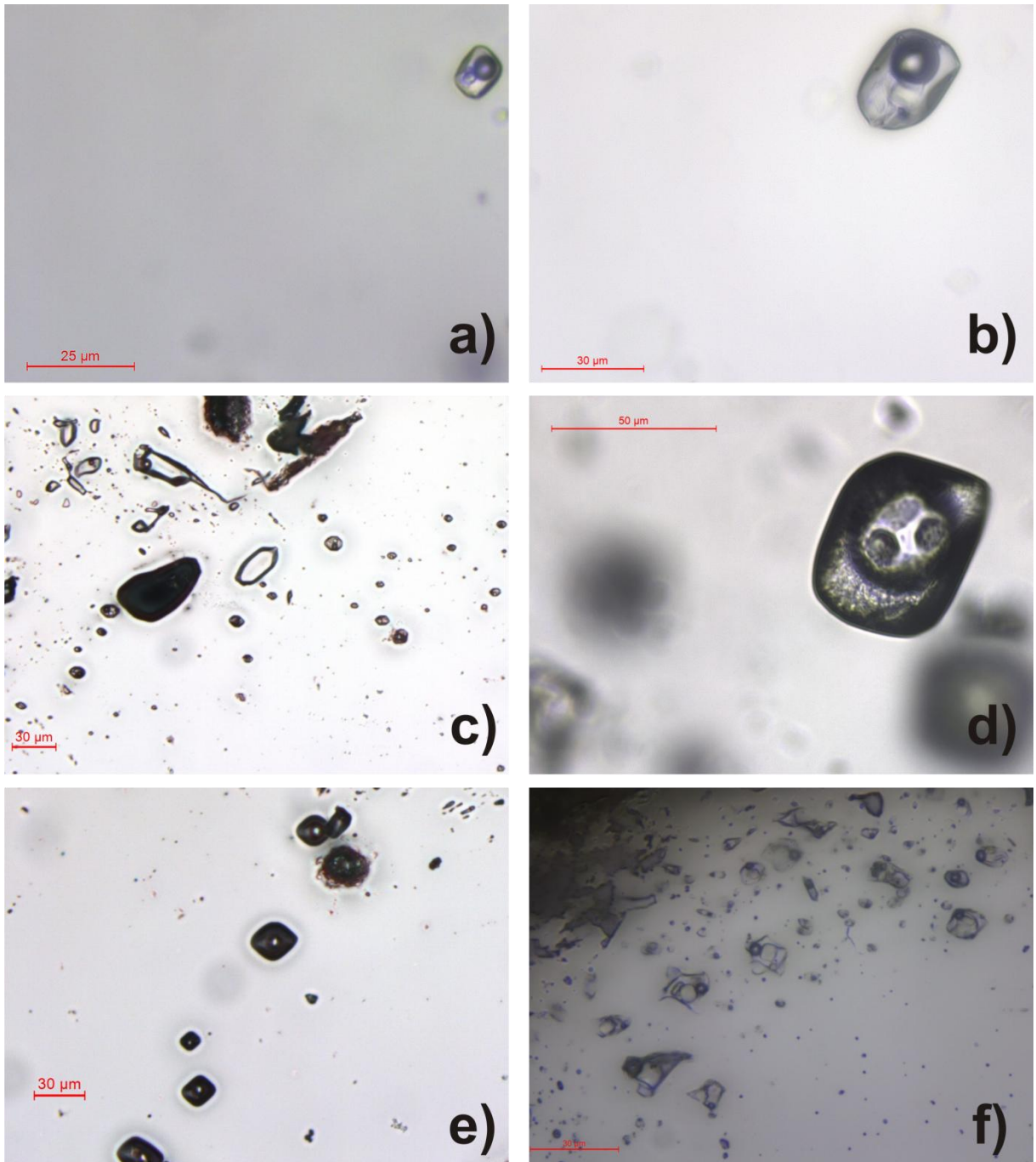


Figure 20: a) Three-phase inclusion from FIA P1 with halite daughter crystal. b) Two-phase inclusion from FIA P3 c) FIA P2, small L+V+S inclusions with halite daughter crystals. d) Secondary FI (FIA S2) in the frozen state. e) Typical appearance of the secondary and pseudosecondary along a trail of FI (FIA S1). f) Brine inclusions in magmatic quartz from the Schellerhau granite with different daughter crystals.

5.4.1.2 Schellerhau granite

The magmatic quartz of the here investigated Schellerhau granite samples hosts a huge number of fluid inclusions that vary in size and type, concerning their filling. More than 90% of the inclusion contingent belongs to the group of two-phase (L+V) inclusions that often accumulate along healed fractures or in proximity to the crystal rims. The inner parts of the crystals are basically less populated with fluid inclusions, but also host a notable amount of inclusions. Fifty-five two-phase inclusions from different quartz crystals have been measured by microthermometry. The salinity has been calculated from the observed ice melting temperatures $T_m(\text{Ice})$ and the majority of the inclusions plot into the field between 9 – 11 mass% NaCl_{eq} . (Figure 21). Only a few exceptions were determined with salinities below 5 mass% NaCl_{eq} . which also applies for a small number of salinities above 13 mass% NaCl_{eq} . The highest observed salinity of a two-phase inclusion is 23.5 mass% NaCl_{eq} . and the lowest one 0.5 mass%.

The focus of this study lies on the high saline inclusions that are suspected to carry significant amounts of metals. Since the L+V+S inclusions (Figure 20f) are rare in this sample, the number of analyzed inclusions was limited to 28 individual inclusions, belonging to two different magmatic quartz crystals (sample SHX1 & SHX2). Further complications during the microthermometric investigations arose when ~ 50% of the inclusions decrepitated by heating. The salinity of the L+V+S inclusions is calculated from the halite melting temperature $T_m(\text{H})$ which makes a homogenization of the inclusions indispensable for precise salinity determinations. The vulnerability of the L+V+S fluid inclusions to decrepitations is the reason why no further homogenization experiments of the L+V inclusions were conducted. For those inclusions that were stable during heating, $T_m(\text{H})$ values of 177 – 450°C could be observed, corresponding to salinities of 29 – 47 mass% NaCl_{eq} . (Figure 21). Liquid-vapor homogenization temperatures $T_h(\text{LVS} \rightarrow \text{LS})$ occurred at temperatures from 100 – 226°C, with homogenization into the liquid phase only. Total homogenization by halite melting with $T_m(\text{H}) > T_h(\text{LVS} \rightarrow \text{LS})$ is the general rule for the L+V+S inclusions. The densities of the trapped fluids lie in a range between 1.04 – 1.39 g/cm³.

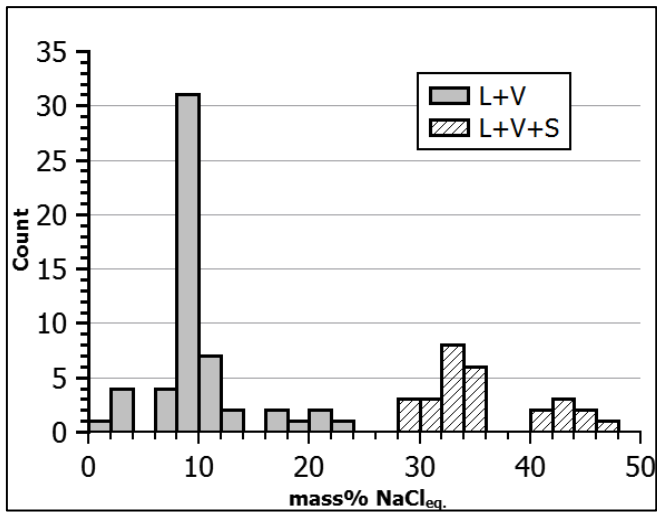


Figure 21: Histogram of the analyzed inclusions in the Schellerhau granite quartz and their salinities.

5.4.1.3 Porth Ledden – tourmaline granite

The investigated fluid inclusions from the Porth Ledden tourmaline granite all belong to the group of L+V+S inclusions (Figure 24). Analogue to the Schellerhau granite samples, we

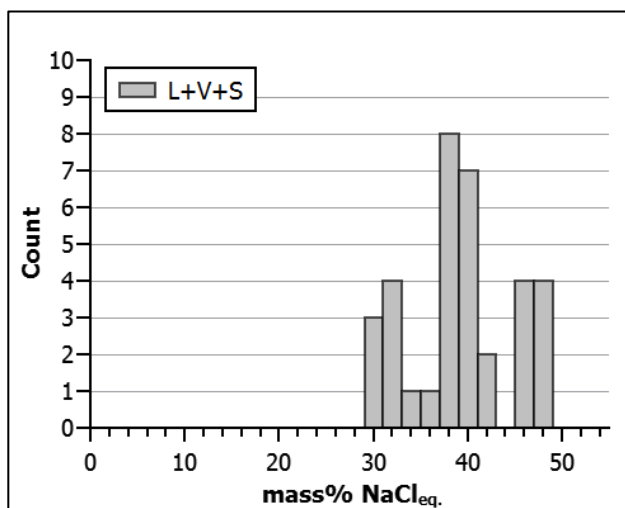


Figure 22: Histogram of the analyzed inclusions in the Porth Ledden granite quartz and their salinities.

focused on the high saline inclusions because it is more likely to find detectable metal concentrations here, rather than in the two-phase inclusions. The quartz grains of the Porth Ledden host a huge number of fluid inclusions that are often located near the crystal rims or along healed fractures. The proportion of L+V+S inclusion is bigger than in the Schellerhau granite and they often appear in spatially related groups. But since the variability of the inclusion content can differ even on

small scaled distances, we decided not to arrange the inclusions in assemblages of chemically identical inclusions. For example, L+V+S inclusions can be adjacent to poly-phase inclusions (L+V+S₁+S₂) with an unknown second solid phase, e.g. accidentally trapped minerals, or the proportions of the liquid, vapor and solid phase may differ too strongly in general. We focused on the investigation of those L+V+S inclusion that were spatially individual without any relation to healed fractures or bigger accumulations of inclusions and thus can be most likely considered to be primary inclusions. Therefore, the selection was limited to a fractional part of the whole fluid inclusion contingent of the quartz grains and 39 individual inclusions were analyzed by microthermometry and fs-LA-ICP-MS. The salinities were determined from the halite melting temperatures $T_m(H)$ and fall in a range between 30 – 48 mass% NaCl_{eq.} (Figure 22). Liquid-vapor homogenization always appeared into the liquid phase with temperatures from 120 – 300°C $T_h(LV \rightarrow L)$. For the total homogenization process $T_h(tot)$ both scenarios, $T_h(tot)$ by halite melting $T_m(H)$ or by liquid-vapor homogenization $T_h(LV \rightarrow L)$ with the halite crystal dissolving at lower temperatures than the vapor bubble, could be observed (Figure 23), but $T_h(tot)$ by halite melting was the more common process. This accounts for two different types of trapped high saline fluids: a) the brine phase of a two-phase fluid which was separated by a boiling process with fluid densities of 1.12 – 1.32 g/cm³ and b) a high saline single-phase fluid with densities of 1.02 – 1.13 g/cm³.

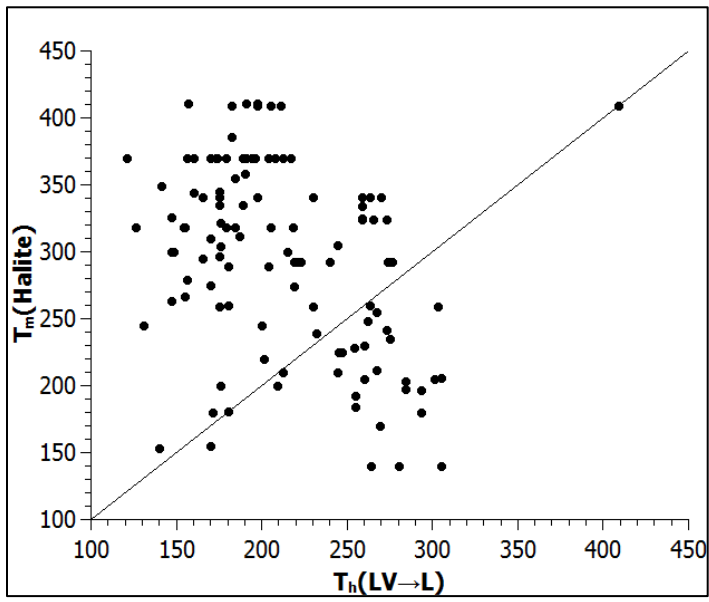


Figure 23: Halite melting temperatures $T_m(\text{Halite})$ versus liquid-vapor homogenization temperatures $T_h(\text{LV} \rightarrow \text{L})$ of the L+V+S inclusions from Porth Ledden granite quartz. All values in °C.

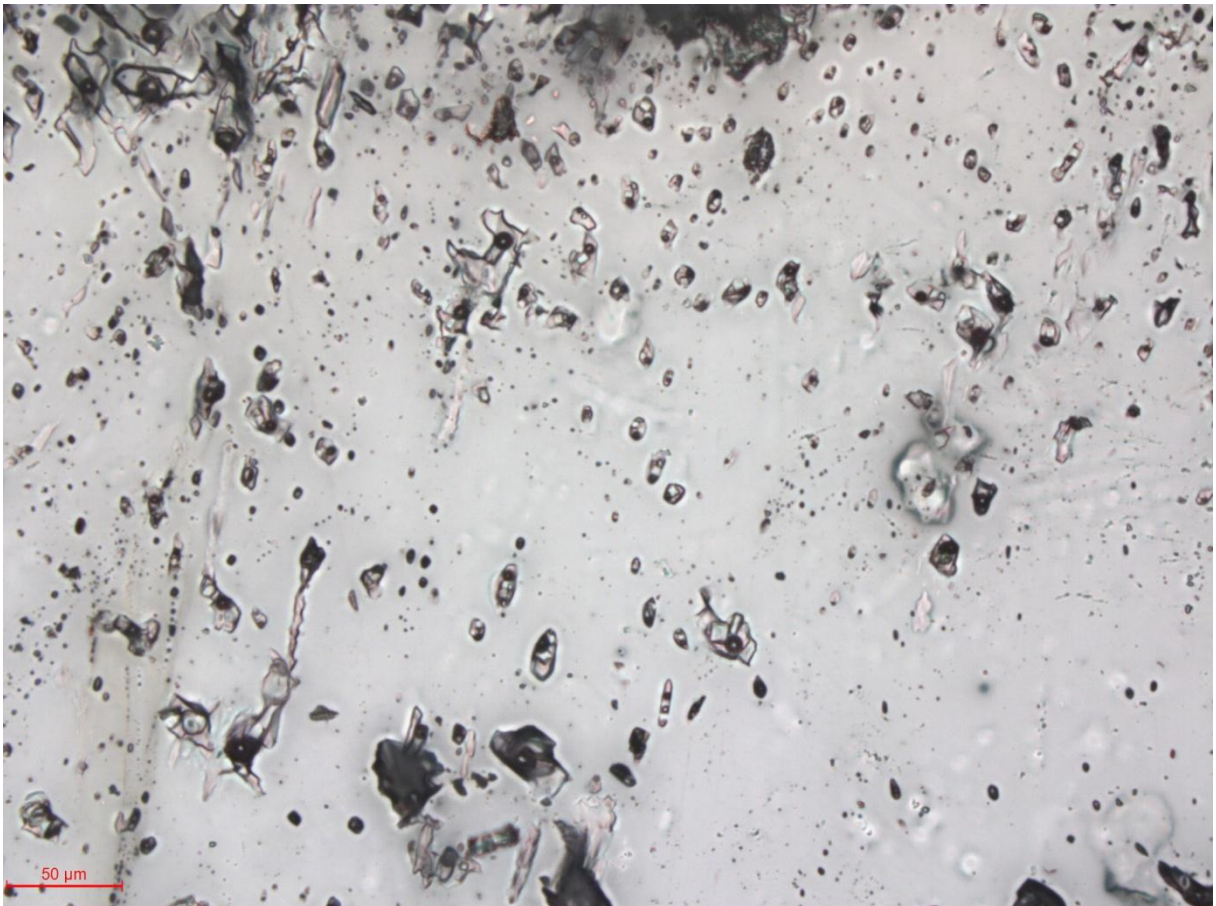


Figure 24: Multiphase fluid inclusions from the Porth Ledden tourmaline granite in quartz.

5.4.1.4 Gottesberg – Grummetstock hydrothermal smoky quartz

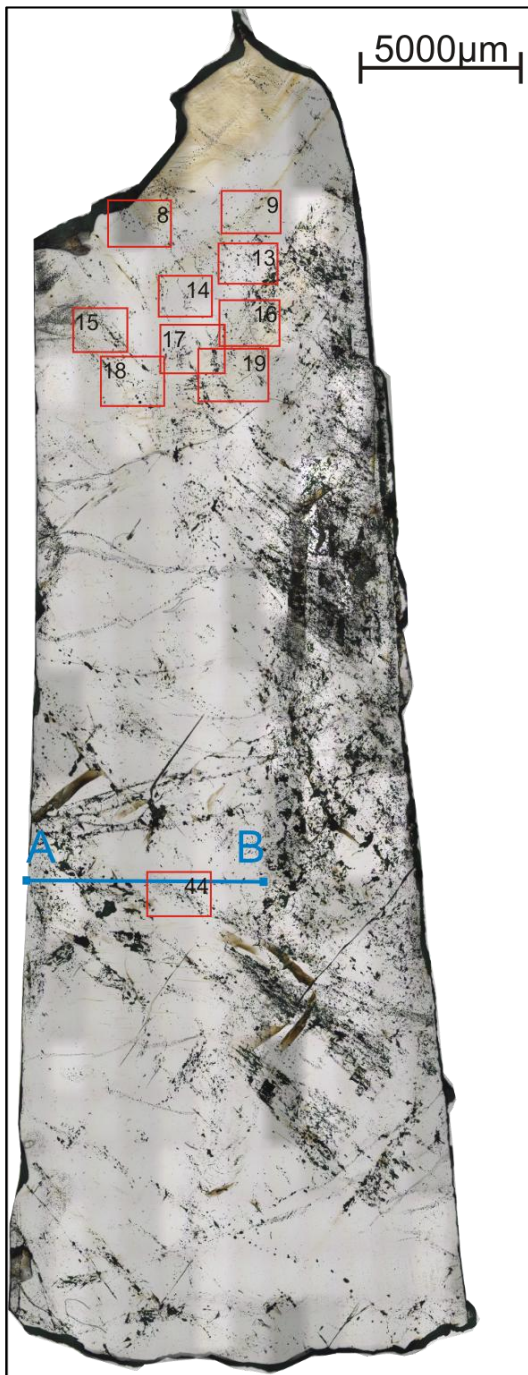


Figure 25: Overview of the sample Grummetstock (Grum) with the areas that include the analyzed FI, marked as red squares.

The former mining site Grummetstock is closely connected with the Sn ore bearing Gottesberg deposit. At Grummetstock, U and Sn-W mineralizations can be found. Typical ore minerals are uraninit, cassiterite and wolframite. The here investigated quartz crystal hosts a large inventory of fluid inclusions, that have been chosen to give a comparable insight to the fluid chemistry of a location that is not related with the ATC, but also shows strong analogies to the greisen and vein style deposits of the eastern Erzgebirge.

For the L+V inclusions from the upper area of the crystal (found in the marked squares in Figure 25), we have conducted the freezing experiments for the determination of fluid salinity by $T_m(\text{Ice})$ only. L+V+S inclusions from the central part of the crystal were heated and homogenized to calculate the salinity from $T_m(\text{H})$. Average salinities of the FIA can be found in Table 11. The fluids are generally high saline between 10 – 43 mass% NaCl_{eq} . FIA 44 is the only brine assemblage with 43 mass% NaCl_{eq} . Total homogenization of those L+V+S inclusions has been observed between 320°C – 370°C, mainly by bubble disappearance into the liquid phase with $T_m(\text{H}) < T_h(\text{LV} \rightarrow \text{L})$. The calculated average

density of the brine is 1.18 g/cm³.

5.4.2 fs-LA-ICP-MS results

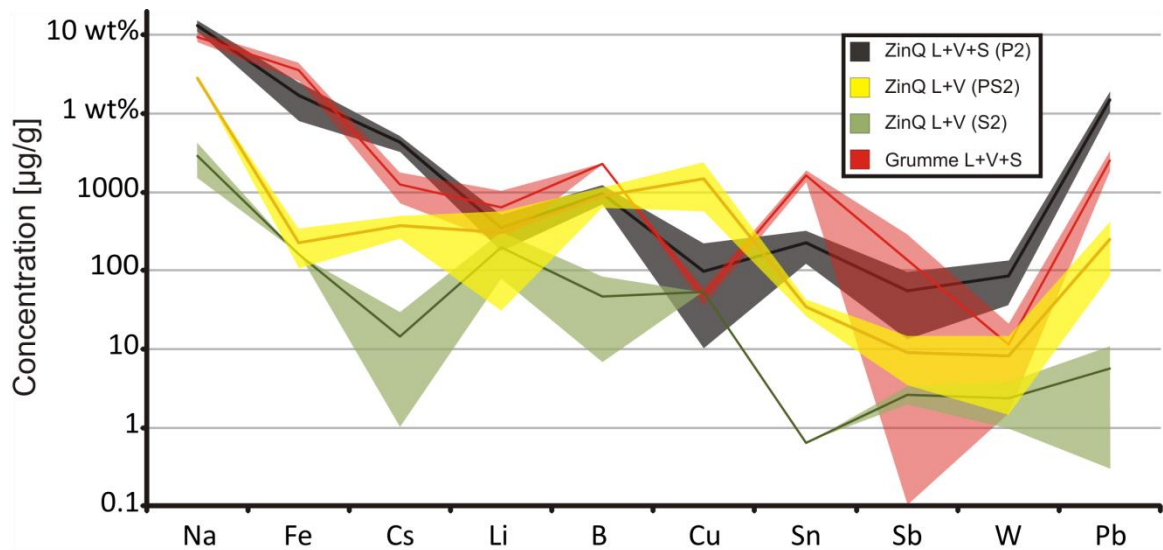


Figure 26: Concentrations of different major to trace elements in fluid inclusion assemblages from sample ZinQ and Grummetstock. Error bands indicate the 1SD values of the measured average concentration values.

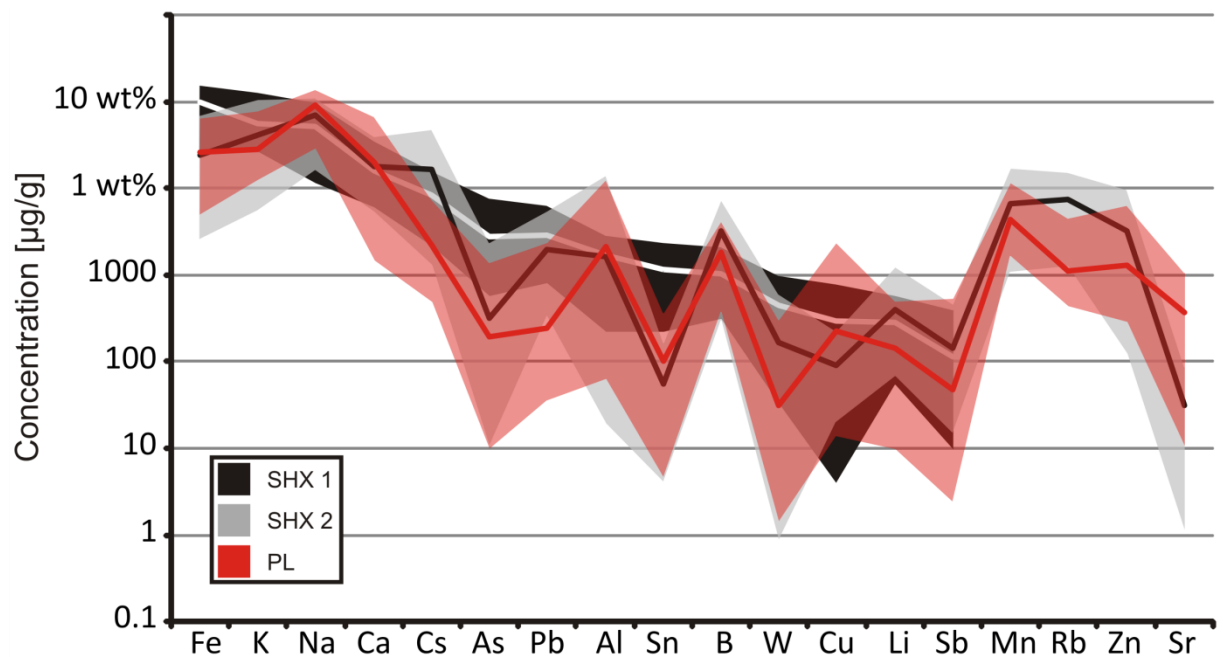


Figure 27: Measured concentration ranges of brine inclusions from two quartz crystals (SHX1 & SHX2) of the Schellerhau granite and 39 individual brine inclusions from five different quartz crystals from the Porth Ledden granite (PL). Error bands indicate the maximum and minimum concentration of each sample; thick lines represent the average values of all individual inclusions.

5.4.2.1 Fluid inclusions: Zinnwald, Schellerhau and Porth Ledden

The laser ablation results of sample ZinQ are presented in Figure 26 and Table 8 as average values of the measured fluid inclusion assemblages. The concentration values of the two-phase FIAs PS2 and S2 have been chosen as representative values for the intermediate dense fluids and FIA P2 for the brine inclusions. Figure 27 shows the measured concentration range of the brine inclusions from the Schellerhau (SHX1 & SHX2) and Porth Ledden (PL). It is obvious that large discrepancies, affecting nearly all elements, can be observed between the brines and the two-phase assemblages. SHX1 brines (Table 9) are high in Fe, Na and K with Fe being the dominant cation ($\bar{\text{O}}$: 9.97 wt%) followed by equal concentrations of Na ($\bar{\text{O}}$: 5.01 wt%) and K ($\bar{\text{O}}$: 4.74 wt%). In contrast, the brines of SHX2 (Table 9, Na: 7.67 wt%, K: 4.28 wt%, Fe: 2.66 wt%) and PL-granites are dominated by Na (9.10 wt%) with a significant lower content of Fe (2.66 wt%) and K (2.76 wt%). The brine assemblages from sample ZinQ (P1 and P2) are also dominated by Na and K with much lesser influence of Fe. P2 brines contain 13.21 wt% Na and 1.67 wt% Fe, whereas P1 brines have concentrations of 6.95 wt% Na, 3.45 wt% K and only 0.81 wt% Fe. Another feature of the brine FIAs from sample ZinQ are the comparatively high Pb concentrations of 1.48 wt% (P2) and 1.06 wt% (P1). The intermediate dense fluids from assemblage PS2 are also dominated by Na (2.79 wt%) with only small effects of K (0.42 wt%) and nearly none of Fe (225 $\mu\text{g/g}$). A low saline and highly diluted fluid is hosted in the inclusions of assemblage S2 with only 0.29 wt% Na, 0.50 wt% K and 164 $\mu\text{g/g}$ Fe.

Cesium shows extraordinary high values in the SHX2 brines ($\bar{\text{O}}$: 2.04 wt%), where it can be considered to be one of the major cations (Table 9). SHX1 ($\bar{\text{O}}$: 0.71 wt%), the ZinQ brines (P2: 0.42 wt%, P1: 0.28 wt%) and PL brines (0.22 wt%) have a distinctly lower Cs content. PS2 and S2 are stronger depleted in Cs (PS2: 373 $\mu\text{g/g}$, S2: 14 $\mu\text{g/g}$) than all other FIAs (Table 8).

A relatively small spread in a concentration range between 1295 $\mu\text{g/g}$ (F02b in Table 8) and 196 $\mu\text{g/g}$ (S2) exists for the lithium concentration of the investigated FIA. The lowest Li value is represented by the PL brines with an average of 139 $\mu\text{g/g}$. In contrast, B values of the PL brines are second highest of all FIA ($\bar{\text{O}}$: 1721 $\mu\text{g/g}$), only surpassed by SHX2 brines ($\bar{\text{O}}$: 3610 $\mu\text{g/g}$) (Table 9). P2, PS2 and SHX1 contain equal B concentrations of about 900 to 960 $\mu\text{g/g}$. P1 and S2 are very low in B with 124 $\mu\text{g/g}$ and 47 $\mu\text{g/g}$, respectively (Table 8).

Concerning the metal concentrations, the investigated fluid types show a strong variability (Figure 26 & Figure 27). Tin concentrations are highest in the brine solutions of the Schellerhau granite (SHX1 max: 2369 µg/g) and lowest in the S2 assemblage in sample ZinQ (< 0.6 µg/g), where Sn does not exceed the lower limit of detection. Compared to the Schellerhau brines (SHX2), Sn values of ZinQ and PL brines are by one order of magnitude lower (P2: 225 µg/g, PL Ø: 102 µg/g, PL max: 373 µg/g). A small amount of Sn (34 µg/g) could be unambiguously detected in the intermediate dense fluids of the PS2 assemblage. Tungsten behaves analogue to the Sn concentrations, with highest values in the Schellerhau brines (SHX2 max: 5319 µg/g) and lowest in the secondary ZinQ FIA S1 (2.3 µg/g). The pseudosecondary two-phase fluids hold up to 8.3 µg/g W. The enrichment of W in the Schellerhau brines is, again like Sn, by one order of magnitude higher than in the Porth Ledden brines (PL max: 307 µg/g).

In the low salinity fluids from sample ZinQ, Sn and W were frequently absent and could not be detected as distinct signal peaks above the detection limit. For example, only 5 of 19 analyzed inclusions from FIA S1 gave significant Sn signals during analysis. For W it was only one single inclusion (of 19) in the case of FIA S1. All signals from inclusions with concentration values close to the calculated detection limit have been carefully examined for possible background related spikes that do not correlate with the other fluid related signal peaks (e.g. Na, Cs, Pb and others) but fall into the sample integration interval and therefore contribute to or being responsible for the generation of a falsely calculated concentration value. Especially W, which can have uninterrupted background count rates of 0 cps for seconds, is prone to those background generated artificial concentration values, if no W is present in the fluid. Only fluid inclusion signals which show a distinct peak that can be separated from the background signal were used for further data evaluation.

The analyses of the individual brine inclusions from the magmatic quartz samples did not result in a continuous detection of Sn and W in each inclusion. 33 of 39 inclusions from PL contain Sn above the LOD and only 18 of 39 inclusions contain detectable W concentrations (Table 9). The rare detection of W in only 8 of 29 inclusions from sample SHX2 makes the results with extremely high concentrations appear in a different light. The distinctive measurements also show high Mo (3314 and 1025 µg/g) and extreme Al values (8.7 wt% and 11.6 wt%). Molybdenum was only found in the four SHX2 inclusions with high W and Sn and seems to be generally uncommon in the SHX and PL brines (Table 9). Aluminum can reach the 10³ µg/g level in the investigated fluids easily, but values of about 10 wt% clearly

suggest the ablation of an accidentally trapped daughter crystal (e.g. mica) that distorted the concentration results of those inclusions.

Due to its high concentrations, Pb can be accounted to be one of the major cations in the ZinQ brines. The Schellerhau brines have significantly lower Pb contents (\emptyset : 2453 $\mu\text{g/g}$), followed by the pseudosecondary FIA in ZinQ (251 $\mu\text{g/g}$), the Porth Ledden brines (\emptyset : 236 $\mu\text{g/g}$) and finally by the secondary fluids of ZinQ (5.7 $\mu\text{g/g}$).

Quite the contrary to the other metals, Cu is not enriched in the brine inclusions compared to the two-phase fluids. The highest concentrations of all FIA have been calculated for the two-phase fluids of pseudosecondary (PS2: 1479 $\mu\text{g/g}$) and primary origin (P3: 824 $\mu\text{g/g}$) (Table 8). Even the high saline SHX1 (\emptyset : 297 $\mu\text{g/g}$) and PL (\emptyset : 240 $\mu\text{g/g}$) brines cannot reach these Cu values, not to mention the ZinQ brines (98 $\mu\text{g/g}$) and the secondary fluids S2 (54 $\mu\text{g/g}$).

5.4.2.2 Fluid inclusions: Gottesberg - Grummetstock

The additionally measured sample from the Gottesberg - Grummetstock Sn mining area shows elevated Sn concentrations for the brine FIA (44) with 1616 $\mu\text{g/g}$ Sn (Figure 26; Table 11). The other analyzed FIA host less than 30 $\mu\text{g/g}$ Sn. Tungsten does not correlate with the high Sn values in the brine FIA (11 $\mu\text{g/g}$) and is relatively low concentrated (0.2 – 7.2 $\mu\text{g/g}$) in the L+V inclusions. The major cations in the L+V+S inclusions are Na (9.5 wt%), K (3.9 wt%), Fe (3.5 wt%) and Mn (2.7 wt%). Zinc is the only metal that has very high contents of 0.78 wt%, followed by Pb (2550 $\mu\text{g/g}$) and B (4955 $\mu\text{g/g}$). Rubidium (1272 $\mu\text{g/g}$), Cs (1255 $\mu\text{g/g}$), Ca (1663 $\mu\text{g/g}$), Li (631 $\mu\text{g/g}$) and Al (524 $\mu\text{g/g}$) reach quiet high concentrations and Cu (48 $\mu\text{g/g}$), Sr (64 $\mu\text{g/g}$), Sb (136 $\mu\text{g/g}$) and Mo (9.9 $\mu\text{g/g}$) could be also detected, but with insignificant amounts.

The composition of the different L+V assemblages from sample Grummetstock is dominated by Na (3.3 – 7.1 wt%), K (0.2 – 2.3 wt%) and Fe (0.6 – 2.4 wt%) with Na always being the most abundant cation followed by either K or Fe that are often close to a 1:1 ratio. Aluminum is the only further element with concentrations in the wt% range (0.3 – 3.5 wt%), which seems to be a bit suspicious since Al values in the wt% range can indicate the ablation of accidentally trapped mineral fragments. None of those foreign particles was observed during

the microscopic observation of the inclusions, but this does not save the analysis from hidden particles and distorted values. 29 of 60 inclusions show Al above the LOD and 10 inclusions show Al above 1 wt%. The overall range of Al concentrations is therefore extremely high. The RSD as a quality feature for the accuracy of the analysis might reveal some unrealistic values, e.g. the RSD of 123% (FIA 9) or 136% (FIA 19). But on the other hand, the 3.5 wt% Al in FIA 16, as the highest value of all, was measured with a very low uncertainty of 29% RSD. The trace element values of the remaining elements are nearly always lower than in the L+V+S inclusions. Lead (0.9 wt%), Zn (0.4 wt%), Li, (0.3 wt%), B (0.4 wt%) and Cs (0.1 wt%) show maximum contents that can be close to or even slightly higher than the contents of the brine inclusions. Antimony concentrations of 0.1 wt% in FIA 19 are significantly higher than in the brines, but the RSD of 132% demonstrates that Sb is negatively affected by foreign matter ablation like observed for Al. Normal Sb values in the L+V assemblages are 90 - 480 µg/g. The maximum values for Rb (600 µg/g), Sr (29 µg/g), Mo (3.2 µg/g) and W (7.2 µg/g) are also relatively close to the brine inclusion values, but the only strongly pronounced difference in trace element contents is observed for Sn (28 µg/g in L+V, 1616 µg/g in L+V+S).

5.4.2.3 Analytical uncertainty

As described in the section above, the relative standard deviation (RSD) of the individual inclusions from one FIA is a quality feature concerning the accuracy of the analysis. The analyses of chemically identical fluid inclusions can be typically conducted with RSDs of 10 – 30%. Sources of error that can increase the RSD value are the incomplete mobilization of the whole fluid inclusion content, e.g. by imprecise positioning of the laser spot or by spot sizes that are only slightly bigger than the inclusion. The latter is especially relevant for analyses that were conducted before the development of the Linux CNC spiral technique, which mainly affects the analyses of sample ZinQ. Another negative impact on the analytical quality can be provided by a wrong interpretation of petrographic and microthermometric observations and the resulting mistakenly summary of inclusions as a homogeneous FIA. The accidental entrapment of mineral fractures (e.g. micas or accessories) can be unnoticed during the microscopic observation of the inclusions, since those fragments are too small or hidden by the bubble. Inclusions from sample ZinQ frequently appeared to be very dark under the microscope which further complicates the identification of possible mineral fragments (Figure

20). Table 8 and Table 11 include the 1SD and RSD in % of the average values of all measured FIAs. Suspicious values can occur for nearly all elements, but accumulations of high RSD can be observed for very few FIA, like FIA PS1 in Table 8. The RSD values of sample Grummetstock (Table 11) are with a few exceptions very low in a wide range and better than the analyses of sample ZinQ, even though the number of the analyzed inclusions per FIA was often very low. Inclusions in sample Grummetstock were often bigger than 30 μm and thus opened with a spiral pattern.

The analyses of individual brine inclusions from the magmatic quartz crystals of the Schellerhau and Porth Ledden granite are not summarized in FIA, thus Table 9 does not provide information about the analytical quality. The standard error of the individual analyses for each element can be found in the electronic supplementary data.

Table 8: Results from LA-ICP-MS analyses of the fluid inclusion assemblages (FIA) from sample ZinQ. Elemental concentrations are given in $\mu\text{g/g}$, salinity in mass% NaCl_{eq} , density in g/cm^3 and $T_{\text{h}}(\text{total})$ in $^{\circ}\text{C}$.

FIA	n		salinity	density	$T_{\text{h}}(\text{total})$	Li	B	Na	Al	K	Ca	Mn	Fe
P1	6	average	28	0.97	367	171	124	69586	2944	34542	2469	15360	8112
LVS		1SD				66	14	2195	1661	4181	-	2412	1611
		RSD%				38	12	3	56	12	-	16	20
P2	10	average	31	1.03	290	350	965	132139	6845	-	4711	22564	16764
LVS		1SD				179	291	23866	8403	-	-	6705	8860
		RSD%				51	30	18	123	-	-	30	53
P3	7	average	8.5	0.63	400	247	518	21041	4393	-	1716	231	622
LV		1SD				67	192	5581	2207	-	-	141	189
		RSD%				27	37	27	50	-	-	61	30
PS1	9	average	5.6	0.59	396	434	845	16866	1401	752	2218	182	567
LV		1SD				202	440	2428	765	349	1460	282	355
		RSD%				47	52	14	55	46	66	155	63
PS1	3	average	5.6	0.59	396	401	899	16899	1414	705	3617	185	479
LV		1SD				195	444	3611	980	310	3669	241	339
		RSD%				49	49	21	69	44	101	130	71
PS2	15	average	7.8	0.65	385	307	679	17705	3488	3583	4508	170	406
LV		1SD				105	299	5296	1752	1725	3286	79	179
		RSD%				34	44	30	50	48	73	47	44
PS2	10	average	7.8	0.65	385	308	901	27919	6664	4225	-	218	225
LV		1SD				277	281	567	4520	862	-	74	121
		RSD%				90	31	2	68	20	-	34	54
PS3	11	average	4.2	0.63	380	1181	170	14714	1321	-	4267	438	814
LV		1SD				380	70	1948	994	-	-	92	-
		RSD%				32	41	13	75	-	-	21	-
PS4	18	average	5.6	0.59	377	879	194	12802	984	-	-	308	-
LV		1SD				412	57	6654	762	-	-	168	-
		RSD%				47	29	52	77	-	-	55	-
S1	19	average	5.7	0.61	386	638	649	17945	1159	-	6236	538	-
LV		1SD				309	348	3913	860	-	2688	265	-
		RSD%				48	54	22	74	-	43	49	-
S2	6	average	0.88	0.52	388	196	47	2904	247	-	1419	117	164
LV		1SD				119	40	1420	150	-	639	194	-
		RSD%				61	86	49	61	-	45	166	-
F02a	6	average	7.8	-	-	1089	156	24228	1659	1216	3083	55	185
LV		1SD				762	38	4619	996	1190	3481	17	71
		RSD%				70	24	19	60	98	112	31	38
F02b	6	average	2.6	-	-	1295	166	7474	1097	1089	-	68	457
LV		1SD				275	160	4077	636	730	-	41	-
		RSD%				21	97	55	58	67	-	60	-

Table 8: Results from LA-ICP-MS analyses of the fluid inclusion assemblages (FIA) from sample ZinQ. Elemental concentrations are given in $\mu\text{g/g}$, salinity in mass% NaCl_{eq} , density in g/cm^3 and $T_{\text{h}}(\text{total})$ in $^{\circ}\text{C}$.

FIA		Zn	Cu	As	Rb	Sr	Sn	n	Sb	Cs	Ta	W	n	Au	Pb
P1	average	32466	-	349	3874	1.2	62	6	16	2831	-	60	6	2.6	10603
LVS	1SD	7271	-	87	332	0	23		1	306	-	22		1.2	2884
	RSD%	22	-	25	9	27	37		8	11	-	36		45	27
P2	average	-	98	825	8765	2.5	224	10	55	4253	-	85	10	-	14849
LVS	1SD	-	127	438	1861		105		42	1029	-	50		-	4873
	RSD%	-	130	53	21		47		76	24	-	58		-	33
P3	average	-	824	254	795	1.7	140	4	12	302	-	33	6	-	133
LV	1SD	-	714	187	273	1	30		1	127	-	19		-	87
	RSD%	-	87	73	34	37	21		4	42	-	59		-	65
PS1	average	-	925	485	-	-	44	9	13	105	0.5	12	5	5.0	234
LV	1SD	-	657	456	-	-	39		15	41	0.05	15		3.6	245
	RSD%	-	71	94	-	-	88		112	39	10	124		71	104
PS1	average	-	912	426	-	-	43	2	12	111	0.5	10	2	5.0	225
LV	1SD	-	618	411	-	-	38		14	42	0.05	14		3.6	222
	RSD%	-	68	97	-	-	88		111	38	10	141		71	99
PS2	average	-	1239	443	-	-	63	14	14	237	0.4	11	14	2.5	202
LV	1SD	-	943	314	-	-	61		28	88	0.1	6.3		1.4	179
	RSD%	-	76	71	-	-	96		196	37	14	59		58	89
PS2	average	-	1479	522	-	-	34	7	9	373	0.4	8.3	9	8.2	251
LV	1SD	-	927	316	-	-	9		6	123	0.2	6.8		-	170
	RSD%	-	63	60	-	-	26		63	33	55	83		-	68
PS3	average	-	-	244	95	-	16.3	3	22	83	-	2.9	3	-	464
LV	1SD	-	-	201	59	-	3.1		1.6	78	-	0.6		-	314
	RSD%	-	-	83	62	-	19		7	93	-	21		-	68
PS4	average	-	32	310	71	-	-	-	22	38	-	2.6	4	-	271
LV	1SD	-	6	409	65	-	-	-	10	43	-	1.6		-	279
	RSD%	-	19	132	92	-	-	-	48	111	-	64		-	103
S1	average	-	618	379	65	-	33.4	5	36	37	-	2.3	1	-	151
LV	1SD	-	674	273	39	-	8		13	24	-	-		-	146
	RSD%	-	109	72	59	-	24		36	64	-	-		-	97
S2	average	-	54	60	31	-	0.6	1	2.7	14	-	2.4	5	-	5.7
LV	1SD	-	-	42	44	-	-	-	0.7	16	-	1.5		-	5.4
	RSD%	-	-	70	142	-	-	-	28	115	-	60		-	95
F02a	average	-	615	74	-	-	42	5	3.6	47	0.2	7.8	6	-	41
LV	1SD	-	202	15	-	-	8		0.9	23	-	1.9		-	6.1
	RSD%	-	32	20	-	-	19		24	50	-	24		-	16
F02b	average	-	7	48	-	-	-	0	4.1	28	-	3.7	5	-	0.9
LV	1SD	-	3	11	-	-	-	-	0.5	11	-	1.7		-	0.4
	RSD%	-	42	23	-	-	-	-	11	40	-	48		-	38

Table 9: Results from LA-ICP-MS analyses of individual fluid inclusions from the Schellerhau granite quartz and Porth Ledden granite quartz. Elemental concentrations are given in $\mu\text{g/g}$, $T_h(\text{LV}>\text{L})$ in $^\circ\text{C}$ and salinity in mass% NaCleq.

Sample	FI #	$T_h(\text{LV}>\text{L})$	salinity	Li	B	Na	Al	K	Ca	Ti	Mn	Fe	
PL_B_1	2	255	31.1	192	2218	90717	1374	19113	11160	64	3196	5968	
	3	292	30.9	158	2358	92392	5110	19910	6707	-	2537	9331	
	4	292	31.7	125	1628	84457	2944	16024	-	240	2278	19424	
	6	244	32.4	175	1593	75844	1710	22304	17275	53	3053	19494	
	10	223	38.4	229	1259	104113	1088	20270	4339	-	11952	24546	
	11	240	38.3	306	4192	95292	1643	41976	-	460	7249	29870	
	12	267	35.0	102	2370	98994	2498	21369	-	-	9116	22424	
	14	275	37.8	198	3744	102584	2378	18847	5110	271	4802	30700	
	15	276	37.8	177	3029	102665	1645	26888	1458	113	4197	30563	
PL_B_2	6	155	39.9	59	1727	102068	581	22465	21665	55	2780	17429	
	8	170	37.3	196	3201	52191	2521	52279	36458	154	4593	21792	
	9	178	40.3	46	1566	99078	640	31221	21254	-	2463	17614	
PL_B_15	12	208	31.9	166	1599	70695	6652	22722	-	-	7405	41577	
	1	126	39.1	-	512	101587	-	21321	7359	117	3990	33713	
	2	130	35.2	93	1463	87259	7468	19118	6650	151	3388	35607	
PL_C_7	5	170	29.9	48	2336	79669	709	23193	12043	-	1994	10539	
	7	165	38.6	22	1687	46151	-	20661	65155	-	2728	19830	
	10	184	40.3	-	1376	106400	3497	23863	17996	51	4063	17224	
	14	205	40.5	91	2073	94315	948	38127	24672	103	2922	14241	
	15	218	40.5	104	1534	106906	1721	24214	28513	92	1654	4965	
PL_C_14	1	175	40.5	156	372	94409	389	19407	-	355	2158	62796	
	5	140	41.3	175	1701	100355	-	25536	26518	-	4004	16285	
	6	147	38.6	150	1633	91446	-	19728	19199	301	3000	29431	
	11	204	38.3	417	2150	34612	12851	28607	43484	1667	2108	57565	
PL_C_14	1	182	45.1	502	4245	28216	-	18959	67608	-	8853	64532	
	2	182	46.7	117	1635	118059	317	35769	18223	-	3477	25419	
	3	197	47.2	53	1191	138450	162	27426	14264	70	2249	15765	
	4	199	44.9	9.5	560	120913	2984	20486	7238	72	2374	17137	
	5	184	43.0	182	1361	64843	62	36345	21469	-	8010	62502	
	6	182	46.7	134	1432	108218	4270	26774	18539	116	6461	40324	
	7	205	44.9	122	605	103315	241	12072	19119	-	3897	26419	
	9	188	44.9	91	1223	100547	-	30610	9560	-	4294	29458	
	11	89	44.9	260	3249	30885	-	77799	43337	446	11453	26027	
	13	182	46.7	63	1191	120539	218	38536	14090	98	5231	24407	
	14	205	47.5	69	780	110956	211	32224	19081	41	2341	40026	
PL_C_14	16	137	44.9	77	1061	75767	373	41946	27774	-	3063	27333	
	17	269	30.5	77	1880	79629	287	26286	13767	152	2593	8283	
	20	197	47.2	96	877	135766	110	52240	1934	482	2883	17840	
	21	409	48.4	101	982	100984	417	13397	21909	-	3096	25231	
		MIN		29.9	9.5	372	28216	62	12072	1458	41	1654	4965
		MAX		48.4	502	4245	138450	12851	77799	67608	1667	11952	64532
	SHX1	1e	142	53.3	269	2112	11452	1731	50130	36119	-	-	154455
1a		173	42.9	255	1283	34867	221	35699	-	-	-	137003	
3g		138	49.7	594	-	98067	-	130451	-	-	-	25106	
3d		114	12.9	914	490	46713	-	2986	-	-	-	-	
3f		129	40.0	53	310	69838	2063	38358	6011	-	-	70534	
3a		226	39.8	267	493	42331	2888	26758	5956	-	-	111162	
	MIN		12.9	53	310	11452	221	2986	5956	-	-	25106	
	MAX		53.3	914	2112	98067	2888	130451	36119	-	-	154455	
SHX2	2		30.6	331	3162	77817	1059	25630	5414	-	5827	27231	
	3	130	35.4	-	3892	92754	-	37285	-	-	7055	22785	
	14		27.7	-	3701	45957	97	50091	-	-	8912	31515	
	16		27.0	-	1689	75967	-	11899	-	-	5610	22493	
	17	142	32.0	1110	2839	44669	2363	57893	39701	-	12037	44972	

Sample	FI #	Th(LV>L)	NaCleg.	Li	B	Na	Al	K	Ca	Ti	Mn	Fe
SHX2_b	18	122	31.5	-	2424	85210	-	32874	-	-	4929	18290
	28		25.0	-	6287	77134	403	29539	-	-	1882	2568
	29		28.3	-	299	54437	-	51286	-	-	7542	24715
	35		29.4	-	998	37585	19	108390	-	-	3589	13916
	36		30.5	-	303	111914	-	6159	-	-	1090	4249
	38	116	32.2	1242	1826	91299	1748	24144	27531	-	4940	20463
	39	123	32.1	-	718	15937	2039	97250	-	-	12980	51521
	40		30.1	142	7075	87711	-	20594	-	-	7725	28587
	41		30.1	-	1873	111852	174	5456	-	-	4686	13165
	42		30.1	-	6560	90249	2253	28603	-	-	7213	20306
	43		30.1	195	5720	73814	-	47685	9305	-	6812	27047
	1	100	34.9	-	9934	115037	87158	2543	-	-	6710	18159
	4		30.6	-	2130	85248	682	21076	-	-	6059	21220
	5	135	32.6	134	1990	99627	1441	38167	-	-	1329	6249
	7		26.4	67	2080	55814	243	47327	-	-	6232	18077
	10	135	24.0	-	3170	97169	1462	35282	-	-	2967	11016
	11		29.6	157	4797	61699	355	57079	-	-	6449	21088
	12	128	32.7	270	4366	88108	348	50184	6245	-	3054	10096
	13		24.0	-	4705	42872	344	14576	-	-	12513	39237
	22		31.5	-	7573	17459	-	59578	-	-	17292	69328
	23		15.6	636	4675	49967	116468	14726	6654	-	512	2669
	32		3.2	-	2008	12014	-	1138	-	-	-	-
	44		29.6	-	1659	39660	160	71813	-	-	9044	34697
	45		29.6	-	1253	79864	14367	27640	-	-	5434	21080
		MIN		3.2	67	299	12014	19	1138	5414	-	512
	MAX		35.4	1242	9934	115037	116468	108390	39701	-	17292	69328

Table 10: Continuation of Table 9, results from LA-ICP-MS analyses of individual fluid inclusions from the Schellerhau granite quartz (SHX) and Porth Ledden granite quartz (PL). Elemental concentrations are given in $\mu\text{g/g}$, $T_h(LV>L)$ in $^{\circ}\text{C}$ and salinity in mass% NaCleq.

Sample	FI #	Zn	Cu	As	Rb	Sr	Mo	Sn	Sb	Cs	Ta	W	Pb
PL_B_1	2	1046	21	54	439	157	-	-	15	1319	-	-	175
	3	880	-	11	666	119	-	4.5	13	1319	-	-	146
	4	456	-	589	729	144	-	373	15	1203	-	73	136
	6	588	-	54	895	405	-	11	9.4	1553	-	-	52
	10	2956	-	18	1290	31	-	-	2.3	4294	-	-	360
	11	1839	59	-	1880	527	-	-	16	3372	-	-	408
	12	2442	-	21	1121	94	-	-	7.0	4909	-	-	235
	14	967	-	14	1021	326	-	16	24	2394	-	-	124
	15	777	28	112	1287	253	-	32	20	2039	-	-	223
PL_B_2	6	526	20	203	799	464	-	15	18	1374	-	1.4	99
	8	888	-	545	1615	832	-	13	34	2948	-	-	149
	9	620	57	184	900	449	-	13	29	1573	-	-	93
	12	2081	-	25	1124	10	-	4.7	24	1918	-	-	208
PL_B_15	1	864	14	114	924	198	-	193	13	1566	-	17	2366
	2	892	34	155	872	247	-	51	29	1928	-	5.7	303
	5	419	-	23	604	265	-	8.8	29	480	-	2.3	138
	7	849	2419	1393	835	645	-	32	540	1689	-	307	102
	10	520	-	218	692	362	-	99	55	1235	-	12	104
	14	744	-	41	1026	515	-	70	22	1906	-	3.0	129
PL_C_7	15	289	13	63	432	430	-	-	15	1376	-	-	71
	1	984	-	799	1220	11	-	183	82	5209	-	-	147
	5	863	-	-	1109	557	-	47	-	2540	-	-	116
	6	852	-	62	1016	421	-	120	18	2596	-	-	111
PL_C_14	11	1575	1124	255	1381	192	-	-	165	1962	-	-	237
	1	4538	-	446	2717	1072	-	215	114	5645	-	-	219
	2	1188	32	222	1067	363	-	133	34	1818	-	-	154
	3	677	17	86	756	290	-	76	12	1094	-	16	78
	4	852	-	42	617	179	-	93	10	739	-	1.9	124
	5	2791	17	93	1424	525	-	302	42	1910	-	39	357
	6	2081	-	39	1352	372	-	214	29	2010	-	14	210
	7	738	29	129	506	353	-	65	19	1690	-	-	142
	9	1613	24	60	1297	254	-	101	8.5	2013	-	14	204
	11	6309	56	41	4584	997	-	213	-	7573	-	-	568
	13	1772	-	176	1534	364	-	177	9.1	1916	-	11	232
	14	397	-	247	817	348	-	46	101	1668	-	3.9	104
	16	657	34	377	986	560	-	77	31	1593	-	20	108
17	748	-	-	537	353	-	22	11	1285	-	-	239	
20	1404	148	191	1269	181	-	324	37	1432	-	12	384	
21	468	-	199	769	446	-	41	108	2026	-	1.9	36	
	MIN	289	13	10.9	432	10	-	4.5	2.3	480	-	1.4	36
	MAX	6309	2419	1393	4584	1072	-	373	540	7573	-	307	2366
SHX1	1e	-	801	7762	-	-	-	2250	406	16059	-	1006	3537
	1a	-	3.8	-	-	-	-	686	9.5	3392	-	47	1398
	3g	-	-	1633	-	-	-	2369	-	14579	3.2	931	6436
	3d	-	-	-	-	-	-	-	-	1060	-	-	45
	3f	-	164	558	-	-	-	215	18	2104	-	32	2521
	3a	-	217	1270	-	-	-	355	29	5216	1.2	201	784
	MIN	-	3.8	558	-	-	-	215	9.5	1060	1.2	32	45
	MAX	-	801	7762	-	-	-	2369	406	16059	3.2	1006	6436
SHX2	2	2361	-	192	2948	17	-	-	150	10751	-	-	1146
	3	2838	88	110	8141	45	-	-	210	17001	-	-	1889
	14	5007	129	164	10547	65	3.6	-	182	23655	-	-	2643
	16	1007	-	61	2927	26	-	-	193	8857	-	-	1184
	17	4110	152	75	15328	89	-	166	234	18811	-	-	3258

Sample	FI #	Zn	Cu	As	Rb	Sr	Mo	Sn	Sb	Cs	Ta	W	Pb
SHX2_b	18	1667	89	111	5389	19	-	6.7	96	9511	-	-	2281
	28	919	-	349	6498	14	-	-	118	14706	-	-	789
	29	3424	-	177	9122	20	-	-	48	17745	-	-	2071
	35	-	227	129	6675	26	-	-	211	2413	-	-	4165
	36	200	20	194	1276	8.4	-	-	51	1570	-	0.9	449
	38	6037	63	-	8105	29	-	40	25	22957	-	-	1691
	39	3884	102	668	15128	48	3.7	44	475	48479	-	-	3289
	40	2469	-	299	3964	2.3	-	-	223	11538	-	-	1106
	41	123	-	-	2302	41	-	-	-	1311	-	-	335
	42	9750	-	659	11439	47	-	-	316	33376	-	16	5572
	43	2912	65	-	6927	37	-	10	22	11394	-	-	1777
	1	873	-	133	167	22	1025	939	49	5485	-	1161	612
	4	2279	53	40	5308	42	-	-	97	10329	-	-	1263
	5	2295	88	285	8120	11	-	-	104	22543	-	-	1433
	7	2071	82	305	9912	18	-	-	71	24938	-	-	1491
	10	2209	35	2379	7057	8.4	96	76	164	15825	-	175	1311
	11	2640	83	215	12216	80	-	-	60	28157	-	-	1896
	12	2065	82	168	6701	8.2	-	-	73	21834	-	-	1098
	13	9226	-	10	2764	1.1	-	4.1	15	5763	-	40	1371
	22	-	-	83	8511	32	184	-	94	10584	-	606	4402
	23	186	-	60	1787	18	3314	354	7.0	7306	-	5319	190
	32	-	-	-	367	-	-	-	-	1120	-	1.3	5.1
	44	4357	93	331	11798	55	-	-	121	22150	-	-	2630
	45	3418	74	-	7446	38	-	90	172	17326	-	-	472
		MIN	123	20	10	167	1.1	3.6	4.1	7.0	1120	-	0.9
	MAX	9750	227	2379	15328	89	3314	939	475	48479	-	5319	5572

Table 11: Results from LA-ICP-MS analyses of the fluid inclusion assemblages (FIA) from sample Grummetstock. Elemental concentrations are given in $\mu\text{g/g}$, salinity in mass% NaCl_{eq} .

FIA		Salinity	Li	B	Na	Al	K	Ca	Mn	Fe	
44	average	43	631	4955	94865	524	38967	1663	27251	35224	
LVS	1SD	1.1	408	5378	14354	-	19047	1301	6699	10150	
	RSD%	2.5	65	109	15	-	49	78	25	29	
16	average	26	1568	2330	65640	35721	19430	-	6998	21759	
LV	1SD	2.7	835	1167	5753	10344	9385	-	1404	9948	
	RSD%	10	53	50	9	29	48	-	20	46	
15	average	27	1386	1445	69915	5270	15990	1868	8210	24861	
LV	1SD	0.7	537	186	5776	3596	5806	1027	1041	2793	
	RSD%	2	39	13	8	68	36	55	13	11	
17	average	22	1746	3628	58387	3067	15146	1893	6394	16908	
LV	1SD	4.5	267	1592	5792	3301	9074	603	2426	12095	
	RSD%	20	15	44	10	108	60	32	38	72	
13	average	13	3253	1079	33169	7800	10675	-	4263	7824	
LV	1SD	6	6180	843	15341	-	5731	-	778	5836	
	RSD%	46	190	78	46	-	54	-	18	75	
9	average	10	1380	1046	25738	11862	9392	-	4076	6976	
LV	1SD	0.5	667	471	1978	14594	2235	-	528	3077	
	RSD%	5	48	45	8	123	24	-	13	44	
19	average	23	2713	4848	71792	12724	2629	-	6717	12944	
LV	1SD	0.4	925	241	4988	17314	492	-	1878	2981	
	RSD%	2	34	5	7	136	19	-	28	23	
14	average	23	1768	4483	62167	7687	18868	-	5784	13237	
LV	1SD	0.1	599	137	3216	-	1132	-	789	2989	
	RSD%	1	34	3	5	-	6	-	14	23	
8	average	25	1959	4497	68101	11185	23096	561	5125	15052	
LV	1SD	1.6	124	623	4808	14122	326	206	511	2472	
	RSD%	7	6	14	7	126	1	37	10	16	
FIA		Zn	Cu	Rb	Sr	Mo	Sn	Sb	Cs	W	Pb
44	average	7869	48	1272	64	9.9	1616	136	1255	11	2550
LVS	1SD	3213	13	376	19	2.2	327	158	562	10	800
	RSD%	41	27	30	30	22	20	116	45	87	31
16	average	4508	33	464	26	1.8	24	336	660	7.2	906
LV	1SD	1327	35	139	4.6	0.8	4.9	219	81	3.4	161
	RSD%	29	105	30	18	46	20	65	12	47	18
15	average	4787	35	327	32	3.2	10.3	86	549	5.7	906
LV	1SD	816	16	75	6.3	0.4	6.1	104	88	1.4	119
	RSD%	17	45	23	19	12	59	121	16	25	13
17	average	3942	23.1	407	29	2.3	3.7	187	655	4.3	770
LV	1SD	1945	7.4	167	20	0.9	1.0	148	76	3.8	456
	RSD%	49	32	41	69	37	26	79	12	88	59
13	average	3262	22	322	10.1	0.9	13.9	130	455	0.5	336
LV	1SD	1839	20	143	6.2	0.5	8.5	10	369	0.6	155
	RSD%	56	89	44	61	57	61	8	81	116	46
9	average	2583	2.9	233	8.1	1.3	28.3	92	271	0.24	208
LV	1SD	457	1.3	41	0.6	0.3	4.1	134	48	0.13	62
	RSD%	18	46	18	7	25	15	144	18	55	30
19	average	4223	20	211	25	2.4	16.7	1239	797	0.4	928
LV	1SD	1920	1.0	64	2.2	0.6	-	1638	265	-	275
	RSD%	45	5	30	9	23	-	132	33	-	30
14	average	3747	19	455	25	2.2	4.5	103	675	3.5	812
LV	1SD	947	2.6	33	6.3	0.2	-	104	43	3.0	144
	RSD%	25	14	7	25	11	-	101	6	87	18
8	average	2833	31	600	20	1.7	5.9	481	1119	3.5	664
LV	1SD	909	17	118	2.4	0.1	4.6	210	349	2.9	116
	RSD%	32	55	20	12	7	78	44	31	83	17

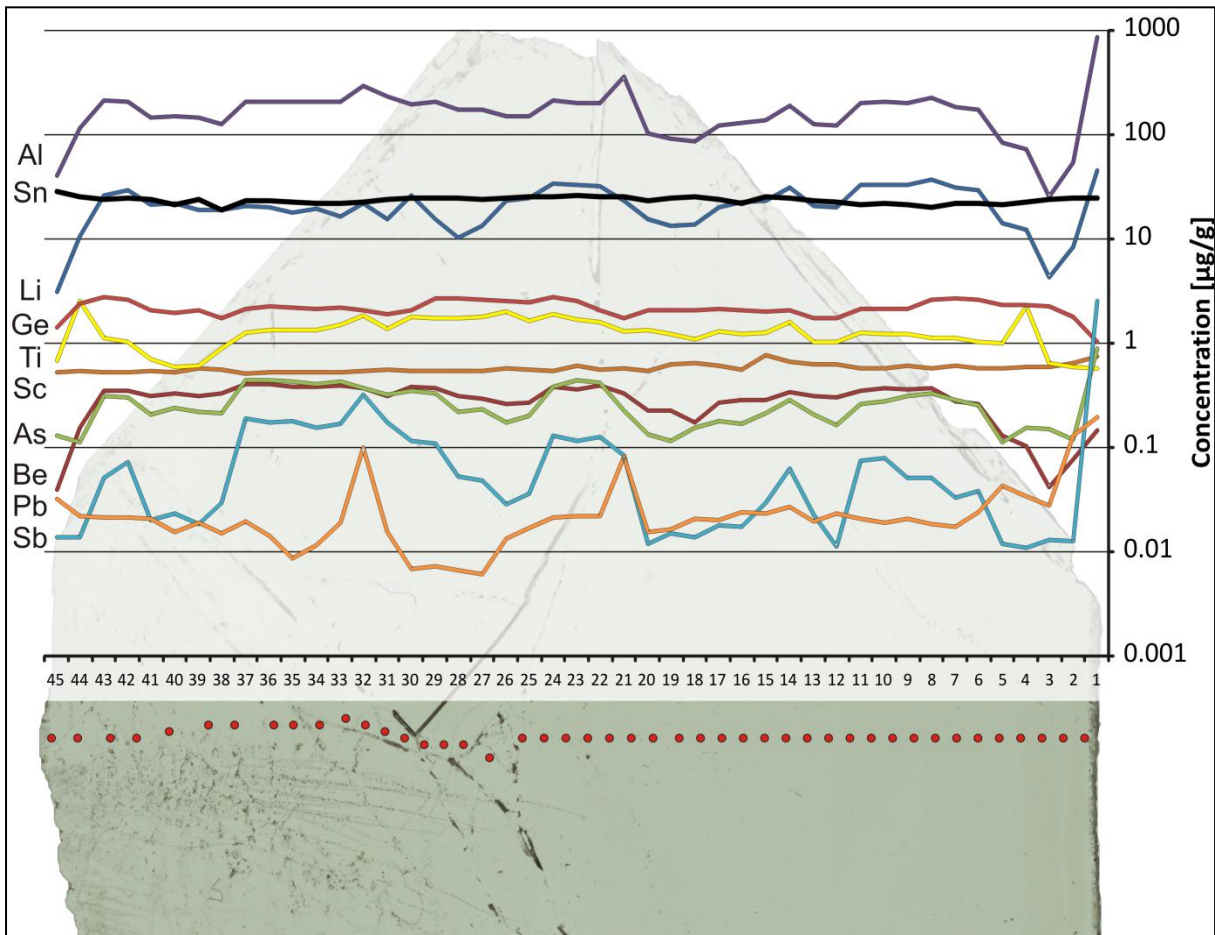


Figure 28: Overview of the trace element data measured by LA-ICP-MS on the hydrothermal single quartz crystal (sample: ZinQ). Red dots represent the laser ablation sites that were arranged along a cross sectional profile to reveal possible internal chemical zonings of the crystal. The presented elemental concentrations are limited to 10 of 31 measured elements.

5.4.2.4 Trace elements in quartz

Figure 28 shows the results from the 45 individual analyses on the ZinQ quartz crystal arranged as a cross sectional profile along the a-axis. There are basically only few characteristic patterns in the trace element cross section that give an undeniable hint about chemical zoning in the crystal. Both rims show lower values of Al, Li, Be, Ge and Ti if compared with the central parts of the crystal. With the exception of analysis No. 1 and 2, which show a strong increase of Al, Li, Sb, Be and Pb. This decrease is reflected by the opposing rims and therefore accounts for a true chemical zoning with the low concentration zones being the latest overgrowth on the quartz crystal.

Aluminium concentrations range between 25 and 365 $\mu\text{g/g}$, with only a few values being $<100 \mu\text{g/g}$ at the crystal rims. The Al concentrations analyzed in the central parts (38 points)

average to 182 $\mu\text{g/g}$ with a standard deviation (1SD) of $\pm 54 \mu\text{g/g}$. Lithium, as the major charge balancing cation, correlates well with Al and is one of the three elements that exceeds the 10 $\mu\text{g/g}$ value. In the crystal center, the Li concentrations reach 23 $\mu\text{g/g} \pm 7 \mu\text{g/g}$ and the decreasing Al values towards the rims are well reflected by decreasing Li values, too (3 – 10 $\mu\text{g/g}$). The melt fractionation-sensitive elements Ti and Ge are present in very low concentrations of 1.3 $\mu\text{g/g} \pm 0.3 \mu\text{g/g}$ and 2.2 $\mu\text{g/g} \pm 0.3 \mu\text{g/g}$ in the crystal center. Titanium concentrations along the crystal center display only small variations, but towards the left rim (with respect to the crystal orientation from Figure 28) there is a significant decrease (1.2 – 0.5 $\mu\text{g/g}$) that goes along with a slight bump in the Al values. Interestingly, the highest Ti values were measured next to the rims with 2.2 $\mu\text{g/g}$ and 2.5 $\mu\text{g/g}$ with a significantly set-off from the adjacent ablation spots and an anti-correlation with the respect to the decrease in Al and Li. Both values might be related to the same crystal growth zone, which is followed on both sides by lower Ti values on the outer most spots. Germanium is slightly higher concentrated than Ti and shows a nearly constant distribution along the whole crystal. Only the two outer most data points at the rims differ significantly from the rest. Here, the lowest Ge values of 1.0 $\mu\text{g/g}$ and 1.4 $\mu\text{g/g}$ were detected. Titanium and Ge, do not correlate with the extraordinary high Al, Li, Sb and Pb values at the right crystal rim and seem to be unaffected by this increase. The Sn concentrations are the only values that appear to be stable all along the profile (23.7 $\mu\text{g/g} \pm 1.7 \mu\text{g/g}$) without any significant decreases/increases. A tin concentration of 23 $\mu\text{g/g}$ in quartz seems to be extraordinary high compared to the existing literature data and the homogeneity of Sn concentration values along the cross sectional profile indicates that the Sn measurements might have been biased. An influence of molecular interferences based on the matrix element Si can be excluded for ^{118}Sn , since the formation of polyatomic cluster molecules like $^{36}\text{Ar}+^{38}\text{Ar}+^{28}\text{Si}+^{16}\text{O}$ (with $m/z = 118$) has never been reported before and is very unlikely to result in the observed count rates of $> 10^5$ cps. Only gas molecules like $^{38}\text{Ar}+^{40}\text{Ar}+^{40}\text{Ar}$ molecules are suspected to be able to interfere with the ^{118}Sn signal, but those are eliminated by the background correction. Sample surface contamination can be excluded, too, since the samples were pre-ablated prior to each analysis. Finally, we identified the laser cell which is partly made of grey colored polymers as a possible source of Sn contamination. The high laser repetition rate of 500 Hz yields to a massive mobilization of quartz particles. The resulting sample aerosol operates as an abrasive material to the polymer of the laser cell and causes a constant input of the Sn-bearing organometallic material to the ICP. Non-biased Sn concentrations in the Zinnwald quartz have been measured during analyses of fluid inclusions with the spiral technique. Since the fluid

inclusion laser cell only consist of Teflon and the Ag heating-freezing block, we can exclude the contamination described above. The host signal intervals delivered Sn concentrations of $0.22 \pm 0.03 \mu\text{g/g}$ ($n = 13$), while the values of other trace elements like Al, Li, Cs and Pb agree well with the here described results, indicating the overall accuracy of the host signal calculations. ^{45}Sc , for example, delivers constant concentrations of $0.58 \mu\text{g/g} \pm 0.05 \mu\text{g/g}$, like Sn without considerable deviations along the profile. But since $^{29}\text{Si}+^{16}\text{O}$ is a frequently generated molecule during quartz ablation, the results for ^{45}Sc are not trustable.

Other elements that have been detected above their lower detection limit on more than 50% of the ablation spots are Be, B, Na, K, Cr, Mn, Zn, As, Rb, Sr, Pb and Bi. All of the mentioned elements are very low concentrated in the ng/g to $1 \mu\text{g/g}$ range, with only a few exceptions like individual Na values of about $5 \mu\text{g/g}$. The beryllium concentrations in the central parts are $0.31 \mu\text{g/g} \pm 0.05 \mu\text{g/g}$ and are following the decrease in Al and Li towards the crystal rims ($0.039 \mu\text{g/g}$), in most cases. Boron concentrations are $0.98 \mu\text{g/g} \pm 0.17 \mu\text{g/g}$ and do not correlate with Al and Li. Sodium and K contents are well correlated and show more scatter than e.g. Be and B (Na: $1.91 \mu\text{g/g} \pm 1.15 \mu\text{g/g}$, K: $0.90 \mu\text{g/g} \pm 0.96 \mu\text{g/g}$). These elements were used as a monitor for fluid inclusions and indeed some of the positive outlier values for Na can reach $5 \mu\text{g/g}$ and exceed the average by a factor of 2.5. Despite these elevated concentration levels, this does not directly indicate the accidentally ablation of a fluid inclusion, because the corresponding time resolved signals do not show extraordinary high Na and K count rates. Chromium ($1.57 \mu\text{g/g} \pm 0.21 \mu\text{g/g}$), Mn ($0.40 \mu\text{g/g} \pm 0.25 \mu\text{g/g}$) and Zn ($0.30 \mu\text{g/g} \pm 0.25 \mu\text{g/g}$) appear to be independent from the decrease in Al and Li towards the rims, but they also have extremely high concentrations at the right rim (Cr: $2.08 \mu\text{g/g}$, Mn: $1.67 \mu\text{g/g}$, Zn: $2.44 \mu\text{g/g}$) compared to their average values. The concentrations of As ($0.27 \mu\text{g/g} \pm 0.10 \mu\text{g/g}$) could be influenced by the ablation of microscopic solid inclusions. Therefore, As was one of the four elements together with Na, K and Pb that have been used as a monitor for inclusions in the quartz. Correlating As and Pb signals may also indicate the ablation of solid inclusions, but no conspicuous signals could be identified during the quality check of the analyses. Rubidium and Sr signals were often low, close to the calculated LOD for both elements. Strontium was detected in 41 ablation sites, Rb only in 25 of 45 analyses. The average concentrations of Rb ($0.024 \mu\text{g/g} \pm 0.059 \mu\text{g/g}$) and Sr ($0.012 \mu\text{g/g} \pm 0.039 \mu\text{g/g}$) are typically very low and barely exceed 3SD of the gas blank signal. Furthermore, Pb and Bi were also detected in very low concentrations with high uncertainties ($0.023 \mu\text{g/g} \pm 0.018 \mu\text{g/g}$ and $0.0019 \mu\text{g/g} \pm 0.0020 \mu\text{g/g}$ 1SD, respectively). Lead concentrations of about one order of magnitude above the LOD were calculated for all 45 analyses, whereas Bi always

was very close to the LOD and could be found in 35 of 45 spots. A group of elements including Mg, V, Fe, Nb, Mo, Ag, Cs, Ba, Ta and W was only in some of the 45 analyses above LOD.

Correlations between the measured elements are visualized in Table 14 by a correlation matrix, based on the calculation of the Pearson product-moment correlation coefficient r . Elements that were detected in less than 50% of all analyses were excluded from the calculation, to overcome insignificant results. The importance of Al in quartz has been discussed above and some unambiguous very strong positive correlations (with $r > 0.7$) with Al can be verified with the correlation matrix, including Na, K, Mn, Zn, As, Rb, Sr, Sb, Pb and Bi. Lithium and Al are characterized by a strong positive correlation ($r = 0.63$), too. Other relevant strong correlations with Li are committed by Be, B and As ($r > 0.5$). Beryllium and B, in turn, reach a very strong correlation ($r = 0.69$) with each other. Titanium and Ge are also of great relevance in quartz. A medium strong positive correlation with Ti can only be found for Ge ($r = 0.49$). Other elements show only weak or very weak ($0.3 < r < -0.3$) correlations with Ti. Germanium is accompanied by a number of negative correlating elements with medium ($-0.3 > r < -0.5$; Na, Al, K, Cu, Sb) and strong ($-0.5 > r < -0.7$; Mn, Zn, Rb, Sr, Pb, Bi) relationships.

Table 12: Trace element concentrations in the host quartz calculated from the host signal intervals from 13 fluid inclusion analyses of the Zinnwald hydrothermal quartz. All values in $\mu\text{g/g}$.

FIA	⁷ Li	¹¹ B	²³ Na	²⁷ Al	³⁹ K	⁵⁵ Mn	⁶⁵ Cu	⁷⁵ As	¹¹⁸ Sn	¹²¹ Sb	¹³³ Cs	²⁰⁸ Pb
host signal	$\mu\text{g/g}$	$\mu\text{g/g}$	$\mu\text{g/g}$	$\mu\text{g/g}$	$\mu\text{g/g}$	$\mu\text{g/g}$	$\mu\text{g/g}$	$\mu\text{g/g}$	$\mu\text{g/g}$	$\mu\text{g/g}$	$\mu\text{g/g}$	$\mu\text{g/g}$
PS1	14.2	0.84	-	137.1	1.23	1.06	0.25	0.15	0.23	0.11	0.03	0.03
PS1	22.1	0.52	0.55	131.8	0.87	0.45	0.10	0.22	0.20	0.05	0.01	-
PS1	21.3	0.50	2.62	122.3	2.07	0.54	-	0.12	0.22	0.04	0.02	0.02
PS2	18.1	0.65	2.29	137.9	3.19	-	-	0.22	0.22	0.05	0.03	0.02
PS2	11.3	0.52	1.15	77.2	0.90	0.70	-	-	0.27	-	0.02	-
PS2	18.1	0.59	6.51	143.1	3.45	-	0.16	0.22	0.19	0.04	0.09	0.02
PS2	10.5	0.54	0.43	108.9	1.91	0.67	-	0.12	0.21	0.03	0.02	-
PS2	10.6	0.58	1.19	109.7	1.70	-	-	0.14	0.23	0.02	0.02	0.01
PS2	10.9	0.55	0.89	107.4	1.62	1.12	-	-	0.22	0.03	0.02	-
PS2	11.1	0.67	3.12	109.4	2.25	1.41	0.57	0.18	0.18	-	0.09	0.06
PS2	11.7	0.76	0.85	112.8	2.01	-	0.14	0.18	0.20	-	0.02	0.02
PS2	13.0	0.70	1.95	113.6	1.54	1.06	0.17	0.20	0.20	-	0.02	0.03
PS2	17.8	0.60	19.7	136.2	3.90	-	1.89	0.55	0.27	0.13	0.05	0.03

Table 13: Concentration values in µg/g for all analyzed elements on the 45 ablation sites on the Zinnwald hydrothermal quartz. 'avrg. LOD' is the average value of the lower detection limit of all single analyses.

Spot	⁷ Li µg/g	⁹ Be µg/g	¹¹ B µg/g	²³ Na µg/g	²⁵ Mg µg/g	²⁷ Al µg/g	³⁹ K µg/g	⁴⁵ Sc µg/g	⁴⁹ Ti µg/g	⁵¹ V µg/g	⁵³ Cr µg/g	⁵⁵ Mn µg/g	⁵⁷ Fe µg/g	⁶⁵ Cu µg/g	⁶⁶ Zn µg/g	⁷⁵ Ge µg/g
1	46.21	0.147	0.878	25.77	1.589	858.8	134.2	0.755	0.573	0.12	2.083	1.675	9.782	1.326	2.439	1.041
2	8.49	0.077	0.807	5.129	-	54.8	0.747	0.659	0.599	0.02	1.781	0.409	-	-	0.521	1.799
3	4.27	0.042	0.732	0.860	-	25.3	0.555	0.590	0.653	-	1.806	0.345	-	0.121	0.220	2.250
4	12.22	0.103	0.783	0.891	-	72.3	0.640	0.591	2.252	-	1.625	0.359	-	-	0.272	2.349
5	14.08	0.130	0.792	0.891	-	84.4	0.674	0.580	1.019	-	1.601	0.305	-	-	0.209	2.365
6	29.44	0.265	0.926	2.018	-	173.6	0.995	0.582	1.022	-	1.796	0.331	-	-	0.200	2.631
7	31.21	0.279	0.990	1.814	-	184.4	0.883	0.616	1.145	-	1.573	0.347	-	0.111	0.171	2.699
8	36.93	0.372	0.997	1.855	-	228.4	0.931	0.581	1.138	-	1.542	0.379	-	-	0.177	2.672
9	33.59	0.368	1.085	2.400	-	204.8	0.988	0.616	1.240	0.02	1.776	0.444	1.960	0.090	0.202	2.147
10	32.98	0.375	1.130	1.947	-	207.6	0.935	0.577	1.239	-	1.688	0.292	-	-	0.197	2.130
11	33.59	0.355	1.113	1.813	-	205.4	0.708	0.584	1.273	-	1.571	0.327	-	0.119	0.247	2.166
12	20.16	0.303	1.000	1.112	-	123.5	0.411	0.625	1.051	-	1.481	0.301	-	0.067	0.226	1.728
13	21.12	0.315	1.131	1.236	-	128.4	0.435	0.637	1.029	-	1.403	0.295	-	0.072	0.361	1.754
14	31.22	0.345	1.145	2.127	-	192.0	0.812	0.662	1.622	-	1.451	0.323	-	-	0.234	2.083
15	23.22	0.292	1.040	1.399	-	137.8	0.652	0.777	1.285	-	1.533	0.269	-	-	0.296	2.036
16	22.55	0.291	1.017	1.525	-	130.3	0.863	0.558	1.224	-	1.997	0.572	-	0.076	0.281	2.105
17	19.98	0.268	0.935	1.478	-	122.0	0.574	0.606	1.297	-	1.488	0.292	-	-	0.192	2.152
18	13.81	0.177	0.886	0.941	-	87.8	0.445	0.641	1.085	-	1.447	0.318	-	-	0.355	2.073
19	13.63	0.226	0.855	0.778	-	91.6	0.502	0.628	1.230	-	1.422	0.330	-	0.097	0.308	2.088
20	15.52	0.231	0.876	1.063	-	102.6	0.733	0.544	1.348	-	1.825	0.378	-	0.173	0.514	2.092
21	23.30	0.330	1.667	2.273	1.674	365.3	1.162	0.583	1.313	0.02	2.277	1.234	6.228	5.219	1.008	1.776
22	32.20	0.395	1.114	1.530	-	199.7	0.414	0.555	1.597	-	1.362	0.313	-	-	0.226	2.061
23	33.70	0.362	1.132	1.578	-	205.2	0.436	0.607	1.703	-	1.545	0.393	-	0.069	0.214	2.556
24	34.22	0.381	1.101	1.480	-	213.3	0.402	0.552	1.898	-	1.543	0.352	-	0.072	0.203	2.775
25	24.69	0.272	0.871	1.370	-	150.9	0.435	0.568	1.670	-	1.459	0.298	-	0.078	0.176	2.517
26	23.57	0.267	0.861	1.083	-	150.5	0.386	0.574	2.031	-	1.549	0.345	-	0.086	0.170	2.580
27	3.11	0.039	0.584	1.283	-	41.3	1.028	0.527	0.684	-	1.604	0.604	-	-	0.304	1.427
28	10.82	0.155	0.665	2.545	-	116.3	1.916	0.542	2.547	-	1.567	0.409	-	-	0.225	2.419
29	26.12	0.351	0.831	5.411	-	213.6	1.339	0.528	1.139	-	1.500	0.241	-	-	0.246	2.769
30	30.02	0.356	1.023	4.615	-	210.7	0.515	0.537	1.034	-	1.458	0.307	-	0.079	0.213	2.619
31	21.49	0.318	1.022	2.260	-	148.0	0.402	0.545	0.710	-	1.403	0.324	-	0.086	0.224	2.083
32	22.26	0.333	1.069	2.479	-	152.3	0.838	0.530	0.598	0.01	1.665	0.586	-	0.072	0.203	1.975
33	18.84	0.315	1.015	1.445	-	146.0	0.651	0.583	0.620	-	1.535	0.453	-	-	0.234	2.077
34	19.08	0.330	0.967	2.412	1.252	128.5	1.013	0.561	0.905	-	1.633	0.412	-	0.113	0.234	1.729
35	20.68	0.412	1.135	3.098	-	207.9	0.986	0.521	1.266	-	1.524	0.277	-	0.087	0.300	2.153
36	20.47	0.405	1.053	1.835	-	207.8	0.396	0.535	1.340	-	1.398	0.309	-	-	0.199	2.249
37	18.11	0.384	1.066	1.773	-	207.5	0.399	0.529	1.352	-	1.513	0.267	-	0.073	0.172	2.230
38	19.40	0.382	1.032	1.470	-	207.8	0.349	0.529	1.361	-	1.306	0.299	-	0.058	0.161	2.165
39	16.40	0.396	1.044	3.617	0.171	210.0	1.501	0.531	1.515	-	1.254	0.282	-	0.263	0.495	2.189
40	22.09	0.369	0.992	3.292	0.993	296.2	4.208	0.544	1.846	-	1.442	0.453	5.299	5.262	1.621	2.095
41	15.79	0.312	0.933	4.600	0.199	235.2	5.606	0.562	1.379	-	1.879	0.560	2.283	0.329	0.342	1.890
42	26.61	0.389	1.035	1.336	-	195.1	0.330	0.551	1.813	-	1.414	0.309	-	0.205	14.34	2.087
43	15.81	0.372	0.942	1.406	-	206.4	0.418	0.548	1.758	-	1.422	0.375	-	0.056	0.146	2.692
44	10.31	0.317	0.875	1.178	-	175.5	0.534	0.542	1.758	-	1.332	0.271	-	0.067	0.158	2.723
45	13.59	0.300	0.884	1.010	2.168	175.0	0.339	0.539	1.795	-	1.512	0.341	-	0.051	0.114	2.660
avrg. LOD	0.401	0.017	0.093	0.115	0.287	0.067	0.149	0.017	0.066	0.020	0.460	0.151	1.575	0.101	0.095	0.066

Table 13: Concentration values in µg/g for all analyzed elements on the 45 ablation sites on the Zinnwald hydrothermal quartz. 'avrg. LOD' is the average value of the lower detection limits of all single analyses.

Spot	⁷⁵ As	⁸⁵ Rb	⁸⁸ Sr	⁸⁹ Y	⁹³ Nb	⁹⁵ Mo	¹⁰⁷ Ag	¹¹⁸ Sn	¹²¹ Sb	¹³³ Cs	¹³⁷ Ba	¹⁸¹ Ta	¹⁸² W	²⁰⁸ Pb	²⁰⁹ Bi
	µg/g	µg/g	µg/g	µg/g	µg/g	µg/g	µg/g	µg/g	µg/g	µg/g	µg/g	µg/g	µg/g	µg/g	µg/g
1	0.890	8.812	0.778	0.039	0.075	0.014	1.328	24.54	2.523	2.751	0.716	0.090	0.057	0.194	0.040
2	0.121	0.015	0.022	0.014	0.022	0.013	0.026	24.54	-	0.003	0.034	0.019	0.036	0.129	0.004
3	0.150	-	-	-	-	-	0.007	24.10	-	-	-	-	-	0.028	-
4	0.155	0.008	0.003	-	-	-	-	22.83	-	-	-	-	-	0.034	0.002
5	0.114	0.010	0.004	0.001	-	-	0.157	21.26	-	-	-	-	-	0.044	0.002
6	0.256	0.013	0.006	-	-	-	0.059	21.91	0.038	-	-	-	0.001	0.024	-
7	0.291	0.008	0.003	0.004	-	-	-	22.36	0.033	-	-	-	-	0.018	-
8	0.336	0.008	0.003	-	0.001	0.002	-	20.21	0.051	0.001	-	0.001	0.001	0.019	0.001
9	0.313	0.031	0.014	0.001	0.009	0.005	-	21.61	0.051	0.003	0.009	0.005	0.004	0.021	0.004
10	0.276	0.010	0.002	-	-	0.004	-	22.02	0.079	-	-	-	-	0.019	0.002
11	0.265	0.005	0.004	-	-	0.002	-	21.69	0.075	0.001	-	-	-	0.021	0.002
12	0.167	-	0.005	-	-	0.003	-	22.51	0.011	-	0.005	-	-	0.023	0.002
13	0.208	-	0.005	-	-	-	-	23.24	0.023	-	-	-	-	0.020	-
14	0.286	0.005	0.005	0.001	0.001	-	-	24.58	0.063	-	-	-	0.002	0.027	0.002
15	0.218	-	0.007	-	-	-	-	25.57	0.030	-	-	-	-	0.023	0.001
16	0.168	0.003	-	-	-	-	-	22.28	0.017	0.002	-	-	-	0.024	0.001
17	0.179	-	0.003	-	-	-	-	23.87	0.018	-	-	-	0.001	0.020	0.001
18	0.154	-	0.006	-	0.005	-	-	25.29	0.014	-	-	-	-	0.021	0.001
19	0.118	0.005	0.004	-	0.001	-	0.011	24.98	0.015	-	-	0.002	0.002	0.017	0.001
20	0.133	0.006	0.004	-	-	-	0.008	23.51	0.012	-	-	-	-	0.016	0.001
21	0.226	-	0.006	0.001	-	0.014	0.049	25.28	0.084	-	0.005	0.003	0.002	0.082	0.003
22	0.420	-	0.005	-	-	-	-	25.49	0.126	-	-	-	-	0.022	0.001
23	0.446	-	0.005	0.001	-	-	-	26.70	0.117	0.003	-	-	-	0.022	-
24	0.389	-	0.002	-	-	-	-	25.45	0.132	-	-	-	-	0.022	0.001
25	0.204	-	0.003	-	-	-	-	25.33	0.036	-	-	-	-	0.017	-
26	0.176	-	0.004	-	-	-	-	24.70	0.028	-	-	-	-	0.014	0.001
27	0.129	0.040	0.032	-	-	-	-	28.79	0.014	0.037	0.026	-	-	0.032	0.002
28	0.114	0.053	0.014	-	-	-	-	25.62	0.014	0.033	0.010	-	-	0.022	0.001
29	0.314	0.004	-	-	-	-	-	23.97	0.051	-	-	-	-	0.021	-
30	0.305	-	-	-	-	-	-	25.00	0.073	-	-	-	-	0.021	0.001
31	0.209	-	0.002	-	-	-	-	24.23	0.020	-	-	-	-	0.021	-
32	0.238	0.003	0.005	-	-	-	-	21.78	0.024	0.001	-	-	-	0.016	-
33	0.223	0.002	0.004	-	0.001	-	-	24.02	0.019	-	0.006	-	-	0.019	0.001
34	0.215	0.003	0.005	0.003	0.002	-	0.008	18.92	0.030	0.002	0.006	0.002	-	0.015	0.001
35	0.443	-	0.003	-	-	-	0.013	23.78	0.191	-	0.002	-	-	0.020	0.001
36	0.441	-	0.002	-	-	-	-	23.13	0.177	-	-	-	-	0.014	0.001
37	0.437	0.003	0.002	-	-	-	-	22.77	0.179	0.002	0.003	-	-	0.009	0.001
38	0.413	-	0.002	0.001	-	-	-	22.42	0.157	-	-	-	-	0.012	0.001
39	0.436	0.003	0.008	-	-	-	1.616	22.30	0.168	-	0.007	0.001	-	0.019	0.001
40	0.378	0.070	0.057	0.001	-	0.003	0.040	22.55	0.326	0.007	0.064	0.001	0.008	0.102	0.011
41	0.324	0.260	0.230	-	-	0.010	0.016	24.35	0.176	0.026	0.257	0.008	-	0.016	0.003
42	0.351	-	0.002	-	-	-	-	24.80	0.118	-	-	-	-	0.007	0.001
43	0.333	-	0.002	-	-	-	-	24.81	0.109	-	-	-	0.004	0.007	0.001
44	0.220	0.010	0.003	-	-	-	-	24.49	0.052	0.008	-	-	0.000	0.007	-
45	0.235	-	0.002	0.001	-	-	0.005	24.30	0.049	0.001	-	0.001	-	0.006	0.001
avrg. LOD	0.036	0.004	0.003	0.001	0.001	0.005	0.010	0.013	0.016	0.001	0.004	0.002	0.002	0.004	0.002

Table 14: Correlation matrix of all measured elements in the Zinnwald hydrothermal quartz with more than 23 calculated concentration values above LOD. Values represent the Pearson product-moment correlation coefficient r .

	Li	Be	B	Na	Al	K	Ti	Cr	Mn	Cu	Zn	Ge	As	Rb	Sr	Sb	Pb	Bi
Li		0.51	0.50	0.42	0.63	0.40	-0.01	0.13	0.28	0.09	0.28	0.06	0.62	0.48	0.37	0.44	0.20	0.45
Be	0.51		0.69	-0.16	0.22	-0.22	0.23	-0.35	-0.23	0.05	-0.17	0.28	0.43	-0.25	-0.25	-0.23	-0.38	-0.25
B	0.50	0.69		-0.07	0.32	-0.09	0.00	0.16	0.20	0.51	0.09	-0.08	0.30	-0.09	-0.13	-0.06	-0.01	-0.08
Na	0.42	-0.16	-0.07		0.86	0.96	-0.29	0.39	0.76	0.17	0.80	-0.46	0.70	0.97	0.97	0.97	0.78	0.95
Al	0.63	0.22	0.32	0.86		0.86	-0.07	0.34	0.77	0.40	0.79	-0.30	0.85	0.91	0.85	0.92	0.64	0.87
K	0.40	-0.22	-0.09	0.96	0.86		-0.24	0.39	0.78	0.14	0.80	-0.49	0.67	1.00	0.97	0.99	0.75	0.97
Ti	-0.01	0.23	0.00	-0.29	-0.07	-0.24		-0.29	-0.26	0.11	-0.15	0.49	-0.01	-0.28	-0.26	-0.23	-0.28	-0.28
Cr	0.13	-0.35	0.16	0.39	0.34	0.39	-0.29		0.72	0.38	0.43	-0.38	0.02	0.49	0.47	0.36	0.51	0.43
Mn	0.28	-0.23	0.20	0.76	0.77	0.78	-0.26	0.72		0.51	0.79	-0.58	0.45	0.93	0.79	0.76	0.75	0.80
Cu	0.09	0.05	0.51	0.17	0.40	0.14	0.11	0.38	0.51		0.65	-0.29	0.14	0.16	0.15	0.19	0.61	0.30
Zn	0.28	-0.17	0.09	0.80	0.79	0.80	-0.15	0.43	0.79	0.65		-0.56	0.55	0.83	0.80	0.83	0.88	0.90
Ge	0.06	0.28	-0.08	-0.46	-0.30	-0.49	0.49	-0.38	-0.58	-0.29	-0.56		-0.15	-0.58	-0.53	-0.47	-0.54	-0.57
As	0.62	0.43	0.30	0.70	0.85	0.67	-0.01	0.02	0.45	0.14	0.55	-0.15		0.80	0.66	0.78	0.40	0.68
Rb	0.48	-0.25	-0.09	0.97	0.91	1.00	-0.28	0.49	0.93	0.16	0.83	-0.58	0.80		0.97	0.99	0.77	0.96
Sr	0.37	-0.25	-0.13	0.97	0.85	0.97	-0.26	0.47	0.79	0.15	0.80	-0.53	0.66	0.97		0.96	0.73	0.94
Sb	0.44	-0.23	-0.06	0.97	0.92	0.99	-0.23	0.36	0.76	0.19	0.83	-0.47	0.78	0.99	0.96		0.87	0.97
Pb	0.20	-0.38	-0.01	0.78	0.64	0.75	-0.28	0.51	0.75	0.61	0.88	-0.54	0.40	0.77	0.73	0.87		0.85
Bi	0.45	-0.25	-0.08	0.95	0.87	0.97	-0.28	0.43	0.80	0.30	0.90	-0.57	0.68	0.96	0.94	0.97	0.85	

5.5 Discussion

5.5.1 Fluid chemistry

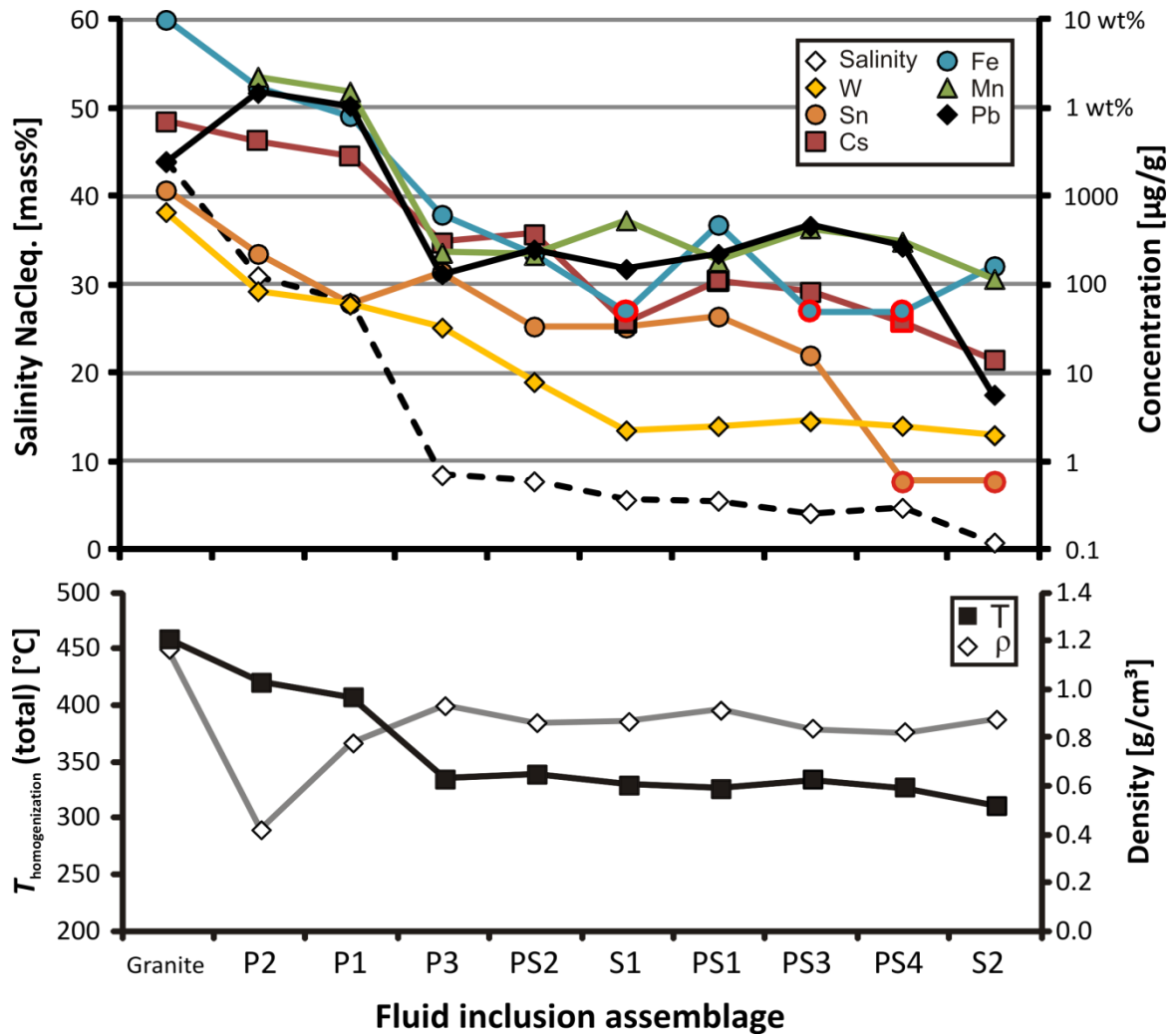


Figure 29: a) LA-ICP-MS results for Sn, W, Cs, Fe, Mn and Pb for all measured fluid inclusion assemblages (FIA) from sample ZinQ and the brine inclusions of the Schellerhau granite quartz samples. The FIAs have been arranged with decreasing salinities towards the right hand side of the diagram. Red marks indicate values below detection limit. b) Total homogenization temperatures determined by microthermometry and the calculated fluid densities for all measured FIAs.

5.5.1.1 Chemical evolution of mineralizing fluids

Figure 29 and Figure 30 include the measured trace element concentrations of all fluid generations and the microthermometric results (density and homogenization temperatures in Figure 29). Data points represent average values for all analyzed individual fluid inclusions from the investigated assemblages. The results from Schellerhau brines (SHX1) were added

for comparison of the hydrothermal stage, represented by sample ZinQ, with the magmatic derived fluids, trapped in the granite quartz. The order of the FIA on the x-axis refers to the calculated fluid salinity, decreasing from the left (Schellerhau brines) to the right (secondary two-phase fluids).

Figure 29b shows the measured average total homogenization temperatures for all fluid inclusion assemblages. The brine inclusions of the Schellerhau granite homogenized around 450°C, while the hydrothermal brine inclusions from sample ZinQ homogenized at considerably lower temperatures (P2: 290°C, P1: 367°C). All two-phase fluid inclusion assemblages fall into a rather narrow range between 377°C (PS4) and 400°C (P3).

The dependency of several elements on the NaCl_{eq} content of the fluid is demonstrated in Figure 29. Tin, W, Cs, Pb, Mn and Fe contents are clearly dependent on the fluid salinity and follow in general the decreasing trend of the NaCl_{eq} content from the brines to the low dense two-phase fluids. The complexation of these elements with Cl^- is therefore very likely. But this does not mean that all elements behave continually analogue to the salinity. Especially both ore forming metals, Sn and W, show relative decreases that are not always as strong as the relative decrease in salinity, e.g. between FIA P1 (brine) and P3 (two-phase). Here, the salinity decreases by -70% whilst the Sn concentration increases by 126% and W is relatively less depleted by only -45%, respectively. Further on, the relative change in salinity from P3 to PS2 is negligible small (-8%) but the simultaneous change in Sn and W is much more pronounced (both -76%). Tin stays constant around 30 – 40 $\mu\text{g/g}$ in the intermediate dense-intermediate saline fluids from (PS2, S1, PS1), but falls below the detection limit in FIA PS4 and S2. The fluids get continuously depleted in W from P2 to S1 until it reaches a very low level of around 2 - 3 $\mu\text{g/g}$ that is constant from S1 to S2. In conclusion this means there is a correlation between both metals and the salinity, but in detail the ratios of Sn/W differ a lot especially in the low saline fluids. The distribution of Sn might imply a precipitation of cassiterite that would explain the strong decrease from FIA PS3 to PS4 and S2. The decrease in salinity, probably achieved by dilution of the fluid due to mixing with meteoric waters, and the resulting lack of the ligand Cl^- can support the precipitation of SnO_2 . Concerning W, the continuous decrease from the brines to the intermediate dense fluids suggests that a precipitation of wolframite mainly occurred between FIA P3 and S1 could have stopped with the trapping of the S1 fluids.

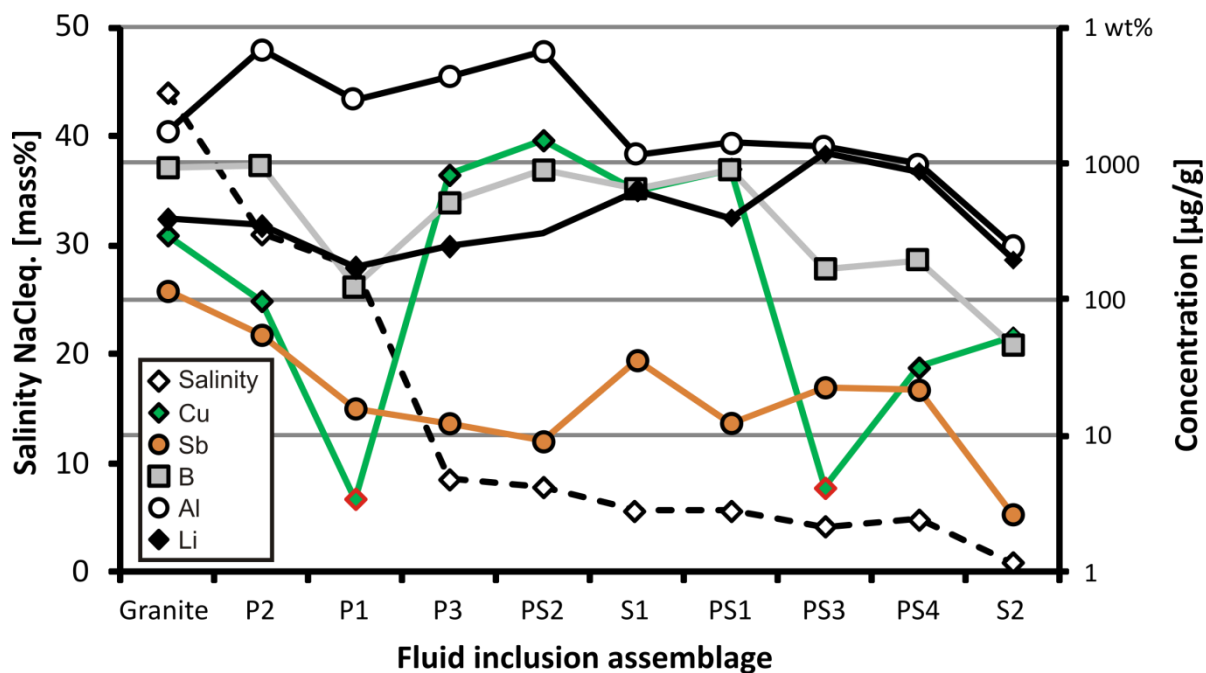


Figure 30: a) LA-ICP-MS results for Cu, Sb, B, Al and Li for all measured fluid inclusion assemblages (FIA) from sample ZinQ and the brine inclusions of the Schellerhau granite quartz samples. The FIAs have been arranged with decreasing salinities towards the right hand side of the diagram. Red marks indicate values below detection limit.

Iron, Mn, Cs and Pb are the elements which reflect the decrease in salinity the most clearest of all. As shown in Figure 29 those elements can be found at very high concentrations in the brines and they reproduce the drop in salinity from FIA P1 to P3 very clearly. The Fe concentrations of six FIA could be determined with concentrations above the LOD. Especially the SHX brines are extremely enriched in Fe and the decrease in salinity is well reflected by the iron values up to FIA PS2. Lead is present in all different inclusion types and also enriched in the brines like Fe, Mn and Cs, with the exception that the concentrations in the granite brines are significantly lower than those of the Zinnwald hydrothermal brines. No relevant changes in concentration can be observed within the two-phase fluids, where Pb stays more or less constant, which an analogy to Mn is. Only the low saline fluids from FIA S2 have deviating very low Pb concentrations. The observation of the correlation with NaCl_{eq} values can be explained by the formation of Cl-complexes like FeCl_2 , PbCl_2 , MnCl_2 and CsCl .

Elements that have a non-correlating content with NaCl_{eq} are Li, B, Al, Sb and Cu (Figure 30). Thereby, Cu shows the most noticeable deviation from the depletion trend with salinity. The two-phase FIAs from P3 to PS1 have the highest Cu concentrations of all investigated groups. In the brines and the low saline fluids of FIA PS4, PS3 and S2, Cu is significantly lower concentrated or even below the detection limit (P1 & PS3). The findings of Heinrich et

al. 1999 that Cu favors to partition into the vapor phase compared to coexisting brine phases, could be a possible explanation for this pattern. The intermediate dense inclusions have a relatively low degree of fill with a significant fraction of vapor bubbles. Although those inclusions homogenize into the liquid phase and they probably did not origin from a phase separation process, the lower dense fluids are still able to carry significantly more Cu than the brine inclusions. Copper is known to be transported in magmatic fluids as HS^- complexes as well as CuCl_2 . The independence from NaCl_{eq} suggests that HS^- complexes might play a role in the Zinnwald fluids, too.

Lithium seems to be another salinity-independent element (Figure 30). The Li contents in the brines are equal to those of the two-phase fluids of P3 and PS2. Fluid inclusion assemblages S1, PS4 and PS3 even show increasing Li concentrations with decreasing salinity. The Li-micas of the Zinnwald granite have been under permanent influence of the F-rich magmatic fluids during the trapping history of the observed inclusions. It cannot be excluded that, additionally to the trace elements like Sn and W, Li was also leached from the micas and resulted in a nearly constant Li content in the evolving fluid.

For B, Al and Sb (Figure 30), there is also no specific enrichment in the brine inclusions like it is described above for other elements. Brines and two-phase fluids have similar concentrations. In relation to all other FIA, the S2-fluids have the lowest contents.

5.5.1.2 Relation Sn and W

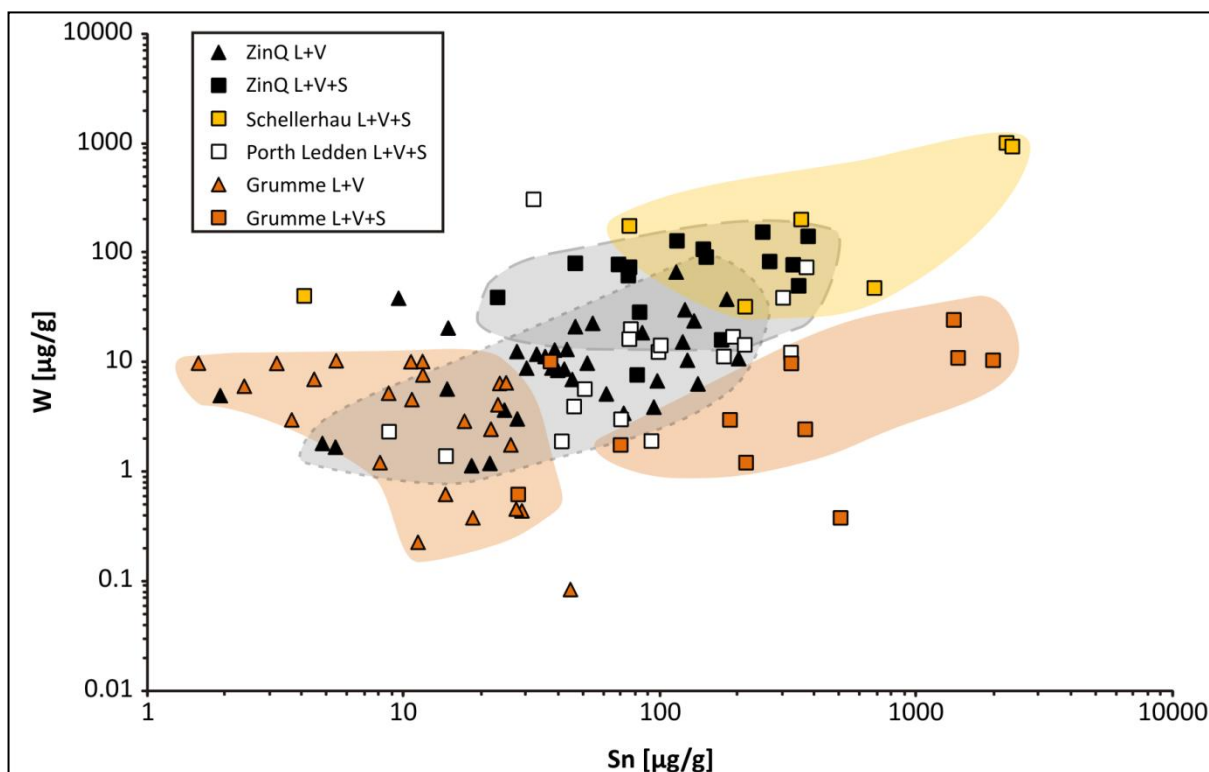


Figure 31: W concentrations plotted vs. Sn concentrations of the individual fluid inclusions from different sample locations. ZinQ L+V represents the results from two-phase inclusions from Zinnwald hydrothermal quartz, ZinQ L+V+S represents the three-phase inclusions from the same quartz sample, Grumme L+V and Grumme L+V+S data points represent the results from the Grummetstock/Gottesberg hydrothermal quartz. Schellerhau L+V+S and Porth Ledden L+V+S data points show the results from the brine inclusions of the respective magmatic quartz.

Focusing on the concentration values of the deposit forming metals Sn and W, both elements show variations over a wide range with respect to their fluid inclusion type and origin. In Figure 31 (W versus Sn) all analyzed fluid inclusions that delivered Sn and W values are plotted and arranged as distinct groups of two-phase (L+V) and three-phase (L+V+S) inclusions from the investigated locations. Of those, the Zinnwald two-phase inclusions (ZinQ L+V) show the most significant positive correlation of Sn and W values of all investigated fluid types. With only few exceptions, Sn displays higher concentrations than W by about one order of magnitude. The three-phase inclusions from the hydrothermal Zinnwald quartz (ZinQ L+V+S) show a flatter correlation trend, with stronger variations in Sn concentration than in W. The analyzed L+V+S inclusions from the Schellerhau granite show a large variability that exceeds that of the ZinQ L+V inclusions towards significantly higher Sn and W concentrations. The pattern itself shows a positive correlation and in addition to the ZinQ L+V inclusions, those high-saline inclusions fit well into the Sn-W correlation trend. Although the L+V+S inclusions are rare in the Schellerhau granite quartz and decrepitated

very often during microthermometry, reducing the available number of concentration values, it seems unambiguous that these brines were able to carry higher metal contents than all other investigated fluid types.

The white squares mark the available data from L+V+S inclusions of the Porth Ledden granite that can be compared with the Schellerhau brine inclusions. There is a general positive correlation between Sn and W and their concentration range reflects the L+V inclusions from sample ZinQ and not the L+V+S inclusions from the Schellerhau granite or the hydrothermal quartz. The maximum concentrations for both elements are significantly lower than in the Schellerhau L+V+S inclusions even though the salinities are very similar in the observed inclusions. This fact raises the question how the difference in concentration was achieved, if both fluids provide a roughly identical amount of Cl⁻ ions. The influence of the potentially higher F⁻ content in the SHX fluids might explain the higher solubility of Sn and W compared to the PL fluids, but this would require that SnCl₂ and SnF₄ complexes have to be stable contemporaneously. Other parameters that could be responsible for the higher Sn solubility in the Erzgebirge fluids are the amount of excess Al and the temperature of the parental melt. Both would increase the available amount of Sn in the melt that could get leached by the Cl⁻ (F⁻) bearing fluid.

The results from the smoky quartz crystal from Grummetstock/Gottesberg are to some extent unique if considered in the overall picture of all results. There is no clear correlation between W and Sn. Analogue to an upper limit in W (10 µg/g), a group of L+V inclusions marks the upper limit in Sn (~30 µg/g) with bigger variations in W. On the contrary, the investigated L+V+S inclusions from the Grummetstock display weakly correlating Sn and W values. The Sn contents equal those of the Schellerhau L+V+S inclusions and can be enriched to more than 1000 µg/g, while W is equal to the L+V inclusions.

Due to the good correlation of Sn and W in the fluids that are associated with the Altenberg-Teplice caldera, it is likely that both metals have been transported simultaneously and as complexes of an ligand that is able to form stable bonds with both metals. These findings are also applicable for the Porth Ledden L+V+S inclusions and the Grummetstock L+V+S inclusions. For the Grummetstock L+V inclusions instead, the non-correlating Sn and W contents suggest a complexation of the metals by different ligands or a temporal difference between the mobilization of Sn and W. The maximum concentration of W that is independent from the respective Sn content might also suggest a buffer reaction which only affects W but not Sn, probably the precipitation of wolframite during the trapping history. The different

observations from the Zinnwald and Grummetstock deposit demonstrate that the hydrothermal transport of Sn and W can proceed individually for both metals, probably related to changing characteristics of the fluid.

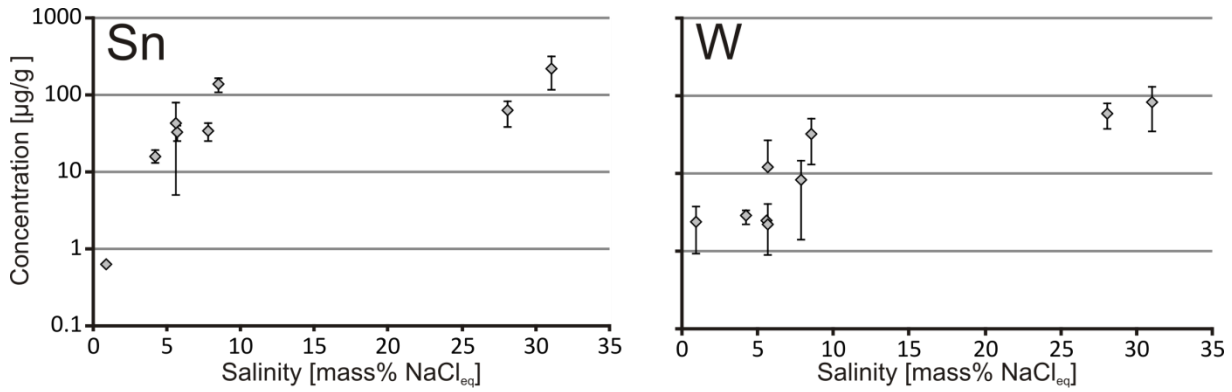


Figure 32: Sample ZinQ; Sn and W concentrations of the investigated FIA plotted against salinity. Error bars are defined by 1SD value of the average concentration values of the FIA. Y-axes are identical for both diagrams.

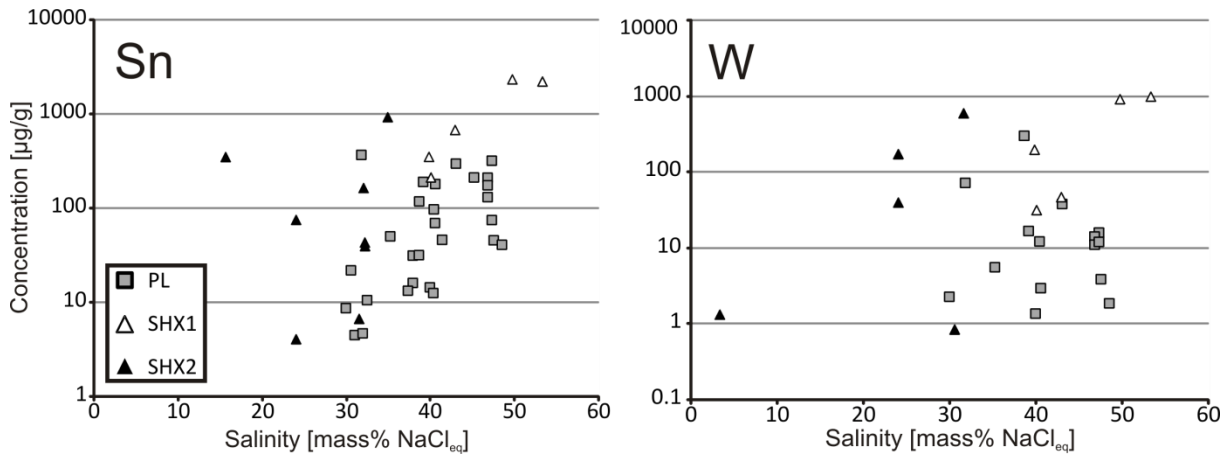


Figure 33: Granite samples: Sn and W concentrations of all measured individual brine inclusions from Schellerhau granite (SHX1 & SHX2) and Porth Ledden granite (PL) plotted against their salinity.

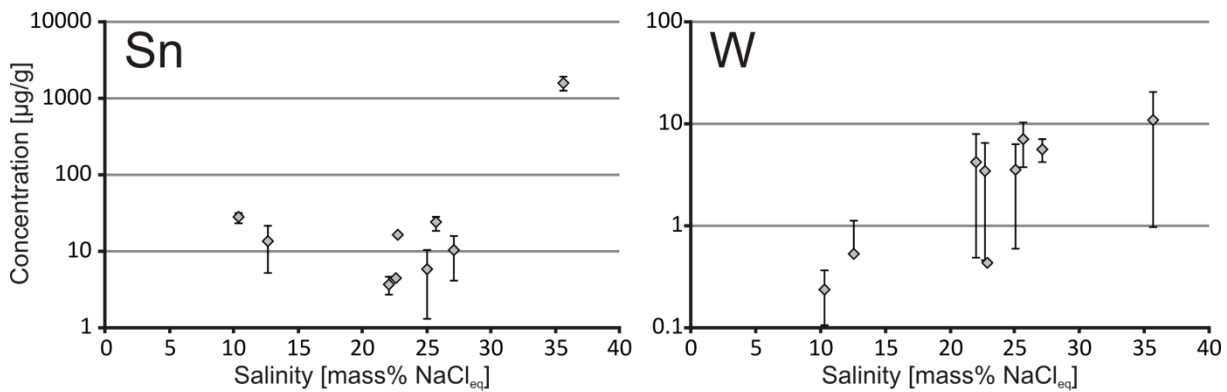


Figure 34: Sample Grummetstock – Gottesberg; Sn and W concentrations of all measured FIAs plotted against their salinity. Error bars indicate the 1SD values of the average concentration of the FIA.

Figure 32 demonstrates the dependency of Sn and W on the fluid salinity, concerning the inclusions from sample ZinQ. Especially the low to medium saline (<10 mass% NaCl_{eq.}) inclusions show a rising metal content with increasing salinity. This trend is not continuing with the high saline (> 26 mass% NaCl_{eq.}) inclusions which do not significantly exceed the metal contents of the medium saline inclusions in their average Sn and W concentrations.

The Sn and W contents of the granite brine inclusions show a different behavior with increasing salinity (Figure 33). Tin is clearly correlating with the salinity which can be especially observed in the PL and SHX1 brine inclusions. Tungsten, however, correlates only in sample SHX1 with the salinity and shows a non-systematic pattern in the other sample types.

A systematic dependence of the W concentrations with increasing salinity can be observed for the fluid inclusions from the Grummetstock hydrothermal quartz (Figure 34). Tin shows an unsystematic distribution with values of ~30 µg/g that were found in medium saline inclusions, as well as in high saline inclusions. Only the brine FIA with > 1000 µg/g demonstrates a rising Sn content that might imply a dependence of Sn on the salinity. However, W is by two orders of magnitude lower concentrated than Sn in the case of the Grummetstock location. There is no clear indication for a possible saturation of Sn in the Grummetstock fluids, as observed in Figure 32 for the Zinnwald deposit, but at least W seems to have an upper limit around 10 µg/g that can be reached by the ~20 mass% NaCl_{eq.} fluids and does not get exceeded significantly by the higher saline brines.

The trapped fluids in the hydrothermal Zinnwald quartz crystal may represent two evolutionary histories of the mineralizing magmatic fluids. As shown in Figure 32, the Sn and W concentration values basically depend on the overall salinity of the fluids with the highest values that can be found in the most saline fluids. Figure 35 shows the sum of the major cations in the fluids measured by LA-ICP-MS plotted versus the associated Sn concentrations. Applying an arrangement of the inclusions into four groups allows further interpretations for the fluid evolution: 1) brine inclusions from the base granite (Schellerhau granite), 2) primary liquid-vapor inclusions from the hydrothermal quartz crystal (ZinQ), 3) brine inclusions from ZinQ and 4) secondary and pseudosecondary two-phase inclusions from ZinQ. The large spread of the granite brine inclusions (blue squares) is related to the selection of individual inclusions that could not be summarized as one fluid inclusion assemblage with identical chemical compositions, as it was the case for the inclusions from the hydrothermal quartz. The brine inclusions from the hydrothermal quartz represent the FIA P1 and P2 (red squares)

and the red triangles represent primary L+V inclusions from FIA P3 with large discrepancies in the major cation contents but with comparatively small variations in Sn concentrations. The fourth group of inclusions summarizes all secondary L+V inclusions from the hydrothermal quartz (green triangles). These inclusions plot in a field with a narrow salinity range but simultaneously having large variations in Sn.

The observed distributions of Sn and major cations with respect to the fluid inclusion type, leads to the following two possible explanations.

1) An intermediate dense, intermediate saline fluid was exsolved from the crystallizing melt and ascended into the upper most parts of the granite cupola where it migrated through faults and fractures and formed the mineralized quartz veins. On its way to the top, the supercritical fluid reacted with the lithian annite granite and leached the metals out of the micas as proposed by Johan et al. 2012, resulting in a metasomatic transition of the lithian annite into trace metal depleted zinnwaldite. This metal carrying single phase fluid was trapped in the growing miarolitic quartz crystal (representative for the “Flöz” mineralization type) and is represented by the primary and pseudosecondary L+V fluid inclusions (triangle symbols in Figure 35). A constant flux of the magmatic fluid resulted in a decreasing metal content with ongoing flux, since the lithian annites lost the biggest trace metal contingent with the first pulses of fluid flow. The younger fluids could not be enriched to the same amount in Sn than the first fluids, resulting in the downwards trend of the hydrothermal secondary inclusions in Figure 35. Subsequently, the single phase fluid underwent phase separation resulting in a high saline brine that was trapped in the L+V+S inclusions (red squares) and a vapor phase that was probably not trapped in the here investigated quartz crystal, since none of the measured low saline inclusions had identical homogenization temperatures like the two brine assemblages, which would be the proof for coexisting brine and vapor phases. A sudden pressure drop like it appears when changing the pressure environment from lithostatic to hydrostatic could have initiated boiling. The secondary low saline inclusions with $\text{NaCl}_{\text{eq.}} < 1$ mass% could give a hint for the interaction of the magmatic derived fluid with meteoric waters, which would support the theory of a change to hydrostatic pressure conditions.

2) A second explanation for the observed Sn distributions in Figure 35 can be based on a continuous depletion from the magmatic stage towards the secondary inclusions in the hydrothermal quartz. A magmatic high saline fluid was exsolved from the highly fractionated melt that was extremely enriched in volatiles, alkalis, incompatible elements and Sn. The supercritical fluid was trapped in the granite quartz and formed the observed brine inclusions

with the daughter minerals precipitating from the fluid by cooling. The rarity of those brine inclusions in the granite quartz leads to the assumption that the largest fractions of the fluid migrated into the cupola part of the pluton and initiated the mineralization in veins and metasomatic greisen zones. The brine inclusions of the hydrothermal quartz may represent the early pulses of this magmatic fluid that was trapped in the hydrothermal growing quartz, still highly enriched in alkalis and metals. With ongoing precipitation of ore minerals like cassiterite and wolframite and other late stage minerals, the solute concentration in the fluid decreased continuously which can be observed in Figure 29 for Sn, W, Cs, Fe and Pb. The secondary two-phase inclusions define the youngest fluids in the quartz crystal and are the most depleted. In this case the late fluids would not be saturated with respect to cassiterite and wolframite. However, the continuous depletion from the magmatic stage towards the hydrothermal stage is not in agreement with the partitioning of Cu determined in the fluid inclusions. Copper is more enriched in the two-phase inclusions than in the brine inclusions (Figure 30), which accounts for the brine inclusions to have originated from boiling, since Cu tends to separate into the vapor phase and the brines are usually getting Cu-poor as it is observed in the analyzed inclusions.

An alternative is that fluids remain saturated with respect to cassiterite and wolframite but that temperature decreases from early to late fluids. This would be in agreement with the observed fluid inclusion homogenization temperatures $T_h(\text{total})$. The granite quartz inclusions have the highest $T_h(\text{total})$ at $\sim 450^\circ\text{C}$, followed by the L+V inclusions with $400 - 380^\circ\text{C}$ and the two brine inclusions assemblages in the hydrothermal quartz (370°C and 290°C). This decrease in temperature from the granite inclusions towards the hydrothermal brines could be another argument for the theory of the fluid evolution starting with the hot high saline magmatic fluid, that was exsolved from the cooling melt and trapped in the granite quartz, and the following continuous depletion in alkalis and trace elements resulting in the intermediate saline fluids, that migrated into upper parts of the cupola where they initiated mineralization. Later boiling of those fluids resulted in the formation of a new brine phase, represented by the brine inclusions in the hydrothermal quartz.

What contradicts the continuous depletion from the magmatic stage towards the hydrothermal stage is the partitioning of Cu in the fluid inclusions. Copper is stronger enriched in the two-phase inclusions than in the brine inclusions (Figure 30), which accounts for the brine inclusions to have originated from boiling, since Cu tends to separate into the vapor phase and the brines are usually getting Cu poor like it is observed in the here analyzed inclusions.

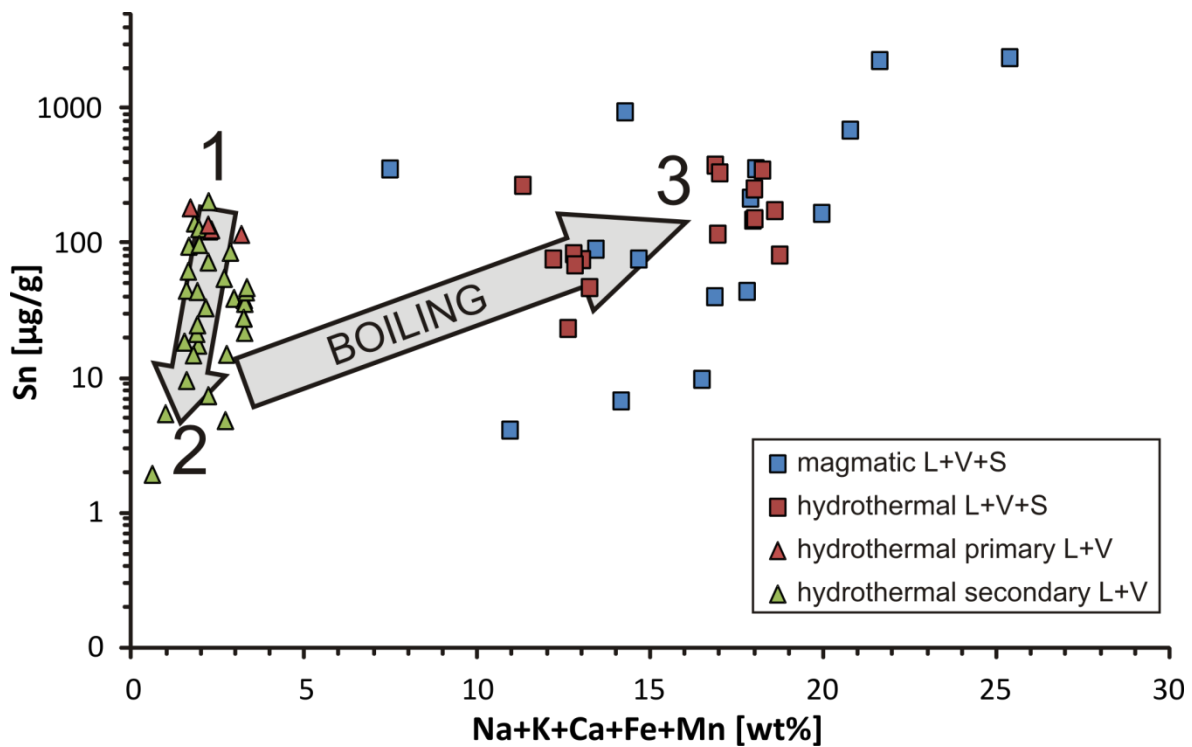


Figure 35: Sn concentrations of the different fluid inclusion types from the hydrothermal Zinnwald quartz and the magmatic Schellerhau granite quartz plotted against the sum of all major cations in the fluids, measured by LA-ICP-MS. Numbers represent the chronological order of fluid inclusion trapping, starting with 1) the primary L+V inclusions and 2) the following depletion of the fluid in Sn and salinity in the secondary inclusions until 3) a phase separation by boiling, causing the re-enrichment of the cations with a high $D_{\text{liquid/vapor}}$ in the L+V+S inclusions.

Our data supply additional insights on the process of metal leaching from an enriched melt. Brine inclusions from the Schellerhau granite quartz show the highest Sn and W contents of all investigated inclusions and a positive correlation between the salinity and metal content could be documented for several locations (Figure 32 - Figure 34). This fact would further support the findings of Audétat et al. 2000b, who also found Sn-rich brine inclusions in the Mole granite. The hydrothermal quartz of the Zinnwald mineralized zone yields further information about the discussed subject. Inclusions of lower salinity have got nearly identical Sn contents as the medium saline inclusions from the Mole granite, which could point at possible analogies between the Zinnwald and Mole granite in terms of metal mobilization and fluid evolution. The hydrothermal brine inclusions show, again, higher Sn-W concentrations than the medium saline inclusions. The highest Sn and W concentrations have been recorded in the granite quartz brine inclusions, suggesting that the maximum metal concentrations exist in the magmatic fluids and a later enrichment after the extraction from the melt does not take place. A clear dependency of the ore forming metals from the Cl content of the fluid is thereby unambiguous, suggesting that Sn was transported as a chlorine complex and thus existed in the divalent state as Sn^{2+} . Since the F content of the inclusions was not determined, we cannot shed further light on the role of F as a ligand for Sn and W, but due to the clear correlation between Sn and the salinity, we can exclude that the metals were *exclusively* transported as fluoride complexes as suggested by Johan et al. 2012.

The correlation between Sn and W is variously strongly pronounced in the respective fluid inclusion types (Figure 31). The hydrothermal L+V inclusions show a clear correlation of Sn and W, whereas it is less obvious for the hydrothermal L+V+S inclusions. A good correlation can be found for the magmatic brine inclusions of the Porth Ledden granite and the hydrothermal brine inclusions of the Grummetstock quartz. The Schellerhau brine inclusions show a larger spread in the Sn vs. W plot, but the lack of data and the difficult sample preparation (decrepitations during microthermometry) do not allow us to make a solid statement about relationships between the Sn and W contents. It is noteworthy that the L+V inclusions of the Grummetstock hydrothermal quartz seem to have an upper limit for their W content at around 10 $\mu\text{g/g}$, which does not get exceeded either by medium saline inclusions with very low Sn contents nor by high saline brine inclusions with up to 1000 $\mu\text{g/g}$ Sn. The good correlation of Sn with W in the other fluid types can be interpreted as the result of a leaching process by an evolving fluid phase that was able to transport both metals, but with different efficiencies, since W is by one order of magnitude lower concentrated in the majority of the inclusions. On the other hand, Sn could have been stronger enriched in the

melt than W, which would also lead to higher Sn contents in the fluid phase. The apparent limit for W in the hydrothermal fluids of the Grummetstock deposit could be a hint on equilibrium between the fluid phase and the W ore mineral wolframite, which was probably precipitating during the time span of quartz growth and fluid trapping, thus buffering the W concentration in the fluid to a maximum of 10 µg/g.

The maximum concentration of Sn in the fluids from both sample locations from the Erzgebirge is similar at ~ 1100 µg/g Sn. The only difference is that those maximum values were reached in the hydrothermal quartz at Grummetstock and in the magmatic quartz in the ATC (Schellerhau granite). Nevertheless, it is possible that some of the earliest exsolved fluids were also trapped in the hydrothermal quartz in the Grummetstock. The observed maximum concentration is probably controlled by the $D_{Sn}^{Fluid/Melt}$ of 2- 4 in peraluminous systems. Thomas et al. 2005 suggest that the initial Sn concentration in the Zinnwald granitic melt was 800 µg/g, as recorded in the earliest entrapped melt inclusions from the Zinnwald granite quartz. But the authors also assume that a large portion of the primary Sn in the melt was extracted into fluids before the MI entrapment was finished because the extraction of Sn started with the onset of volatile saturation and ended with the final solidification of magmas. To generate a concentration of 1100 µg/g Sn in the fluid with a $D_{Sn}^{Fluid/Melt}$ of 2 – 4, the observed 800 µg/g in the MI are too low, at a typical H₂O solubility of 5 wt% in the melt. Unfortunately there is no data for MI from the Gottesberg and its related deposits, but the Sn concentrations in the fluid might suggest that both locations were enriched in Sn to the same extent. Melt inclusions from other peraluminous settings were measured with up to 7000 µg/g Sn (Webster et al. 2004), which demonstrates on the one hand the ineffective leaching capability of aqueous fluids for Sn, but on the other hand a Sn concentration that is high enough for the formation of the here observed Sn-enriched fluids.

Our study further confirms the high degree of fractionation by the measured chemistry of the hydrothermal quartz which has got high Al, Li and Ge contents as well as low Ti contents (Figure 37). The trace element contingent of the quartz crystal indicates that it has precipitated from a strongly fractionated source melt or fluid. The extraordinary high Sn content may also give a hint on the metal load of this source, but the observed concentration of 24 µg/g seems to be extremely high in relation to the measured concentrations in fluid inclusions, which ranges from 378 – 30 µg/g in the brine and primary L+V inclusions, respectively, and under the point of view that the quartz lattice generally does not favor an incorporation of large amounts of trace elements. Nevertheless the independent factors quartz and fluid chemistry

definitely allow us to conclude that the parental fluid must have been incorporated into the mineralization process and was capable of transporting the metals Sn and W into the upper parts of the Zinnwald pluton. The fluid and quartz chemistry also yield information about the pluton internal fractionation processes, but it is impossible to contribute to the above described discussion about the origin of metals. When considering the granite quartz fluid inclusions, we can investigate an aqueous fluid that must have emanated from one of highest fractionated melts in the system at near solidus conditions. The parental melt was influenced by various geochemical processes like wall rock assimilation, crystal fractionation, differentiation, fluid-rock interaction and metasomatic reactions. By sampling the exsolved fluid phase, we are looking at the final product of a long process chain where it is getting ambitious to make a detailed statement about the raw material that was used at the beginning of this production chain.

5.5.1.3 Comparison of Zinnwald fluid inclusion literature data

Fluid inclusions from the Zinnwald Sn-W deposit have been measured in earlier studies by Heinrich et al. 1999 and Graupner et al. 2005. Both studies focused on the analyses of vapor-rich low-salinity inclusions hosted in quartz crystals from the Zinnwald quartz veins. Graupner et al. 2005 included not only primary inclusions in their measurements but also secondary inclusions that are assumed to be magmatic fluids diluted by meteoric waters. These authors described a first evolutionary trend of the Zinnwald mineralizing fluids with a decrease in salinity from high temperature fluid inclusion to low temperature secondary inclusions going along with a decrease in solutes like Fe, Sn, W, Pb, As, Rb and Sr. This decrease is interpreted to reflect a dilution of the magmatic fluids with external fluids. The observed homogenization temperatures of 390 – 350°C of the primary two-phase inclusions agree well with our $T_h(LV \rightarrow L)$ values of 400 – 380°C for the same type of inclusions, which can be also observed for the salinities between 5 – 10 mass% NaCl_{eq}. For the comparison of the determined trace, minor and major element contents in the three studies, we found 11 elements that were measured in at least two of the three studies (Li, Na, K, Fe, As, Rb, Sr, Sn, W, Mn, Pb). Figure 35 shows the published average concentration values from Heinrich et al. 1999 and Graupner et al. 2005 data sets in comparison with four different fluid inclusion types from our sample. The columns ‘Heinrich L+V’, ‘Graupner primary L+V’ and ‘Albrecht primary L+V’ represent similar fluid inclusion types that allow a direct comparison with each other. The concentrations of some elements like Na, Rb, Sr, Sn and W are similar for the three independent studies (see also Table 15). Other element concentrations like Pb, Fe, As and Mn have higher discrepancies, with our values always being the lowest, which is particularly

Table 15: Concentration values of fluid inclusions from Zinnwald mineralized quartz veins from Heinrich et al. (1999), Graupner et al. (2005) and this study. All values in µg/g.

	Heinrich	Graupner		Albrecht			
	L+V	primary L+V	secondary L+V	brine 1	brine 2	primary L+V	secondary L+V
Li		570	355	350	171	247	196
Na	20,000	23,900	4,500	132,139	69,586	21,041	2,904
K	6,000	6,800	841		34,542		
Fe	7,000	3,350	238	16,764	8,112	622	164
As	800	1,300	309	825	349	254	60
Rb	800	1,700	160	8,765	3,874	795	31
Sr	2	5	1	3	1	2	0.3
Sn		130		225	62	140	0.6
W	50	30	12	85	60	33	2
Mn	1,000	690		22,564	15,360	231	117
Pb	5,000	950	3	14,849	10,603	133	6

striking for Pb with a range from 5000 $\mu\text{g/g}$ (Heinrich et al. 1999) to 133 $\mu\text{g/g}$ (this study) or Fe (7000 $\mu\text{g/g}$ Heinrich; 622 $\mu\text{g/g}$ this study). The variations might be related to different sample localities since the three studies used individual quartz samples that might have trapped solutions of differing chemistries due to spatial fluctuations of the fluids. It is also worth to mention that three different combinations of laser types and mass spectrometers have been used in the three studies. Nevertheless, a very good agreement could be found for the Sn and W concentrations between all publications.

Especially Sn of this study is in very close agreement to the values reported by Graupner et al. 2005 (140 and 130 $\mu\text{g/g}$). Tungsten was measured with 33 $\mu\text{g/g}$ (this study), 50 $\mu\text{g/g}$ (Heinrich et al. 1999) and 60 $\mu\text{g/g}$ (Graupner et al. 2005) and is in agreement within a factor of 2. The similar Sn and W concentrations is a solid verification for the theory that the high temperature, intermediate saline fluids were responsible for the metal transport into the mineralized veins of the Zinnwald Sn-W deposit.

Another comparison can be drawn for the secondary low saline fluid inclusions that have been measured by Graupner et al. 2005 and in our study. Except for Pb, it seems that concentration values for all elements are higher in the study of Graupner et al. 2005 than in our study. This might be based on the fact that the secondary inclusions from Graupner et al. 2005 are of higher salinity than ours, as reflected by the Na concentrations in Table 15 (4500 $\mu\text{g/g}$ vs. 2904 $\mu\text{g/g}$). Regardless of these small differences, both data sets show the same dilution trend from primary inclusions towards secondary inclusions, when considering the chemical composition of the inclusions only. Graupner et al. 2005 also describes a decrease in $T_h(\text{LV} \rightarrow \text{L})$ from $\sim 400^\circ\text{C}$ to $< 300^\circ\text{C}$ between primary and secondary inclusions, resulting in the theory that cool meteoric waters were mixed with the magmatic derived fluids. This decreasing trend in T_h cannot be observed in our sample, where homogenization occurs in a more or less stable range between $380 - 400^\circ\text{C}$. It might be possible, that the low saline secondary fluids in our quartz crystal were not influenced by intruding meteoric waters and that the dilution trend is solely related to the precipitation of ore minerals from the fluid. Tin and W are clearly depleted with respect to the initial concentration in the primary inclusions. While Sn could be found above the LOD in our study in only one secondary inclusion with 0.6 $\mu\text{g/g}$, it was constantly below the LOD of Graupner et al. Tungsten, however, was detected with 2 $\mu\text{g/g}$ here and 12 $\mu\text{g/g}$ by Graupner et al., where the dilution seems to be much less relevant for W than for the other elements.

Graupner et al. 2005 measured also two brine inclusions, giving the highest concentration values for all elements in their study. Analogue to our brine inclusion data that is based on two FIA, the brines are rich in Fe (14 wt% Graupner; 16 – 8 wt% this study), Na (9 wt% Graupner; 13 – 6 wt% this study) and K (1.7 wt% Graupner; 3,4 wt% this study). The extreme high values for Mn (2.2 – 1.5 wt%) and Pb (1.4 – 1.0 wt%) in our brine inclusions, cannot be reproduced by Graupners data (Mn: 2200 µg/g; Pb: 4300 µg/g). The maximum Sn (550 µg/g) and W (128 µg/g) concentrations of the brine inclusion from Graupner et al. 2005 are nearly identical to the maximum values in our brine FIA P1 and P2 (Sn: 378 µg/g; W: 154 µg/g).

From the here presented concentration values of distinct fluid inclusion types, we can draw the conclusion that two types of aqueous fluids contributed to the transport of the metals into the mineralized zones. A supercritical fluid of intermediate salinity and density and a high saline brine, probably originated from a boiling process, played both an important role in the formation of the Sn-W mineralization of the Zinnwald deposit.

Furthermore, our results confirm the nearly constant Li concentrations in all types of inclusions. Only small variations could be detected between the brine, primary and secondary inclusions presented in Figure 30. Two explanations can be proposed: As it can be also seen from the Zinnwald quartz chemistry, where Li is enriched with 23.3 µg/g, the granitic melt was highly fractionated and therefore enriched in Li which allows a constant feed of Li into the fluids. On the other hand, the permanent fluid – rock interaction with the already Li-enriched Zinnwald granites yields a second possible Li source for the fluids.

Webster et al. 2004 suggest that a high Li content in the fluid phase played a role in the precipitation of hydrothermal Li-micas in the greisen bodies, even though the Li abundances were primary dominated by crystal fractionation during differentiation. The distribution coefficients for Li (D_{Li}) between F-enriched melts and aqueous fluids were determined with 2 - 13 at 500 – 2000 bars (Webster et al. 1989), suggesting that the fluids exsolving from the Zinnwald granitic melt (with 0.15 wt% Li; Webster et al. 2004) should have dissolved < 900 µg/g Li, which is in good agreement with our fluid inclusion data and other studies of fluids in granite related Sn-W deposits, like the Mole Granite, Australia (Audétat et al. 2000b). Webster also suggests that these Li values are not high enough to generate the large amounts of Li-micas and that similar granitic melts with higher Li contents (0.68 wt% Li) could be able to supply magmatic-hydrothermal fluids with 4 wt% Li, considering the maximum D_{Li} value of 13. None of our data, neither the brine inclusions in the granite quartz, nor the different inclusions types in the hydrothermal quartz, do approach those high Li values to

some extent, leading to the conclusion that the Li-micas have not precipitated from the fluid phase and supporting Webster's theory of post-magmatic, subsolidus reactions of fluids with hot granitic rocks that were the key process for the transport of Li in the Zinnwald greisens.

5.5.1.4 Comparison: Erzgebirge vs. Cornwall

Brine inclusions from two different localities have been measured to investigate possible differences in the fluid chemistry and their ability to transport metals. We put our focus on high saline brine inclusions in the magmatic quartz of the Schellerhau granite, which can be seen as an equivalent to the Zinnwald granite, and the Porth Ledden tourmaline granite from the Land's End region in Cornwall, UK. Both granites are associated with Sn-W mineralizations and appear to be the magmatic precursors of the hydrothermal fluids that formed the mineralized zones (Müller et al. 2006b). The Cornwall Sn-specialized granites are basically known to be rich in B while the Zinnwald granite is a representative of the F-rich, B- and P-poor intrusive complexes of the eastern Erzgebirge. Primary brine inclusions in magmatic quartz are suspected to have trapped a fluid phase which emanated from the highly fractionated melt, rich in volatiles and incompatible elements, including metals like Sn and W. Drivenes et al. 2016 published a two-stage model of crystallization for the Land's End granite, which matches with earlier published two-stage models for granites of the Erzgebirge, where the magma exsolved an aqueous fluid at the emplacement level of 5-9 km depth after getting oversaturated in water due to its ascent. The aqueous fluid coexisted with the crystal-melt mush and the process of fluid exsolution was repeated several times during the ascent of further melt fractions into the emplacement level (Drivenes et al. 2016). Therefore, a complex fluid inclusion trapping history can be observed in the granite quartz crystals with inclusions of different salinities and chemistries. The highest salinities were provided by the earliest fluids whereas later fluid pulses became progressively more primitive in chemistry and depleted in alkalis and fluid mobile elements.

In our study, we analyzed the high saline inclusions in magmatic quartz crystals from both localities to investigate a possible pre-enrichment of metals in the earliest exsolved fluids of a Sn-specialized granite system. Figure 27 reveals chemical differences between both locations in terms of major, minor and trace element composition. Since we have measured individual inclusions that cannot be summarized as a fluid inclusion assemblage, Figure 27 shows the range between the maximum and minimum concentration values of all analyzed inclusions. Average values would not represent the composition of the earliest exsolved fluid phase in the granitic pluton, but following the assumption that the earliest fluids also have got the highest salinities and solute loads the maximum values might give a hint about the ability of the fluids to carry different types of cations. The Schellerhau brine inclusions reach significantly higher

maximum concentrations for the majority of elements, except Ca, Cu, Sb and Sr. Iron, K, Al and Na can cross the 10 wt% threshold in the Schellerhau brines, but only Na was found constantly in the wt% range and shows the smallest spread of all major cations. Especially the very high Fe and Al values raise the question of a possible accidental entrapment of daughter minerals like small fragments of mica crystals. The wide range of five orders of magnitude for Al supports this theory. An iron, K and Na dominated magmatic fluid however is not unrealistic and the Porth Ledden brines reflect this major cation composition, where Al does not play an important role anymore. Cesium can also be found in the wt% range in the Schellerhau brines, but do not pass the 1 wt% line in the Porth Ledden brines. Since Cs is a fractionation sensitive and highly incompatible element, the discrepancy between both locations might imply that the Porth Ledden brines exsolved from a less fractionated melt than the Schellerhau brines. Further conspicuous differences in the maximum concentrations were detected in the minor and trace element range. Arsenic, Pb, Sn, W and Li can be stronger concentrated in the Schellerhau brines, even including values of one order of magnitude higher for Sn and W than in the Porth Ledden brines. Boron, As, Zn and Pb were found in the 10^3 $\mu\text{g/g}$ range in both locations, whereas Sn and W do not exceed the 10^2 $\mu\text{g/g}$ range in Porth Ledden but can be found in the 10^3 $\mu\text{g/g}$ range in the Schellerhau inclusions. On the contrary, Cu and Sr maximum values do exceed 1000 $\mu\text{g/g}$ in the Porth Ledden brines but not in the Schellerhau fluids. The distribution of metals, especially Sn, W and Cu, is in good accordance with the specific granite associated mineralization of each locality. The St. Just mining district in Cornwall is well known for its Sn-Cu deposits and the elevated Cu values in the magmatic fluids might already demonstrate that Cu was highly mobile and enriched in the earliest magmatic fluids. The lower Sn and W values in the Porth Ledden brines can be related to the lower F content in those fluids. Fluorine is meant to be one of the major ligands for Sn (and W) in the Erzgebirge fluids and the transport and complexation of both metals is more effective with F than with Cl. On the other hand, the pre-concentration in the granitic source rocks also controls the magmatic enrichment of Sn and W and therefore in the magmatic fluids. The trace metal content in the fluid is therefore a fingerprint of the source rock chemistry and the extent of fractionation in the granitic melt. A stronger enrichment in the source rock would result in a stronger enrichment in the magmatic fluid, given that the magmatic fractionation is at an equal level. Nevertheless, all observed and here described metal concentrations are still in the range of a mineralization initiating fluid and give an idea about how the metals were transported from the melt to the mineralized zones, namely by a high saline magmatic brine. We analyzed a limited number of brine inclusions due to the

difficult microthermometric measurements and the general lack of brine inclusions especially in the Schellerhau granite quartz. The here presented results give us information from a short snapshot of the long lasting fluid evolution in the granitic systems and it must be kept in mind that our samples possibly did not trap the very oldest magmatic fluids with the highest salinities and metal loads, but nevertheless, the here investigated brine inclusions belong to one of the oldest magmatic fluid pulses and give at least a close approximation to the composition of the initially exsolved fluids.

5.5.2 Quartz chemistry

The here presented quartz trace element data set can be considered as a fitting completion of the data set from Breiter et al. 2012, that represents the quartz chemistry of the underlying base granites of the Zinnwald Sn-W deposit. The insight into the chemistry of the mineralization hosting hydrothermal stage, with gangue quartz as the main matrix mineral, was missing to get a complete picture of the melt differentiation processes in the cupola part of this pluton from the eastern Erzgebirge. The trace elements in quartz that can be used to make statements about the magma differentiation processes like Al, Li, Ti and Ge have been measured in both studies and allow a comparative look into both data sets.

The classification of the associated deposit type by means of the Al and Ti content in quartz after Rusk 2012 reveals the hydrothermal quartz from Zinnwald to have an identical chemical composition like quartz from orogenic Au deposits (Figure 36). The quartz from orogenic Au deposits is known to be the product of metamorphic fluids. Therefore it seems to be surprising that our data points fit into this area field and not into the quartz from porphyry type deposits, which also have a magmatic origin like the Sn-W deposits of the Erzgebirge. The shift to lower Ti values $< 2 \mu\text{g/g}$ separates the Zinnwald hydrothermal quartz from the porphyry type quartz, whereas the Al content of both types are in agreement with each other.

Figure 37a shows the Ti vs. Ge plot with the hydrothermal quartz being by far the most depleted in Ti of all quartz types. The biotite granite and Zinnwald granite form the base below the mineralized zone with the biotite granite as the older and less differentiated granite type. This genetic feature is well reflected in the quartz chemistry, as it can be observed in the Ge vs. Ti plot where the biotite granite separates from the Zinnwald granite especially by higher Ti concentrations of 15 – 30 $\mu\text{g/g}$. The Zinnwald granite plots mainly in the range of 5 – 10 $\mu\text{g/g}$ and shows an increase in Ge (1 – 3 $\mu\text{g/g}$) towards lower Ti values, whereas the Ge content in the biotite granite samples is more or less stable around 1 $\mu\text{g/g}$. The hydrothermal quartz follows this differentiation trend of its parental granites and is even stronger depleted in Ti (1.3 $\mu\text{g/g}$) than the Zinnwald granite. A large proportion of all measured spots are also stronger enriched in Ge (1.7 – 2.8 $\mu\text{g/g}$) than the granite quartz crystals. Compared to the literature data that propose Ge to stay $< 3 \mu\text{g/g}$ even in the strongest fractionated granites, our values reproduce well the behavior of Ge in late residual melts and support the thesis that especially the latest and extremely high fractionated melts yield elevated Ge values that differ significantly from those of low to moderately high fractionated melts.

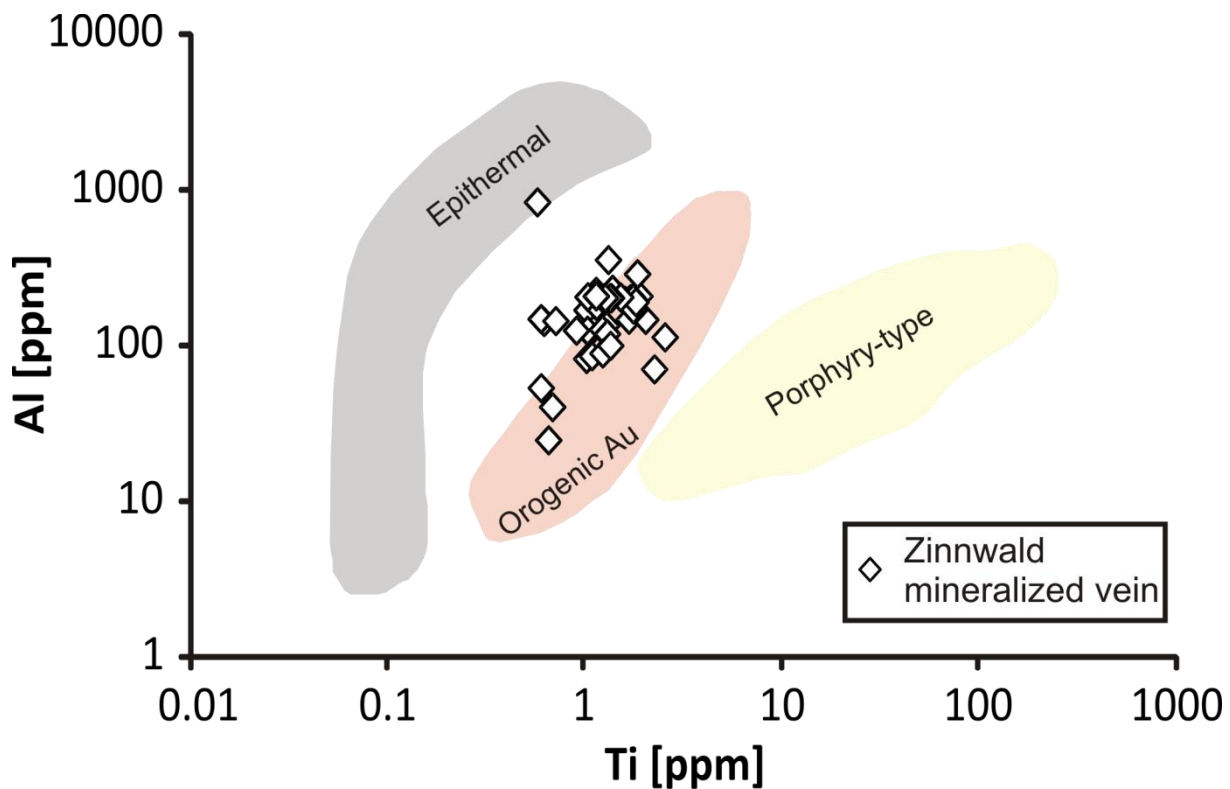


Figure 36: Titanium versus aluminium concentrations in hydrothermal quartz from different geological settings. The fields of epithermal, orogenic Au and porphyry-type deposits have been adapted from Götze and Möckel (2012). The analyzed Zinnwald hydrothermal quartz falls into the range of orogenic Au vein quartz and is significantly depleted in Ti compared to porphyry-type hydrothermal quartz, while the Al values are in good agreement with both porphyry-type and orogenic Au deposits.

Another important chemical feature in quartz is the incorporation of Al and its charge balancing cations Li, Na, K, and Rb. The ratio of Al/Ti as an indicator of the degree of melts fractionation and provides a good basis for the description of other trace elements in quartz. In Figure 37b, the evolution trend from the biotite granite towards the hydrothermal stage is visualized by a plot of the Al/Ti vs. Ge/Ti ratios. The Ge/Ti ratio rises with increasing Al/Ti values and the Zinnwald granite clearly sets off from the biotite granite. The positive correlation trend between the Ge/Ti and Al/Ti is continued in the hydrothermal quartz. Here, the Ge/Ti reaches values > 1 and appears to be constant compared to the Al/Ti values that spread over a wide range from 50 – 300. Nevertheless, both ratios are significantly higher in the hydrothermal quartz than in the granite quartz which indicates an extremely high fractionated source of the hydrothermal quartz. The large variability of Al/Ti is a typical feature of quartz that formed from a late residual melt and is mainly produced by varying Al concentrations, rather than by the smaller variations in Ti content. Al/Ti ratios of > 100 have been published by Breiter et al. 2013 for high fractionated granites of the Erzgebirge, that are in good agreement with the here presented data.

Compared to the hydrothermal quartz from a stockwork vein from the center of the Bingham porphyry Cu-Au-Mo deposit, Utah (Landtwing et al. 2005), the Zinnwald hydrothermal quartz shows Ti concentrations by two orders of magnitude lower and in average a significantly higher Ge content. The Bingham vein quartz plots in the Ge/Ti vs. Al/Ti diagram below all measured quartz crystals of the Zinnwald pluton. This might imply that the Bingham Cu-Au-Mo porphyry deposit developed from a less fractionated pluton than the Zinnwald Sn-W-Li deposit.

The low Rb and Sr values in the ppb range (Figure 37c) appear to be controversial and might suggest that the quartz formed from a less fractionated melt, because magmatic quartz from less fractionated granites have been measured with $<1 \mu\text{g/g}$ Rb, whereas values up to $12 \mu\text{g/g}$ have been found in the higher fractionated granites (Breiter et al. 2013). Obviously, this cannot be the reason for the very low Rb contents in the Zinnwald hydrothermal quartz. However, since quartz crystallization occurs late in the Zinnwald pluton the earlier crystallized micas and feldspars likely incorporated most of the initially available Rb, which may explain the low Rb and Sr contents in quartz. The late stage formation from an already Rb/Sr-depleted source and the fact that Rb and Sr tend to partition into the liquid phase, which is important in the H₂O-fluid dominated regime, are the most likely reasons for the low Rb and Sr values in the hydrothermal quartz assuming that no re-equilibration between quartz and biotite and alkalifeldspar occurs during the quartz growth.

The lithium contents of $23.3 \mu\text{g/g}$ are relatively high compared to the average of the existing data, which is $<10 \mu\text{g/g}$. Since Li is known to increase with proceeding magma differentiation and the Zinnwald granite belongs to the group of highly developed granites from the eastern Erzgebirge, it seems likely that the Li contents in the hydrothermal quartz are related to the close relationship of the quartz to the Zinnwald granite.

Tin was found at concentrations of $0.22 \mu\text{g/g}$ in 13 host signal measurements during fluid inclusion analyses. In the literature, Sn is described not to exceed $10 \mu\text{g/g}$ and in the Zinnwald granite it was found with $0.15 \mu\text{g/g}$ (Rusk 2012). Thus, the here presented values do not seem to point on the specific conditions in the Sn-W mineralized zone, but at least the existence of Sn in the quartz generating (and mineralizing) fluids has been further confirmed.

The relative high concentrations of some elements like Al, Li, Sb, Pb and Be on the outer most data point #1 (Figure 28) do not fit to the opposing rim and seem to be unrealistically high in comparison to the average values on the profile. For example, Al on spot No.1

increases to 858 $\mu\text{g/g}$ from the adjacent 54 $\mu\text{g/g}$ on spot #2. Identical increases can be observed for Li (from 8.4 $\mu\text{g/g}$ to 46.2 $\mu\text{g/g}$), Rb (from 0.015 $\mu\text{g/g}$ to 8.8 $\mu\text{g/g}$) or Zn (from 0.5 $\mu\text{g/g}$ to 2.5 $\mu\text{g/g}$). It is unlikely that an internal zoning of the quartz crystal is the reason for those differing values. A ~ 50 μm thick cloudy shade along the crystal rim gets visible under the microscope, which was hit by the ablation spot No.1. This secondary overgrowth can be considered to be the reason for the enriched trace values and might consist of tiny mineral inclusions that stitched on the quartz rim during cooling.

The correlation matrix of all measured elements (Table 14) reveals some strong relationships between Al, as the most present trace element in quartz, and a whole range of different elements. The strong correlation of Al with Li^+ , Na^+ , K^+ , Rb^+ can be considered as an effect of the interstitial incorporation of those monovalent ions for charge compensation of the $[\text{AlO}_4]^-$ centers. Further strong correlations of Al with Mn^{2+} , Zn^{2+} , Sr^{2+} , Pb^{2+} , As^{3+} , Sb^{3+} , and Bi^{3+} could be proven. As those ions do not act charge-balancing with the $[\text{AlO}_4]^-$ centers, it is more likely that they are hosted in interstitial positions in the crystal lattice and their correlation to Al is based on other reasons. The range of elements that correlate with Al is also common and sometimes highly concentrated in fluid inclusions, including Mn, Zn, Sr, Pb, As and Sb. Therefore, it seems possible that the general availability of those elements in the parental fluid enables their incorporation into quartz and the observed correlations are a direct reflection of the fluid chemistry.

The independency of Ti and Ge from all other elements could be a result of the formation of diamagnetic $[\text{TiO}_4]^0$ and $[\text{GeO}_4]^0$ centers in the quartz lattice (anions). Both ions are known to be able to substitute for Si^{4+} , but as described by Götze 2009 gamma-irradiation of the diamagnetic precursors $[\text{TiO}_4]^0$ and $[\text{GeO}_4]^0$ leads to the transformation into paramagnetic $[\text{TiO}_4/\text{M}^+]$ and $[\text{GeO}_4/\text{M}^+]$ centers with Li^+ and H^+ being the most abundant charge-balancing cations. This irradiation should be ubiquitous in smoky quartz crystals (O'Brien 1955, Cohen 1956), which should establish a correlation of Ti/Ge with Li, but the correlation coefficients of $r = -0.01$ (Ti) and $r = 0.06$ (Ge) confirm the exact opposite and suggest that the paramagnetic centers have not been formed. The temperature dependence of the Ti incorporation into quartz must be considered as a possible reason for the independent behavior of Ti, since Ti is the only ion with proven temperature dependence. The average value of 1.3 $\mu\text{g/g}$ Ti in the hydrothermal quartz is very low compared to magmatic quartz. The lower temperatures in the hydrothermal regime and the smaller amount of available Ti in the melt compared to the magmatic stage are likely reasons for those low Ti concentrations.

Germanium, however, is a compatible ion in the quartz lattice and does not need a high energy supply to get integrated into quartz. The amount of Ge in the quartz is limited by the amount of available Ge in the melt. The concentration values of 2.2 $\mu\text{g/g}$ Ge in the here presented data set and the limitation of ~ 3 $\mu\text{g/g}$ Ge in the literature data, are under primary control of the average crustal concentration values of 1.4 $\mu\text{g/g}$ Ge (Wedepohl 1995).

The absence of Fe in the Zinnwald hydrothermal quartz is typical feature of highly evolved melts. Quartz crystals from less evolved melts have been measured with 100 – 1000 $\mu\text{g/g}$ Fe (Müller et al. 2010), since Fe is one of the few elements that are able to substitute for Si^{4+} in the quartz lattice. Even though it is possible that Fe concentrations < 1 $\mu\text{g/g}$ exist in the Zinnwald hydrothermal quartz but could not be resolved with our analytical setup, it is unambiguous that most of the Fe was consumed in the earlier stages during the evolution process of the Zinnwald pluton.

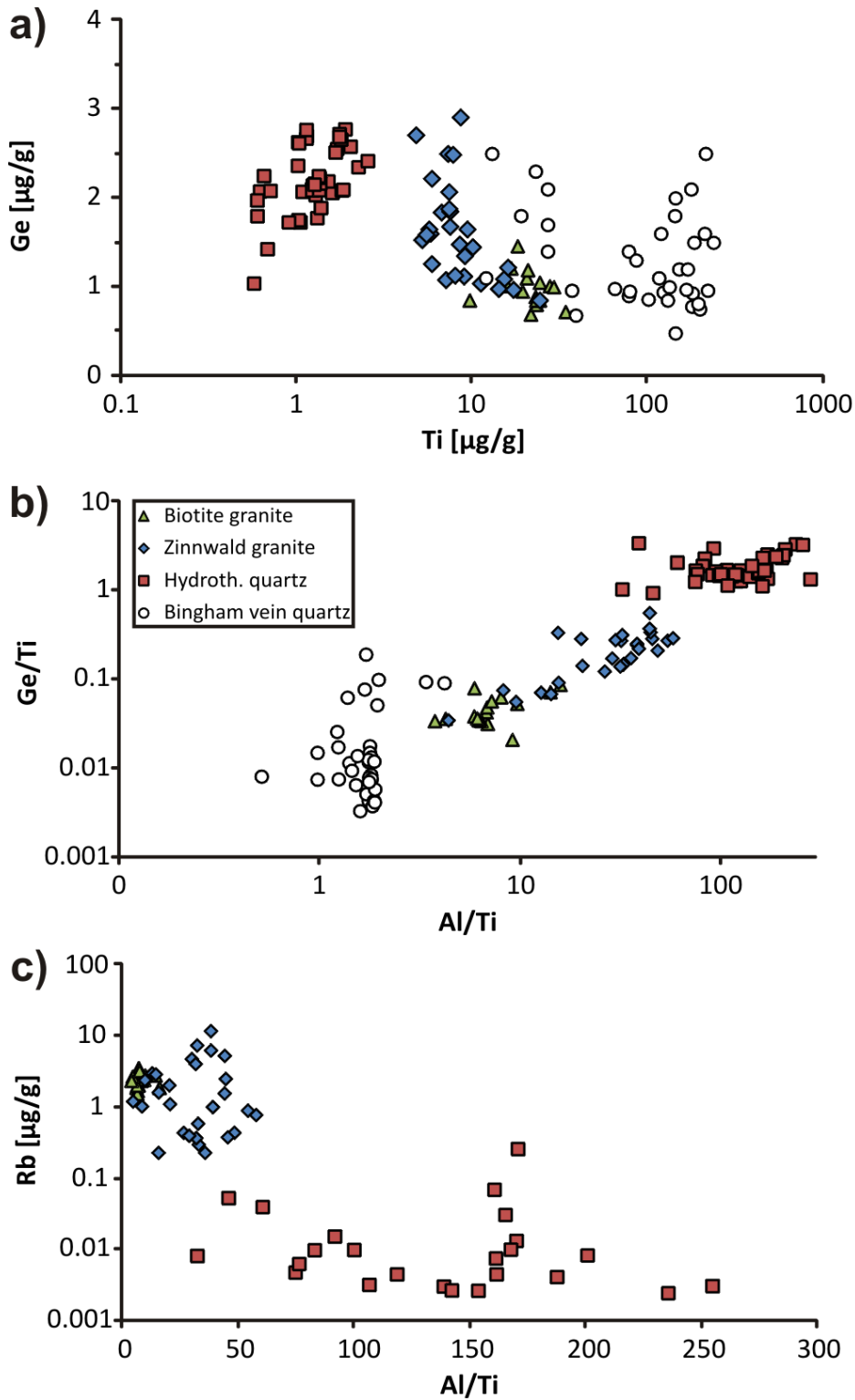


Figure 37: Trace element concentration data of the Zinnwald hydrothermal quartz (red squares), quartz from the Zinnwald granite (blue diamonds) and the biotite granite (green triangles) (both from Breiter et al. 2012). Vein quartz data of the Bingham porphyry Cu-Mo-Au deposit (white circles) is from Landtwing et al. (2005). a) In the Ti vs. Ge diagram, a continuously decrease in Ti from the biotite granite towards the hydrothermal quartz can be observed, while Ge increases with the rising degree of fractionation. b) The ratios of Al/Ti vs. Ge/Ti indicate the genetic trend from low ratios in the biotite granite towards higher ratios in the hydrothermal quartz. The Bingham vein quartz has higher Ti values and suggests a less fractionated source of the mineralization than in the Zinnwald pluton. c) Al/Ti vs. Rb plot is affected by very low Rb values in the hydrothermal quartz, which is contradictory to the high Rb values in quartz from strongly fractionated granites (Breiter 2013).

5.5.2.1 Comparing fluid and quartz chemistry

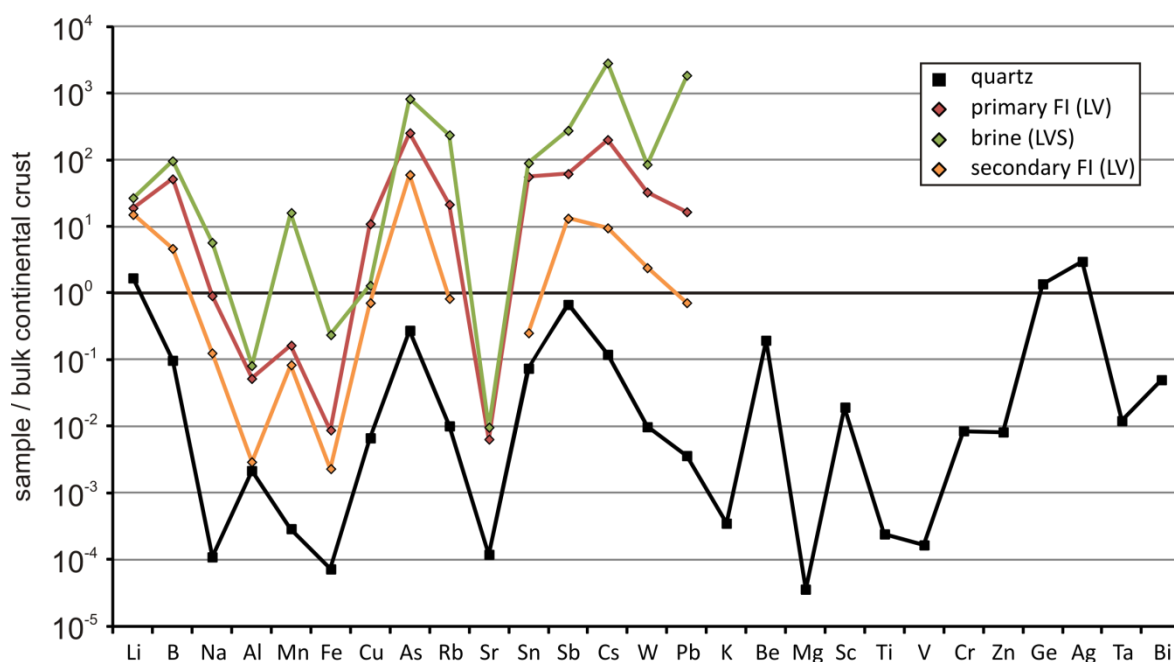


Figure 38: Bulk continental crust normalized concentration values of the hydrothermal Zinnwald quartz and different fluid inclusion types. Concentrations of the bulk continental crust are from Taylor and McLennan 2001.

Due to the small capacity of quartz to incorporate trace elements, it is difficult to search for analogies between the quartz trace element chemistry and the fluid inclusion chemistry. Most elements do not allow a connection and interpretation of their distribution in both phases, but for a small number of the elements that reach noticeable concentrations in quartz it is possible to explain their enrichment with the fluid chemistry. To make such a comparison basically meaningful, it is necessary to have a look at the primary fluid inclusions in the quartz that were trapped contemporaneously with the crystal growth and are not suspected to be the result of a healed fracture, for instance.

Analogies can be found for Al, Li, and Sn. All of these elements show elevated contents in the fluid that probably directly explain their enrichment in quartz. The very high Al values in the hydrothermal quartz (182 $\mu\text{g/g}$) correspond to concentrations of up to 4400 $\mu\text{g/g}$ in the primary FIA_P3. Further possible relations in the chemistry between quartz and fluid become resolved after normalizing the trace element data against the composition of the bulk continental crust (BCC). It appears that the primary inclusions show a similar pattern than quartz with some differences that can be explained by the compatibility/incompatibility of the concerned element in the fluid or quartz phase, respectively (Figure 38). Boron, for example, is a fluid mobile element which explains the positive anomaly in the primary and brine inclusions compared to the quartz pattern. Aluminum is compatible in the quartz lattice and

has therefore a positive anomaly in the quartz pattern, which cannot be observed in the fluids. Manganese, in turn, shows a strong enrichment in the fluids and an opposing trend in the quartz, based on the incompatibility of the Mn^{2+} ion the quartz and its high mobility in geothermal fluids. A very good agreement between all presented sample types can be observed for the elements Fe, Cu, As, Rb and Sr. Arsenic shows the strongest positive anomaly of all these elements in all samples, accompanied by the negative anomalies for Fe and Sr. The conformity of the patterns gets proceeded with Sn, that is one of the few elements which is enriched in the fluids and quartz compared to the BCC. Following discrepancies between the different sample types appear for Sb, Cs, W and Pb. While the quartz pattern is descending from Sn to Pb, the fluids have got, at least partially, positive anomalies for Sb, Cs and Pb. Cesium is strongly enriched in the fluids due to the high degree of fractionation in the granitic system and its high mobility in fluids. Antimony, W and Pb are enriched in the fluids, except for the secondary inclusions. Considered these facts together with the enrichment of Sn, the ability of the here investigated fluids to transport metals and form mineralizations is demonstrated.

The general agreement of the primary inclusion pattern with the quartz trace element pattern might be interpreted as a prove for the close relation of the quartz to the fluid phase, that has obviously precipitated from a fluid phase. The strong enrichment of the ore metals in the fluids compared to the BCC supports the theory that those fluids must have been responsible for ore generation.

5.5.3 Geothermobarometry with “TitaniQ”

The concentration of Ti in quartz can be used as a geothermobarometer to deduce information on the crystallization conditions of quartz in magmatic or metamorphic systems (high temperature and pressure). The calibration of the PT-dependent Ti solubility in quartz has been firstly performed by Wark and Watson 2006 with the focus on the temperature dependence at 10 kbar only and was further refined by Thomas et al. 2010, who conducted experiments from 5 – 20 kbar and demonstrated the pressure dependence of the Ti solubility. Huang and Audétat 2012 extended the calibration to pressures from 1 – 10 kbar and published Ti solubilities that are three times lower than the previous values. Following Huang and Audétat 2012, the discrepancies may have originated from the rapid quartz crystal growth rates in the experiments of Thomas et al. 2010, which may have lead to a Ti incorporation that his higher than at equilibrium conditions. A further study by Thomas et al. 2015 confirmed that the Ti-in-quartz contents used to calibrate the PT dependencies of the Ti solubility determined by Thomas et al. 2010 represent the equilibrium concentrations of Ti in quartz by conducting quartz, rutile and zircon growth experiments under SiO₂, TiO₂ and ZrSiO₄ saturation. The calculated Ti-in-quartz isopleth and the Zr-in-rutile isopleth intersected close to the experimental conditions. Thus, Thomas et al. 2015 suggested that the experiments of Huang and Audétat 2012 did not represent equilibrium conditions between Ti in quartz and rutile and that changing Ti activities were prevailing during the experiments.

Nevertheless, a large number of studies with different purposes have been conducted in the last years using the Ti-in-quartz thermobarometry, showing the need for a proper barometer especially for felsic igneous rocks. Thomas et al. 2010 expected a wide range of applicability for crustal rocks in the magmatic, metamorphic and hydrothermal environment. The strength of the described tool is the chemical stability of quartz against alteration reactions and the preservation of the original Ti concentration. The use of the Ti-in-quartz thermobarometer requires the accurate determination of the titanium activity (a_{TiO_2}) in the investigated system and the combination with an independent estimation of either T (to calculate pressure) or P (to calculate temperature). Typical solutions to determine an additional P or T constrain are the Zr-in-rutile thermobarometry if rutile was in equilibrium with quartz or the thermobarometer based on Zr-in-sphene solubility for systems that have got a lack in rutile. By now, many petrogenetic models including the pressure and temperature of crystallization, timescales of

thermobarometric events and deformation histories in quartz-bearing rocks were realized with the help of Ti-in-quartz thermobarometry (Thomas et al. 2015).

For igneous rocks that crystallized under fluid-saturated conditions the combination of Ti-in-quartz thermobarometry with calculated isochores from fluid inclusion microthermometry can be a sufficient application, yielding to a precise determination of PT conditions of quartz formation when crossing the fluid inclusion isochores with the Ti-in-quartz isopleths, as described by Thomas et al. 2010.

As mentioned above, the calculation of the $a\text{TiO}_2$ is a prerequisite for the use of Ti-in-quartz thermobarometry. To get a precise estimation of the $a\text{TiO}_2$ in the here investigated Zinnwald mineralized vein, we have used the composition of melt inclusions in quartz from the Zinnwald granite, published by Thomas et al. 2005. The minimum trapping temperature of 720°C of those melt inclusions has been used for the determination of $a\text{TiO}_2$ following the equation of Kularatne and Audétat 2014. According to this, the calculation resulted in a $a\text{TiO}_2$ value of 0.11. This value was subsequently used for the calculation of the Ti-in-quartz isopleths. Since the LA-ICP-MS measurements of the investigated hydrothermal quartz resulted in slightly fluctuating Ti concentrations with an average value of $1.31 \pm 0.45 \mu\text{g/g}$ (1SD), the isopleths were calculated for this range of Ti concentrations with a $a\text{TiO}_2$ of 0.11 and on the basis of pressures in small steps from 0.1 – 20 kbar. However, it must also be considered that the $a\text{TiO}_2$ may not have been constant during the fast crystal growth in the hydrothermal vein, too. This could explain the variable Ti content in the quartz crystal. The isochores from several pseudosecondary (FIA_PS2) and primary (FIA_P3) two-phase fluid inclusions from assemblages representing intermediate dense fluids (Figure 19) that were quite likely responsible for the transport of metals into the cupola part of the intrusion and therefore directly involved in the mineralization process have been used to visualize the possible PT-range of entrapment conditions of the magmatic-hydrothermal fluids. Furthermore, the isochores of those fluids were chosen, because they can be assumed to be co-genetic with the hydrothermal quartz and therefore were entrapped during the period of growth of the quartz, which would not be applicable for secondary inclusions that are hosted in healed fractures. This choice of isochores further enables a precise and realistic estimation of PT conditions for the quartz crystal growth.

An independent pressure estimate for the crystallization conditions of the Zinnwald granite has been given by Thomas et al. 2005, who considered the entrapment pressure of magmatic melt inclusions to be 1140 ± 200 bar by intersecting the isochores with the experimentally

determined water saturated granite solidus. This pressure estimation serves as an upper limit for the crystallization conditions of the here investigated hydrothermal quartz, since it is very unlikely that the magmatic granite quartz crystallized later and under lower pressure than the hydrothermal vein quartz. It is well accepted that the granitic melt exsolved an aqueous fluid phase during its crystallization which migrated into the upper parts of the pluton. The melt inclusions in the granite quartz may have coexisted with the fluid phase and could have been trapped under equal PT conditions, but it is very unlikely that the fluid was trapped under higher pressures than the melt inclusions, enabling the pressure estimation from Thomas et al. 2005 to represent an upper pressure limit for the here investigated fluid inclusions.

Figure 39 shows the calculated isochores of the homogenized individual fluid inclusions from the assemblages FIA_PS2 and FIA_P3, starting at the respective temperature and pressure of homogenization. The slope of the isochores was calculated according to the PVTX properties of the H₂O-NaCl system using the MS Excel spreadsheet HOKIE_FLINCS (Steele-MacInnis et al. 2012). The here presented isopleths were calculated following the equation of Huang and Audétat 2012:

$$\log Ti(\mu g / g) = -0.27943 * 10^4 / T - 660.53 * (P^{0.35} / T) + 5.6459 \quad (1)$$

where T is given in K and P in kbar. A target value search for variable P values from 0.1 – 20 kbar and constant $aTiO_2$ has been conducted with T was being the adjustable value and the measured $Ti(\mu g/g)$ being the target value (here: 1.31 $\mu g/g$).

The $aTiO_2$ is taken into account when converting $\log Ti(\mu g / g)$ into $Ti(\mu g / g)$:

$$Ti(\mu g / g) = 10^{\log Ti} * aTiO_2. \quad (2)$$

For the estimation of the PT conditions of crystallization it is necessary to take the upper most and lower most isochore into account for the definition of the area that includes an intersection of the isochores with the isopleths (Figure 39). Both isochores define the first independent PT estimation for the entrapment and crystallization conditions. The second independent PT constrain is defined by the Ti-in-quartz isopleths for the upper Ti concentration limit (1.76 $\mu g/g$) and the lower limit (0.86 $\mu g/g$). The isopleth for 1.3 $\mu g/g$ Ti can be considered to represent the most likely values, since it is based on the average Ti content, with the two adjacent isopleths defining its range of uncertainty. It is conspicuous that the crossing of the upper isochore with the 1.76 $\mu g/g$ isopleth exactly reproduces the pressure from Thomas et al. (1.14 kbar) at 510°C. The lower isochore crosses at a slightly

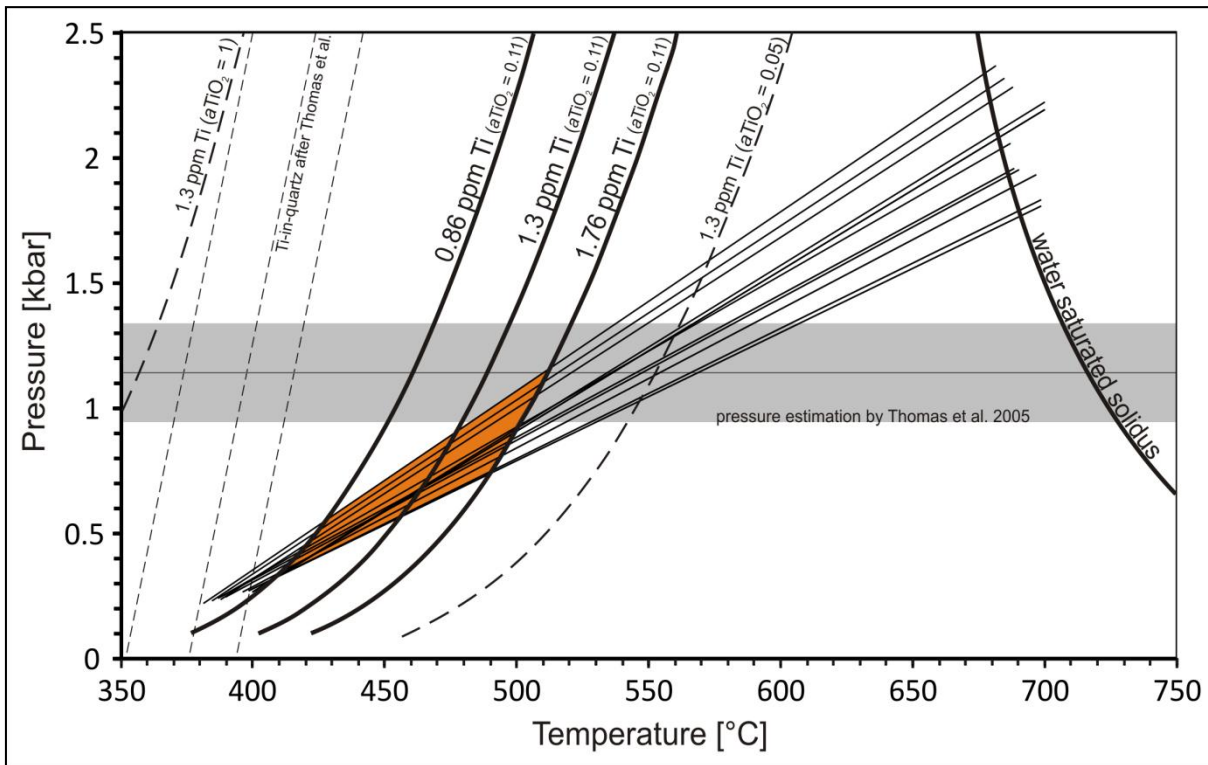


Figure 39: Pressure-temperature diagram with the calculated fluid inclusion isochores and Ti-in-quartz isopleths for the hydrothermal vein quartz from Zinnwald Sn-W mineralized vein. The orange marked area represents the PT-range of possible fluid entrapment and quartz crystallization conditions. The bold dashed lines show the overlapping T-range of the Ti-in-quartz isopleths and fluid inclusion isochores with the pressure estimation of Thomas et al. (2005), defining a further limitation for the possible trapping conditions of the fluid inclusions.

lower temperature (490°C) but at a pressure that is significantly below the value of Thomas et al. (0.7 kbar). The crossing range of the average Ti isopleth lies in the area of 0.55 – 0.9 kbar and 455 – 475°C. The lower isopleth barely crosses all isochores and intersects close to the PT conditions at homogenization (0.35 – 0.55 kbar and 405 – 425°C).

In the calculation above the equation from Huang and Audétat 2012 was used because it was calibrated in the low pressure range which is approaching the conditions in a hydrothermal quartz vein. But since there is no clear recommendation which equation for the Ti-in-quartz thermobarometry is more accurate, we have also checked the applicability of the Thomas et al. 2010 equation for our results, but those isopleths underestimate the temperature (overestimate the pressure) conditions and intersect only partly with the isochores (Figure 39).

The here presented PT constraint for the Zinnwald hydrothermal quartz is based on the assumption of a stable $a\text{TiO}_2$ of 0.11 from which a possible uncertainty of the calculations arises. The Ti concentration of melt inclusions from the Zinnwald granite quartz does probably not represent exactly the same activity of TiO_2 as in the aqueous parental fluid of the hydrothermal quartz, but it yields a good approximation. The effect of a changing $a\text{TiO}_2$ can

be seen in Figure 39 when comparing the 1.3 $\mu\text{g/g}$ Ti isopleths for $a\text{TiO}_2 = 1$, $a\text{TiO}_2 = 0.11$ and $a\text{TiO}_2 = 0.05$. A lower titanium activity results in a shift of the isopleths to higher temperatures and would result in combination with the isochores in higher temperatures and pressures of crystallization. The real chemical behavior of Ti in the fluid can only be roughly estimated because ^{49}Ti was constantly below the LOD during the LA-ICP-MS analyses of fluid inclusions. Ti is supposed to be mobile in hydrothermal F-rich fluids due the generation of F-Ti complexes like $\text{Ti}(\text{OH})_3\text{F}$ or K_2TiF_6 , which would account for a low $a\text{TiO}_2$ of the fluid due to its high solubility (He et al. 2015, Ryzhenko et al. 2006). In addition, Lester et al. 2013 determined the partition coefficient ($D_{\text{Ti}}^{\text{Melt/Fluid}}$) for Ti and other trace elements between a peraluminous, water saturated, F-bearing melt and the aqueous fluid phase. The $D_{\text{Ti}}^{\text{Melt/Fluid}}$ of 7.2 suggests that Ti preferentially partitions into the melt during fluid-melt separation.

Our results are in good agreement with earlier studies of primary fluid inclusions in cassiterite (Sushchevskaya et al. 1996, Durisova et al. 1979) and quartz (Webster et al. 2004) from a mineralized quartz vein of the Zinnwald Sn-W deposit. Microthermometric investigations of fluid inclusions in cassiterite indicate that the earliest mineralizing fluids were trapped at < 0.8 kbar at temperatures between $400 - 500^\circ\text{C}$ (Sushchevskaya et al. 1996). The measurements of Webster et al. (2004) lead to slightly higher entrapment pressures of 0.97 kbar. Our results suggest a possible PT range of crystallization from 0.35 – 1.14 kbar at $405 - 510^\circ\text{C}$, when considering the Ti-in-quartz isopleths and fluid inclusion isochores, only. This surely represents realistic PT conditions of a hydrothermal vein environment. The fact that the maximum pressure of the calculated PT window exactly reproduces the pressure estimate of Thomas et al. gives a hint about the reliability of these results. As already mentioned, the pressure estimate from melt inclusions in magmatic quartz is a natural upper limit for the entrapment conditions of the fluid inclusions in hydrothermal vein quartz, since the exsolved magmatic fluid migrated into shallower depths. Thus, the Ti-in-quartz thermobarometry in combination with the fluid inclusion isochores resulted in a good approximation of the crystallization conditions of the Zinnwald mineralized quartz vein.

5.6 Conclusions

In this study we have used the fluid inclusion and quartz chemistry to gain new information about the ore forming processes of a Sn-W specialized granite. A hydrothermal smoky quartz crystal from a mineralized vein of the Zinnwald Sn-W deposit in the eastern Erzgebirge was investigated for its fluid inclusion contingent and its trace element distribution. Further fluid inclusions have been analyzed in magmatic quartz samples from the underlying base granite (Schellerhau granite) and a comparable Sn-specialized granite from Cornwall, UK (Porth Ledden granite). By microthermometric measurements and subsequent UV-fs-LA-ICP-MS analyses of the fluid inclusions, we could demonstrate that the intermediate saline (5 – 8 mass% NaCl_{eq}), intermediate dense (0.6 g/cm³) two-phase fluid inclusion hosted significant amounts of Sn (140 µg/g) and W (30 µg/g). Those L+V inclusions were identified as primary and pseudosecondary inclusions and thus could provide a direct insight into the fluid chemistry of the parental fluid/melt of the smoky quartz, which is in turn in a close genetic and temporal relation to the mineralization and cassiterite and wolframite precipitation. The homogenization temperatures of the inclusions were determined with 380 – 400°C, which can be interpreted as the minimum trapping conditions and also give a first hint about the ore forming conditions at the Zinnwald locality. Secondary inclusions that are hosted in healed cracks and therefore include a younger stage of the evolving aqueous fluid show a decreasing salinity and lower trace element contents than the primary inclusions. The metal contents of the fluids also decrease with the salinity, whereas the homogenization temperatures stay constant. These observations can be ascribed to the progressive leaching of Sn, W and other trace elements from the micas (lithian annite) of the underlying biotite granite by the Cl- and F-rich magmatic fluid that were exsolved from the H₂O oversaturated granitic melt. The occurrence of L+V+S fluid inclusion assemblages in the hydrothermal quartz is strongly limited to only two assemblages with 28 – 31 mass% NaCl_{eq}. Tin (224 µg/g) and W (84 µg/g) are enriched in those Na, K, Mn and Pb rich brines but the discrepancy to the primary L+V inclusions is not as huge as the difference in salinity. Thus, the L+V+S inclusions probably originated after phase separation when the already Sn-W depleted medium dense supercritical fluid began to boil. The trace elements and metals like Sn, W, Mn, Fe, Rb, Cs and Pb were enriched in the brine phase. Low-saline secondary inclusions (0.88 mass% NaCl_{eq}) might be a relic of intruding meteoric water and an associated pressure drop from lithostatic to hydrostatic conditions, which could have initiated boiling. The results imply that both, a medium saline supercritical single-phase fluid and the brine of a two-phase fluid were directly

involved in the formation of the greisens and vein style Sn-W deposits in the Zinnwald granite cupola.

Tin and W show a positive correlation in the investigated inclusions from the Zinnwald hydrothermal quartz that is stronger pronounced in the L+V inclusions than in the L+V+S inclusions. This correlation is not the general case for Sn-W specialized systems, as demonstrated by the additional measurement of fluid inclusions from the Gottesberg/Grummetstock Sn-W deposit, where W has a maximum concentration at 10 µg/g and does not correlate with the Sn content that can reach up to 1000 µg/g in the L+V+S inclusions.

By UV-fs-LA-ICP-MS analyses of the hydrothermal quartz we could demonstrate that the quartz must have formed from an extremely fractionated siliceous aqueous fluid. The trace elements in quartz that are sensitive to fractional crystallization processes (Ge, Al, Ti, Li) show concentrations that reflect the extreme high degree of fractionation of the residual fluid/melt, especially when compared to the trace element data of magmatic quartz from the underlying biotite and zinnwaldite granite (from Breiter et al. 2012). Correlations between Al and a range of elements (Li, Na, K, Rb) is related to the charge balancing interstitial incorporation of the correlating monovalent ions with the Si⁴⁺ substituting Al³⁺ ion. Further correlations of Al with Mn, Sr, Pb, As, and Sb might be related to the generally high concentrations of those elements in the fluids

The pressure and temperature dependent incorporation of Ti into quartz allows us to estimate the PT conditions of the quartz formation. By intersecting the calculated Ti-in-quartz isopleths, generated with the equation from Huang and Audétat 2012, with the isochores of the primary fluid inclusions, calculated from the microthermometric results, we were able to limit the P-T range of quartz formation to 0.35 – 1.14 kbar and 405 – 510°C (for a Ti concentration in quartz of 1.31 ± 0.45 µg/g (1SD))

Another purpose of this study was to investigate the ability of magmatic fluids to leach and transport metals from a pre-enriched granitic melt. The Schellerhau granite as a reference location from the Altenberg-Teplice caldera in the eastern Erzgebirge and the Land's End granite in Cornwall are two Sn-W specialized granites with different chemical compositions in terms of their volatile components. The granites of the eastern Erzgebirge are known for their high F and Cl contents and the Cornwall granites for their high B and Cl contents. With the analyses of primary brine inclusions in the magmatic quartz from both locations we could

reveal that the earliest exsolved magmatic fluids were able to leach Sn and W from the enriched melts. The Schellerhau brines carry up to 2300 $\mu\text{g/g}$ Sn and 1000 $\mu\text{g/g}$ W, whereas the Land's End fluids were measured with maximum values of 370 $\mu\text{g/g}$ Sn and 300 $\mu\text{g/g}$ W. The difference in concentration of one order of magnitude between both locations could be a result of the higher F content in the Schellerhau granite or a stronger pre-enrichment in the melt.

6. Outlook

With the here presented method for fluid inclusion analyses via UV-fs-LA-ICP-MS, we could demonstrate that the combined application of an ultrafast pulsed femtosecond laser and a freezing cell for ablation at low temperatures can yield to an improvement of the previous UV-ns-LA method for fluid inclusion analyses. The high control during the opening procedure allows a precise determination of trace element contents in fluid inclusion of diameters from 8 – 25 μm using spot analysis, and of any inclusion diameter between 20 – 100 μm with the *Linux CNC* based spiral pattern controlled ablation. Thereby, the maximum of 100 μm is estimated and based on our findings that the *Linux CNC* stage has the ability to drill craters of such large volumes in a time span which is suitable for ICP-MS data acquisition. We expect that it is possible to generate suitable craters of 150 μm in diameter, presupposing a very high laser repetition rate of up to 500 Hz. With respect to the volume dependent lower limit of detection (LOD) in laser ablation, the significance of the CNC controlled patterns gets even more pronounced, since the LODs can be improved by orders of magnitude (Figure 40). The majority of fluid inclusions in natural samples or generated by high pressure, high temperature experiments are often smaller than 10 μm in diameter. The higher sensitivity of the here used magnetic sectorfield ICP-MS compared to the quadrupole devices used in earlier studies (e.g. Heinrich et al. 2003) provides the basis for successful analyses of these small sample volumes. By freezing the inclusions prior to analysis, we ensure that none of the sample material gets lost by sputtering or leakage through laser induced cracks, as often observed during ns-LA of fluid inclusions in quartz. The most important achievements of the UV-fs-LA freezing technique are therefore the possibility to analyze smallest inclusions as well as inclusions $> 30 \mu\text{m}$ with an excellent control and a reliable production of feasible time resolved signals without spikes in more than 90 % of all conducted individual analyses.

The development of the freezing technique for fluid inclusions has opened a large field of possible applications. We have conducted a case study with natural samples from Sn-W specialized granites and their related mineralized quartz veins. But the low LOD for other ore forming metals like Au, Cu, Mo, Pb, Zn or Ag is a good prerequisite for analogical studies of the magmatic-hydrothermal fluids from these ore deposits. Especially analyses of Au require a detection limit in the ppb level that can be reached by the CNC technique. But also metamorphic or basinal fluids could become the object of research with this technique. Other

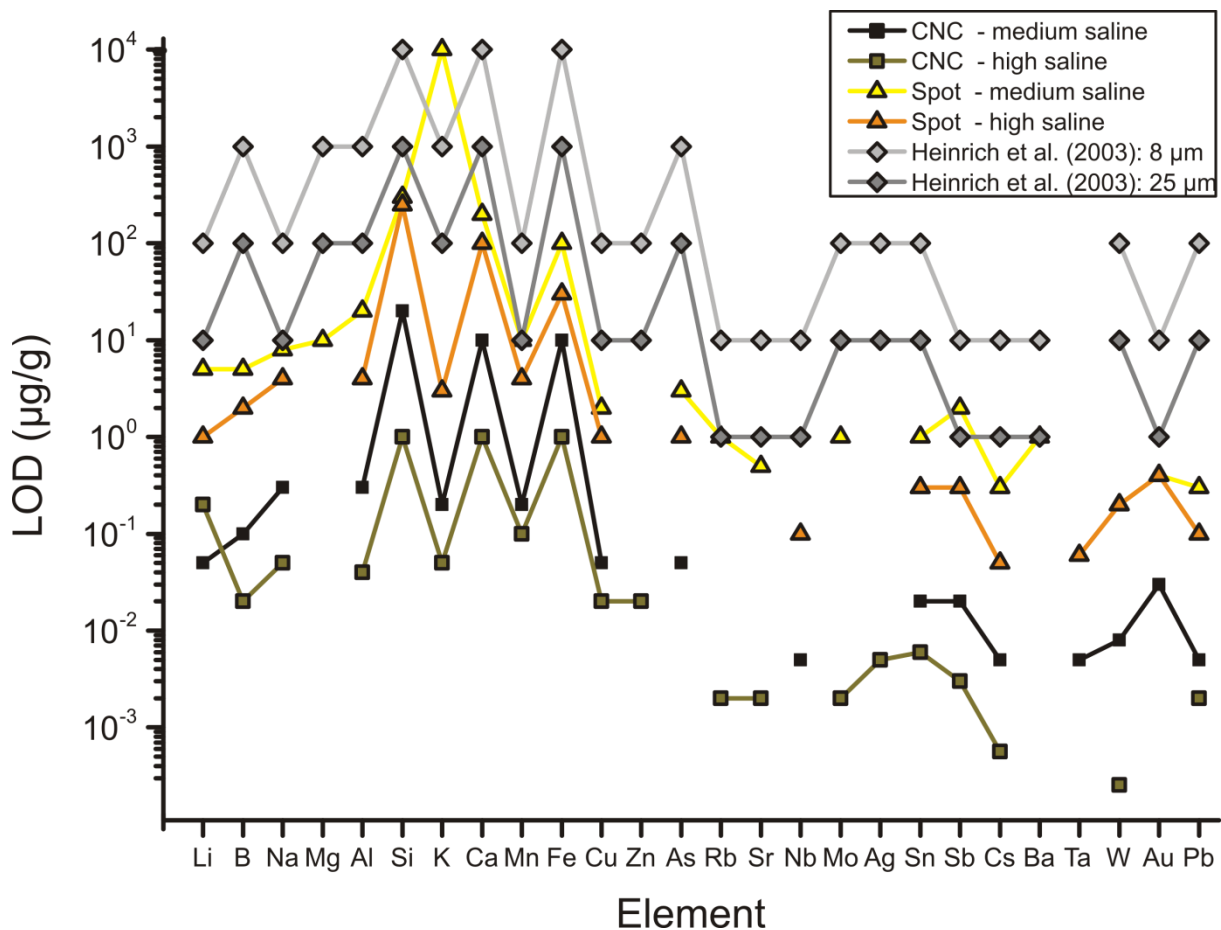


Figure 40: Comparison of lower limits of detection from the here presented UV-fs-LA-ICP-MS method including spot and CNC spiral pattern analyses with LODs from Heinrich et al. 2003. Values from this study represent minimum values from all analyzed fluid inclusions.

host minerals than quartz are challenging for LA-ICP-MS, due to their more complex chemical composition and possible interferences with the fluid signal, but the analyses do not need to be restricted to quartz host and can be extended to inclusions in fluorite or calcite, too. Melt inclusion analyses by LA-ICP-MS are closely related to fluid inclusion analyses and represent another field of research that is accessible with the here presented technique. Analyses of melt inclusions with a liquid-vapor phase could also benefit from the freezing technique.

The measurement of isotopic compositions in fluid inclusions is hampered by the small sample volumes and the resulting time resolved signals that are often too short, accompanied by spikes or unstable in count rates with fast decreasing signals after the initial input of material. Pettke et al. 2012 were the first and by now the only ones who published Pb isotopic signatures measured by LA-MC-ICP-MS in fluid inclusions, demonstrating the feasibility of isotopic analyses in fluid inclusions. With the *Linux CNC* spiral technique, we have created

best preconditions at the Institute for Mineralogy Hannover to extend the fluid inclusion analyses by the UV-fs-LA freezing technique from trace element determinations to isotopic analyses via MC-ICP-MS. Inclusions of 30 – 100 μm in diameter were able to produce significant count rates in the order of minutes, sometimes even outlasting the chosen data acquisition time span of the ICP-MS device. This observation is not applicable for all detected isotopes and is dependent on the concentration in the fluid and the instrumental sensitivity of the specific isotope. In a first experiment, $\delta^{11}\text{B}$ and $\delta^7\text{Li}$ values have been measured by UV-fs-LA-MC-ICP-MS from fluid inclusions with several hundreds of $\mu\text{g/g}$ of both elements, giving the indication that this concentration range is high enough for data production. Thereby, the detector constellation of the MC-ICP-MS can be the deciding factor. An ion counting unit in combination with a Faraday cup provided the basis for the simultaneous detection of the high and low abundant isotopes, which can be also achieved by the integration of $10^{14} \Omega$ resistors. Further improvements in the design of the CNC spiral pattern that have been made after the first $\delta^{11}\text{B}$ - / $\delta^7\text{Li}$ -experiments can smooth the signals and yield to higher internal precisions. Stable isotope analyses in *individual* fluid inclusion were an inaccessible field of research by now, but might give an important insight into isotope fractionation processes that are commonly described as a shift in the isotopic composition between two (crystallized) phases. Determining the isotopic composition of different fluid inclusion assemblages could result in an evolving isotopic composition of the fluid phase and could give completely new insights into hydrothermal processes. $\delta^{56}\text{Fe}$ values could provide information about the redox potential of the fluid phase. Inclusions with Fe contents in the wt% range are frequently found and should provide proper signals for MC-ICP-MS analyses. It is also worth considering analyses of Pb signatures that are a promising application in terms of fluid source identification.

The implementation of the *Linux CNC* controlled laser stage provides a huge extension of possible applications of the here used UV-fs-LA system at all – not only for fluid inclusions. The CNC program allows the generation of user defined laser patterns in the X-Y-Z space. Depth profiles can be precisely ablated from the surface by a stepwise concentric pattern without the need of a longitudinal cut of the sample. Diffusion profiles, isotopic or elemental, might be possible applications for this example. First tests resulted in ablation craters with a surface roughness in the low nanometer range, showing that a precise determination with a high spatial resolution into the Z-space will be possible.

Concerning the here presented case study about magmatic-hydrothermal fluids in Sn-W granites, additional measurements with Raman spectroscopy are recommendable to quantify

the F⁻ content in the fluid inclusion and gain more information about the crucial question of metal complexation. Our data show a correlation between Cl⁻ and Sn in the Zinnwald mineralizing fluids, suggesting metal transport as Cl-complexes. But the possible involvement of F⁻ and other anions needs to be revealed and discussed on the basis of further micro analytical results.

The combination of trace element determinations in primary fluid inclusions and their host quartz is a promising method to estimate the PT conditions of quartz formation and fluid trapping. Titanium-in-quartz geothermobarometry in combination with the calculated isochores from primary inclusions yielded to a realistic PT range for hydrothermal quartz growth. This specific combination of independent isochores and isopleths has not been reported before and the calibration of the Ti-in-quartz geothermobarometer has not been made for pressures < 1 kbar, but our results indicate that this approach is worth to be repeated in further studies, even though it is still developable and hampered by the calibration of the thermobarometer.

7. References

- Albrecht, M., Derrey, I. T., Horn, I., Schuth, S. and Weyer, S., 2014, Quantification of trace element contents in frozen fluid inclusions by UV-fs-LA-ICP-MS analysis, *Journal of Analytical Atomic Spectrometry*, 29, 1034–1041.
- Allan, M., Yardley B.W.D., Forbes L.J., Shmulovich K.I., Banks D.A. and Shepherd T.J., 2005, Validation of LA-ICP-MS fluid inclusion analysis with synthetic fluid inclusions, *American Mineralogist*, 90, 1767–1775.
- Appold, M. S. and Wenz, Z. J., 2011, Composition of ore fluid inclusions from the Viburnum Trend, Southeast Missouri district, United States: Implications for transport and precipitation mechanisms, *Economic Geology*, 106, 55–78.
- Audétat, A., Günther, D. and Heinrich, C. A., 2000a, Causes for Large-Scale Metal Zonation around Mineralized Plutons: Fluid Inclusion LA-ICP-MS Evidence from the Mole Granite, Australia, *Economic Geology*, 95, 1563–1581.
- Audétat, A., Günther, D. and Heinrich, C. A., 2000b, Magmatic-hydrothermal evolution in a fractionating granite: a microchemical study of the sn-w-f-mineralized mole granite (Australia), *Geochimica et Cosmochimica Acta*, 64, 3373–3393.
- Audétat, A., Pettke, T., Heinrich, C. and Bodnar, R., 2008, Special paper: The composition of magmatic-hydrothermal fluids in barren and mineralized intrusions, *Economic Geology*, 103, 877–908.
- Audétat, A., 2013, Origin of Ti-rich rims in quartz phenocrysts from the Upper Bandelier Tuff and the Tunnel Spring Tuff, southwestern USA, *Chemical Geology*, 360-361, 99–104.
- Audétat, A., 2014, Compositional evolution and formation conditions of magmas and fluids related to porphyry mo mineralization at Climax, Colorado, *Journal of Petrology*, 56, 1519–1546.
- Bennett, J. N. and Grant, J. N., 1980, Analysis of fluid inclusions using a pulsed laser microprobe, *Mineralogical Magazine*, 43, 945–947.
- Berry, A. J., Hack, A. C., Mavrogenes, J. A., Newville, M. and Sutton, S. R., 2006, AXANES study of Cu speciation in high-temperature brines using synthetic fluid inclusions, *American Mineralogist*, 91, 1773–1782.

- Bertelli, M., Baker, T., Cleverley, J. and Ulrich, T., 2009, Geochemical modelling of a Zn-Pb skarn: Constraints from LA-ICP-MS analysis of fluid inclusions, *Journal of Geochemical Exploration*, 102, 13–26.
- Beuchat, S., Moritz, R. and Pettke, T., 2004, Fluid evolution in the W-Cu-Zn-Pb San Cristobal vein, Peru: Fluid inclusion and stable isotope evidence, *Chemical Geology*, 210, 201–224.
- Beurlen, H., Müller, A., Silva, D. and Da Silva, M., 2011, Petrogenetic significance of LA-ICP-MS trace-element data on quartz from the Borborema Pegmatite Province, northeast Brazil, *Mineralogical Magazine*, 75, 2703–2719.
- Bhalla, P., Holtz, F., Linnen, R. and Behrens, H., 2005, Solubility of cassiterite in evolved granitic melts: Effect of T, fO₂, and additional volatiles, *Lithos*, 80, 387–400.
- Bodnar, R. and Sterner, S., 1985, Synthetic fluid inclusions in natural quartz. II. Application to PVT studies, *Geochimica et Cosmochimica Acta*, 49, 1855–1859.
- Bodnar, R., Burnham, C. and Sterner, S., 1985, Synthetic fluid inclusions in natural quartz. III. Determination of phase equilibrium properties in the system H₂O-NaCl to 1000°C and 1500 bars, *Geochimica et Cosmochimica Acta*, 49, 1861–1873.
- Bodnar, R., 1993, Revised equation and table for determining the freezing point depression of H₂O-NaCl solutions, *Geochimica et Cosmochimica Acta*, 57, 683–684.
- Bodnar, R. J. and Vityk, M. O., 1994, Interpretation of microthermometric data for H₂O-NaCl fluid inclusions, *Fluid Inclusions in Minerals, Methods and Applications, De Vivo, B. and Frezzotti, M. L.*, 117–130.
- Borisova, A., Thomas, R., Salvi, S., Candaudap, F., Lanzasova, A. and Chmeleff, J., 2012, Tin and associated metal and metalloid geochemistry by femtosecond LA-ICP-QMS microanalysis of pegmatite-leucogranite melt and fluid inclusions: New evidence for melt-melt-fluid immiscibility, *Mineralogical Magazine*, 76, 91–113.
- Breiter, K. and Müller, A., 2009, Evolution of rare-metal granitic magmas documented by quartz chemistry, *European Journal of Mineralogy*, 21, 335–346.
- Breiter, K., Svojtka, M., Ackerman, L. and Švecová, K., 2012, Trace element composition of quartz from the Variscan Altenberg–Tepllice caldera (Krušné hory/Erzgebirge Mts, Czech

- Republic/Germany): Insights into the volcano-plutonic complex evolution, *Chemical Geology*, 326–327, 36–50.
- Breiter, K., Ackerman, L., Svojtka, M. and Müller, A., 2013, Behavior of trace elements in quartz from plutons of different geochemical signature: A case study from the Bohemian Massif, Czech Republic, *Lithos*, 175-176, 54–67.
- Burisch, M., Walter, B., Wälle, M. and Markl, G., 2016, Tracing fluid migration pathways in the root zone below unconformity-related hydrothermal veins: Insights from trace element systematics of individual fluid inclusions, *Chemical Geology*, 429, 44–50.
- Catchpole, H., Kouzmanov, K., Fontboté, L., Guillong, M. and Heinrich, C., 2011, Fluid evolution in zoned Cordilleran polymetallic veins - Insights from microthermometry and LA-ICP-MS of fluid inclusions, *Chemical Geology*, 281, 293–304.
- Charoy, B. and Evans A.M., 1982, Tourmalinization in Cornwall, England, *Metallization Associated with Acid Magmatism*,
- Charoy, B., 1986, The genesis of the cornubian batholith (South-West England): The example of the carnmenellis pluton, *Journal of Petrology*, 27, 571–604.
- Chen, Y., Clark, A. H., Farrar, E., Wasteneys, H., Hodgson, M. J. and Bromley, A. V., 1993, Diachronous and independent histories of plutonism and mineralization in the Cornubian Batholith, southwest England, *Journal - Geological Society (London)*, 150, 1183–1191.
- Claverie, F., Fernández, B., Pécheyran, C., Alexis, J. and Donard, O., 2009, Elemental fractionation effects in high repetition rate IR femtosecond laser ablation ICP-MS analysis of glasses, *Journal of Analytical Atomic Spectrometry*, 24, 891–902.
- Cohen, A. J., 1956, Anisotropic Color Centers in α Quartz. Part I. Smoky Quartz, *The Journal of Chemical Physics*, 25, 908.
- Derrey, I. T., Albrecht, M., Dupliy, E., Botcharnikov, R. E., Horn, I., Weyer, S. and Holtz, F., 2016, Experimental tests on achieving equilibrium in synthetic fluid inclusions: results for scheelite, molybdenite and gold solubility at 800 °C and 2 kbar, *American Mineralogist*,
- Drivenes, K., Larsen, R. B., Müller, A. and Sørensen, B. E., 2016, Crystallization and uplift path of late Variscan granites evidenced by quartz chemistry and fluid inclusions: Example from the Land's End granite, SW England, *Lithos*, 252-253, 57–75.

- Duc-Tin, Q., Audétat, A. and Keppler, H., 2007, Solubility of tin in (Cl, F)-bearing aqueous fluids at 700 °C, 140 MPa: A LA-ICP-MS study on synthetic fluid inclusions, *Geochimica et Cosmochimica Acta*, 71, 3323–3335.
- Durisova, J., Charoy, B. and Weisbrod, A., 1979, Fluid inclusion studies in minerals from tin and tungsten deposits in the Krusne Hory Mountains, *Bulletin of The Mineral Research and Exploration*, 655–675.
- Eugster, H. P., 1985, Granites and hydrothermal ore deposits: a geochemical framework, *Mineralogical Magazine*, 49, 7–23.
- Fietzke, J. and Frische, M., 2016, Experimental evaluation of elemental behavior during LA-ICP-MS: Influences of plasma conditions and limits of plasma robustness, *Journal of Analytical Atomic Spectrometry*, 31, 234–244.
- Flem, B., Larsen, R., Grimstvedt, A. and Mansfeld, J., 2002, In situ analysis of trace elements in quartz by using laser ablation inductively coupled plasma mass spectrometry, *Chemical Geology*, 182, 237–247.
- Förster, H.-J. and Tischendorf, G., 1994, In: Metallogeny of Collisional Orogens (Seltmann, R., Kämpf, H., Möller, P., 35–48.
- Förster, H.-J., Seltmann, R. and Tischendorf, G., 1995, High-fluorine, low-phosphorus A-type (post-collision) silicic magmatism in the Erzgebirge, *Terra Nostra*, 32–35.
- Förster, H.-J., Davis, J. C., Tischendorf, G. and Seltmann, R., 1999, Multivariate analyses of Erzgebirge granite and rhyolite composition: Implications for classification of granites and their genetic relations, *Computers and Geosciences*, 25, 533–546.
- Förster, H.-J. and Rhede, D., 2006, The Be-Ta-rich granite of Seiffen (eastern Erzgebirge, Germany): Accessory-mineral chemistry, composition, and age of a late-Variscan Li-F granite of A-type affinity, *Neues Jahrbuch für Mineralogie, Abhandlungen*, 182, 307–321.
- Frank, M., Simon, A., Pettke, T., Candela, P. and Piccoli, P., 2011, Gold and copper partitioning in magmatic-hydrothermal systems at 800°C and 100MPa, *Geochimica et Cosmochimica Acta*, 75, 2470–2482.
- Fusswinkel, T., Wagner, T., Wenzel, T., Wälle, M. and Lorenz, J., 2013, Evolution of unconformity-related MnFeAs vein mineralization, Sailauf (Germany): Insight from major and trace elements in oxide and carbonate minerals, *Ore Geology Reviews*, 50, 28–51.

- Fusswinkel, T., Wagner, T., Wenzel, T., Wälle, M. and Lorenz, J., 2014, Red bed and basement sourced fluids recorded in hydrothermal Mn-Fe-As veins, Sailauf (Germany): A LA-ICPMS fluid inclusion study, *Chemical Geology*, 363, 22–39.
- Giordano, D., Romano, C., Dingwell, D. B., Poe, B. and Behrens, H., 2004, The combined effects of water and fluorine on the viscosity of silicic magmas, *Geochimica et Cosmochimica Acta*, 68, 5159–5168.
- Goldstein, R. and Reynolds, T. J., 1994, Systematics of fluid inclusions in diagenetic minerals, *Society of Sedimentary Geology Short Course*, 199.
- Götze, J., 2009, Chemistry, textures and physical properties of quartz - geological interpretation and technical application, *Mineralogical Magazine*, 73, 645–671.
- Götze, J. and Möckel, R., 2012, Quartz: Deposits, Mineralogy and Analytics, *Springer-Verlag Berlin Heidelberg*,
- Graupner, T., Brätz, H. and Klemd, R., 2005, LA-ICP-MS micro-analysis of fluid inclusions in quartz using a commercial Merchantek 266 nm Nd: YAG laser: A pilot study, *European Journal of Mineralogy*, 17, 93–102.
- Guillong, M., Latkoczy, C., Seo, J. H., Günther, D. and Heinrich, C. A., 2008a, Determination of sulfur in fluid inclusions by laser ablation ICP-MS, *Journal of Analytical Atomic Spectrometry*, 23, 1581–1589.
- Guillong, M., Meier, D., Allan, M., Heinrich, C. and Yardley B.W.D., 2008b, SILLS: A MATLAB-based program for the reduction of laser ablation ICP-MS data of homogeneous materials and inclusions, *Mineralogical Association of Canada Short Course*, 40, 328–333.
- Günther, D., Audétat A., Frischknecht R. and Heinrich C.A., 1998, Quantitative analysis of major, minor and trace elements in fluid inclusions using laser ablation-inductively coupled plasma mass spectrometry, *Journal of Analytical Atomic Spectrometry*, 13, 263–270.
- Günther, D., Hattendorf, B. and Audétat, A., 2001, Multi-element analysis of melt and fluid inclusions with improved detection capabilities for Ca and Fe using laser ablation with a dynamic reaction cell ICP-MS, *Journal of Analytical Atomic Spectrometry*, 16, 1085–1090.

- Hack, A. and Mavrogenes, J. b., 2006, A synthetic fluid inclusion study of copper solubility in hydrothermal brines from 525 to 725 °C and 0.3 to 1.7 GPa, *Geochimica et Cosmochimica Acta*, 70, 3970–3985.
- Hall, D. L., Sterner S.M. and Bodnar R.J., 1988, Freezing point depression of NaCl-KCl-H₂O solutions, *Econ. Geol.*, 83, 197–202.
- Halter, W. E., Pettke, T., Heinrich, C. A. and Rothen-Rutishauser, B., 2002, Major to trace element analysis of melt inclusions by laser-ablation ICP-MS: Methods of quantification, *Chemical Geology*, 183, 63–86.
- Halter, W. E. and Webster, J. D., 2004, The magmatic to hydrothermal transition and its bearing on ore-forming systems, *Chemical Geology*, 210, 1–6.
- Hammerli, J., Rusk, B., Spandler, C., Emsbo, P. and Oliver, N., 2013, In situ quantification of Br and Cl in minerals and fluid inclusions by LA-ICP-MS: A powerful tool to identify fluid sources, *Chemical Geology*, 337-338, 75–87.
- Hanley, J., Pettke, T., Mungall, J. and Spooner, E., 2005, The solubility of platinum and gold in NaCl brines at 1.5 kbar, 600 to 800°C: A laser ablation ICP-MS pilot study of synthetic fluid inclusions, *Geochimica et Cosmochimica Acta*, 69, 2593–2611.
- Heijlen, W., Banks, D. A., Muchez, P., Stensgard, B. M. and Yardley, B. W. D., 2008, The nature of mineralizing fluids of the Kipushi Zn-Cu deposit, Katanga, Democratic Republic of Congo: Quantitative fluid inclusion analysis using laser ablation ICP-MS and bulk crush-leach methods, *Economic Geology*, 103, 1459–1482.
- Heinrich, C., Pettke T., Halter W.E., Aigner-Torres M., Audétat A., Günther D., Hattendorf B., Bleiner D., Guillong M. and Horn I., 2003, Quantitative multi-element analysis of minerals, fluid and melt inclusions by laser-ablation inductively-coupled-plasma mass-spectrometry, *Geochimica et Cosmochimica Acta*, 67, 3473–3496.
- Heinrich, C. A., Günther D., Audétat A., Ulrich T. and Frischknecht R., 1999, Metal fractionation between magmatic brine and vapor, determined by microanalysis of fluid inclusions, *Geology*, 27, 755–758.
- He, J., Ding, X., Wang, Y., Sun, W. and Fu, B., 2015, The effect of temperature and concentration on hydrolysis of fluorine-rich titanium complexes in hydrothermal fluids:

- Constraints on titanium mobility in deep geological processes, *Acta Petrologica Sinica*, 31, 802–810.
- Hergenroeder, R., 2006, A model of non-congruent laser ablation as a source of fractionation effects in LA-ICP-MS, *Journal of Analytical Atomic Spectrometry*, 21, 505.
- Hirayama, Y. and Obara, M., 2005, Heat-affected zone and ablation rate of copper ablated with femtosecond laser, *Journal of Applied Physics*, 97, 64903.
- Horn, I. and Blanckenburg, F. von, 2006, In situ iron isotope ratio determination using UV-femtosecond laser ablation with application to hydrothermal ore formation processes, *Geochimica et Cosmochimica Acta*, 70, 3677–3688.
- Horn, I. and Blanckenburg, F. von, 2007, Investigation on elemental and isotopic fractionation during 196 nm femtosecond laser ablation multiple collector inductively coupled plasma mass spectrometry, *Spectrochimica Acta - Part B Atomic Spectroscopy*, 62, 410–422.
- Huang, R. and Audétat, A., 2012, The titanium-in-quartz (TitaniQ) thermobarometer: A critical examination and re-calibration, *Geochimica et Cosmochimica Acta*, 84, 75–89.
- Hu, X., Bi, X., Hu, R., Shang, L. and Fan, W., 2008, Experimental study on tin partition between granitic silicate melt and coexisting aqueous fluid, *Geochemical Journal*, 42, 141–150.
- Jacamon, F. and Larsen, R. B., 2009, Trace element evolution of quartz in the charnockitic Kleivan granite, SW-Norway: The Ge/Ti ratio of quartz as an index of igneous differentiation, *Lithos*, 107, 281–291.
- Jochum, K. P., Weis, U., Stoll, B., Kuzmin, D., Yang, Q., Raczek, I., Jacob, D. E., Stracke, A., Birbaum, K. and Frick, D., Günther, D. and Enzweiler, J., 2011, Determination of reference values for NIST SRM 610-617 glasses following ISO guidelines, *Geostandards and Geoanalytical Research*, 35, 397–429.
- Johan, Z., Strnad, L. and Johan, V., 2012, Evolution of the Cínovec (Zinnwald) Granite Cupola, Czech Republic: Composition of feldspars and micas, a clue to the Origin of W, Sn mineralization, *Canadian Mineralogist*, 50, 1131–1148.
- Keppler, H., 1993, Influence of fluorine on the enrichment of high field strength trace elements in granitic rocks, *Contributions to Mineralogy and Petrology*, 114, 479–488.

- Kinnaid, J. A., 1985, Hydrothermal alteration and mineralization of the alkaline anorogenic ring complexes of Nigeria, *Journal of African Earth Sciences*, 3, 229–251.
- Klemm, L., Pettke, T., Graeser, S., Mullis, J. and Kouzmanov, K., 2004, Fluid mixing as the cause of sulphide precipitation at Albrunpass, Binn Valley, Central Alps, *Schweizerische Mineralogische und Petrographische Mitteilungen*, 84, 189–212.
- Kostova, B., Pettke, T., Driesner, T., Petrov, P. and Heinrich, C. A., 2004, LA ICP-MS study of fluid inclusions in quartz from the Yuzhna Petrovitsa deposit, Madan ore field, Bulgaria, *Schweizerische Mineralogische und Petrographische Mitteilungen*, 84, 25–36.
- Kotzeva, B., Guillong, M., Stefanova, E. and Piperov, N., 2011, LA-ICP-MS analysis of single fluid inclusions in a quartz crystal (Madan ore district, Bulgaria), *Journal of Geochemical Exploration*, 108, 163–175.
- Kroslakova, I. and Günther, D., 2007, Elemental fractionation in laser ablation-inductively coupled plasma-mass spectrometry: Evidence for mass load induced matrix effects in the ICP during ablation of a silicate glass, *Journal of Analytical Atomic Spectrometry*, 22, 51–62.
- Kularatne, K. and Audétat, A., 2014, Rutile solubility in hydrous rhyolite melts at 750-900°C and 2kbar, with application to titanium-in-quartz (TitaniQ) thermobarometry, *Geochimica et Cosmochimica Acta*, 125, 196–209.
- Landtwing, M. R., Pettke, T., Halter, W. E., Heinrich, C. A., Redmond, P. B., Einaudi, M. T. and Kunze, K., 2005, Copper deposition during quartz dissolution by cooling magmatic-hydrothermal fluids: The Bingham porphyry, *Earth and Planetary Science Letters*, 235, 229–243.
- Larsen, R. B., Henderson, I., Ihlen, P. M. and Jacamon, F., 2004, Distribution and petrogenetic behaviour of trace elements in granitic pegmatite quartz from South Norway, *Contributions to Mineralogy and Petrology*, 147, 615–628.
- Lecumberri-Sanchez, P., Steele-MacInnis, M. and Bodnar, R. J., 2015, Synthetic fluid inclusions XIX. Experimental determination of the vapor-saturated liquidus of the system H₂O-NaCl-FeCl₂, *Geochimica et Cosmochimica Acta*, 148, 34–49.
- Lehmann, B., 1982, Metallogeny of tin: magmatic differentiation versus geochemical heritage, *Economic Geology*, 77, 50–59.

- Lerchbaumer, L. and Audétat, A., 2009, Partitioning of Cu between vapor and brine - an experimental study based on LA-ICP-MS analysis of synthetic fluid inclusions, *19th Annual VM Goldschmidt Conference*, A744.
- Lerchbaumer, L. and Audétat, A., 2013, The metal content of silicate melts and aqueous fluids in subeconomically mineralized granites: Implications for porphyry mineral genesis, *Economic Geology*, 108, 987–1013.
- Lester, G. W., Kyser, T. K., Clark, A. H. and Layton-Mathews, D., 2013, Trace element partitioning between immiscible silicate melts with H₂O, P, S, F, and Cl, *Chemical Geology*, 357, 178–185.
- Linnen, R. L., Pichavant, M., Holtz, F. and Burgess, S., 1995, The effect of f_{o2} on the solubility, diffusion, and speciation of tin in haplogranitic melt at 850°C and 2 kbar, *Geochimica et Cosmochimica Acta*, 59, 1579–1588.
- Linnen, R. L., Pichavant, M. and Holtz, F., 1996, The combined effects of f_{o2} and melt composition on SnO₂ solubility and tin diffusivity in haplogranitic melts, *Geochimica et Cosmochimica Acta*, 60, 4965–4976.
- Li, W., Audétat, A. and Zhang, J., 2015, The role of evaporites in the formation of magnetite-apatite deposits along the Middle and Lower Yangtze River, China: Evidence from LA-ICP-MS analysis of fluid inclusions, *Ore Geology Reviews*, 67, 264–278.
- Longerich, H., Jackson, S. and Günther, D., 1996, Laser ablation inductively coupled plasma mass spectrometric transient signal data acquisition and analyte concentration calculation, *Journal of Analytical Atomic Spectrometry*, 11, 899–904.
- Loucks, R. and Mavrogenes, J. b., 1999, Gold solubility in supercritical hydrothermal brines measured in synthetic fluid inclusions, *Science*, 284, 2159–2163.
- Marsala, A., Wagner, T. and Wälle, M., 2013, Late-metamorphic veins record deep ingression of meteoric water: A LA-ICPMS fluid inclusion study from the fold-and-thrust belt of the Rhenish Massif, Germany, *Chemical Geology*, 351, 134–153.
- Mathews, W., Linnen, R. and Guo, Q., 2003, A filler-rod technique for controlling redox conditions in cold-seal pressure vessels, *American Mineralogist*, 88, 701–707.
- Miron, G., Wagner, T. b., Wälle, M. and Heinrich, C., 2013, Major and trace-element composition and pressure-temperature evolution of rock-buffered fluids in low-grade

- accretionary-wedge metasediments, Central Alps, *Contributions to Mineralogy and Petrology*, 165, 981–1008.
- Morales, M., Figueiredo e Silva, R., Lobato, L., Gomes, S., Gomes, C. and Banks, D., 2016, Metal source and fluid-rock interaction in the Archean BIF-hosted Lamego gold mineralization: Microthermometric and LA-ICP-MS analyses of fluid inclusions in quartz veins, Rio das Velhas greenstone belt, Brazil, *Ore Geology Reviews*, 72, 510–531.
- Müller, A., Seltmann, R. c. and Behr, H.-J., 2000, Application of cathodoluminescence to magmatic quartz in a tin granite - case study from the Schellerhau granite complex, Eastern Erzgebirge, Germany, *Mineralium Deposita*, 35, 169–189.
- Müller, A. and Seltmann, R., 2002, Plagioclase-mantled K-feldspar in the carboniferous porphyritic microgranite of Altenberg-Frauenstein, Eastern Erzgebirge / Krušné Hory, *Bulletin of the Geological Society of Finland*, 74, 53–78.
- Müller, A., Kronz, A. and Breiter, K., 2002, Trace elements and growth patterns in quartz: A fingerprint of the evolution of the subvolcanic Podlesí Granite System (Krušné hory Mts., Czech Republic), *Vestník Ceskeho Geologickeho Ustavu*, 77, 135–145.
- Müller, A., Breiter, K., Seltmann, R. and Pécskay, Z., 2005, Quartz and feldspar zoning in the eastern Erzgebirge volcano-plutonic complex (Germany, Czech Republic): Evidence of multiple magma mixing, *Lithos*, 80, 201–227.
- Müller, A., Seltmann, R., Halls, C., Siebel, W., Dulski, P., Jeffries, T., Spratt, J. and Kronz, A., 2006a, The magmatic evolution of the Land's End pluton, Cornwall, and associated pre-enrichment of metals, *Ore Geology Reviews*, 28, 329–367.
- Müller, A., Thomas, R., Wiedenbeck, M., Seltmann, R. and Breiter, K., 2006b, Water content of granitic melts from Cornwall and Erzgebirge: A Raman spectroscopy study of melt inclusions, *European Journal of Mineralogy*, 18, 429–440.
- Müller, A., Ihlen, P. M. and Kronz, A., 2008, Quartz chemistry in polygeneration sveconorwegian pegmatites, Froland, Norway, *European Journal of Mineralogy*, 20, 447–463.
- Müller, A., van Den Kerkhof, A., Behr, H.-J., Kronz, A. and Koch-Müller, M., 2010, The evolution of late-Hercynian granites and rhyolites documented by quartz - A review, *Special Paper of the Geological Society of America*, 472, 185–204.

- Müller, B., Frischknecht, R., Seward, T., Heinrich, C. A. and Camargo Gallegos, W., 2001, A fluid inclusion reconnaissance study of the Huanuni tin deposit (Bolivia), using LA-ICP-MS micro-analysis, *Mineralium Deposita*, 36, 680–688.
- O'Brien, M. C. M., 1955, The Structure of the Colour Centres in Smoky Quartz, *Proceedings of the Royal Society A: Mathematical, Physical and Engineering Sciences*, 231, 404–414.
- Péchevran, C., Cany, S., Chabassier, P., Mottay, E. and Donard, O., 2007, High repetition rate and low energy femtosecond laser ablation coupled to ICPMS detection: A new analytical approach for trace element determination in solid samples, *Journal of Physics: Conference Series*, 59, 112–117.
- Pelch, M. A., Appold, M. S., Emsbo, P. and Bodnar, R. J., 2015, Constraints from fluid inclusion compositions on the origin of mississippi valley-type mineralization in the illinois-kentucky district, *Economic Geology*, 110, 787–808.
- Pettke, T., Oberli F., Audétat A., Wiechert U., Harris C.R. and Heinrich C.A, 2011, Quantification of transient signals in multiple collector inductively coupled plasma mass spectrometry: Accurate lead isotope ratio determination by laser ablation of individual fluid inclusions, *Journal of Analytical Atomic Spectrometry*, 26, 475–492.
- Pettke, T., Oberli, F., Audétat, A., Guillong, M., Simon, A. C., Hanley, J. J. and Klemm, L. M., 2012, Recent developments in element concentration and isotope ratio analysis of individual fluid inclusions by laser ablation single and multiple collector ICP-MS, *Ore Geology Reviews*, 44, 10–38.
- Pirajno, F., 2010, Hydrothermal Processes and Mineral Systems, *Springer Science+Business Media B.V.*,
- Pollard, P. J., Taylor, R. G. and Cuff, C., 1983, Discussions: Metallogeny of tin: Magmatic differentiation versus geochemical heritage-a discussion, *Economic Geology*, 78, 543–545.
- Powell, T., Salmon, S., Clark, A. H. and Shail, R. K., 1999, Emplacement styles within the Land's End Granite, west Cornwall, *Geoscience in South-West England*, 9, 333–339.
- Pronko, P., Dutta, S., Du, D. and Singh, R., 1995, Thermophysical effects in laser processing of materials with picosecond and femtosecond pulses, *Journal of Applied Physics*, 78, 6233–6240.

- Rankin, A., Ramsey, M., Coles, B., van Langevelde, F. and Thomas, C., 1992, The composition of hypersaline, iron-rich granitic fluids based on laser-ICP and Synchrotron-XRF microprobe analysis of individual fluid inclusions in topaz, Mole granite, eastern Australia, *Geochimica et Cosmochimica Acta*, 56, 67–79.
- Rauchenstein-Martinek, K., Wagner, T., Wälle, M. and Heinrich, C., 2014, Gold concentrations in metamorphic fluids: A LA-ICPMS study of fluid inclusions from the Alpine orogenic belt, *Chemical Geology*, 385, 70–83.
- Richard, A., Pettke, T., Cathelineau, M., Boiron, M., Mercadier, J., Cuney, M. and Derome, D., 2010, Brine-rock interaction in the Athabasca basement (McArthur River U deposit, Canada): Consequences for fluid chemistry and uranium uptake, *Terra Nova*, 22, 303–308.
- Romer, R. L., Thomas, R., Stein, H. J. and Rhede, D., 2007, Dating multiply overprinted Sn-mineralized granites - Examples from the Erzgebirge, Germany, *Mineralium Deposita*, 42, 337–359.
- Romer, R. L. and Kroner, U., 2014, Sediment and weathering control on the distribution of Paleozoic magmatic tin-tungsten mineralization, *Mineralium Deposita*,
- Romer, R. L. and Kroner, U., 2016, Phanerozoic tin and tungsten mineralization-Tectonic controls on the distribution of enriched protoliths and heat sources for crustal melting, *Gondwana Research*, 31, 60–95.
- Rusk, B., Lowers, H. A. and Reed, M. H., 2008, Trace elements in hydrothermal quartz: Relationships to cathodoluminescent textures and insights into vein formation, *Geology*, 36, 547–550.
- Rusk, B., 2012, Cathodoluminescent Textures and Trace Elements in Hydrothermal Quartz, in Götze and Möckel: Quartz: Deposits, Mineralogy and Analytics, *Springer-Verlag Berlin Heidelberg*,
- Ryan, C., Cousens, D., Heinrich, C., Griffin, W., Sie, S. and Mernagh, T., 1991, Quantitative PIXE microanalysis of fluid inclusions based on a layered yield model, *Nuclear Inst. and Methods in Physics Research, B*, 54, 292–297.
- Ryzhenko, B. N., Kovalenko, N. I. and Prisyagina, N. I., 2006, Titanium complexation in hydrothermal systems, *Geochemistry International*, 44, 879–895.

- Scambelluri, M., Pettke, T. and Cannà, E., 2015, Fluid-related inclusions in Alpine high-pressure peridotite reveal trace element recycling during subduction-zone dehydration of serpentized mantle (Cima di Gagnone, Swiss Alps), *Earth and Planetary Science Letters*, 429, 45–59.
- Schlegel, T., Wälle, M., Steele-MacInnis, M. and Heinrich, C., 2013, Accurate and precise quantification of major and trace element compositions of calcic-sodic fluid inclusions by combined microthermometry and LA-ICPMS analysis, *Chemical Geology*, 334, 144–153.
- Seltmann, R., Thomas, R. and Gottesmann, B., 1993, The Gottesberg tin deposit (Saxony) II. Geothermobarometry and breccia pipe formation, *Conference: Metallogeny of Collisional Orogens of the Hercynian type*, Geyer, 130.
- Seltmann, R., Müller, A. and Schilka, W., 2001, Geochemical characteristics of the rapakivi-textured porphyritic microgranites in the Altenberg-Teplice caldera, *Mineral Deposits at the Beginning of the 21st Century*, 481–484.
- Seo, J. H., Guillong, M., Aerts, M., Zajacz, Z. and Heinrich, C. A., 2011, Microanalysis of S, Cl, and Br in fluid inclusions by LA-ICP-MS, *Chemical Geology*, 284, 35–44.
- Shepherd, T. J., Rankin, A. H. and Alderton, D. H. M., 1985, A practical guide to fluid inclusion studies,
- Shepherd, T. J. and Chenery, S. R., 1995, Laser ablation ICP-MS elemental analysis of individual fluid inclusions: An evaluation study, *Geochimica et Cosmochimica Acta*, 59, 3997–4007.
- Sherman, D. M., Ragnarsdottir, K. V., Oelkers, E. H. and Collins, C. R., 2000, Speciation of tin (Sn²⁺ and Sn⁴⁺) in aqueous Cl solutions from 25°C to 350°C: an in situ 5EXAFS6 study, *Chemical Geology*, 167, 169–176.
- Simon, A. C., Pettke, T., Candela, P. A., Piccoli, P. M. and Heinrich, C. A., 2004, Magnetite solubility and iron transport in magmatic-hydrothermal environments, *Geochimica et Cosmochimica Acta*, 68, 4905–4914.
- Simon, A. C., Frank, M. R., Pettke, T., Candela, P. A., Piccoli, P. M. and Heinrich, C. A., 2005, Gold partitioning in melt-vapor-brine systems, *Geochimica et Cosmochimica Acta*, 69, 3321–3335.

- Simon, A. C., Pettke T., Candela P.A., Piccoli P.M. and Heinrich C.A., 2006, Copper partitioning in a melt-vapor-brine-magnetite-pyrrhotite assemblage, *Geochimica et Cosmochimica Acta*, 70, 5583–5600.
- Simon, A. C., Pettke, T., Candela, P. A., Piccoli, P. M. and Heinrich, C. A., 2007, The partitioning behavior of As and Au in S-free and S-bearing magmatic assemblages, *Geochimica et Cosmochimica Acta*, 71, 1764–1782.
- Simon, A. C. and Pettke, T., 2009, Platinum solubility and partitioning in a felsic melt-vapor-brine assemblage, *Geochimica et Cosmochimica Acta*, 73, 438–454.
- Sirbescu, M., Krukowski, E. G., Schmidt, C., Thomas, R., Samson, I. M. and Bodnar, R. J., 2013, Analysis of boron in fluid inclusions by microthermometry, laser ablation ICP-MS, and Raman spectroscopy: Application to the Cryo-Genie Pegmatite, San Diego County, California, USA, *Chemical Geology*, 342, 138–150.
- Smirnov, V. I., 1976, Geology of mineral deposits, *MIR, Moscow*, 520pp.
- Steele-MacInnis, M., Esposito, R. and Bodnar, R., 2011, Thermodynamic model for the effect of post-entrapment crystallization on the H₂O-CO₂ systematics of vapor-saturated, silicate melt inclusions, *Journal of Petrology*, 52, 2461–2482.
- Steele-MacInnis, M., Lecumberri-Sanchez, P. and Bodnar, R., 2012, HokieFlincs_H₂O-NaCl: A Microsoft Excel spreadsheet for interpreting microthermometric data from fluid inclusions based on the PVTX properties of H₂O-NaCl, *Computers and Geosciences*, 49, 334–337.
- Steele-MacInnis, M., Lecumberri-Sanchez, P. and Bodnar, R. J., 2015, Synthetic fluid inclusions XX. Critical PTx properties of H₂O-FeCl₂ fluids, *Geochimica et Cosmochimica Acta*, 148, 50–61.
- Steinboefel, G., Horn, I. and Blanckenburg, F. von, 2009a, Matrix-independent Fe isotope ratio determination in silicates using UV femtosecond laser ablation, *Chemical Geology*, 268, 67–73.
- Steinboefel, G., Horn, I. and Blanckenburg, F. von, 2009b, Micro-scale tracing of Fe and Si isotope signatures in banded iron formation using femtosecond laser ablation, *Geochimica et Cosmochimica Acta*, 73, 5343–5360.

- Steinboefel, G., Blanckenburg, F. von, Horn, I., Konhauser, K., Beukes, N. and Gutzmer, J., 2010, Deciphering formation processes of banded iron formations from the Transvaal and the Hamersley successions by combined Si and Fe isotope analysis using UV femtosecond laser ablation, *Geochimica et Cosmochimica Acta*, 74, 2677–2696.
- Štemprok, M., Holub, F. V. and Novák, J. K., 2003, Multiple magmatic pulses of the Eastern Volcano-Plutonic Complex, Krušné hory/Erzgebirge batholith, and their phosphorus contents, *Bulletin of Geosciences*, 78, 277–296.
- Sternner, S. M., Hall, D. L. and Bodnar, R. J., 1988, Synthetic fluid inclusions. V. Solubility relations in the system NaCl-KCl-H₂O under vapor-saturated conditions, *Geochimica et Cosmochimica Acta*, 52, 989–1005.
- Stoffell, B., Appold, M. S., Wilkinson J.J., McClean N.A. and Jeffries T.E., 2008, Geochemistry and evolution of mississippi valley-type mineralizing brines from the Tri-State and Northern Arkansas districts determined by LA-ICP-MS microanalysis of fluid inclusions, *Economic Geology*, 103, 1411–1435.
- Sun, X. H., Hu, M.-Y., Liu, C. L., Jiao, P. C., Ma, L. C., Wang, X. and Zhan, X. C., 2013, Composition determination of single fluid inclusions in salt minerals by laser ablation ICP-MS, *Fenxi Huaxue/ Chinese Journal of Analytical Chemistry*, 41, 235–241.
- Sushchevskaya, T. M., Ďurišova, J., Yerokhin, A. M., Knyazeva, S. N., Kokina, T. A., Kalinichenko, A. M., Lokhov, K. I. and Prisyagina, N. I., 1996, A Study of the Chemical Characteristics of the Medium of Cassiterite-Quartz-Type Tin Mineralization Based on the Fluid Inclusions in Minerals, *Geochemistry International*, 33, 1–22.
- Su, W., Heinrich, C. A., Pettke, T., Zhang, X., Hu, R. and Xia, B., 2009, Sediment-hosted gold deposits in Guizhou, China: Products of wall-rock sulfidation by deep crustal fluids, *Economic Geology*, 104, 73–93.
- Thomas, J. B., Watson, E. B., Spear, F. S., Shemella, P. T., Nayak, S. K. and Lanzirrotti, A., 2010, TitaniQ under pressure: The effect of pressure and temperature on the solubility of Ti in quartz, *Contributions to Mineralogy and Petrology*, 160, 743–759.
- Thomas, J. B., Watson, E. B., Spear, F. S. and Wark, D. A., 2015, TitaniQ recrystallized: experimental confirmation of the original Ti-in-quartz calibrations, *Contributions to Mineralogy and Petrology*, 169,

- Thomas, R., Förster, H.-J., Rickers, K. and Webster, J. D., 2005, Formation of extremely F-rich hydrous melt fractions and hydrothermal fluids during differentiation of highly evolved tin-granite magmas: A melt/fluid-inclusion study, *Contributions to Mineralogy and Petrology*, 148, 582–601.
- Thomas, R. and Davidson, P., 2016, Revisiting complete miscibility between silicate melts and hydrous fluids, and the extreme enrichment of some elements in the supercritical state - Consequences for the formation of pegmatites and ore deposits, *Ore Geology Reviews*, 72, 1088–1101.
- Tsui, T. F. and Holland, H. D., 1979, The analysis of fluid inclusions by laser microprobe, *Economic Geology*, 74, 1647–1653.
- Ulrich, T., Günther, D. and Heinrich, C., 2001, The evolution of a porphyry Cu-Au deposit, based on LA-ICP-MS analysis of fluid inclusions: Bajo de la Alumbrera, Argentina, *Economic Geology*, 96, 1743–1774.
- Ulrich, T. and Mavrogenes, J., 2008, An experimental study of the solubility of molybdenum in H₂O and KCl-H₂O solutions from 500 °C to 800 °C, and 150 to 300 MPa, *Geochimica et Cosmochimica Acta*, 72, 2316–2330.
- Van Marcke De Lummen, G., 1986, Geochemical evolution of the Land's End granite (south-west England) in relation to its tin potential in the light of data from western marginal areas, *Proceedings - Ussher Society*, 6, 398–404.
- Vanko, D. A., Bodnar, R. J. and Sterner, S. M., 1988, Synthetic fluid inclusions: VIII. Vapor-saturated halite solubility in part of the system NaCl-CaCl₂-H₂O, with application to fluid inclusions from oceanic hydrothermal systems, *Geochimica et Cosmochimica Acta*, 52, 2451–2456.
- Veksler, I. V., 2004, Liquid immiscibility and its role at the magmatic-hydrothermal transition: A summary of experimental studies, *Chemical Geology*, 210, 7–31.
- Wark, D. and Watson, E., 2006, TitaniQ: A titanium-in-quartz geothermometer, *Contributions to Mineralogy and Petrology*, 152, 743–754.
- Wark, D. A., Hildreth, W., Spear, F. S., Cherniak, D. J. and Watson, E. B., 2007, Pre-eruption recharge of the Bishop magma system, *Geology*, 35, 235–238.

- Watt, G. R., Wright, P., Galloway, S. and McLean, C., 1997, Cathodoluminescence and trace element zoning in quartz phenocrysts and xenocrysts, *Geochimica et Cosmochimica Acta*, 61, 4337–4348.
- Webster, J., Thomas, R., Förster, H.-J., Seltmann, R. and Tappen, C., 2004, Geochemical evolution of halogen-enriched granite magmas and mineralizing fluids of the Zinnwald tungsten mining district, Erzgebirge, Germany, *Mineralium Deposita*, 39, 452–472.
- Webster, J. D., Holloway, J. R. and Hervig, R. L., 1989, Partitioning of lithophile trace elements between H₂O and H₂O + CO₂ fluids and topaz rhyolite melt, *Economic Geology*, 84, 116–134.
- Wedepohl, H. K., 1995, The composition of the continental crust, *Geochimica et Cosmochimica Acta*, 59, 1217–1232.
- Wiebe, R. A., Wark, D. A. and Hawkins, D. P., 2007, Insights from quartz cathodoluminescence zoning into crystallization of the Vinalhaven granite, coastal Maine, *Contributions to Mineralogy and Petrology*, 154, 439–453.
- Williams-Jones, A., Samson, I., Ault, K., Gagnon, J. and Fryer, B., 2010, The genesis of distal zinc skarns: Evidence from the Mochito deposit, Honduras, *Economic Geology*, 105, 1411–1440.
- Yardley, B., Banks, D. A., Bottrell, S. H. and Diamond, L. W., 1993, Post-metamorphic gold-quartz veins from NW Italy: the composition and origin of the ore fluid, *Mineralogical Magazine*, 57, 407–422.
- Zajacz, Z., Seo, J. H., Candela, P. A., Piccoli, P. M., Heinrich, C. A. and Guillong, M., 2010, Alkali metals control the release of gold from volatile-rich magmas, *Earth and Planetary Science Letters*, 297, 50–56.
- Zajacz, Z., Candela, P., Piccoli, P., Wälle, M. and Sanchez-Valle, C., 2012, Gold and copper in volatile saturated mafic to intermediate magmas: Solubilities, partitioning, and implications for ore deposit formation, *Geochimica et Cosmochimica Acta*, 91, 140–159.
- Zhitova, L. M., Kinnaird, J. A., Gora, M. P. and Shevko, E. P., 2016, Magmatogene fluids of metal-bearing reefs in the Bushveld Complex, South Africa: Based on research data on fluid inclusions in quartz, *Geology of Ore Deposits*, 58, 58–81.

8. Acknowledgements

I would like to thank Prof. Dr. Stefan Weyer and PD Dr. Ingo Horn for giving me the opportunity to work as a scientific researcher in the geochemistry group and for their trust in me to perform this doctoral research study. It was a pleasure for me to work on this outstanding project with the chance to use a high-end analytical system and to develop a new method with such great technological progress. I would also like to thank them for giving me the chance to visit several short courses and conferences.

I would like to thank PD Dr. Ingo Horn for his technical support at the Femtosecond laser and the mass spectrometers, for his ideas that were a big support for me in the realization of this project and for his readiness to act as a referee.

Special thanks go to Prof. Dr. Axel Müller for his readiness to support this project and to provide the sample material. His spontaneous idea to provide the samples from the Sn-W granites was a very important step in the execution of this project and gave me the chance to complete this doctoral study with a meaningful case study. I am very grateful for all his support during the last three years and his willingness to act as a referee for my graduate thesis.

Prof. Jörg Bachmann is thanked for being the chairman of the examination board.

Prof. Dr. Francois Holtz is thanked for reviewing this thesis, his helpful discussions and his contributions to the GeoFluxes Graduate School.

I would also like to thank the initiators of the GeoFluxes Graduate School and the “Niedersächsisches Ministerium für Wissenschaft und Kultur” for funding this project.

Julian Fiege is thanked for providing the sample from the Gottesberg deposit and his sample preparations.

Many thanks go to Insa Cassens for being a perfect team-player, her good ideas, fruitful discussions and the time that we spend together in the labs, at meetings, conferences and field trips.

Furthermore I would like to thank Dr. Stephan Schuth for his support with the mass spectrometer and for his intense care for the laboratories.

Evgeniya Dupliy and Linda Oppermann made a great job at the microthermometry and measured hundreds of inclusions for this work. Thank you very much for this.

Dr. Stefan Dultz is thanked for the help at the laser microscope.

Many thanks go to the colleagues from the geochemistry group and from the Institut für Mineralogie. I enjoyed working in this nice atmosphere, and especially the “coffee brakes” with my colleagues from the geochemistry.

Finally, I would like to thank my parents who made all this possible with their support for my studies from the beginning in 2006 until the end in 2016, and Désirée for her support and the time we spend together in the last years.

9. Curriculum Vitae

Moritz Albrecht

Kronenstraße 36

30161 Hannover

born on 28th of April 1986 in Hannover

Education

06/2012 - today: PhD candidate, Leibniz Universität Hannover, Institut für Mineralogie

- PhD thesis: „The role of the fluid composition in the formation of hydrothermal Sn-W ores“, supervised by Prof. Stefan Weyer & PD Dr. Ingo Horn

06/2012 – 12/2015: Research Scientist, Institut für Mineralogie Hannover, Geochemistry group, Prof. Stefan Weyer

- Development of a laser ablation method for trace element determinations in fluid inclusions (fs-LA-SF-ICP-MS, Thermo Fisher Element XR)
- Support of guest scientists and their analysis with fs-LA-ICP-MS

10/2009 – 06/2012: M.Sc. in Geosciences, Leibniz Universität Hannover

- Master thesis: „Si-Isotopie in den Brennhaaren der *Urtica dioica* in der Wachstumsperiode“
- Determination of silicon isotope fractionation via laser analytics (fs-LA-MC-ICP-MS, Thermo Fisher Neptune)

10/2006 – 09/2009: B.Sc. in Geosciences, Leibniz Universität Hannover

- Bachelor thesis: „Si-Isotopien in Gesteinen der ozeanischen Kruste“

10/2005 – 06/2006: Alternative service

- City administration Barsinghausen, environmental service

08/2002 – 06/2005: Abitur, Hannah-Arendt Gymnasium, Barsinghausen

08/1998 – 06/2002: KGS Goetheschule, Gymnasialzweig, Barsinghausen

08/1996 – 06/1998: KGS Goetheschule, Orientierungsstufe, Barsinghausen

08/1992 – 06/1996: Primary School Großgoltern, Barsinghausen

Scientific experiences and field trips

01/2013: Short Course: “Fluid and Melt Inclusions, Theory and Practice”, ETH Zürich

10/2012: Short Course “Fluids in the Earth”, University of Naples

09/2012: Fluid Inclusion Short Course, University of Leoben

02/2009: Practical training, Bundesanstalt für Geowissenschaften und Rohstoffe, Hannover

- Section „marine resource exploration“, Dr. Bernd Schreckenberger

04/2008 – 12/2011: Student assistant, Institute for Mineralogy Hannover, Geochemistry group, Prof. Friedhelm von Blanckenburg

- Analyses with MC-ICP-MS and ICP-OES
- Geochemical sample preparation
- Administrative work in the clean lab facility

07/2014: Euro-Granites field trip, Cornwall, UK

08/2010: Iceland field trip

07/2009: Geological mapping: “Münchberger Gneissmasse”

02/2007: Geological mapping: “Ahlsburg”, Mesozoic

Competences

- German, English (very good), French (basics)
- IT: Microsoft Office, CorelDraw, ArcGIS.
- Analytical skills: LA-ICP-MS, MC-ICP-MS, microthermometry (expert knowledge), ICP-OES, Raman-spectroscopy, electron microprobe, microscopy, clean lab work
- Driving license class „B“

Hannover, 23th of August 2016

10. List of Publications

Journals

M. Albrecht, I.T. Derrey, I. Horn, S. Schuth and S. Weyer, 2014: Quantification of trace element contents in frozen fluid inclusions by UV-fs-LA-ICP-MS analysis, *Journal of Analytical Atomic Spectrometry*, 29, 1034 – 1041.

Abstracts

M. Albrecht, I.T. Derrey, I. Horn, A. Müller, F. Holtz, S. Weyer, 2015: UV-fs-LA-ICP-MS analyses of fluid inclusions: Insights into the formation of tin ore deposits , *Goldschmidt Conference 2015*, Prague.

M. Albrecht, I.T. Derrey, I. Horn, A. Müller, F. Holtz, S. Weyer, 2015: UV-fs-LA-ICP-MS Analyses of Fluid Inclusions from Tin Ore Deposits, *GeoBerlin 2015*.

M. Albrecht, I.T. Derrey, I. Horn, A. Müller, S. Schuth, S. Weyer, 2014: A new Procedure for Trace Element Analysis of Fluid Inclusions with UV-fs-LA-ICP-MS and its Application on Tin Granites, *DMG Tagung 2014*, Jena.

M. Albrecht, I.T. Derrey, I. Horn, S. Schuth, S. Weyer, 2014: A new Procedure for Trace Element Analysis of Fluid Inclusions with UV-fs-LA-ICP-MS, *European Workshop on Laser Ablation 2014*, London.

M. Albrecht, I.T. Derrey, I. Horn, S. Schuth, F. Melcher; S. Weyer, 2013: Analysis of fluid inclusions with fs-LA-ICP-MS, *Goldschmidt Conference 2013*, Florence.